Joints in MgB_2 Superconducting Coils

Muslum Guven

St Catherine's College

A thesis submitted for the degree of Doctor of Philosophy

Supervised by

Chris Grovenor & Susannah Speller

Department of Materials

University of Oxford

Trinity Term 2024

Abstract

Superconducting materials have been utilized for over a century, with applications expanding in various fields, including Magnetic Resonance Imaging (MRI) systems, which require highly stable magnetic fields. These systems rely on superconducting coils that maintain a persistent current to generate stable magnetic fields at operating temperatures below the material's critical temperature (T_c). Currently, most MRI systems use low-temperature Nb-Ti superconductors, cooled to 4.2 K with liquid helium (LHe). However, the growing demand for such systems has increased helium consumption and costs, prompting the search for alternative materials. MgB_2, with its higher critical temperature (39 K), offers a promising solution for helium-free superconducting magnets.

This thesis presents a method for fabricating persistent joints using monofilament reacted MgB_2 wires. The process involves inserting the wires into pre-drilled holes filled with unreacted Mg+B powder, followed by pressing to ensure close mechanical contact. A two-step heat treatment is then applied to optimize density, connectivity, and reduce non-superconducting impurities. The resulting joints demonstrate excellent connectivity, achieving residual resistances below 10^{-13} Ω. Persistent currents of 172 A at self-field and 160 A under a 1 T background field were measured, corresponding to a critical current ratio (CCR) of 78% at 20 K. These results indicate the feasibility of producing persistent-mode MgB_2 magnets operating below 20 K, which could significantly reduce costs for MRI systems using cryogen-free technology.

Additionally, for the first time in the literature, a superconducting joint has been produced between Nb-Ti wires using an MgB_2 filler. A coil fabricated with this joint achieved an ultra-low resistance of approximately 4.2×10^{-15} Ω and a trapped current of 7 A under 4.7 K and self-field conditions. This study highlights the potential of MgB_2 filler as a non-toxic alternative to the Pb-based filler currently used in Nb-Ti wire joints.

Acknowledgements

During the course of my thesis journey, I have been fortunate to receive invaluable support, guidance, and companionship from a remarkable array of individuals, to whom I owe an immense debt of gratitude.

First and foremost, I would like to express my sincere gratitude to my DPhil supervisors, Chris Grovenor and Susie Speller. I am truly grateful for your invaluable guidance, unwavering commitment, profound scientific knowledge, and relentless encouragement to pursue unconventional experiments. Your meticulous editing and insightful feedback have played a pivotal role in shaping the final outcome of this research.

The studies presented in this thesis would not have been possible without the material and moral support of the Republic of Türkiye. I extend my deepest gratitude to the government for its invaluable contributions to the YLSY scholarship, established by the Ministry of National Education in 1929 under the leadership of Mustafa Kemal Atatürk. This pioneering initiative has been instrumental in enabling my academic journey, and I am profoundly thankful for the unwavering dedication of all involved in sustaining this prestigious program.

I am also grateful to my esteemed industrial collaborator, whose contributions have been indispensable. I extend my thanks to Mehmet Kutukcu and Serdar Atamert and EPOCH Wires Ltd for their generous provision of materials, insightful guidance, their technical expertise, invaluable assistance with samples, and access to cutting-edge equipment that propelled this project forward.

To the entire staff at Oxford materials, whose collective efforts have made my time in the department truly enjoyable, I offer my sincere appreciation. Although it is impossible to acknowledge each individual, I am grateful for your contributions.

My heartfelt thanks also go to my fellow office/lab mates, who provided much-needed respite from my academic endeavours. Petr Zagura, Zilin Gao, Jarrod Lewis, William Iliffe, Clara Barker and Tayebeh Mousavi, your camaraderie and support were invaluable.

Lastly, I take great pleasure in expressing my deepest appreciation to my dear wife, Merve, who has been by my side in every decision I made and has been my closest supporter during all the challenging times. I am truly grateful to my beloved mother, Meryem, and father, Mustafa, who have raised me and guided me to reach this point, always providing unwavering support. I would also like to extend my heartfelt gratitude to my brother, Adem, and his wife, Eda, and most importantly, to my beloved nephew, little Mustafa Eren, who never fails to bring joy into our lives.

Statement of Originality

The research presented in this thesis was conducted by the author within the Department of Materials at the University of Oxford, spanning the period from October 2020 to June 2024. Under the guidance and supervision of Prof. C.R.M. Grovenor and Prof. S.C. Speller, this work represents an original contribution to the field.

It is important to note that no portion of this thesis has been previously submitted for the attainment of a degree at this or any other academic institution. While the insights and findings of other authors have been incorporated into the text, proper attribution has been duly provided. A comprehensive list of references is included at the conclusion of the thesis to acknowledge all relevant sources.

Several aspects of the research described in this thesis have been published in a reputable scholarly journal and have also been shared through presentation at esteemed conferences. The specific publication and conference presentations are outlined below:

Publication:

- M. Guven et al., “Persistent MgB2 joints for react and wind magnets,” Supercond. Sci. Technol., Oct. 2023, doi: 10.1088/1361-6668/AD06C3.

Key Conference Presentations:

Oxford Material Poster Symposium Oxford, UK, April 2022, Oral Poster Presentation - \ MgB_2 Joints in Superconducting Coils

International Conference on Superconductivity and Magnetism Muğla, Türkiye, May 2023, Oral Poster Presentation - \ MgB_2 Joints in Superconducting Coils

Science and Technologies in High-Magnetic Fields - Wolfson College, Oxford, 6 Dec 2023

Oral Poster Presentation -\ Persistent MgB_2 joints for react and wind magnets.

Contents

List of Tables

List of Figures

Chapter 1 Introduction

1.1 Background and Motivation

The application of superconducting materials has revolutionized engineering, enabling advanced electromagnets with state-of-the-art wires. Successful wire development depends on intrinsic properties (like coherence length and penetration depth), microstructure (including crystal structures and defects), and wire architecture (like 20,000 filament Nb-Ti strands [1] and Rutherford cables [2]) ensuring stability and cryogen circulation. These factors ensure efficient operation. Technologically, wires come in single or multifilament configurations. Multifilament wires bundle multiple filaments for enhanced capacity, strength, and AC loss control, while single filament wires consist of one continuous filament.

The electromagnets made of superconducting wires find extensive use in-situations requiring fields over prolonged periods. Notably, they play a pivotal role in critical applications such as magnetic resonance imaging (MRI) scanners [3], nuclear magnetic resonance (NMR) devices [4], superconducting magnetic energy storage systems (SMES) [5], particle physics experiments like the “A Toroidal LHC Apparatus" (ATLAS) detector magnet [6], and high-field facilities like those at the National High Magnetic Field Laboratory (NHMFL) [7].

Superconducting materials sustain stable magnetic fields by generating supercurrents without resistance. In MRI scanners, precise measurements rely on the "persistent mode" (PM), where electromagnets function as quasi-permanent magnets. Achieving this involves injecting a current and closing a superconducting switch to create a closed circuit. If the circuit has low enough resistance, the current persists, ensuring a stable magnetic field. For example, a typical 21 Tesla, 900 MHz NMR magnet contains joints with a working current of 250 A [8], requiring resistance lower than 10^{-12} Ω for stability [9]. Commercially, joints

with operational resistances ranging from 10^{-12} to 10^{-14} Ω are routinely fabricated for MRI magnets using various superconducting materials. Producing these joints requires establishing a genuinely superconducting current path between the parent conductors.

Expense is the significant consideration in the construction of superconducting technologies. An estimate of the cost versus operating temperature performance of commercially available superconducting wires is given in **Figure 1.1**. The inset shows more detailed prices of MgB_2, Nb-Ti, and Nb_3Sn.

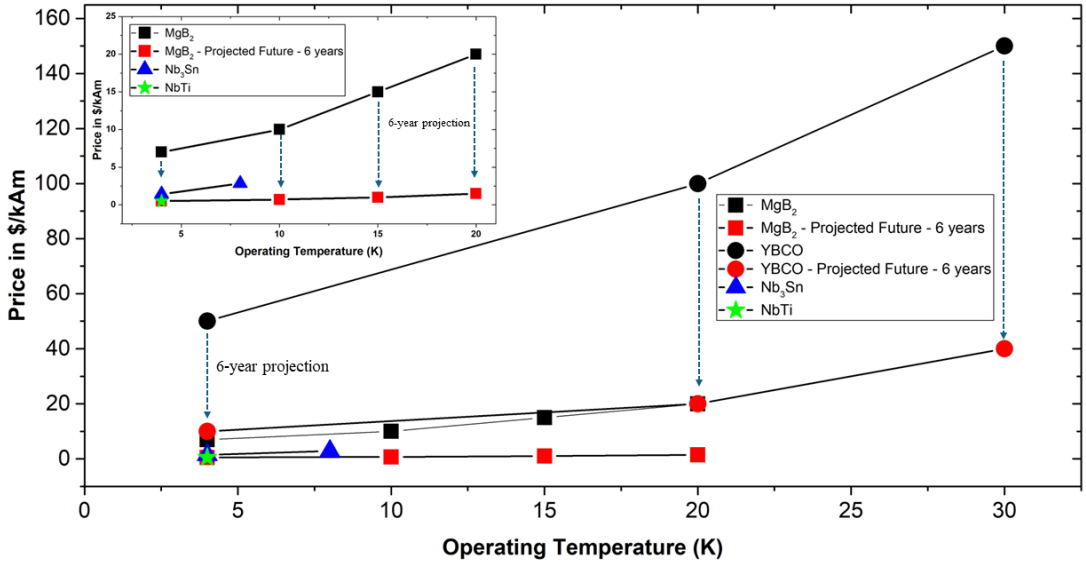

Figure 1.1 *Comparison of the cost of the different superconducting wires at 2 T. Data were obtained from* [10]

The pricing information presented in the graph covers temperatures between 4 K and 30 K, with forecasts suggesting that the prices of Nb-Ti and Nb_3Sn will remain same. Although Nb-Ti and Nb_3Sn are relatively cheap, they only operate at low temperatures, and to increase the current carrying capacity are normally operated at 4.2 K or below. In terms of MgB_2, it has a wider range of operating temperature (4.2-20 K) but is more expensive (20 $/kAm maximum) than Nb_3Sn or Nb-Ti. However, it remains cheaper than the commercially available high temperature materials, YBCO and BSCCO.

Developing effective jointing techniques is crucial for magnetic resonance applications, especially with the integration of advanced materials like high-temperature superconductors (HTS) and intermediate temperature ceramics such as magnesium diboride (MgB_2). Challenges in designing reliable jointing processes include chemical compatibility between wires and filler materials, joint mechanical strength, optimizing heat treatment, and ensuring reproducibility. Despite some progress, achieving commercially viable jointing methods remains an ongoing pursuit, potentially impacting the practical deployment of these materials in real-world magnet systems. Particularly, while many studies have explored joints for MgB_2 wires assembled before heat treatment of precursor wires, there is a notable gap in the literature regarding joints fabricated after the wires undergo the reaction to form the superconducting compound. Addressing this gap presents a compelling research opportunity that could yield novel solutions and advance commercial applications of applied superconductivity.

1.2 Research objectives of this thesis

The primary aim of this thesis is to investigate and address the critical gap in jointing techniques for superconducting coils, with a specific focus on jointing already reacted MgB_2 wires because this is more suited to commercial magnet manufacture. To achieve this overarching goal, the following research objectives have been identified:

Understanding the structural characteristics of MgB_2: Production of MgB_2 bulk samples was carried out before initiating the manufacturing of MgB_2 joints. These initial inquiries predominantly centred around investigating the effects of different ratios of constituents and various methods of heat treatment on the structural attributes.

Characterization of reacted MgB_2 wires: Epoch Wires Ltd., a collaborating partner situated in Cambridge, United Kingdom, specializes in the production of monofilament

MgB_2 wires. Before studying the manufacturing of joints, it was necessary to evaluate the starting wire. Wires were procured in both reacted and unreacted states from Epoch. Initially, the reacted wires underwent characterization, followed by replicating commercial thermal treatments and comparing the performance of wires reacted in the laboratory setting.

Production of reacted MgB_2 joints: To achieve a comprehensive understanding of the MgB_2 joint technology available in the market, I carried out the manufacturing of MgB_2 joints using Epoch wires and their patented process at their facilities to compare to the innovative design introduced in this thesis.

Characterization of reacted MgB_2 joints: The initial goal encompassed performing a comprehensive characterization of joints fabricated using reacted MgB_2 wires. This entails an examination of the joints' structural, electrical, and mechanical attributes, with the intention of clarifying their behaviour under diverse operational circumstances. This involves assessing key parameters such as heat treatment procedures, electrical conductivity, and design parameters.

Coil fabrication with developed joint technology: It is crucial to determine the resistance of the joint in a coil, particularly when considering its use in applications like MRI scanners. In this context, the use of persistent mode operation for the joint becomes essential. To address this need, coils were manufactured using the mentioned joining techniques.

Dissimilar Joint Fabrication Attempts: Using the same jointing strategy, efforts have been made to form joints between MgB_2 and some other advanced technological superconductors, including monofilamentary Nb-Ti and multifilamentary Bi-2212. A few short joints and coils were produced, and their characterization completed.

Chapter 2 Literature Review

2.1 Introduction

This chapter provides a comprehensive review of the theoretical foundations of superconductivity, followed by an overview of MgB_2 superconductors. It discusses their physical and superconducting properties, temperature-dependent synthesis characteristics, and the effects of doping elements. It covers wire production methods, including recent advancements and their impact on superconducting properties. Additionally, it evaluates joint fabrication procedures, coil manufacturing techniques, and related challenges through case studies. The chapter concludes with an examination of dissimilar joint studies from the literature.

2.2 Theoretical background

In 1911, Heike Kamerlingh Onnes discovered the phenomenon of superconductivity when mercury's resistance vanished below a critical temperature [11]. This breakthrough led to the exploration of numerous elements and compounds, resulting in the discovery of new superconducting materials. These discoveries paved the way for the development of various small and large-scale superconducting technologies. Small-scale applications include superconducting quantum interference devices (SQUID) [12], SIS photon detectors [13], rapid single flux quantum circuits [14], and quantum qubits [15]. On the other hand, large-scale applications encompass Nuclear Magnetic Resonance (NMR) [16], Magnetic Resonance Imaging (MRI) [17], magnets for the Large Hadron Collider [18], and superconducting electric motors [19]. Some of the key superconducting materials used in these applications include Nb-Ti, Nb_3Sn, $Bi_2Sr_2CaCu_2O_8$, $YBa_2Cu_3O_7$, and MgB_2, which can be employed in various forms such as films, wires, bulks, and tapes. **Table 2.1**. provides examples of how these materials may be utilized in different applications. In large-scale

applications like MRI, the very high field stability has driven the need for systems based on superconducting magnets [9] without power supplies.

Table 2.1 *Some superconducting material options for different applications.*

Superconducting Material	Application	Form	Ref.
Nb-Ti	-Magnetic Resonance Imaging Magnets	-Wire	[20]
	-Large Hadron Collider	-Wire	[21]
Nb_3Sn	-Fusion Research Magnets	-Wire	[22]
	-International Thermonuclear Experimental Reactor (ITER)	-Wire	[23]
$Bi_2Sr_2CaCu_2O_8$	-Solid-State Terahertz sources	-Film	[24]
	-High Field Magnets	-Wire	[25]
$Bi_2Sr_2Ca_2Cu_3O_{10}$	-Current Leads	-Tape	[26]
NbN	-Single-photon optical detectors	-Film	[27]
$REBa_2Cu_3O_7$	-HTS microwave Filter Technologies	-Film	[28]
	-DC Power Cables	-Film	[29]
MgB_2	-Fault current limiters	-Wire	[30]
	-Bolometers	-Film	[31]
	-MRI	-Wire	[32]
	- Leads for High Luminosity Upgrade LHC	-Wire	[33]

After the required current is set, the power supply is removed from the system and the device continues to operate as long as it is cooled below T_c [34]. The ability to operate for years with a single installation is critical in hospitals that do not have expert cryogenic or magnet system engineers. One important consideration is that even a persistent-mode magnet has a slight circuit resistance, which causes field decay at a rate given by the formula derived from modelling it as an inductor (L) and a resistor (R) circuit below.

$$I(t) = I_0 e^{\frac{-R}{L}t} \tag{2.1}$$

where $I(t)$ is the current at time, t, I_0 is the current at t=0, R is the overall circuit resistance, and L is the self-inductance which depends on the coil geometry. If the resistance value is zero, there is no energy dissipation and the current will remain the same. However, if there is a finite resistance, R, in the system, the current will slowly decay [35].

2.3 Basic theory of superconductivity

During the early 1900s, there was no precise theory addressing the impact of temperature on the resistance of metals. Heike Kamerlingh Onnes's breakthrough achievement in liquefying helium in 1908 marked a significant advancement in this research. In 1911, Onnes conducted further experiments to explore the effect of temperature on resistance. Using mercury for its ease of purification, he discovered that its resistance abruptly vanished at a temperature of 4.2 K [11]. This discovery led to the classification of materials exhibiting this unique electrical property as superconductors, with the temperature at which resistance disappears designated as the *critical temperature*, T_c.

2.3.1 Meissner effect

In 1933, Meissner applied a magnetic field to superconducting materials, and observed that the material expelled the magnetic field [36]. He also noticed the magnetic field was not expelled when the applied magnetic field increased beyond a specific value. This point was named as the *critical field*, H_c and is related to temperature in conventional superconductors by the equation;

$$H_c = H_0 \left[1 - \left(\frac{T}{T_c}\right)^2\right] \tag{2.2}$$

where H_0 is the critical field at 0 K.

Above the transition temperature, the normal region exhibits no critical field (H_c=0) and experiences complete penetration of an applied magnetic field. As the superconductor undergoes cooling below the transition temperature, the critical field gradually increases towards its maximum value H_0. The specific temperature dependencies of $H_c(T)$ and related parameters like the *penetration depth*, $\lambda(T)$, which describes how far an applied magnetic field may enter a superconductor, and the *coherence length*, $\xi(T)$, which indicates that at the interface between the superconducting state and the normal state, the concentration of superelectrons increases gradually over a finite length scale rather than suddenly. Ginzburg and Landau recognized that the ratio between the *coherence length* and the *penetration depth* affects the nature of superconductivity, leading to the introduction of the Ginzburg-Landau parameter, κ;

$$\kappa = \frac{\lambda}{\xi} \tag{2.3}$$

They classified superconductors in terms of κ. If the κ value of a superconductor is $< \frac{1}{\sqrt{2}}$, the material is a *Type I* superconductor, otherwise if, $\kappa > \frac{1}{\sqrt{2}}$, it is a *Type II* superconductor. In *Type I* superconductors $\xi >> \lambda$, but in the *Type II* superconductors, $\lambda >> \xi$ [37].

2.3.2 Type I and Type II superconductors

After Meissner's theory about H_c, it was also discovered that while *Type I* superconducting materials exhibit complete loss of superconductivity abruptly at H_c, *Type II* superconductors have two critical fields, H_{c1} and H_{c2}. **Figure 2.1** shows that, while *Type I* superconductors exist only in a narrow range of magnetic field, in *Type II* materials superconductivity typically exists up to much higher magnetic fields. *Type II* superconductors exhibit the *Meissner state* (complete flux exclusion) up to the *lower critical field* (H_{c1}). Magnetic flux begins to penetrate the superconductor at fields above H_{c1} as discrete, quantised flux lines

within the superconducting matrix. When a superconducting material is exposed to an external magnetic field, denoted as H_{c1} as illustrated in **Figure 2.1**b, it maintains its superconducting properties until it reaches a critical threshold known as H_{c2}.

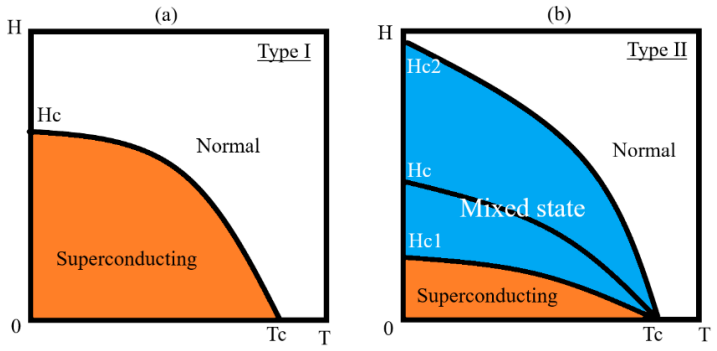

Figure 2.1 *The difference between Type I and Type II superconductors. Reprinted from* [37] *(Copyright © 2015 John Wiley & Sons, Ltd)*

This phenomenon is characteristic of *Type II* superconductors exclusively. The magnetic field range between H_{c1} and H_{c2} is referred to as the *irreversible field*, denoted as H_{irr}. This is also known as the mixed state (also called the Shubnikov phase), shown schematically in **Figure 2.2**. As the field is increased further, the flux line density increases, and the *upper critical field* (H_{c2}) is reached when the non-superconducting flux line cores touch and the material becomes completely normal [37].

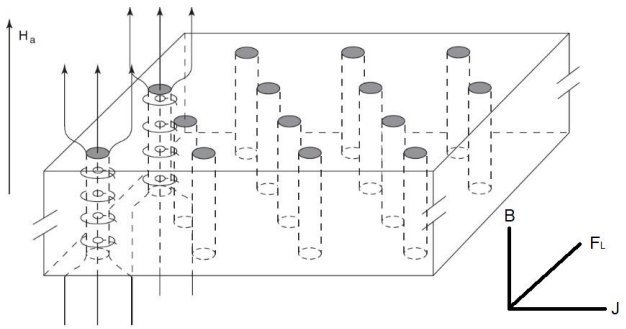

Figure 2.2 *Illustration of Shubnikov Phase. Reprinted from* [37] *(Copyright © 2015 John Wiley & Sons, Ltd)*

In the Shubnikov phase, circulating supercurrents flow around the magnetic flux lines, which are also called Abrikosov vortices or fluxons.

2.3.3 Flux pinning

When we have a current moving from the left to the right, the positive *J* direction (**Figure 2.2**), this movement generates a magnetic field *B*, and a magnetic force called the *Lorentz Force*, F_L. These are aligned as shown in **Figure 2.2**. The Lorentz Force can be calculated;

$$\overrightarrow{F_L} = \vec{B}\ x\ J = N\Phi_0\ x\ nq\vec{v} \tag{2.4}$$

where *N* is the number of flux lines per unit area, n is the density of superelectrons, Φ_0 is the single quantum of flux going through each flux line, v is the velocity of superelectrons, and q is the charge of the superelectrons. There is no pinning force in perfect (undoped, perfect crystal with no defects) *Type II* superconductors that can resist F_L, so these vortices are constantly in motion. Since each flux carries electrons at velocity v, an electric field *E* is induced;

$$\vec{E} = N\vec{v}\ x\ \Phi_0 = \vec{v}\ x\ \vec{B} \tag{2.5}$$

This formula explains that flux line motion creates an electric field, *E*, that causes the material to lose its zero-resistance property. This mobility, which creates resistance in a perfect *Type II* superconductor, must be minimized in materials for practical applications. The I_c of a *Type II* superconductor is the current that can be carried before resistance is introduced, and therefore engineering the microstructure to make it difficult for flux lines to move will lead to an increase in I_c.

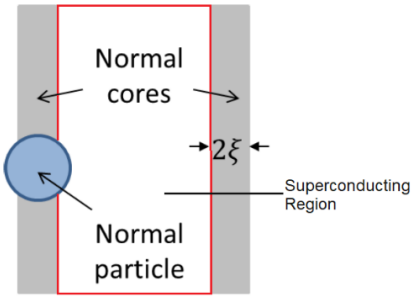

Figure 2.3 *Simple explanation of the pinning mechanism.*

There are several ways to stop this movement and this process is called *flux pinning*. The core of the vortices containing the magnetic flux lines are small volumes of normal material with a free energy higher than the surrounding material. A normal particle put in the middle of the flux line, showed as the blue particle in **Figure 2.3**, reduces the total free energy of the system because it is already in the normal state and reduces the total volume of superconductor that has to be turned normal to create the flux line core. That is the mechanism for flux pinning where flux lines are trapped in a potential well created by crystalline defects in the superconducting material. Many defects can contribute to generating the pinning force, as shown schematically for an YBCO thin film in **Figure 2.4**.

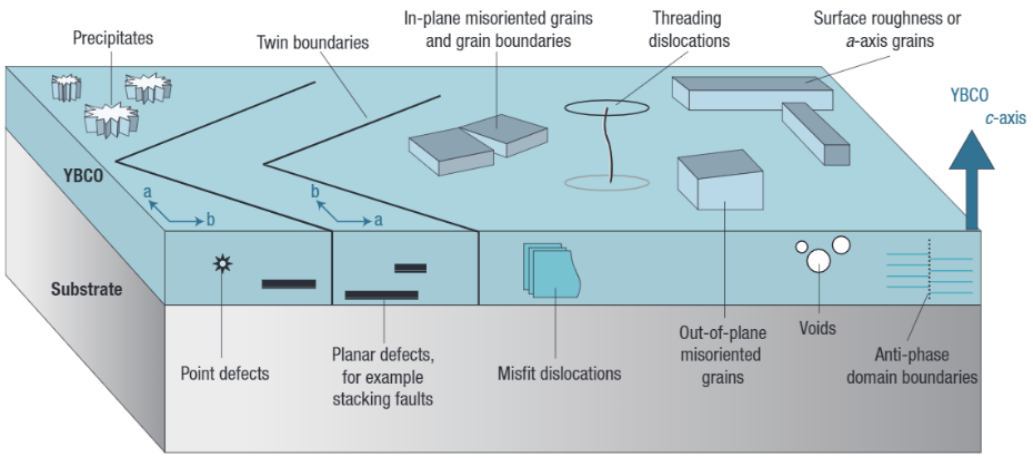

Figure 2.4 *Some pinning mechanisms in YBCO. Reprinted from* [38] *(Copyright © 1969, Springer Nature Limited)*

When the pinning force F_p exceeds the F_L, the vortices are pinned at 0 K and the total resistance becomes zero. At higher temperatures, however, there is a small probability of thermal activation of a flux line unless pinning is very strong which enables the pinned vortices to move and again generate resistance. This mechanism called *thermally activated flux flow* or *flux creep*.

2.4 Performance of technological superconductors

Figure 2.5 compares the engineering critical current densities of various technological superconductors, plotted as a function of the applied magnetic field at 4.2 K [62–65]. This comparison focuses on the entire wire rather than just the critical current density (J_c) of the superconductor itself. Despite demonstrating the lowest J_c/B performance in the graph, MgB_2 showcases greater suitability for specific applications compared to other materials, particularly in lower field applications (<5 T), owing to its relatively lower cost as given in **Figure 1.1**. Additionally, the cooling expense is relatively lower for MgB_2 compared to Nb-Ti and Nb_3Sn, thanks to its higher T_c.

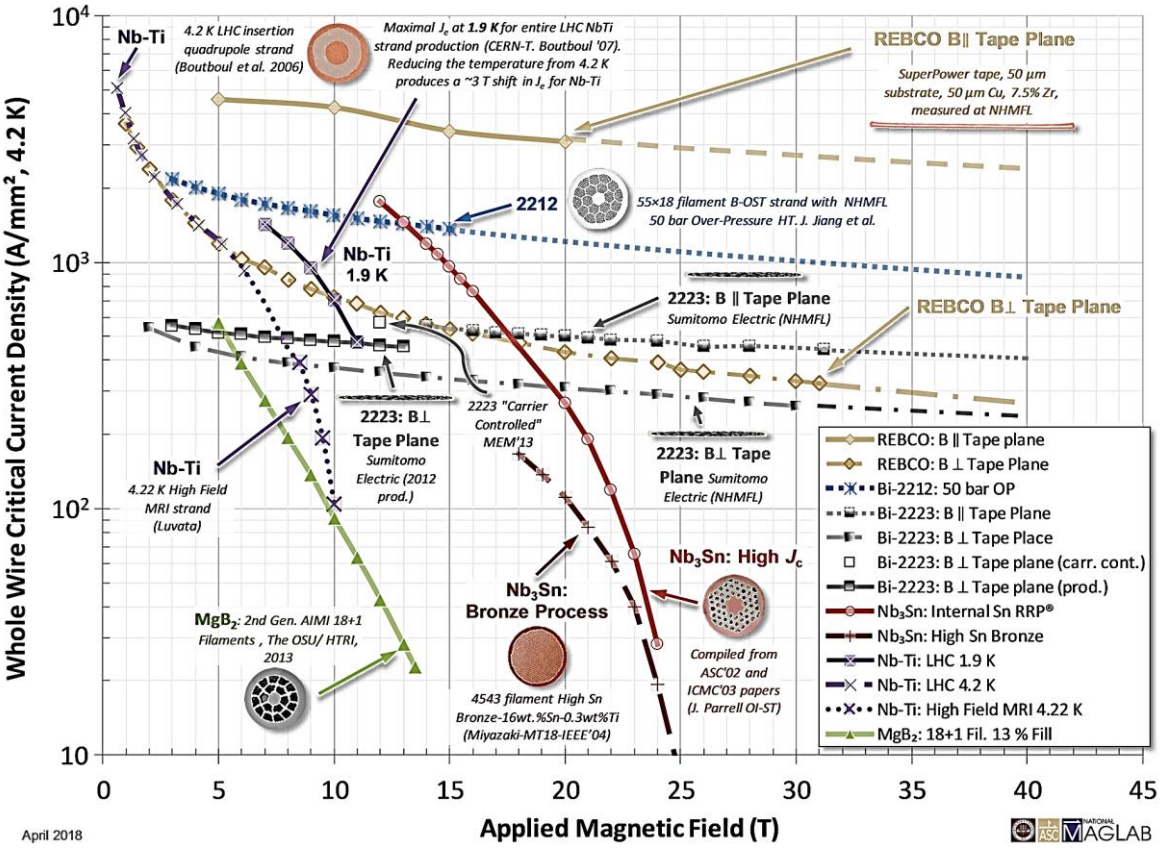

Figure 2.5 *J_c/B performance of technical superconductors at 4.2 K* [43].

The versatile applications of MgB_2 include its use in poloidal coils within fusion reactors [44], low-field coils for MRI [45], the development of test coils for low-field magnets up to 3 T [46], power transmission cables [47] and power generation [48]. However, this plot only

illustrates the J_c properties of superconductors at 4.2 K. Referring to **Figure 2.6**a-b, it is evident that the irreversibility line and upper critical field of MgB_2 surpass those of low-temperature superconductors (LTS) at elevated temperatures. This renders MgB_2 particularly advantageous for operations, especially at higher temperatures (39 K > T > 4.2 K).

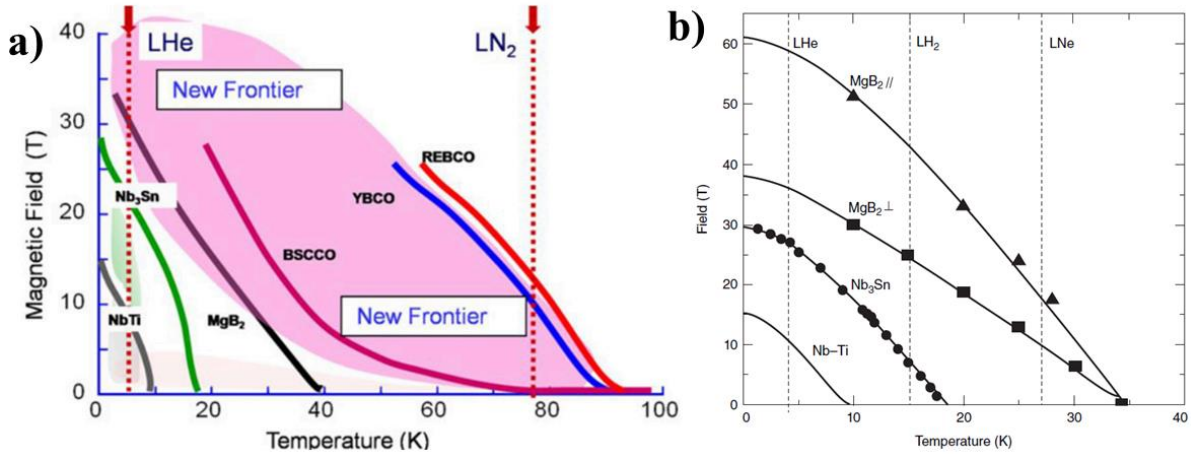

Figure 2.6 *a) Variations in irreversibility fields with temperature differ among technological superconductors like HTS, MgB_2 and alloys. Reprinted from* [49] *and b) upper critical field (H_{c2}) versus temperature for MgB_2 films, bulk Nb-Ti, and bulk Nb_3Sn are depicted. The triangular and square data points represent MgB_2 with the test sample's ab planes oriented parallel (//) and normal (⊥) to the field, respectively. Dashed vertical lines mark the normal saturation temperatures of liquids: helium (LHe), hydrogen (LH_2), and neon (LNe). Reprinted from* [50] *(Copyright © 2006, IEEE)*

2.4.1 Physical properties and characteristics of MgB_2

MgB_2 has been known since the 1950s and became the centre of attention among the superconducting community after the discovery of its superconducting properties below 39 K by Nagamatsu et al. in 2001 [51]. MgB_2 has a hexagonal crystal structure, shown in **Figure 2.7**, with lattice parameters a=0.3086 nm, c=0.3524 nm. The layer of B atoms has strong covalent bonds, while the bonding between the boron and magnesium layers is metallic [52]. Moreover, MgB_2 is a *Type II* superconductor and its conventional superconducting behaviour can be explained by the Bardeen-Cooper-Schrieffer (BCS) theory [35].

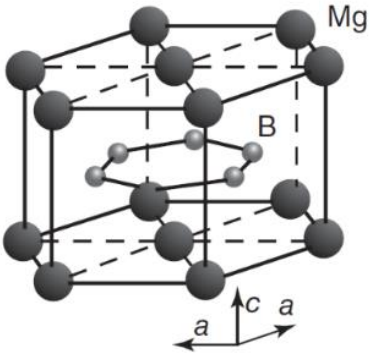

Figure 2.7 *The crystal structure of MgB_2 (adapted from* [51]*, Copyright © 2001, Macmillan Magazines Ltd.)*

Additionally, the alternating structure of magnesium and boron layers causes anisotropic properties [51]. Due to this anisotropy, the upper critical field depends on the orientation of the magnetic field relative to the crystallographic directions.

Hinks et al.[53] investigated the magnesium isotope effect in $^{26}MgB_2$ and $^{24}MgB_2$ using isotopically pure samples. The observed difference in critical temperatures was only 0.1 K. This minimal effect implies that the coupling of Mg electrons is predominantly influenced by phonons in the B planes, suggesting MgB_2 behaves as a conventional metallic superconductor. The elevated critical temperature of MgB_2 is attributed to the high phonon frequencies arising from the low atomic mass of boron.

However, MgB_2 exhibits more intricate physical properties than simple metallic superconductors due to the presence of two superconducting energy gaps. The highest occupied electronic states at the Fermi level primarily consist of σ or π-bonding boron orbitals [52, 54, 55]. A distinctive characteristic of MgB_2 is the incomplete filling of the two σ-bands, where electrons of the σ-bands are confined within the boron planes. The electrons from boron p_z orbitals fill two three-dimensional metallic π-bands. The non-bonding boron π bands have a lowered energy compared to the bonding boron σ bands, resulting in charge transfer from the σ- to π-bands and the formation of hole-doped σ-bands.

Band calculations indicate that the superconductivity in MgB_2 is predominantly governed by the holes in the σ-bands [54]. The σ-band states and the in-plane vibrations of the boron atoms exhibit strong coupling, leading to robust pairing with an energy gap of approximately 7 meV [55]. This strong pairing, confined to the boron planes, only occupies certain regions of the Fermi surface. Additionally, weaker electron pairs are formed by the π-band electronic states on the remaining portions of the Fermi surface, with an associated energy gap of approximately ~2 meV [55].

Some physical properties of MgB_2 are given in **Table 2.2**. In pure MgB_2, the upper critical field parallel to the *c* axis can reach 3 T, but perpendicular to the *c* axis it can reach 15-20T.

Table 2.2 *Physical properties of MgB_2*

Feature	Value	Ref.
T_c	39 K	[51]
Coherence length, ε_c	35±10 nm	[56]
Coherence length, ε_{ab}	39±11 nm	[56]
Penetration depth, λ_{ab}	100 ± 35 nm	[56]
Penetration depth, λ_c	120±15 nm	[56]
Electron mean free path, l	60 nm	[57]
Upper critical field H_{c2}, clean, ($l >> \varepsilon$)	16 T	[57]
dirty, ($l << \varepsilon$)	50 T	[58]
Irreversibility field H_{irr}, clean	7 T	[57]
dirty	15 T	[57]
Lower critical field H_{cl}	30 mT	[57]
Critical current density J_c clean, 5K, Self-field	$5x10^5$ A cm^{-2}	[57]
Critical current density J_c clean, 5K, Self-field, dirty	$1.4x10^7$ A cm^{-2}	[59]

If the MgB_2 is 'dirty' (doped with chemical impurities) these values can be increased to 50-70 T in MgB_2 films [66–69].

2.4.2 Connectivity properties of MgB_2

Rowell [64] showed high electrical resistivity in polycrystalline MgB_2 at above T_c of MgB_2. Typically, in the normal state, if an MgB_2 sample exhibits high resistivity owing to intrinsic defects that scatter free electrons, its T_c should be lowered through alterations in the electron-phonon interaction [65]. However, impure MgB_2 samples with optimal T_c and very high resistivity (~100 Ωcm) have been observed [66], much higher than single crystals [67]. Normal state "connectivity" reflects typical resistance in polycrystalline materials, influenced by intrinsic resistance and additional resistances from the microstructure, such as grain boundaries and defects like MgO. This connectivity dictates overall resistance [68]. Impurity scattering minimally affects temperature-dependent resistivity due to electron-phonon interactions, so normal state connectivity K can be characterized as [68]:

$$K = \frac{\Delta\rho}{\Delta\rho_{single}} \tag{2.6}$$

where $\Delta\rho$ is the resistivity difference between the resistivity values at 300 K and 40 K and $\Delta\rho_{single}$ is the ideal resistivity of a single crystal MgB_2 which is 4.3 μΩcm as measured by Eltsev et al. [67] and Rowell [64]. Matsushita et al. [69] illustrated that the variation in the phonon-related resistivity, denoted as $\Delta\rho$, can be explained through utilization of the three-dimensional site percolation model. This understanding was derived from assessments of the normal-state conductivity performed on MgB_2 bulk samples, where packing factors were deliberately adjusted, as documented by Yamamoto et al. [70] and Matsushita et al. [69].

$$\Delta\rho = \frac{1 - P_c^2}{(aP)^2 - P_c^2}\Delta\rho_{single} \tag{2.7}$$

P represents the packing factor of a MgB_2 sample, with P_c = 0.3117 denoting the critical packing factor for a three-dimensional cubic site percolation system, while 'a' signifies the

proportion of grains not covered by insulating barriers. This suggests that inadequate packing density and insulating phases at grain boundaries are the main factors reducing electrical connectivity in MgB_2. Therefore, improving microstructure densification and ensuring well-connected, uncontaminated grain boundaries are crucial for enhancing MgB_2 connectivity.

In contrast to high temperature superconductors, it was also found that grain boundaries in MgB_2 do not inhibit supercurrent and the conductivity owing to the longer coherence length of MgB_2 [71]. As a result of this finding, it is not necessary to create materials with a strong crystallographic texture to achieve high current densities. Therefore, the industrial manufacture of MgB_2 is potentially much easier than other superconducting materials like REBCO [37].

2.4.3 Thermodynamic properties of MgB_2 during the synthesis

Figure 2.8 shows the Mg-B phase diagram under 101.325 kPa (1 atm) pressure. The diagram indicates decomposition temperatures of 1174°C for MgB_2, 1273°C for MgB_4, and 2509°C for MgB_7. The melting point of Mg is 650°C, with a boiling point of 1090°C, while boron has a melting point of 2050°C. Synthesizing MgB_2 would present significant challenges if it required reacting them at the respective melting points of both elements. The literature provides both upper and lower bounds for the formation enthalpy at 298 K for MgB_2 expressed as -51.97 kJ/g-mol $\leq \Delta_f H_{298}^0 \leq -17.17$ kJ/g-mol and for MgB_4 as -21.0 kJ/g-mol $\leq \Delta_f H_{298}^0 \leq -14.39$ kJ/g-mol [78–80] which makes the MgB_2 more stable.

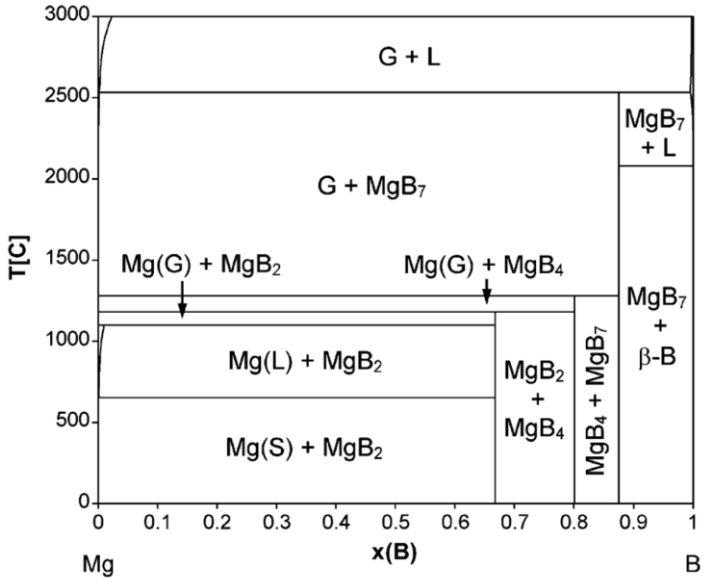

Figure 2.8 *The Mg-B binary phase diagram at 1 atm pressure* [72] *(Copyright © 2008 Elsevier B.V)*

However, it is known that the $\Delta_f H^0_{298}$ value of MgO is about -601.6 kJ/mol [73] which makes the formation of MgO more favourable than that of MgB_2 [75]. This underscores the necessity of a protective atmosphere during MgB_2 synthesis.

Boron and magnesium exhibit starkly contrasting physical characteristics. While boron remains largely inert at temperatures below its melting point, magnesium begins to evaporate even prior to reaching its melting point [76]. Due to magnesium's low melting point and propensity for evaporation, the formation and stabilization of MgB_2 necessitate precise control over the partial pressure of magnesium.

2.4.3.1 MgO presence in MgB_2 during the production

Some studies have observed that MgO is easily formed in MgB_2 samples [83–85]. Excess MgO may result from powder contamination before reaction or oxygen presence during heat treatment. MgO can integrate into MgB_2 in various forms: as nanometre-sized coherent $MgB_2{-}xO_x$ precipitates within the grains [80], as MgO particles within the grains' interior [81], as BO_x–MgO_y–BO_z layers between the grains [82], or as MgO layers [83]. While coherent nonstoichiometric precipitates and MgO particles within the MgB_2 matrix enhance

flux pinning, leading to higher J_c [84], MgO layers at grain boundaries decrease J_c due to reduced connectivity [85]. Oxygen-rich MgB_2 thin films containing nano MgO particles have shown improved H_{c2} and J_c values [86]. Singh et al. [87] conducted a comprehensive study on the impact of oxygen doping on MgB_2, investigating its effects on properties such as T_c, J_c, connectivity, and H_{c2}, as shown in **Figure 2.9**. The study involved *in-situ* incorporation of oxygen into MgB_2 films through vacuum annealing of magnesium-rich films. The relationship between oxygen concentration and T_c, $\Delta\rho$, and $\Delta\rho_{0,corrected}$ suggests that oxygen is distributed within and between the grains of the films. $\Delta\rho_{0,corrected}$, obtained through Rowell analysis [64], corrects for residual resistivity by deriving intragrain resistivity values, removing the influence of intergrain connectivity.

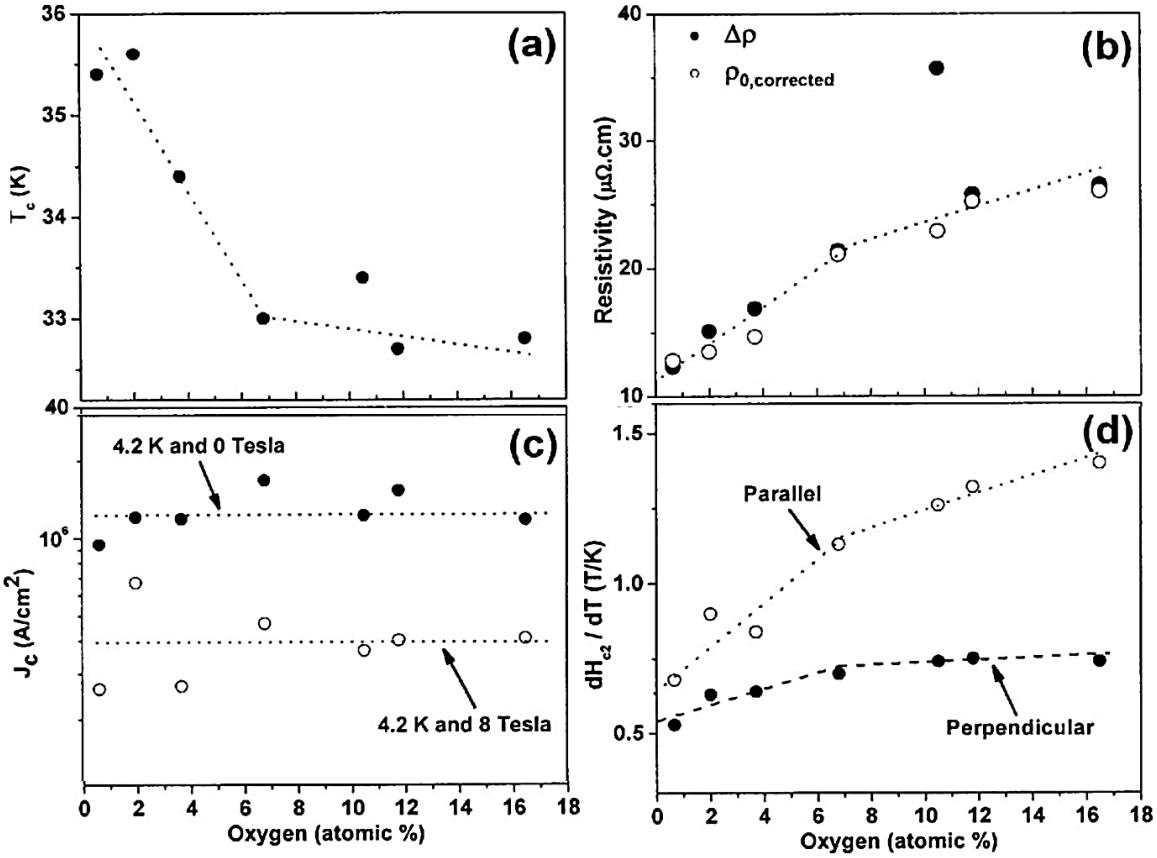

Figure 2.9 *Variations in T_c (a), $\Delta\rho$ and $\Delta\rho_{0,corrected}$ (b), J_c (c), and (d) dH_{c2}/dT near T_c as a function of oxygen concentration in MgB_2 films are depicted. Dashed lines are included as visual aids and do not stem from analytical fits to the data. Reprinted from* [87] *with Copyright ® by AIP Publishing.*

Notably, the corrected resistivity, T_c (**Figure 2.9**a), and Δ_ρ (**Figure 2.9**b) show no significant changes beyond an oxygen concentration of 7%. The exact reason for this phenomenon remains unclear. However, it is proposed that additional oxygen primarily leads to the coarsening of existing particles within and between grains, rather than creating new defects. Consequently, minor alterations in scattering and associated electrical properties occur. Despite this, J_c is largely unaffected by excess oxygen (0.65%), maintaining a value of 1.5×10^6 A/cm² at 0 T and 4.2 K across all samples (**Figure 2.9**c). This stability in J_c is attributed to the potential increase in effective pinning centres from oxygen being offset by reduced connectivity and increased grain size.

The rate of change of the upper critical field (dH_{c2}/dT) near the T_c increases with higher oxygen concentration but significantly decreases after oxygen concentrations exceed 7%. The dependence of dH_{c2}/dT suggests a stronger effect of oxygen on H_{c2} when the magnetic field is parallel to the *ab* plane, attributed to the texturing in the films. Transmission electron microscopy studies reveal columnar grains oriented along the (0001) direction, indicating that increased oxygen concentration enhances grain texturing and influences the superconducting properties of the films.

2.4.3.2 Thermal decomposition of MgB_2

Brutti et al. [88] investigated the decomposition reaction of MgB_2. They identified the reaction as;

$$2MgB_2(s) \rightarrow MgB_4(s) + Mg(g)$$

by comparing experimental data on the decomposition of MgB_2 under both kinetic and thermodynamic conditions, as well as examining the vaporization coefficient of MgB_2 and the activation enthalpy and entropy of the reaction. They reported that MgB_2 has a small, slightly temperature-dependent vaporization coefficient of $\alpha_{v,1000\,K} = (5.9 \pm 1.0) \times 10^{-2}$.

The activation enthalpy for the high-temperature decomposition of MgB_2 was determined to be $\Delta_{act}H^*_{1010K} = 266 \pm 5.6$ kJmol^{-1} which can be compared to the measured equilibrium decomposition enthalpy of $\Delta_r H^0_{992K} = 239.1 \pm 5.6$ kJ mol^{-1}.

Dancer et al. [89] investigated the effect of the heat treatment temperature on the density of *ex-situ* MgB_2 bulks produced by pressure-less sintering. The density changes of the samples were provided in **Figure 2.10**. They claimed that this fluctuation may be attributed to the density change caused by MgB_4 formation during heat treatment after magnesium evaporation.

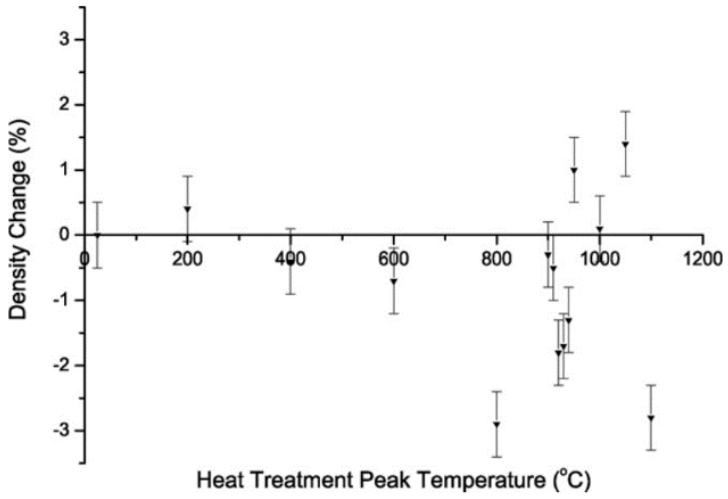

Figure 2.10 *Density change versus Heat treatment of pellet MgB_2 reprinted from* [89] *(Copyright © 2008 Elsevier Ltd.)*

Sintering temperatures between 900-1000 °C are generally preferred in *ex-situ* PIT wire production for two reasons: (1) at higher temperatures decomposition of the MgB_2 starts and reactions between the outer layers and the core can become more severe [90], (2) at lower temperatures it is not possible to achieve densification [91].

In the first scenario, it is demonstrated that the primary impurity phase in *ex-situ* heat-treated (≥800°C) MgB_2 wire is MgO [92], with additional phases such as MgB_4 [93] and the non-

stoichiometric phases $MgB_{4+\delta}$ and $MgB_{7+\delta}$ [94] being detected in *ex-situ* samples following heat-treatment, as also depicted in the phase diagram in **Figure 2.8**.

In the second scenario, potential reactions between MgB_2 and the sheath material create a non-superconducting layer, reducing the superconducting cross-sectional area [95]. Such reactions can also decrease Mg in the core, forming B-rich compounds like MgB_4 [93] and MgB_7 [96]. Kario et al. [99, 97] studied the influence of heat treatment temperature on the efficiency of the *ex-situ* MgB_2 and the copper sheath and found that heat treatment at 750°C resulted in minimal Mg-Cu reaction and optimal MgB_2 content (90 wt%), with 9 wt% MgO and 1 wt% Mg-Cu. At 800°C, MgB_2 content dropped to 88 wt%, with increased MgO (10 wt%) and Mg-Cu (2 wt%), mainly forming on the copper sheath side.

2.4.4 Effect of impurity addition on the superconducting properties of MgB_2

In order to improve the superconducting properties of MgB_2, impurity atoms like carbon play a key role. Substitution of B by C [103–112] has two effects. The primary one is a substantial increase in H_{c2} (by substitution of B atoms by C, often called a doping effect) which allows operation in higher magnetic fields, and strain of the crystal lattice (or the introduction of normal state impurity phase nanoparticles) which helps in the reduction of flux motion , thus enhancing J_c and values.

Dou et al. [107] substituted B atoms with C using carbon nanotubes as C source and showed an enhancement in J_c to 10^4 A cm^{-2} at a relatively high field, 4 T, 20 K. In another study, Kodama et al. [108] used coronene ($C_{24}H_{12}$) as a carbon source in their MgB_2 wire manufacturing process and obtained relatively high J_c, 14.7×10^5 A cm^{-2} at 20 K and self-field. Choi et al.[109] have used pyrene ($C_{16}H_{10}$) to increase J_c of their $MgB_{2-x}(C_{16}H_{10})_{x/16}$

and $MgB_2(C_{16}H_{10})_{x/16}$ wire. The field dependence of J_c values with regards to the x value is given in **Figure 2.11**.

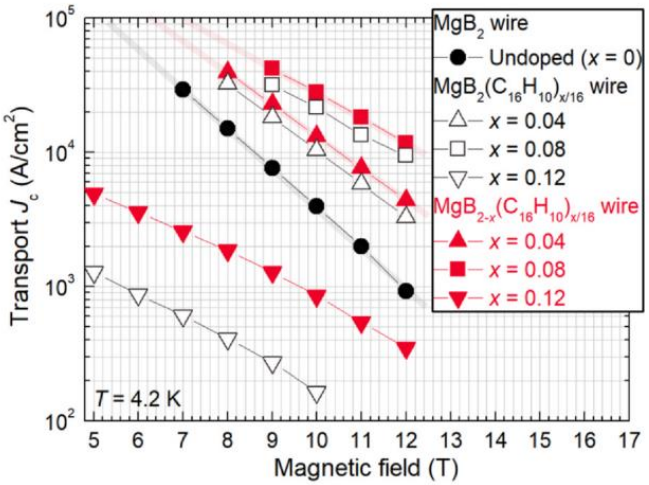

Figure 2.11 *J_c versus Magnetic Field of $MgB_{2-x}(C_{16}H_{10})_{x/16}$ and $MgB_2(C_{16}H_{10})_{x/16}$ wires at 4.2 K reprinted from* [109] *(*Copyright© *2021 Elsevier B.V.)*

Carbon is not the only the impurity addition element that can alter the properties of MgB_2. Dy_2O_3 [110], SiC [108, 116–120] and AlN [116] have been used to enhance flux pinning. In SiC doping, two effects are observed in [103]: firstly, the substitution of B by C leads to an increase in H_{c2}, and secondly, the reaction of Si with Mg results in the formation of nano-particle Mg_2Si, which acts as pinning particles to enhance J_c. It is worth noting that particle size plays a critical role; it is claimed that smaller SiC or Si particles yield smaller Mg_2Si particles and stronger flux pinning.

Moreover, Si_3N_4 addition [117] was used to increase the J_c which is attributed to slight Si substitution for B leading to lattice distortion by solid solution substitution. Such substitution may have taken place in the nano-doped samples, given the slight elongation of the lattice parameter. Additionally, introducing more than 1% nanoparticles could only result in the introduction of impurities.

2.5 Production methods for MgB_2 wires

The hardness of boron and MgB_2 prevents plastic deformation during wire drawing or rolling, necessitating the use of powder metallurgy in MgB_2 production. Optimal transport properties in MgB_2 wires depend on high purity, doping, and small particle sizes. Vinod et al. [118] demonstrated that larger Mg particles reduce reactivity with B, leading to a less homogeneous MgB_2 microstructure and lower J_c. However, acquiring submicron Mg particles smaller than 1 μm is costly and hazardous, while pure nanoscale boron powders also pose considerable challenges in terms of production, handling [119] and cost [120]. Consequently, industrial MgB_2 wires often exhibit slightly lower J_c compared to those made with theoretically pure powders due to practical constraints.

Due to the strong covalent bonding and high Peierls stress [121], borides, especially AlB_2-type borides like MgB_2, are brittle and difficult to sinter and deform [122]. Even with its brittleness, MgB_2 can be made into both mono-filamentary and multi-filamentary wires (see **Figure 2.12**) using various production technologies such as powder-in-tube (PIT) processing and the variation called internal Mg diffusion (IMD).

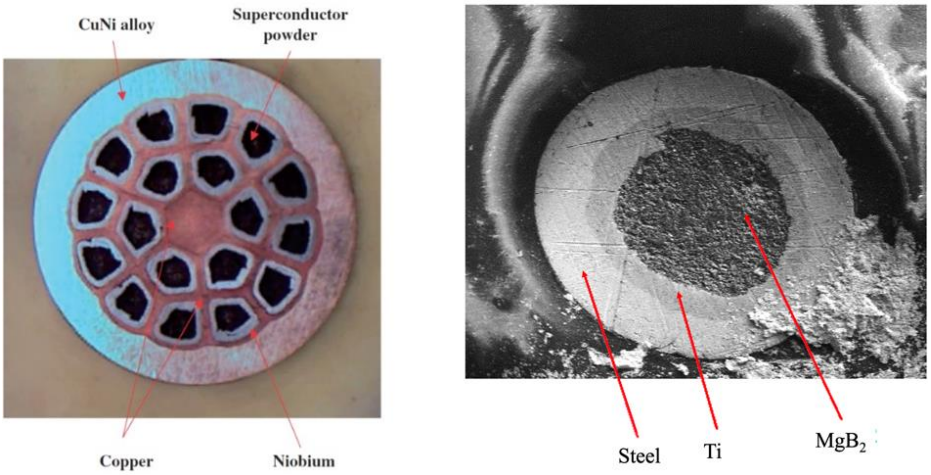

Figure 2.12 *Cross section image of a) multifilament* [123] *(Copyright© The American Ceramic Society) and b) monofilament MgB_2 wires*

The PIT method for MgB_2 wire production encompasses both *in-situ* and *ex-situ* processes, each with distinct advantages and drawbacks. In the *ex-situ* process, pre-reacted MgB_2 powders are utilized to fabricate the wire, followed by a sintering step to form a continuous superconducting path. Conversely, the *in-situ* approach involves creating a wire from elemental Mg and B powders, which are then reacted to generate the superconducting phase. While both methods are suitable for large-scale applications due to their simpler heat treatment and forming procedures compared to the IMD method, which involves the reaction of an Mg rod with surrounding B powders, the *in-situ* process struggles to achieve high J_c values due to void formation during heat treatment [124].

Figure 2.13 illustrates the typical microstructure of MgB_2 wires prepared *ex-situ* (a-b) and *in-situ* (c-d) via the PIT method, after heat treatment at 950°C for 3 hours [125]. *In-situ* MgB_2 (**Figure 2.13**c-d) shows intrinsic volume change, with the reactants' volume exceeding that of the product, leading to void formation.

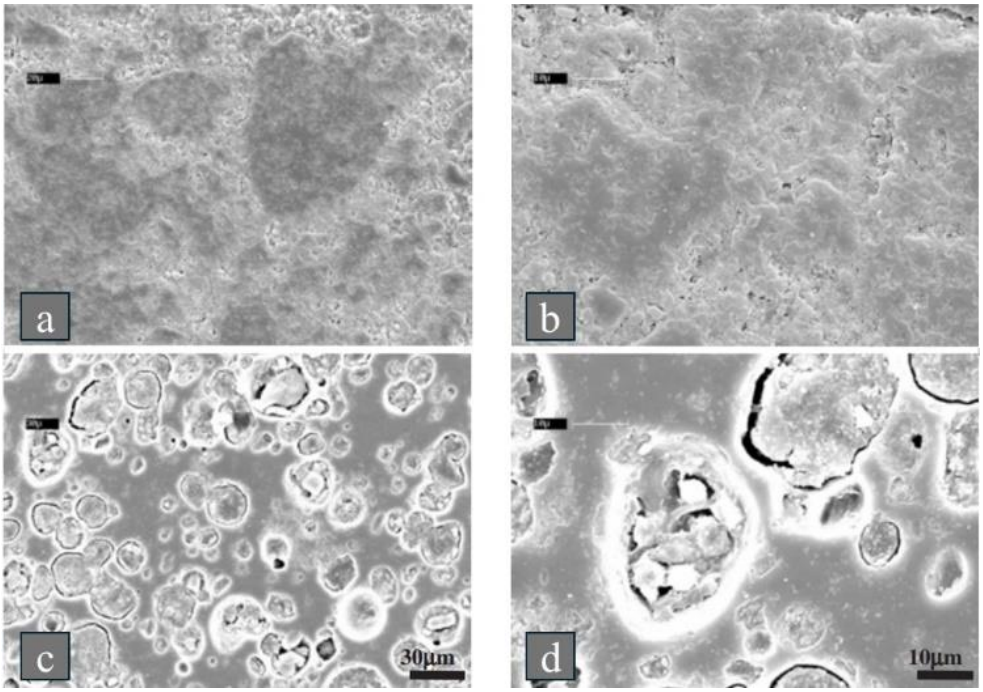

Figure 2.13 *The typical ex-situ (a-b) and in-situ (c-d) microstructure of wires that produced PIT method* [125] *((Copyright© 2003, IOP Publishing). The magnification for images a-c is 30 μm, and for images b-d, it is 10 μm.*

Conversely, in *ex-situ* MgB_2 (**Figure 2.13**a-b), the product's volume is nearly the same as the initial reactants, preventing void formation. The important drawback of the *in-situ* process is the low resulting density (described as the packing factor, *P*) which is determined by the intial packing factor, P_i, and the reduction in volume during reaction.

$$P = P_i(1 - \Delta v) \tag{2.8}$$

where P_i is packing factor of the precursor powder after wire production, Δv is the volume reduction [108]. This fractional volume reduction is about Δv=0.25 [126] for MgB_2 because the mass density of the preliminary Mg+2B mixture is considerably lower than the final product MgB_2. Therefore, this phase transformation causes low density and porous microstructures that compromises the macroscopic current density [125].

In order to prevent the low density caused by voids, applying external high-pressure and different heat treatment procedures during MgB_2 production [132–134] have been carried out, as explained in detail in the following sections.

2.5.1 *In-situ* wire production processes using PIT

Typically, monofilamentary MgB_2 wire is manufactured using the PIT method, outlined in **Figure 2.14**a [130, 131]. This process involves pouring Mg and B powders into a cylindrical tube, with variations in tube diameter across different studies. To enhance superconducting properties, doping elements are often incorporated into the initial powder mixture. Jiang et al. [130] investigated the impact of monofilamentary MgB_2 wire diameter on J_c and they suggest that increasing the deformation rate from pre-annealed wires to final wires resulted in a higher density of MgB_2 core. In the manufacture of multifilamentary MgB_2 wire, a common method involves packing unreacted Mg+B powders into tubes containing a chemical barrier material such as Ti or Nb. These tubes are then stacked inside a larger tube typically made of steel or Monel, filled with a Cu matrix as illustrated in **Figure 2.12**a.

Husek et al. [131] fabricated multifilament MgB_2 wires using a stainless-steel tube with an outer diameter of 8 mm and an inner diameter of 6 mm, incorporating a Ti barrier. These wires were drawn to an outer diameter of 0.86 mm and heat-treated under to investigate the effect of the temperature on the reaction between layers and the J_c values of the wires. Their findings revealed a J_c of 2.2×10^4 A cm^{-2} at 800 °C for 0.5h, compared to 1.45×10^4 A cm^{-2} at 600 °C for 2.5h.

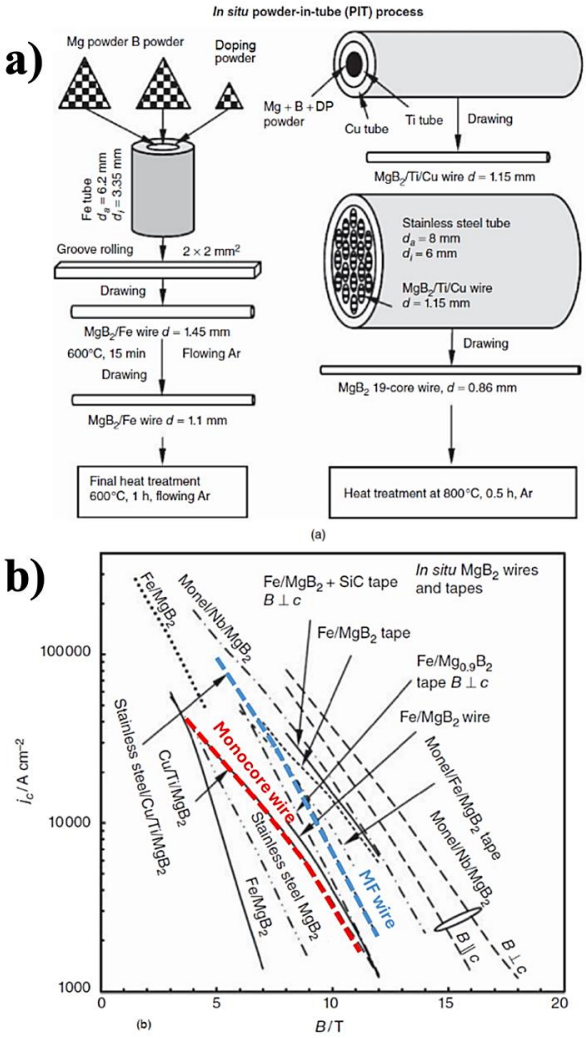

Figure 2.14 *a) Manufacturing process of in-situ wire* [130,131] *and b) current density vs applied magnetic field of some in-situ processed MgB_2 wires and tapes at 4.2 K [64] (Copyright IOP Publishing).*

Notably, achieving good grain boundary connectivity at relatively low temperatures, typically between 600-650°C, helps avoid potential reactions between the outer layer and

the superconducting core with barrier layers such as Fe, Ti, Nb, Ta, and Ni. This allows for thinner barrier layers, positively impacting cost considerations [37]. In **Figure 2.14**b, it is seen that the engineering J_c values of multifilamentary (MF) MgB_2 wires are higher than the monofilamentary versions (mono-core wires). Monel/Nb sheathed monofilament MgB_2 wires have exhibited one of the best results, achieving a J_c value of 10^4 A cm^{-2} at 13.2 T and 4.2 K [132]. The doping element was C and they used malic acid ($C_4H_6O_5$) as a source. **Table 2.3** summarizes literature findings on *in-situ* PIT method for wire production. Doping materials, mainly C from various compounds, are commonly used to enhance J_c.

Table 2.3 *Some in-situ PIT wire production studies in the literature.*

Ref.	Heat Treatment	Sheath Material	Doping	Process	Filament Type	J_e A/cm^2	Test Environment
[130]	600 °C – 15 Min +600 °C – 1 h	Fe	10% Nano SiC	Groove Rolling and drawing	Mono	0.88×10^4	4.2 K – 10 T
[131]	800 °C 30 min	Stainless Steel	5% SiC	Drawing	Multi	2.2×10^4	4.2 K – 8 T
[133]	600 °C 24 h	Fe	C	Drawing	Mono	10^5 10^5 10^5 2.7×10^5	10 K - 6.1 T, 15 K -4.8 T, 20 K -3.3 T 4.2 K - 6T
[134]	650 °C 2 h	Fe	3.75% C	Groove rolling and die drawing	Mono	1.82×10^4	4.2 K -10 T
[135]	600 °C 1 h	Fe	4.5%-carbon-coated boron	Swaging	Mono	1.1×10^4	4.2 K- 10 T
[136]	650 °C 1 h	Fe	Xylene	Groove-rolling and cassette roller drawing	Mono	6.3×10^3	4.2 K -10 T
[137]	700 °C 20 min	Monel	C-encapsulated amorphous boron powder	Drawing	Mono	8×10^4	4.2 K - 10 T

Fe is favoured as a sheath material for its ease of shaping, cost-effectiveness, and resilience under harsh conditions. Among studies conducted under identical conditions (4.2 K, 10 T), [137] achieved the highest J_c value. They used C-encapsulated amorphous boron powder as a B source and Fe as the outer sheath, with a heat treatment temperature of 700°C for 20 minutes. The superior J_c is attributed to reduced porosity and denser structure achieved through Cold High-Pressure Densification (CHPD) and Hot Isostatic Pressing (HIP). However, the complex manufacturing process and high energy consumption warrant cost-effectiveness evaluation, despite MgB_2's potential for cost reduction compared to other technological superconducting materials.

2.5.2 *Ex-situ* wire production process via PIT

In **Figure 2.15**a, unlike *in-situ* routes, the process starts with already reacted MgB_2 powder and the rest of the process is similar to the *in-situ* process but the heat treatment comprises sintering processes rather than a reaction. The *ex-situ* method using pressure-less sintering typically yields a higher bulk density of around 75% resembling the close packing of rigid spheres. However, research indicates that grain connectivity in *ex-situ* MgB_2 bulks and wires is inferior to that of *in-situ* fabricated MgB_2 samples [138]. This disparity is ascribed to weak-links and poor particle-particle connectivity persisting even after sintering at temperatures reaching approximately 1100°C [89]. *Ex-situ* wires are typically subjected to heat exceeding 800 °C to optimize their superconducting characteristics. Braccini et al. [139] assert that a high heat-treatment temperature is essential for allowing the *ex-situ* MgB_2 wire to recover from cold work and regain its high T_c. In their study, they fabricated a range of Ni-Cr alloy-sheathed wires annealed at peak temperatures ranging from 200°C to 950°C. They observed that both T_c and the J_c under low magnetic fields (H < 5 T) increased with higher heat-treatment temperatures.

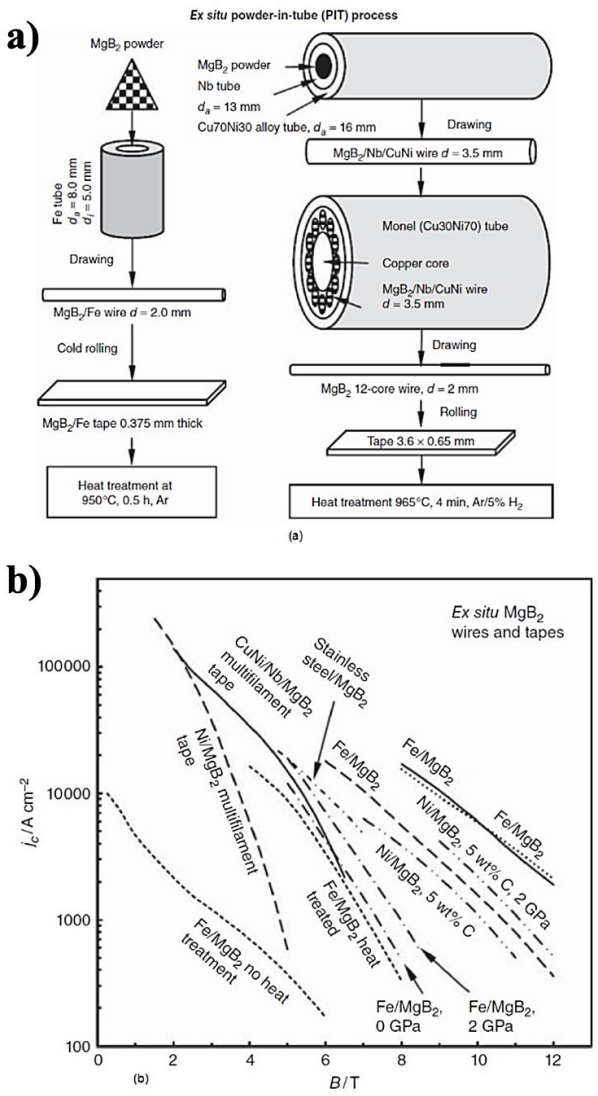

Figure 2.15 *a) manufacturing process of PIT ex-situ wires* [140, 141] *and b) current density vs applied magnetic field of some ex-situ processed MgB_2 wires and tapes at 4.2 K* [37] *(Copyright IOP Publishing).*

Fuji et al. [142] observed that heat-treating *ex-situ* stainless steel and iron-sheathed wires below 700 °C for 30 min did not notably enhance their performance in terms of J_c. However, heat treatment above 800 °C 30 min significantly improved J_c performance (more than ten times that of 700 °C).

Table 2.4 illustrates various *ex-situ* PIT MgB_2 wire production studies. The challenge of choosing the best process arises from the differing test environments, complicating the comparison of J_c values. Generally, these studies have employed Ni or Fe-Ni-Co alloys as

ferromagnetic sheath materials. Notably, Ni has demonstrated resilience to elevated temperatures, crucial for the efficient sintering of *ex-situ* MgB_2 wires. However, in [143], no thermal treatment was applied after the *ex-situ* MgB_2 powders were tightly packed inside the Ni sheath and subjected to wire drawing. Presumably the intimate mechanical contact achieved between the MgB_2 particles generated a significant J_c even without sintering.

Table 2.4 *Some ex-situ PIT wire production studies in the literature.*

Ref.	Heat Treatment (under Ar)	Sheath Material	Doping	Process	Filament Type	J_e A/cm^2	Test Environment
[143]	unsintered	Ni	-	Cold rolling	mono	10^5	4.2 K, self field
[144]	900 °C	Ni	-	Cold rolling	mono	10^5	20 K, 1 T
[153]	950 °C, 30 min	Fe-Ni-Co alloy	-	Swaging and 2-axial rolling	mono	10^4	4.2 K, 5 T
[145]	800 °C 1 h	Ni	-	Groove rolling	multi	4×10^5	5 K, 1 T
[146]	920 °C 0.3 h	Ni	-	Groove rolling	Mono	3×10^5	4.2 K, 2 T

Nonetheless, other studies, such as [145] and [146], revealed higher J_c values compared to unsintered wire, even in the presence of background fields, underscoring the significant impact of temperature on achieving the optimised performance for applications in magnets.

2.5.3 Wire production via internal Mg diffusion (IMD) technique

In general, the internal Mg diffusion technique (IMD) can be considered as a development of the PIT method. While the MgB_2 density produced by the *ex-situ* PIT method reaches 2.34 g/cm^3 [147], which is 90% of the theoretical density, it is only around 1.4 g/cm^3 in the *in-situ* method [148] due to the intrinsic shrinkage mentioned above. However, the density of MgB_2 produced by the IMD method reaches up to 2.4 g/cm^3 [148]. With this method, the stages of producing MgB_2 wire are given in **Figure 2.16**. The Mg rod is placed in the metal

tube, which is the outer layer of the wire, and the remaining volume is filled with B or MgB_2 powder. Afterwards, it is subjected to the rolling process. The internal magnesium diffusion method and Reactive Liquid Mg Infiltration (RLI) method are fundamentally similar [149], differing mainly in their applied heat treatments. RLI employs temperatures above 750 °C, while IMD uses lower temperatures between 600°C and 700 °C.

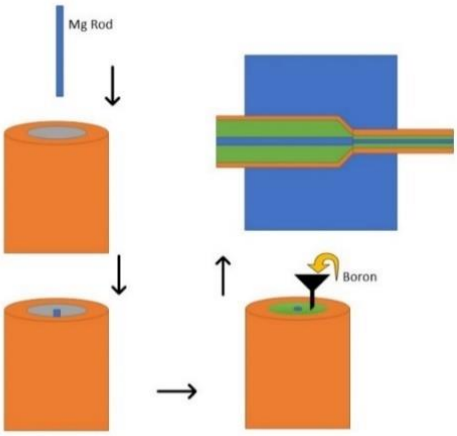

Figure 2.16 *IMD processed MgB_2 wire producing steps.*

These heat treatments either melt the Mg to encourage reaction with boron to form MgB_2 or stimulate solid-state reaction. Numerous studies have demonstrated the effectiveness of this method, achieving very high current densities [154–157].

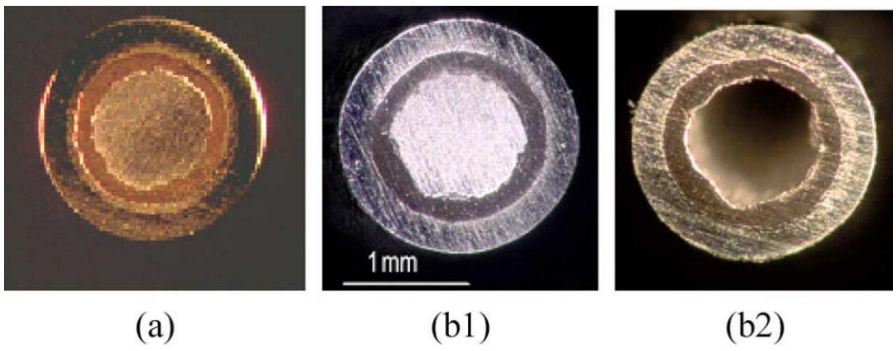

Figure 2.17 *Optical images of cross-sections of (a) the initial monofilamentary wire, comprising Mg, B, Nb, and Fe; (b1) the wire composed of Mg, MgB_2, Nb, and Fe from inner to outer layer. Basically, it is the version of b2 that is filled with Mg powder, and (b2) the hollow superconducting wire made of MgB_2, Nb, and Fe. The arrangement of components progresses from the innermost part to the outer surface of the wire* [149] *(Copyright © 2007, IEEE)*

In 2007, Giunchi et al. [149] introduced a 50 m long, 1.15 mm diameter IMD-based MgB_2 wire. In **Figure 2.17**a, the wire consists of an Mg rod, B powder, Nb sheath, and Fe from inside to outside. In **Figure 2.17**b1, the wire consists of an Mg rod doped with C, already reacted to form MgB_2, and the iron sheath. In **Figure 2.17**b2, the b1 wire heat-treated at approximately 750 °C reveals visible voids resulting from shrinkage during MgB_2 formation. The achieved J_c value was 5×10^3 A cm^{-2} at 10 T and 4.2 K, notably lower than the best *in-situ* or *ex-situ* wires previously mentioned. The method's limitations include being only applicable for winding onto coils using the wind and react method, and a restricted bending radius due to the hollow centre formed in the wire.

Hur et al. [150] developed an IMD processed monofilament MgB_2/Fe wire doped with 5 mol% SiC and heat-treated at 670 °C for 1 hour. The engineering current density reached 10^5 Acm^{-2} at 10 T and 4.2 K, similar to those achieved with simple PIT processing. Microstructural comparison in **Figure 2.18** shows that while PIT-based MgB_2 wire exhibited a granular and porous microstructure, IMD-based wires demonstrated a denser and less porous microstructure.

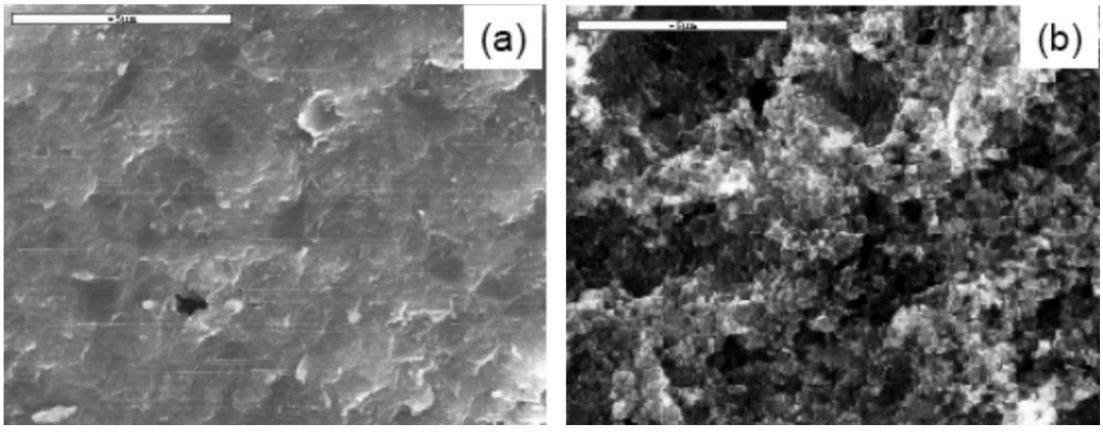

Figure 2.18 *SEM images of both SiC doped a) IMD processed and b) PIT processed MgB_2 wire*[153] *reprinted from* [150] *(Copyright © 2008, IOP Publishing)*

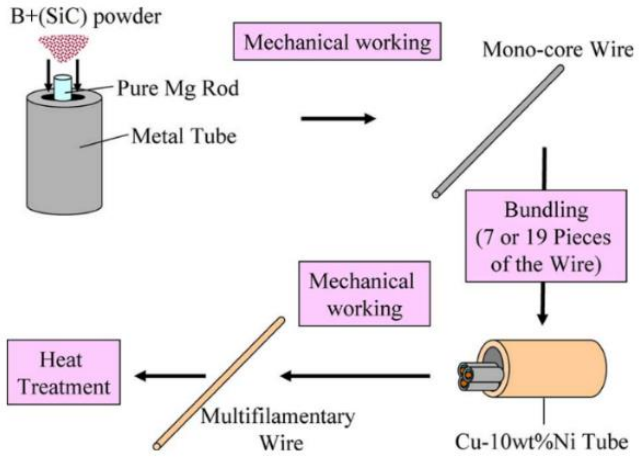

Figure 2.19 *IMD based MgB_2 wire fabrication of* [151] *(Copyright © 2011, IEEE)*

Kumakura et al. [151] fabricated seven and 19-multifilament SiC-doped MgB_2 wires by the process illustrated in **Figure 2.19**, and achieved 0.7×10^5 A/cm^{-2} and 1.3×10^5 A/cm^{-2} respectively at 10 T and 4.2 K.

Some properties of MgB_2 wires made by IMD are listed in **Table 2.5**. They all use C substitution to increase the J_c values.

Table 2.5 *Some IMD wire production studies in the literature.*

Ref.	Heat Treatment (under Ar)	Sheath Material	Doping	Process	Filament Type	Engineering J_c A/cm^2	Test Environment
[149]	750 °C	Nb	5 at% C	Drawing	mono	5×10^3	4.2 K, 10 T
[150]	670 °C 3 h	Fe	5 at% SiC	Drawing	mono	4.1×10^4	4.2 K, 10 T
[153]	700 °C 1 h	Fe	SiC	Groove Rolling	mono	7×10^3	4.2 K, 4 T
[152]	645 °C 1 h	Cu-Ni	10 mol% SiC	Groove Rolling	multi	10^5	4.2 K, 9 T
[151]	640 °C 1 h	Ta	10 mol% SiC	Groove Rolling and swaging	multi	0.7×10^5	4.2 K, 10 T
[154]	700 °C 1 h	Nb	Nano C	Rotary swaging	multi	6.1×10^4	4.2 K, 10 T

When we compare the results from [149] and [150], the effect of heat treatment on J_c can be seen. 750 ^{o}C is above the melting point of Mg therefore it is likely that Mg is lost during the heat treatment.

2.5.4 Reactions with sheath materials

Kumar et al. [155] investigated the reactivity of various sheath materials, including stainless steel, copper, silver, iron, nickel, and tantalum, within the *in-situ* MgB_2 route. They found that silver and copper reacted with magnesium from the core, while nickel reacted with both magnesium and boron, forming $MgNi_{2.5}B_2$. Stainless steel and tantalum did not form secondary phases with the precursor powder, but stainless steel had limited ductility, and tantalum is expensive. Iron is recommended for single sheath MgB_2 conductors due to its favourable workability and low reactivity, despite the formation of FeB_2 as a reaction layer in some studies [156, 157]. For magnet applications involving MgB_2 conductors, using a non-magnetic sheath offers advantages in reducing unwanted dissipation (eddy currents and fields created by the sheath) [97].

Zhou et al.[158] investigated the effect of sheath materials on J_c properties of the wire.

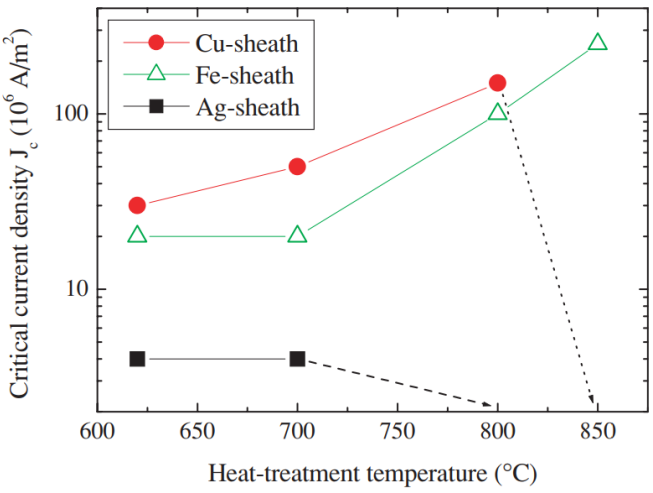

Figure 2.20 *The J_c varies with the heat treatment temperature for tapes sheathed with various metals. In the case of tapes sheathed with Ag, and Cu, the disappearance of J_c is indicated by the dashed arrows* [158] *(Copyright © 2001, IOP Publishing).*

As observed in **Figure 2.20**, the J_c of the tapes dramatically drops to almost zero when it is sheathed with Ag and Cu above certain heat treatment temperatures, specifically 700°C for Ag and 800°C for Cu. The detrimental effect observed in Cu sheathed tapes at elevated temperatures, resulting in severe bubbling and subsequent damage to the tapes, leading to the loss of J_c, is noteworthy.

In addition, reactions between the core and the sheath material, as well as MgB_2 decomposition, may happen at the same time. Chen et al. [159] studied copper inclusion in MgB_2 to replicate the potential reaction between Cu matrix and MgB_2 and they prepared both *in-situ* (0.8Mg + 0.2Cu + 2B) and *ex-situ* (MgB_2 + 0.2Cu) samples subjected to various heat treatments (600–900°C, 1 hour). They found heightened reactivity of pure magnesium with copper compared to MgB_2 in *in-situ* reaction. It is claimed that Mg_2Cu formation was unstable above 600°C, favouring $MgCu_2$ according to Gibbs free energy. No reaction was observed between Cu and MgB_2 in *ex-situ* samples at 600–700°C [160]. At 800°C and 900°C, MgB_2 decomposes into MgB_4 for *ex-situ* and *in-situ* reactions, respectively. $MgCu_2$ formation indicates that evaporated Mg can react with Cu at these temperatures. At >800°C, MgB_4 and MgB_6 likely form due to Mg loss to Mg-Cu alloys. To prevent core-copper reactions, a barrier material like niobium, tantalum, iron, tungsten, molybdenum, chromium, or their alloys must be used. The barrier must be thick enough to prevent diffusion between the core, stabilizer, and sheath.

2.6 Superconducting joints and their characterisation methods

Extensive studies in the literature have explored design, heat treatment, doping elements, pressure variations, and ambient conditions to enhance joint performance. The physical structure of MgB_2 joints and its effects on performance will be addressed in this section,

along with examination of production techniques and design processes reported in the literature. Subsequently, measurement techniques for MgB_2 joints will be discussed.

2.6.1 Approaches for fabricating persistent MgB_2 joints

Next-generation persistent electromagnet systems need cheaper, efficient materials for higher temperature operation. MgB_2 is a strong candidate for superconducting coils due to low raw material costs and ease of production. However, persistent mode magnets require suitable joints. The production process of MgB_2 joints depends on the coil production method: in wind & react (W&R), joints are made between unreacted wires and heat-treated with the coil; in react & wind (R&W), the joint heat treatment is done separately [161–163].

One of the electromagnet systems where the applicability of MgB_2 has been extensively studied is the MRI machine. Segmented coils are a common feature in the design of most MRI systems, leading to the requirement for wire-to-wire joints. Various studies have been carried out so far to connect both monofilament and multifilament MgB_2 wires with joints [7, 35, 174–177, 83, 166, 168–173].

The diameter of MgB_2 wires varies based on whether they are monofilamentary or multifilamentary [175]. Monofilament wires can be as small as 0.08 mm, while multifilament wires have variable diameters based on application and current capacity. The magnetic field strength and field drift depend on the wire type. Multifilament wires, typically chosen for large-scale MgB_2 magnet production, exhibit high engineering J_c values and greater stability against flux jumps [176].

2.6.2 Wire preparation for joining

The challenge with both monofilamentary and multifilamentary wires lies in precisely cutting the ends for joints without damaging the wire. The state of the wire—reacted or unreacted—is crucial. In unreacted MgB_2 wires, unsintered powders increase the risk of

spillage during cutting. This risk is lower in reacted wires, but fractures can occur due to MgB_2's brittleness. Various studies have aimed to minimize these issues. Yoo et al. [32] investigated the effect of cutting angle on the I_c value of MgB_2 joints between unreacted multifilament wires. They conducted heat treatment at 675°C for 1 hour under an Ar atmosphere and found that I_c increases with decreasing cutting angle.

In **Figure 2.21**, a lower cutting angle results in a larger contact area between the filament and the joint. Voids at this interface reduce both I_c and local J_c values by impeding supercurrent flow. **Figure 2.21**a shows numerous voids at the joint-wire interface, likely due to density changes.

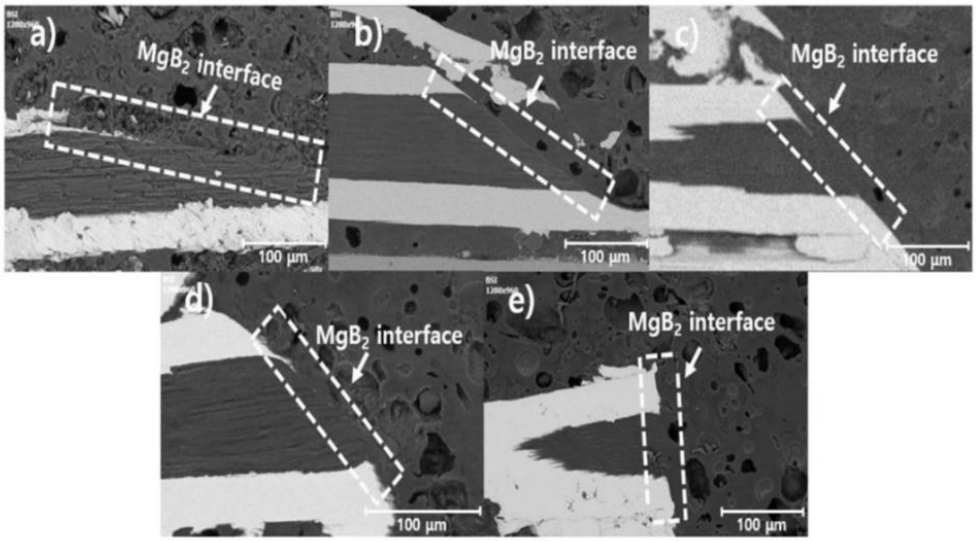

Figure 2.21 *SEM images of the interface between wire and bulk. The cutting angles are 13° 30° 45° 60° 90° respectively. Reprinted from* [32] *(Copyright © 2010, AIP Publishing)*

Joints with a 13° cutting angle had the highest I_c value of 262 A at 20 K, representing 83% of the CCR. Pressures of 150, 300, 450, 600, and 750 MPa on the joints were also tested. At 150 MPa, joint I_c values were lower, indicating insufficient pressure for a multifilament MgB_2 joint. At 300 MPa, joint I_c values increased, but pressures above 300 MPa (450 and 750 MPa) significantly decreased joint I_c values due to MgB_2 filament deformation.

2.6.3 Structural aspects of joints

Joint design is one of the most important factors affecting the efficiency of the magnet systems, depending on the type of magnet and its application. Various ways of linking the ends of wires coming from coils were detailed previously by Brittles et al. [177]. The four methods given in **Figure 2.22**. can be used to join two wires to make a superconducting joint.

- Butt joint (a)
- Lap joint b),
- Continuation joint (c),
- Termination joint (d),

It is quite difficult to link MgB_2 wires with butt and lap joint methods owing to the small diameter of these wires (< 1mm), the small amount of contact surface at the joint and the method of keeping the wires together for a long-time during the heat treatment.

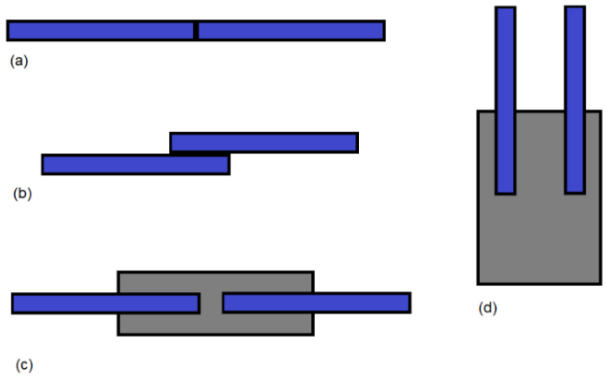

Figure 2.22 *Basic joint structures (a) butt joint, (b) lap joint, (c) continuation joint, (d) termination joint. Reprinted from* [177]. *Blue represents the wires, while gray indicates the case or filler within the wires. The size of the wires, the case or filler, as well as the gaps between the wires, may vary.*

Therefore, termination and continuation joint methods have been the most popular for joining wires. Joint systems generally consist of the following parts;

- Outer die, also called case,

- Chamber inside the case where the powder will be compressed,
- The way to position the cables in the die,

These factors vary from study to study. Since design plays a key role in the commercial production of superconductive electromagnet systems, companies keep them as commercial secrets and protect their designs with patents such as [181–195] .

Two approaches exist for forming joints with MgB_2 wires: joining two unreacted wires or joining two reacted wires. Joining unreacted wires is necessary for the W&R coil-making technique, while joining reacted wires is used in the R&W method.

Yao et al. [170] described a joint-making technique capable of carrying 200 A at 10 K and 250 A at 4.2 K under self-field, with joint resistance at 4.2 K reported as 10^{-9} Ω. The PIT *in-situ* MgB_2 wire used was a 0.84 mm multifilament with 18 filaments in Mg/Nb/Cu/Monel. The process, shown in **Figure 2.23**, involves placing unreacted and reacted wires separately in a stainless-steel die, then pouring Mg and B powders into the chamber. The powders are compressed using steel bars, but pressure is limited to prevent wire breakage or bending, likely resulting in lower MgB_2 density, though no specific value was provided.

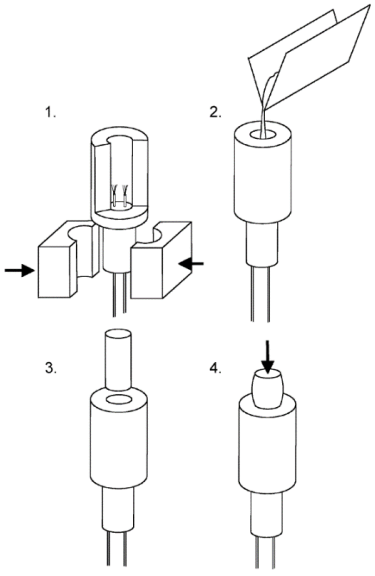

Figure 2.23 *MgB_2 joint design of Yao et al* [170] *(Copyright © 2009, IEEE)*

They prepared two bundles of joints. The first bundle of unreacted wire joints was heat-treated at various temperatures: 570°C for 40 hours, 630°C for 20 hours, 640°C for 30 minutes, 675°C for 30 minutes, 700°C for 15 minutes, and 900°C for 15 minutes. The second bundle of reacted wire joints was heat-treated at 570°C for 40 hours and 630°C for 20 hours. I_c values in the first bundle were 150 A at 640°C and 670°C for 30 minutes. In the second bundle, the I_c was 25 A at 630°C and 250 A at 570°C. All measurements were taken at 4.2 K in a self-field using the 4-point V-I method. The performance of the joints cannot be interpreted without knowing the I_c of the virgin wire.

Giunchi et al. [167] presented a method with two configurations for linking PIT *in-situ* reacted monofilamentary MgB_2 wires using the reactive Mg-liquid infiltration (RLI) process, as illustrated in **Figure 2.24**. In this process, B powder serves as an intermediary between the wires, enclosed by a Mg source. A local heat treatment between 800 and 850 °C liquefies the Mg, which reacts with the B to form MgB_2, effectively joining the wire ends in a process resembling superconducting welding. The joint resistance was measured at 9×10^{-9} Ω at 4.2 K, self-field. However, due to the absence of external pressure, the resistance is likely high because of the low density of the formed MgB_2.

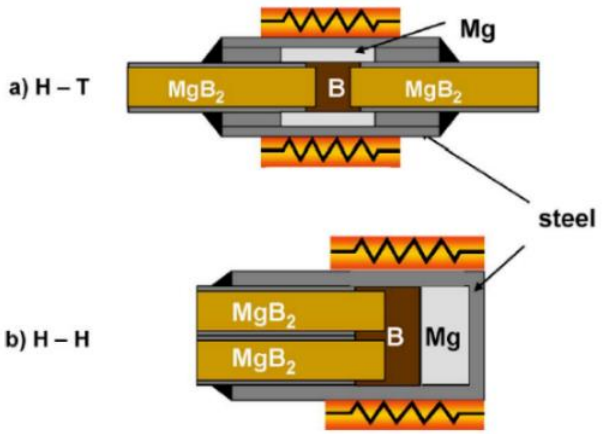

Figure 2.24 *Two configurations of joints fabricated with the RLI method. a) head-tail b) head-head reprinted from* [167] *(Copyright © 2010, IEEE).*

Another study conducted by Pradhan et al. [193] focused on increasing the density of the joint interface. They claimed that the initial packing density can be elevated up to 74% (the maximum packing factor achievable in incompressible spherical powders) by pressing the Mg+2B powders. They reported that this density limitation in the pressing method can be overcome by the groove-rolling process. In their process, tubes filled with powder are rolled to decrease their diameter, resulting in the densification of the powder. They utilized PIT *in-situ* monofilament MgB_2/Nb/Cu wires, depicted as numbers 1 and 2 in **Figure 2.25**. Number 3 represents the pre-filled Nb case (outer diameter: 7.5mm, inner diameter: 5.5mm) with Mg+2B powders, into which wires will be inserted from both ends. Number 4 illustrates the final joint produced from wires 1 and 2. The wire's I_c was measured at 380 A at 21 K in self-field conditions. Before removing the Cu layer with HNO_3, they pinched the wire tips to prevent core-acid reaction. After Cu layer removal, these tips were inserted into the Nb case, which was then refilled with *in-situ* powders and rammed for better packing.

Figure 2.25 *MgB_2 joint design by groove-rolling process reprinted from* [193] *(Copyright © 2016, IEEE). As a scale reference, the wire diameter is 1.6 mm.*

Subsequently, the Nb tube case was rolled in a groove roller to reduce diameter and achieve compact Mg+B mixed powder around the filaments. The outer diameter of the Nb case (used for joint preparation) after groove rolling was reduced to 4.3 mm. Heat treatment was conducted at 675°C for 1 hour in an Ar atmosphere.

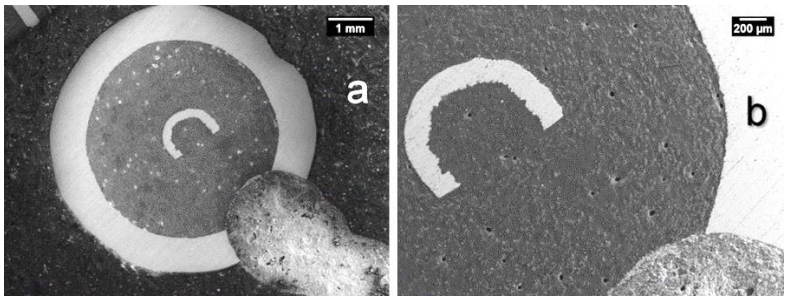

Figure 2.26 *SEM images of the cross-section of the joint* [193] *(Copyright © 2016, IEEE).*

After the heat treatment, the cross-section image of the joint can be seen in **Figure 2.26**. There seems to be no obvious interface, and the MgB_2 portion in the wire and the case is almost not distinguishable. They obtained I_c as 345 A at 21 K in self-field resulting in a CCR of 91%. This study had the highest I_c value among the studies conducted before 2016, and it demonstrates the importance of powder densification when designing the MgB_2 joint.

All of the MgB_2 wires used in these studies so far were produced by the PIT method. In 2017, Matsumoto et al. [164] was the first group to introduce the MgB_2 joint design that consists of unreacted IMD based monofilament MgB_2 wires. These wires, consisting of Fe as the outer layer and boron as the second layer (see **Figure 2.27**b) which surrounds the Mg rod (see the white strip in the middle of **Figure 2.27**a.)

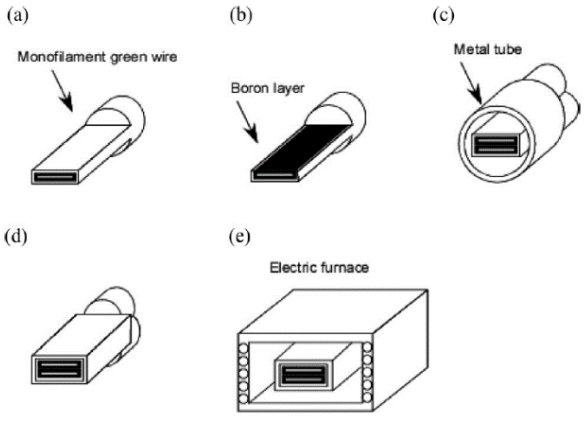

Figure 2.27 *MgB_2 Joint design consisting of IMD processed MgB_2 wires. Reprinted from* [164] *(Copyright © 2018, IEEE)*

The step-by-step explanation of **Figure 2.27** is as follows:

(a) The edges of two IMD-processed wires are pressed (just one of the wires is shown here).

(b) The Fe sheath on one side of each wire is removed by polishing to expose the B powder layer (just one of the wires is shown here).

(c) After positioning the B powder layer faces of the two wires on top of each other, they were placed inside a stainless-steel tube.

(d) The metal tube containing the two inserted wires was pressed.

(e) Heat treatment is carried out at 670°C for 6 hours in an Ar atmosphere.

After the heat treatment procedure, a joint resistance of 10^{-13} Ω at 15 K and 3 T was obtained from inductive resistance test (IRT). However, the authors pointed out that the transport I_c (with a 1 μV cm^{-1} field criterion) was as low as 1/3 of that of the wires themselves.

In 2020, Dipak et al. [77] introduced a low resistance MgB_2 joint design quoting resistance values as low as 5.48×10^{-15} Ω at 20 K in self-field and at a persistent I_c of 91.3 A at 20 K in self-field. The I_c of the wire at 20 K and 2 T is 86 A. The unreacted *in-situ* multifilament MgB_2 wires were cut at 20° and inserted inside a die.

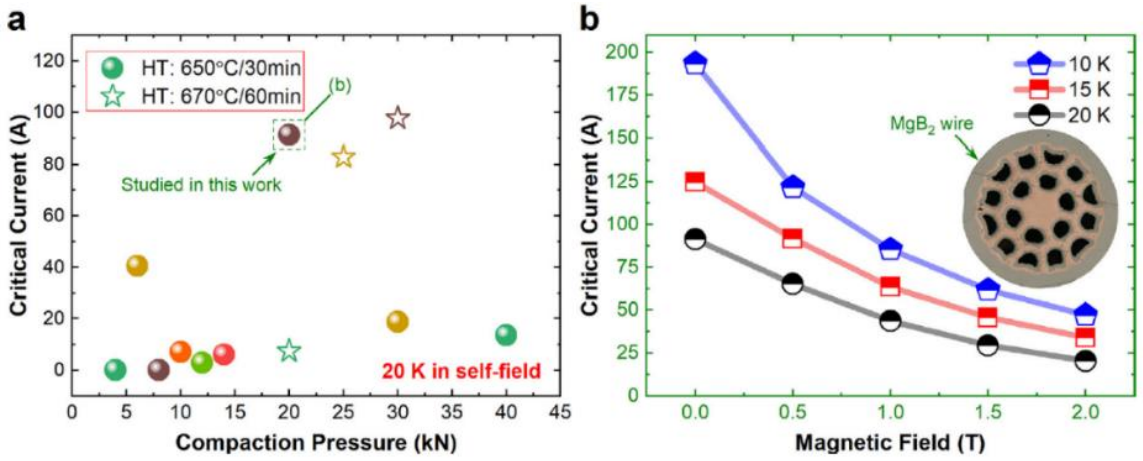

Figure 2.28 *a) Compaction pressure versus critical current of the joints. The circles represent the 650°C/30-minute heat treatment, while the stars represent the 670°C/60-minute heat treatments. b) Magnetic field versus I_c of the joint heat treated 650 °C/30 min with 20 kN pressure. (Copyright © 2019 Acta Materialia Inc. Published by Elsevier Ltd.)*

Then the die was filled with Mg and B powder and pressed. The pressing force was varied from 2 kN and 30 kN and results are given in **Figure 2.28**a.

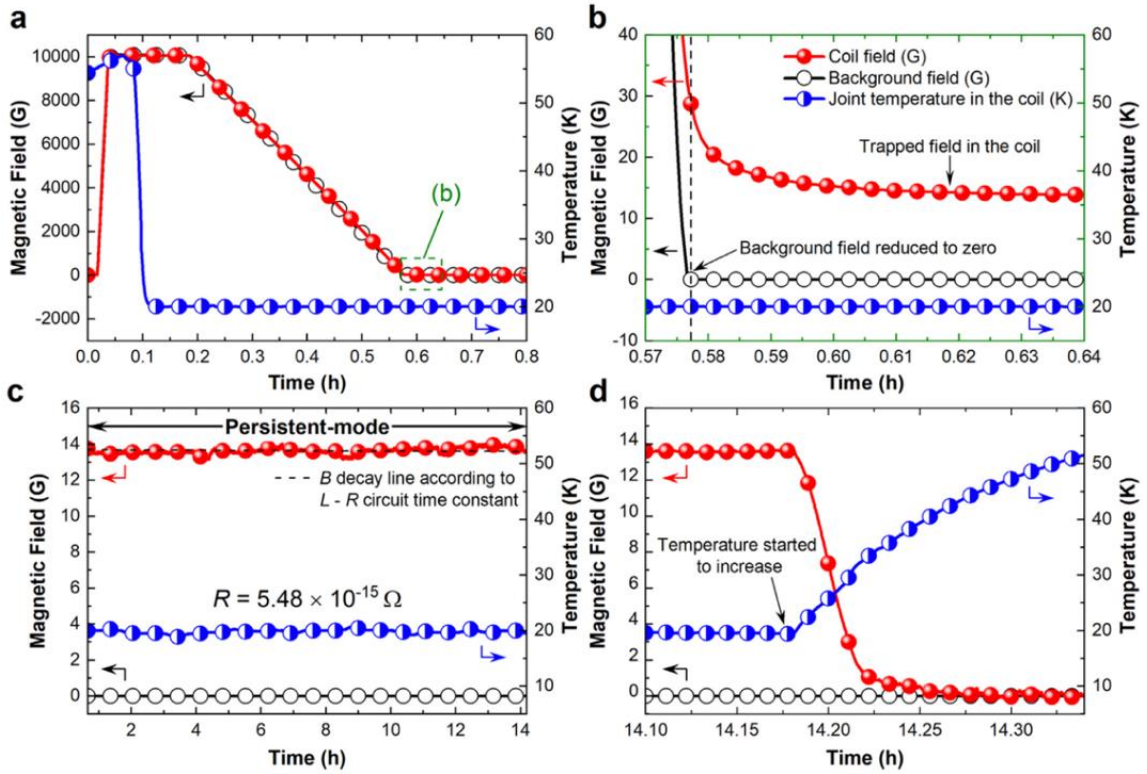

Figure 2.29 *Persistent current measurement: a) illustrates the externally applied magnetic field, b) depicts the region where the applied field is reduced to zero and the trapped field inside the coil, c) demonstrates the persistent mode lasting for almost 14 hours, and d) indicates the region where the persistent mode is interrupted via externally applied heat. (Copyright © 2019 Acta Materialia Inc. Published by Elsevier Ltd.)*

As illustrated in the diagram, the joint subjected to a heat treatment at 650 °C for 30 minutes and a compaction pressure of 20 kN exhibited a highest transport I_c value of 91.3 A (at 20 K in self-field) of joints prepared at this temperature.

A joint treated at 670 °C for 60 minutes under a compaction pressure of 30 kN displayed a highest transport I_c of 97.7 A at 20 K in self-field and 43.7 A at 1 T. Comparing this with the wire's transport I_c of 86 A at 20 K and 2 T, the CCR is less than 50%.

Table 2.6 *Some MgB_2 joint studies in the literature and the results obtained.*

Wire type	Applied field (T)	Temperature (K)	Joint Resistance (Ω)	Wire I_c (A)	Joint I_c (A)	Year	Ref.
PIT- *in-situ* Monofilament	1.46	4.2	1.0×10^{-12}	-	-	2006	[162]
PIT- *in-situ* Multifilament	Self-field 10	4.2 10	10^{-9} -	-	250 200	2009	[170]
in-situ Monofilament	Self-field	10	$<2\times10^{-7}$	-	270	2012	[174]
PIT- *in-situ* Monofilament	Self-field	4.2	9×10^{-9}	-	-	2010	[167]
PIT- *in-situ* Monofilament	Self-field	4.2	6.6×10^{-10}	-	150	2013	[166]
PIT- *in-situ* monofilament	Self-field 2	4.2 20	1.4×10^{-12} -	- 155	- ~100	2015	[194]
PIT- *in-situ* Monofilament	Self-field	21	-	380	345	2016	[193]
IMD-Monofilament	3	15	10^{-13}	x	x/3	2017	[164]
PIT- *in-situ* monofilament	Self-field Self-field	4.2 -	- -	- -	- 51	2019	[168]
PIT- *in-situ* multifilament	Self-field	20	5.48×10^{-15}	-	91,3	2020	[77]
in-situ monofilament	Self-field 2	15 15	$<10^{-12}$ -	- >200	450 -	2021	[195]
in-situ IMD-Monofilament	Self-field	20	6.44×10^{-16}	62	-	2023	[196]

In persistent mode operation, as shown in **Figure 2.29**, the trapped field was 13.7 G, corresponding to a trapped current of 22.4 A.

Table 2.6 compares developments in MgB_2 joints but calculating the CCR is often not possible as either the wire I_c or the joint I_c is not reported in most studies.

2.7 MgB_2 superconducting coil production techniques

The focus now shifts to manufacturing processes for superconducting coils using MgB_2 wires. The winding process of MgB_2 wires depends on the magnitude of the magnetic field to be produced, categorized into two groups: low magnetic field (0.5 T) and high magnetic field (2-4 T) [197].

Tanaka et al. [198] manufactured a W&R superconducting coil wound from multifilamentary 300m-long *in-situ* PIT-based MgB_2 wire. Determining the minimum radius of the coil relied on the maximum allowable bending radius of the wire without compromising its I_c. They evaluated the I_c values of bent wires through measurements in liquid helium at 6.5 T, normalizing them by the I_c of the non-bent wire. The wire bent at 60 mm radius exhibited a normalized I_c of 103%, indicating minimal degradation. Conversely, the wire bent at a 45 mm radius showed a normalized I_c of 93%, demonstrating clear degradation. Consequently, they opted to design the minimum coil radius as 60 mm, ensuring optimal performance. Coil parameters of the small solenoid are given in **Table 2.7**.

Table 2.7 *Coil parameters of Tanaka et al.* [198]

Inner diameter	120 mm
Outer diameter	190 mm
Height	41 mm
Inductance	55 mH
Number of turns	589
B_{max}	2.6 T at 300 A

The coil was prepared by the W&R method, but the heat treatment procedure was not declared. In **Figure 2.30**, the wound and heat-treated coil is shown. The wires are covered

with s-glass-reinforced epoxy material to give mechanical protection against the strains introduced as the magnet is energised.

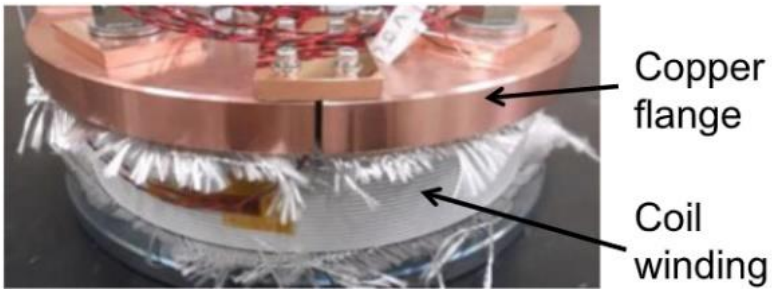

Figure 2.30 *Sintered coil ready for epoxy impregnation* [198] *(Copyright © 2017, IEEE)*

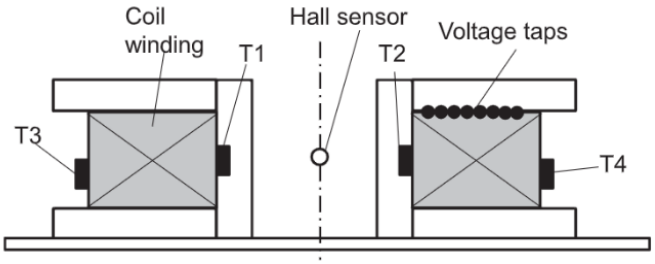

Figure 2.31 *Illustration of the set-up where electromagnetic tests to be performed* [198] *(Copyright © 2017, IEEE)*

The position of the sensors and the coil is given in **Figure 2.31**. Coil temperature was measured by T1-T4 sensors and the total coil temperature controlled automatically. Additionally, the magnetic field in the centre of the coil was measured by the Hall sensor. They estimated coil I_c and B_{max} were 262 A and 2.2 T at 24 K and 187 A and 1.6 T at 27 K, respectively.

Zhang et al. [199] described R&W superconducting coils wound from multifilamentary 1744 m-long *in-situ* PIT MgB_2 wire. They claimed that it is easier to produce this coil with the R&W method rather than W&R because there is no need to do a difficult process such as heat treatment of the entire coil at temperatures above 650 °C. The multifilamentary MgB_2 wire was first heat-treated at 650 °C for 60 min under Ar and then wound onto the coil. The general coil parameters are given in **Table 2.8**.

Table 2.8 *Coil parameters of Zhang et al.* [199]

Inner diameter	857 mm
Outer diameter	901 mm
Height	50,6 mm
Inductance	0,744 H
Number of turns	636,5
B_{max}	0,75 T 200 A

They measured critical current while heating the coil, aiming for 200 A at 13 K. The magnet was designed for 0.75 T at 200 A. The coil exceeded this, with 280 A at 15 K and 1.93 T in the winding.

2.8 Dissimilar joint studies between different technological superconductors

The designs of joints between MgB_2 wires, both reacted and unreacted, have been explained, with detailed examples from the literature. However, there is a lack of studies on joints between different technological superconductors. This area is crucial for future applications, such as power transmission cables requiring connections between different superconductors. Understanding the compatibility and behaviour of various superconductors when joined is essential. Banno et al. [200] studied joints between Nb-Ti and Nb_3Sn for NMR devices, which require superconducting joints between these materials due to their use in high-frequency NMR magnets. These magnets typically use an outer coil of Nb-Ti and an inner coil of Nb_3Sn, necessitating effective magnetic field sharing and cost efficiency. Similar requirements might arise for MgB_2 as its application in NMR and MRI devices grows. However, research on MgB_2-NbTi joints is limited.

Takahashi et al. [162] reported a joint between PIT *in-situ* monofilamentary MgB_2-NbTi wires in 2005, using four joints in an electromagnet system with a total resistance of about

1.0×10^{-12} Ω, suitable for persistent operation. The operational current was 105 A, and the magnetic field was trapped for 12 hours at 4.2 K in 1.46 T without decay. However, the joint design was not detailed.

The literature review has shown that MgB_2 is an emerging material with promising potential in superconducting technologies. One of the most significant applications of these technologies is considered to be the development of persistent mode superconducting coils. To facilitate the development of these coils and to enable them to replace existing counterparts, such as Nb-Ti and Nb_3Sn, several permanent improvements are necessary. Among these, the development of persistent-grade joints holds the utmost importance. In the literature, studies involving joints made between unreacted wires have been quite popular and have yielded excellent results, as discussed above. However, in current technology, companies are placing more emphasis on joints made with reacted wires. The primary reason for this is that large-scale coils wound with unreacted MgB_2 wires must undergo heat treatment in a furnace, which results in significant energy consumption and a high error rate. Therefore, it is crucial to conduct research that addresses this need, but to date, literature has not yet reported the development of joints between reacted MgB_2 wires with high critical current ratios (CCR) and low resistance. The main aim of this thesis as established through the literature review, is to conduct research to address the identified challenges in the development of MgB_2 joints, with a particular focus on creating high-CCR, low resistance joints between reacted MgB_2 wires. This research employs an experimental approach, using MgB_2 fillers to create joints with reacted wires and evaluating their performance through critical current and resistivity measurements. This approach is justified by the emphasis in the literature on the need for efficient and scalable solutions to address the limitations of existing persistent-mode superconducting coil technologies, particularly those associated with reacted MgB_2 wires.

In addition, there is a lack of literature on the development of joints using MgB_2 fillers for other technological superconducting wires, such as Nb-Ti and Bi-2212. This thesis also examines the feasibility of replacing lead-based solders, which are commonly used in Nb-Ti joint technology and are set to be banned by the European Union in 2027 due to their harmful effects on human health [201]. In light of this impending regulation, the research investigates the potential of environmentally friendly MgB_2 as a sustainable alternative. The study aims to evaluate MgB_2's suitability as a joint material, particularly within the context of Nb-Ti, which is a prevalent material in the current MRI sector. Ultimately, this research seeks to determine the effectiveness of MgB_2 in replacing lead-based joints in Nb-Ti magnets.

2.9 Conclusions

This chapter introduced the fundamental properties and thermodynamics of MgB_2. It also reviews various methods for producing MgB_2 wires, coils, and joints from the literature. Despite existing research, challenges remain in creating high CCR and high I_c joints between reacted MgB_2 wires. Therefore, this thesis focuses on the efforts to make joints between reacted MgB_2 wires in Chapter 6. Additionally, studies on Nb-Ti/Nb-Ti wire joints (see Chapter 9) and Bi-2212/Bi-2212 joints (see Chapter 8) using MgB_2 filler are also presented.

Chapter 3 Experimental Methods and Characterisation Techniques

This chapter comprises two parts, offering an overview of:

- Processing methods of cold-pressed MgB_2 powders, reacted/unreacted monofilament and multifilament MgB_2 wire joint preparation methods, dissimilar jointing methods and coil preparation methods.
- Techniques for characterizing phases, microstructures and superconducting properties of MgB_2 bulk samples, joints and coils as well as sample preparations for characterisations.

3.1 Processing methods

3.1.1 Cold-pressed MgB_2 bulk production

The purpose of this work is to create the first MgB_2 compound including steps such as powder preparation, cold pressing, heat treatment, characterization and magnetic measurements. Magnesium (MGP-100/150, 100-150 microns from Almamet) and boron (PVZ Boron 95 nanosize, amorphous boron powder 95% purity from PAVEZYUM) powders were mixed in different ratios and ground by mortar for 10 mins under laboratory ambient conditions.

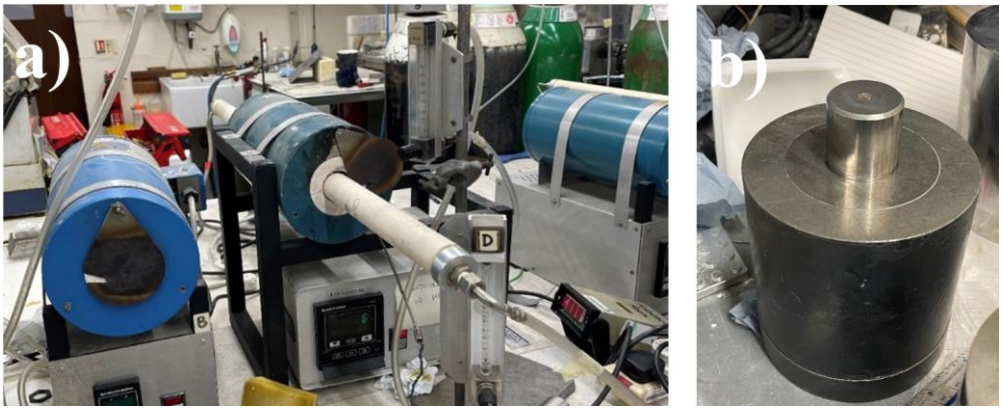

Figure 3.1 *a) tube furnace (into the middle) that was used for heat treatments of bulks, wires and joints and b) 32 mm diameter stainless steel die.*

The mortars were cleaned with acetone after each sample preparation to eliminate possible contamination. These mixed powders were then cold pressed with 30 MPa uniaxial pressure using a manual hydraulic pressing machine for 10 minutes in a 32 mm diameter die shown in **Figure 3.1**b. The particular pressure is established due to the die limit. During these 10 minutes, the pressure gauge was monitored and repressed to 30 MPa as it dropped down. Then the samples were placed in an open crucible exposed to the furnace atmosphere. Afterwards, heat treatments were carried out for each sample at 700-800 ^{o}C in a tube furnace (shown in **Figure 3.1**a) under Ar atmosphere with a 10 PSI gas pressure.

3.1.2 Reacted and unreacted monofilament MgB_2 joining preparation methods

Monofilament wires were obtained from Epoch Wires Ltd in both reacted and unreacted forms. The joining processes for both unreacted and reacted wires, with continuous joint orientation were undertaken in Epoch's laboratories. The joining processes for reacted wires with termination joint orientation were carried out in the Centre for Applied Superconductivity (CfAS) laboratories in Oxford. Wire specifications that were investigated are given in section 5.2.1, **Table 5.2**.

Joint cases (see **Figure 3.2a**) are used to define and give mechanical strength to the joint region of the wires. It employs short segments (22 mm) of a comparable monofilament wire extracted during an earlier phase of the manufacturing process, while the external diameter remains at 5.5 mm. This joint component, referred as a case is already filled with unreacted Mg and B powders (magnesium powder atomized, D50, with an average size of 30 μms, and PVZ nano boron powder, 95% pure).

3.1.2.1 Monofilament MgB_2 wire joining technique used at Epoch

The joint technology employed by Epoch initially involved the use of both reacted and unreacted wires. During my visit to their laboratories, I actively participated in the creation of several joints for testing purposes using the protocol they developed. The production steps for these joints are shown in **Figure 3.2** and listed below:

i. 2.2 cm lengths of the Mg and B filled case were cut (1-a) and drilled from both ends using a 1.25 mm diameter drill to required drill depth (1-b).

ii. Unreacted MgB_2 wire ends were scarfed by a grinding machine to increase the interfacial area. (2). The grinding paper used was 400 grits and the grinding process was conducted manually until the core could be observed roughly under an optical microscope.

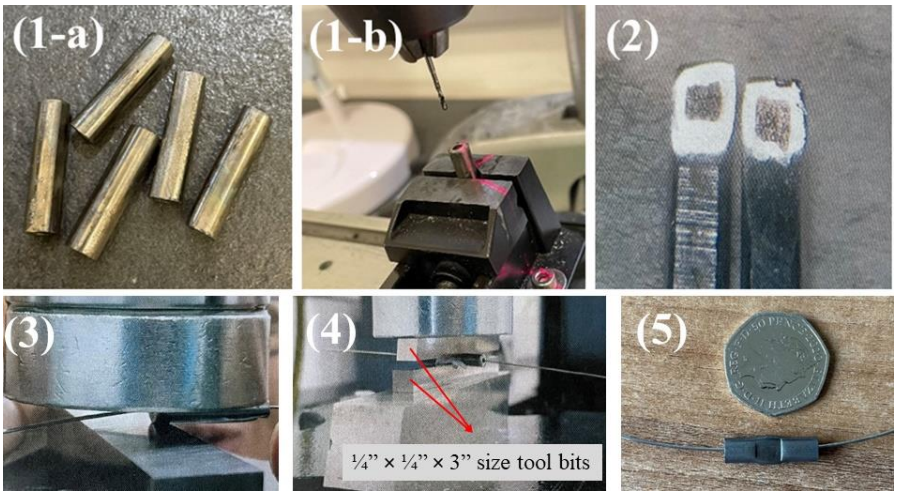

Figure 3.2 *Epoch Wire Ltd MgB_2 joint production steps.*

iii. The wire ends were inserted into the drilled holes with their exposed faces pointing upwards.

iv. 1 metric ton of flat pressure was applied at both ends of the case (3) ensuring that both ends are sealed.

v. To ensure the filling powder and wire ends were in good mechanical contact, pressure was applied to the middle of the case using ¼", ¼" ,3" size tool bits and a pressure of 2 metric tons was applied for 10 minutes (4).

vi. The size comparison of the joint compared to a coin is shown in (5).

vii. In some cases, unreacted wires were pressed under different loads as described in Chapter 5, **Table 5.1**. Pressing on the wire has been carried out as schematized in **Figure 3.3**. The wire is placed between tool bits and simply pressed.

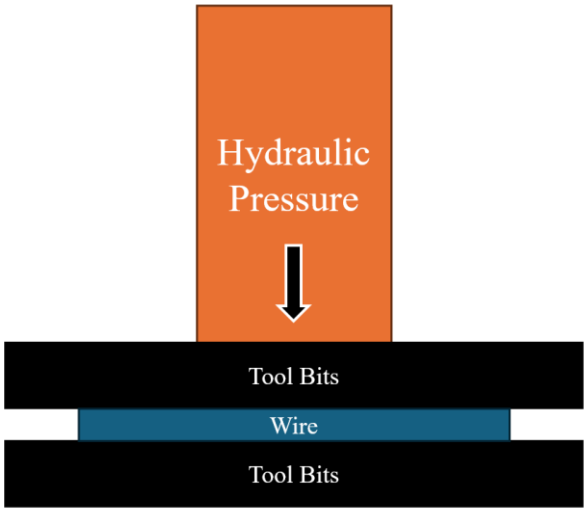

Figure 3.3 *The pressing mechanism employed for wire pressing.*

3.1.2.2 A novel joining methodology for reacted monofilament MgB_2 wires

Epoch Wires identified significant challenges in their manufactured joint structures. These challenges, along with proposed solutions, are discussed in Chapter 5 and Chapter 6. In this section, the methodology of joint-making procedures between reacted monofilament wires I developed is introduced.

In **Figure 3.4**, the production processes of the design of MgB_2 joint are schematized.

➢ The idea discussed here is to connect two superconducting MgB_2 wires physically inside a large diameter composite Steel/Ti/Mg+2B wire from earlier in the drawing procedure, called the 'case'.

➢ 2 cm lengths of the Mg+2B powder filled case were cut and two holes drilled in the Mg+2B core.

➢ MgB_2 wires were ground by grinding wheel to increase the interfacial area.

➢ Wires were placed in the drilled holes and 1.7 MPa was applied to the case for 10 minutes.

➢ Finally, the joint was heat-treated at various temperatures as detailed in Chapter 6.

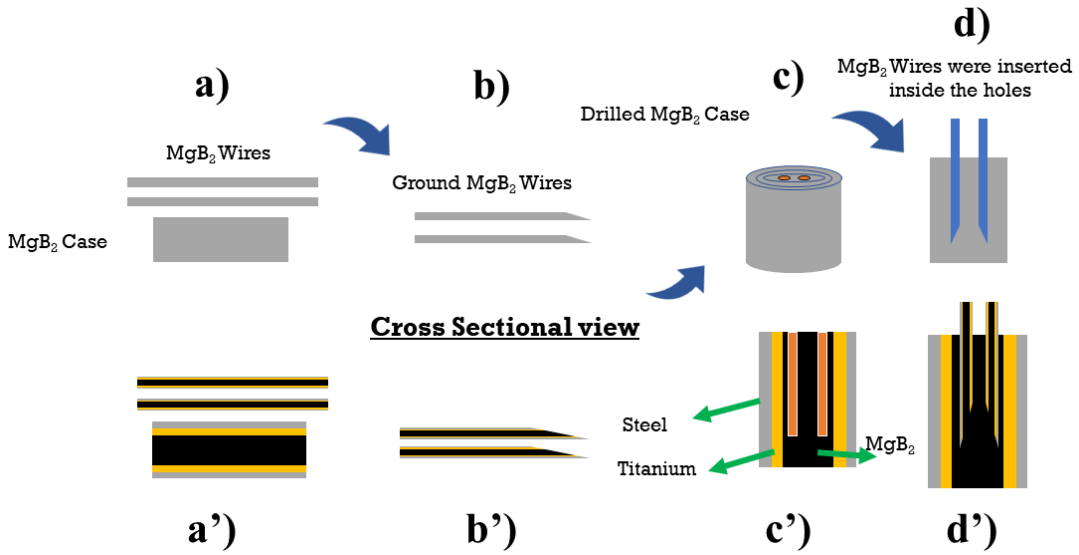

Figure 3.4 *Novel MgB_2 joint design. a)-a') are the wires to be joined. b)-b') is the second step, scarfing the ends of the wires. c)-c') is the third step, drilling two holes for the wires. Holes are shown in orange. d)-d') shows the joined wires inside the case.*

To compare with existing literature given in section 2.6.1:

- ✓ Size: Many previous studies have not specified the dimensions of the joints. In this study, however, the joint measures 2 cm in length and 5.5 mm in diameter which is small enough and desirable for magnet engineers.
- ✓ Practicality: The joint case resembles a monofilament wire at an earlier stage of the manufacturing process when the external diameter is still 5.5 mm, thus obviating the need for additional manufacturing steps specifically for the joint case. Moreover, the design simplifies construction and pressing procedures by avoiding complexity.

- ✓ Accessibility: The proposed joint design boasts accessibility across various MgB_2 wire manufacturers as they typically possess joint cases within their wire production processes. The steps involved are straightforward and adaptable to any industrial setting.
- ✓ Reproducibility: Consistency in joint performance is paramount, especially considering the potential demand for multiple joints within magnet designs comprising multiple coils. The joints consistently demonstrate lower resistivity as evidenced by the results presented in section 6.2.5, where two different coils exhibited lower resistances ($<10^{-13}$ Ω).

3.1.3 Reacted multifilament MgB_2 joining preparation methods

I investigated the feasibility of a similar jointing process for multifilamentary wires beginning with the acquisition of unreacted 6-filament MgB_2 wire (see **Figure 3.5**) from an external source (Abant Izzet Baysal University, Türkiye). These wires were obtained in an unreacted state to minimize the risk of damage during transportation as they were shipped from Türkiye.

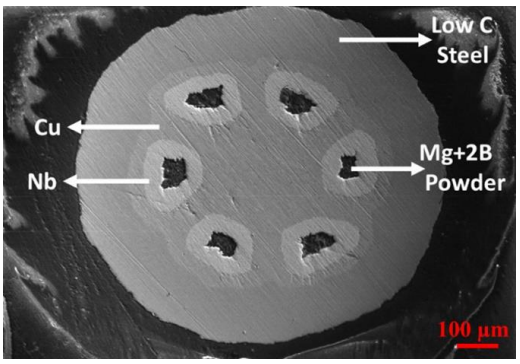

Figure 3.5 *SEM image of the MgB_2 Multifilament wire cross-section.*

The details of wire specifications are indicated in section 7.2.1. The wires underwent heat treatment at 700°C for 15 minutes to compare the performance with the monofilament I have used. Afterward, the filaments were carefully scarfed using a grinding wheel and then the scarfed surfaces washed with ethanol. The procedures for joint fabrication and the

subsequent heat treatments closely mirrored those outlined for the jointing process involving reacted monofilament wires as expounded upon in the preceding section.

3.1.4 Dissimilar joint preparation methods

The dissimilar joint studies in the literature have already been discussed in section 2.8. As detailed in that section, there is no concrete study between different technological superconductors. Here in this section, the method of creating dissimilar joints is detailed.

Several dissimilar joints were created between Nb-Ti/Nb-Ti wires and Bi-2212/Bi-2212 wires utilizing the same unreacted Mg+2B powder cases previously employed. The objective of these experiments was to examine the interactions between MgB_2 and other superconducting phases during the heat treatment. In these experiments, the Nb-Ti wires were monofilament, while the Bi-2212 wires were multifilamentary. Detailed specifications of the wires are provided in Chapter 8 and Chapter 9 for Bi-2212 and Nb-Ti wires respectively. The joint-making procedures for these wires mirrored those used for the previous joints. Heat treatments were conducted individually starting at 600°C, followed by 650°C, and finally 700°C, each lasting for 15 minutes for Nb-Ti joints. The heat treatment of 700°C for 15 minutes is applied to the Bi-2212 joints. More details about these temperature selections are detailed in corresponding chapters.

3.1.5 Coil preparation methods

Determining the actual resistance of the joints within a solenoid is of utmost importance, particularly in the context of their application in large magnets such as MRI scanners. In this scenario, the persistent mode operation is necessary for the joints. To address this, coils were fabricated using the most promising joining method. The former is made of Inconel and measures 2 cm in length with an outer radius of 7 mm and an inner radius of 6 mm.

3.1.5.1 Coil making process with mono/multifilament reacted MgB_2 wires

Although the preparation of joints in a real magnet manufacturing process would probably employ the R&W strategy that could not be used for these small test coils as shown in **Figure 3.6**.

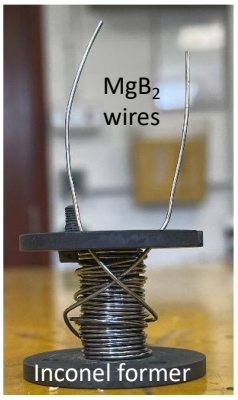

Figure 3.6 *The wound coil consists of unreacted MgB_2 filament wrapped around an Inconel former.*

This is because the radius of the coil falls below the minimum bending radius of the reacted MgB_2 wire (which is 12 cm, as verbally reported by Epoch, but not published.) not to break the wire and preserve the superconducting properties an alternative approach was implemented. Initially, the unreacted MgB_2 wire was wound around the coil without joining and subsequently subjected to heat treatment to induce the reaction to form MgB_2. Following this, the wire ends were connected within the pre-drilled case in accordance with the joint making procedure elucidated in section 3.1.2.2. Subsequently, the assembly underwent heat treatment under various conditions as delineated in section 6.2.

3.1.5.2 Coil making process with Nb-Ti and Bi-2212 wires

The procedure for creating coils with Bi-2212 wires closely mirrors the coiling method used for monofilament MgB_2 wire. Unreacted Bi-2212 wires are wound around a former and heat-treated under different conditions in a box furnace, detailed in Section 8.2. Preheating the wound-former is necessary due to the extreme brittleness of reacted Bi-2212, making it unsuitable for winding around such a small radius former. After heat treatment, the non-

jointed Bi-2212 coil is ready for joining. Wire ends are gently ground using a grinding wheel before insertion into the pre-drilled case. 1.7 MPa pressure is applied using hydraulic pressure to the joint and monitored via its gauge.

As for the coil-making process for Nb-Ti wire, since it is already reacted and lacks concerns about bending radius, the wire is simply wound around the former and Nb-Ti wire ends were scarfed and placed into the pre-drilled cases. Then, 3.4 MPa pressure (twice of previous pressures) applied to the joint. The reason of doubling the pressure is ductility of Nb-Ti enabling the high pressures. Then joint is subjected to different heat treatment conditions as discussed in Section 9.2.

3.1.5.3 Heat treatments of the coils

The heat treatments for the jointed coils were conducted using the same tube furnace illustrated in **Figure 3.1**a. An alumina wool isolator, as shown in **Figure 3.7**a, was utilized to prevent over-reaction of the wire wound on the former, thereby effectively isolating the joint from the coil. Subsequently, the joint portion of the coil was positioned inside the tube furnace, while efforts were made to keep the remainder of the coil away from excessive heat as depicted in **Figure 3.7**b.

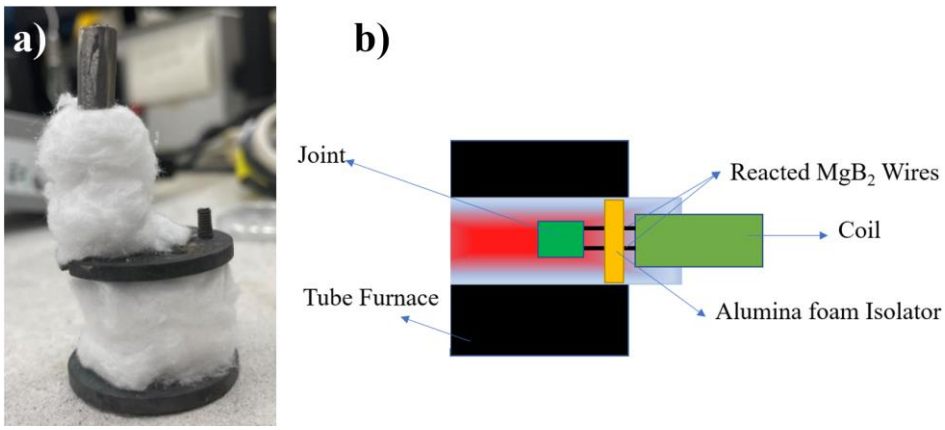

Figure 3.7 *Targeted heat treatment of the joint. On the left, the coil is wrapped in alumina wool and on the right is the position of the coil in the tube furnace.*

The temperature of the furnace was monitored using both external and the internal thermometers. These standardized heat treatment procedures were uniformly applied to all jointed coils.

3.2 Sample preparation for characterisation

In this section, the sample preparation methods for bulks, wires and joints intended for SEM-EDX, PPMS and XRD characterization techniques are described. Note that no liquid medium or water was used during the grinding/polishing processes of joints, wires and bulks.

3.2.1 Bulk sample preparation for XRD, SEM and EDX analysis

Before XRD characterization, no surface treatment such as polishing/grinding or conductive coating was applied to bulk samples. The samples were tested as they were removed from the furnace. All samples were 3.2 cm in diameter and were placed onto the sample holder as shown in **Figure 3.8**.

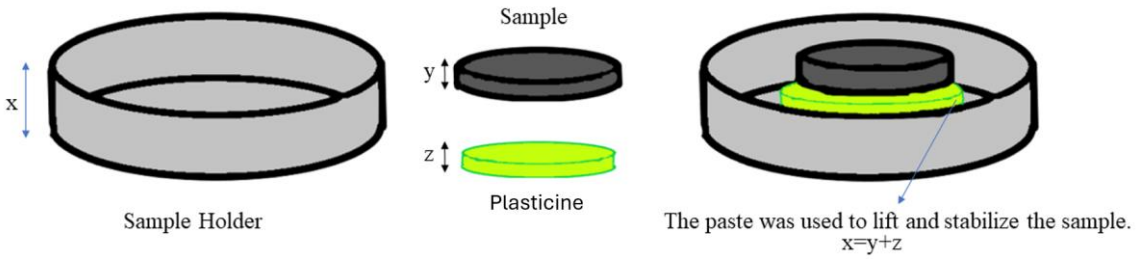

Figure 3.8 *Placing bulk samples into the sample holder for XRD.*

Since the thickness of the samples was smaller than the inner length of the sample holder, plasticine has been employed beneath the sample. It also helped to keep the bulk steady during the XRD operation while the sample was being spun. The bulk samples were positioned in an aluminium holder on top of a small piece of plasticine, ensuring complete coverage by the sample. A glass slide was then used to press the sample down, aligning its

top with the upper edge of the sample holder. This method minimizes peak shifts resulting from variations in sample height.

Following XRD characterization, the pellets were sectioned into smaller pieces using the same cutting machine employed in the PPMS sample preparation section. Subsequently, it was observed that the bulk pieces exhibited significant current charging and shifting during SEM and EDX characterizations, attributed to their insufficient normal state conductivity. Hence, the smaller pieces underwent a carbon coating process with a thickness of 18 nm.

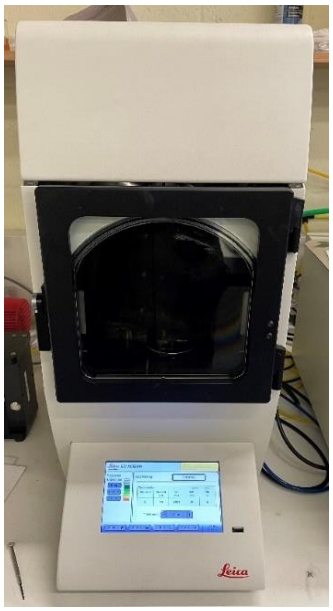

Figure 3.9 *Leica EM ACE 600 high vacuum sputter coater.*

This specific thickness was chosen to minimize the influence of carbon on the surface. Initially, a 9 nm coating was attempted, which was the limit of the coating machine, but shifting still occurred during characterization. Subsequently, an additional 9 nm coating was applied, resolving the shifting issue. The carbon coating was performed using the Leica EM ACE 600 high-vacuum (10^{-7} mbar) sputter coater (**Figure 3.9**) at the David Cockayne Centre for Electron Microscopy.

For the powder sample preparations for XRD, a square glass cover slip was placed in a suitable aluminium holder to maintain consistent positioning across all samples. The powder

was carefully applied to the glass slide, ensuring full coverage of the surface area. Background scans were conducted in each case to identify and eliminate any peaks associated with the holder and the plasticine.

3.2.2 Powder sample preparation from the case for XRD analysis

To characterize the XRD patterns of the samples subjected to heat treatments under various conditions, five distinct cases were prepared. Each case measured 2 cm in length and 5.5 mm in diameter, as previously shown in **Figure 3.2** 1a, with their specifications outlined in Section **3.1.2**. The cases were then heat treated according to the conditions provided in **Table 3.1**.

Table 3.1 *The heat treatment regimens for prepared cases.*

Case number	Heat treatment
1	700 ^{o}C 15 min
2	700 ^{o}C 15 min + 900 ^{o}C 30 min
3	700 ^{o}C 15 min + 900 ^{o}C 30 min + 650 ^{o}C 1h
4	900 ^{o}C 30 min
5	900 ^{o}C 30 min + 650 ^{o}C 1h

All heat treatments were conducted in a tube furnace, as shown in **Figure 3.1**a, under an argon-protecting atmosphere. **Figure 3.10** illustrates the process of removing the reacted powder from inside the case following heat treatment. The sample was securely compressed, and a small metallic crucible was positioned beneath the case to serve as a reservoir for the collected powder. As the drill operated slowly, it ground the ceramic inside the case into a powder, which then collected in the reservoir below. In this way, the ceramic inside the case was carefully collected and made ready for XRD testing.

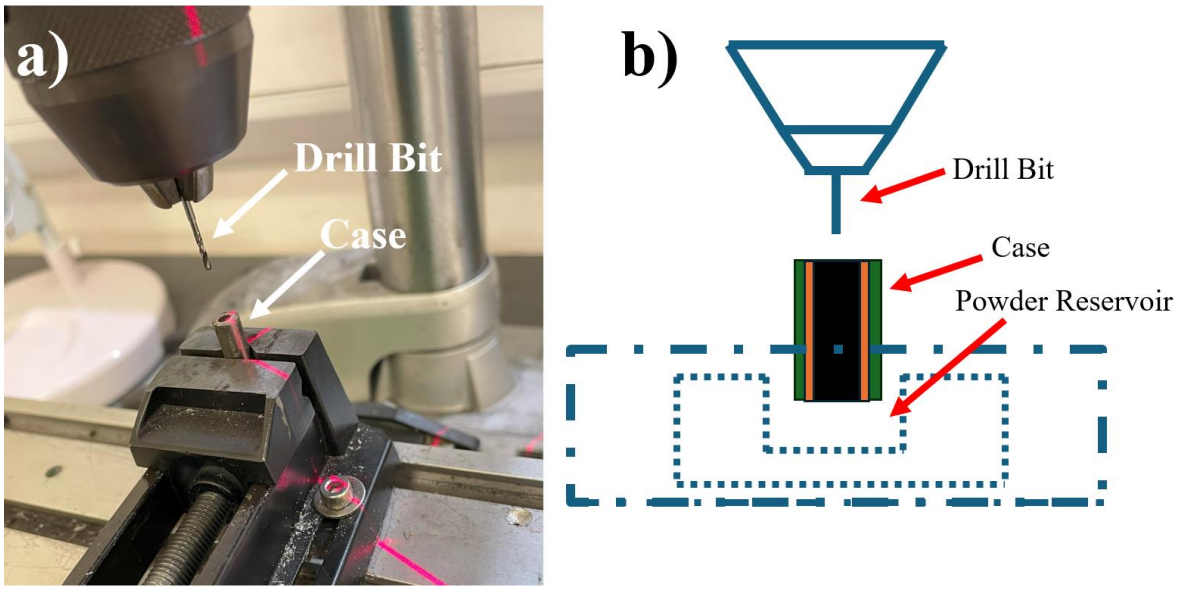

Figure 3.10 *(a) MgB_2 removal from heat-treated case using drill assistance; (b) Cross-sectional schematic of process: Black denotes MgB_2, orange represents Ti, and green indicates Steel.*

3.2.3 Bulk sample preparation for PPMS analysis

After XRD analysis, each individual sample underwent a cutting process utilizing the Buehler Isomet low-speed precision cutter, specifically designed to prepare samples suitable for the Physical Property Measurement System, Vibrating Sample Magnetometer (PPMS-VSM). The schematic below illustrates the sample preparation steps.

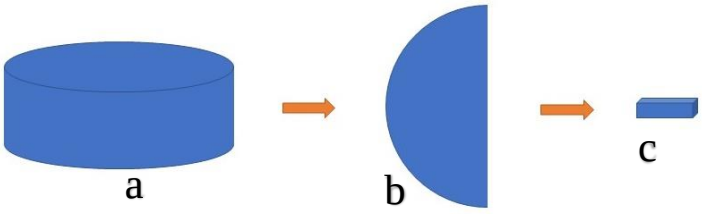

Figure 3.11 *Diagram of sample for PPMS Characterization*

The slice obtained from the cutting procedure (as depicted in **Figure 3.11**c) was measured using a micrometre, ensuring approximate dimensional accuracy. Subsequently, it was ground to attain a cuboid shape. No liquid medium, such as water, was used during the grinding process.

Table 3.2 *The measured sizes of samples and their approximated error values.*

Sample No	Measured sizes a × b × c in mm	Approx. Error
1	2.1 × 1.9 × 3	0.1 × 0.1 × 0
2	2 × 2 × 2.9	0 × 0 × 0.1
4	1.9 × 2 × 2.9	0.1 × 0 × 0.1

Due to the inherent difficulty in achieving precise cuts for small samples, some size discrepancies are expected. **Table 3.2** displays the measured dimensions of the samples alongside their estimated errors.

3.2.4 Wire sample preparation for SEM-EDX and XRD analysis

Before making joint, reacted, unreacted, monofilament and multifilament wires were characterized by SEM and XRD analysis. **Figure 3.12** illustrates the wire sample preparation steps for characterization. In **Figure 3.12a**, a 35 mm rubber mould was employed to fabricate an epoxy mount. Initially, the inside of the rubber was sprayed with a Si lubricant to facilitate the removal of the sample after epoxy curing. Subsequently, the wire (**Figure 3.12b**) was cut into small pieces (**Figure 3.12c**).

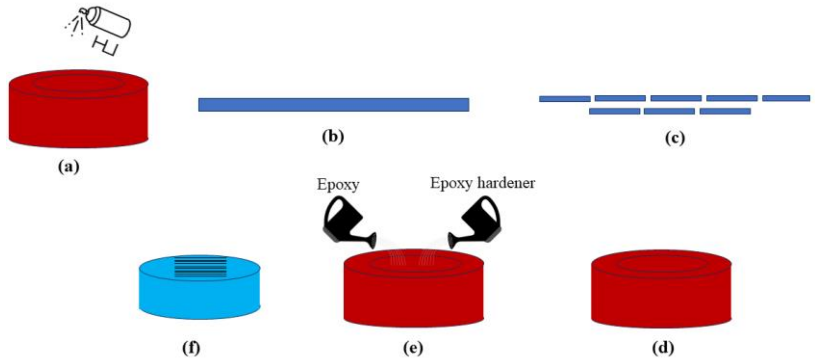

Figure 3.12 *The wire preparation steps for XRD and SEM characterization.*

These small cut wires were then arranged within the rubber mould (**Figure 3.12d**), in a parallel orientation ensuring minimal spacing between them. Next, a mixture of 18 grams of epoxy (15 g) and hardener (3 g) was prepared in a glass beaker and mixed for 5 minutes. The mixture was poured into the rubber mould (**Figure 3.12**e) and left under a fume hood

overnight. Following curing, the epoxy was extracted from the rubber mould (**Figure 3.12**f). The samples were subsequently ground using SiC grinding discs ranging from #400 to #1200 for 30 minutes to expose the inside of the wires for XRD analysis. Neither a liquid medium nor water was used during the grinding process.

3.2.5 Joint sample preparation for SEM-EDX analysis

The joint preparation steps for SEM characterisation are similar to the wire preparation steps to some extent. Joints are directly put into the rubber mould in a carefully chosen orientation to aim for the interface between wire and filler MgB_2. **Figure 3.13** elucidates the rationale behind positioning the joint within the rubber for epoxy moulding. After all joint production procedures are completed and removed from the furnace, the shape of the joint is shown in **Figure 3.13a** with wire orientation illustrated below for clarity. Subsequently, in **Figure 3.13b**, the joint is rotated and placed into the rubber mould as shown. The wire orientation in this position is also delineated. In **Figure 3.13c**, the epoxy and hardener are poured into the rubber mould and left under a fume hood overnight.

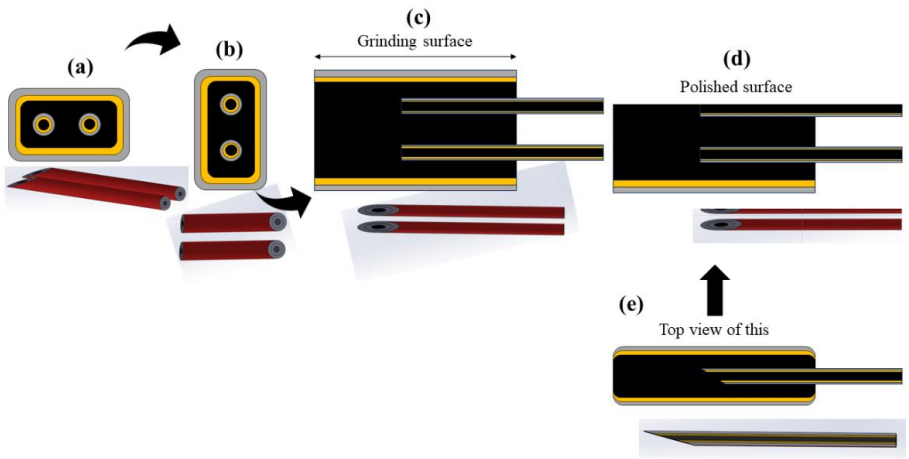

Figure 3.13 *Mounting the joints into the rubber mould. Wire orientations for each step are provided for clarity.*

This stage also includes a depiction of the grinding surface and wire orientation. **Figure 3.13**d presents a schematic of the joint post-grinding. No liquid medium or water was

employed during the grinding process. Finally, **Figure 3.13e** provides a top view of **Figure 3.13d**, showcasing the final image of the joint and filler interface.

3.3 Characterisation techniques

3.3.1 X-Ray diffraction

XRD measurements were conducted employing a PANalytical Empyrean diffractometer utilizing Cu *K-α* radiation (λ = 0.154 nm) at 40 kV and 40 mA, along with a Pixcel 1D scanning detector. To ensure a consistent irradiated area of 5 mm×5 mm on the specimen, a 5 mm incident beam mask and a programmable variable incident slit were utilized. The measurements were performed in Bragg-Brentano geometry with a scan range of 2θ = 20° to 90°, employing a step size of 0.026. Lattice parameters, crystallite size, strain and weight fractions of the various phases present in the samples were deduced from the XRD spectra utilizing Rietveld refinement. The refinement process involved several steps using the PANalytical HighScore Plus software. The images illustrate the steps involved in the case work for various instances.

- Correcting instrumental broadening by referencing a recent scan obtained from a single crystal Si standard.
- Fitting the background using the *determine background* function.

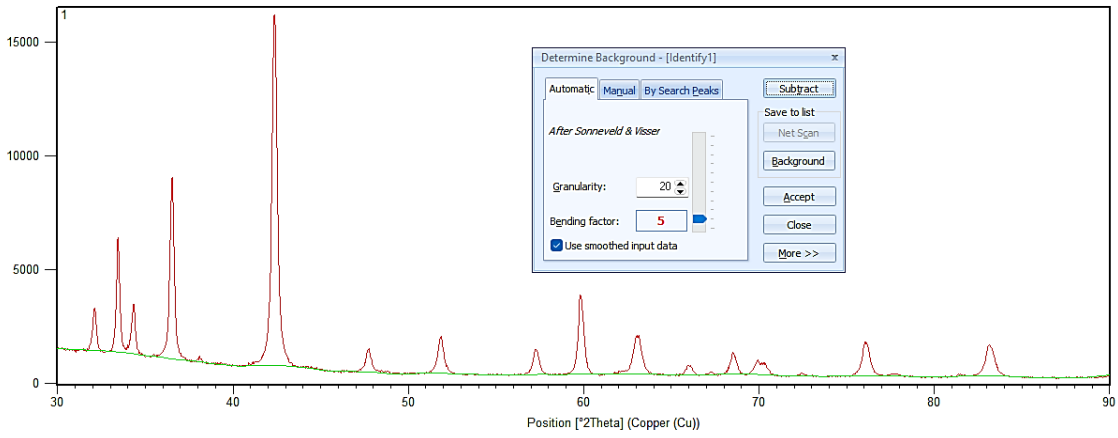

Figure 3.14 *Background fitting performed by the software.*

- Locating peaks using the *peak search* function.

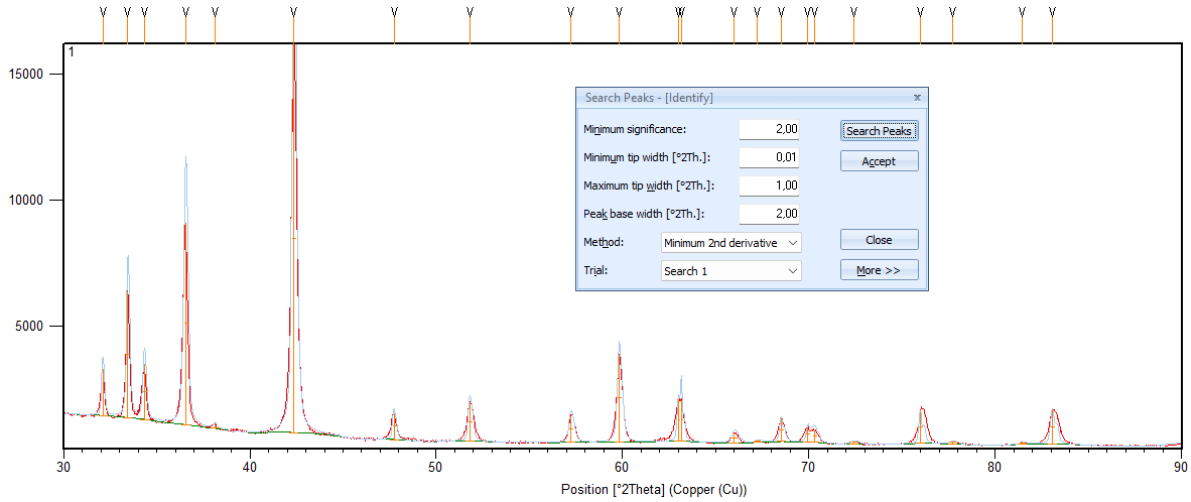

Figure 3.15 *Peak search conducted by the software. The identified peaks are indicated above with arrows.*

- Matching experimental peaks to MgB_2, MgO, MgB_4 and, in some cases, Nb-Ti reference patterns (for the dissimilar joint studies) found in the Inorganic Crystal Structure Database (ICSD) database.

No.	Ref. Code	Score	Compound Name	Chemical Formula	Scale...	ML	NML	TL	SUL	Displac...	Q	Subfiles	Cryst. Syst.	Database ID
1	Cod 96-90...	80	9008506	Mg2.00	0,476	12	12	12	0	-0,108		User I...	Hexagonal	E:\Programl...
2	Cod 96-90...	80	9012001	Mg2.00	0,476	12	12	12	0	-0,108		User I...	Hexagonal	E:\Programl...
3	Cod 96-90...	80	9013057	Mg2.00	0,478	12	12	12	0	-0,157		User I...	Hexagonal	E:\Programl...
4	Cod 96-90...	80	9013056	Mg2.00	0,478	12	12	12	0	-0,157		User I...	Hexagonal	E:\Programl...
5	Cod 96-10...	78	1000026	Mg1.00 B2.00	0,932	11	11	11	0	-0,077		User I...	Hexagonal	E:\Programl...
6	Cod 96-90...	78	9013055	Mg2.00	0,474	12	12	12	0	-0,170		User I...	Hexagonal	E:\Programl...
7	Cod 96-90...	77	9012434	Mg2.00	0,478	12	12	12	0	-0,173		User I...	Hexagonal	E:\Programl...
8	Cod 96-90...	77	9013054	Mg2.00	0,472	12	12	12	0	-0,185		User I...	Hexagonal	E:\Programl...
9	Cod 96-90...	74	9013058	Mg2.00	0,498	12	12	12	0	-0,023		User I...	Hexagonal	E:\Programl...
10	Cod 96-15...	73	1512519	Mg2.00	0,424	12	12	12	0	-0,331		User I...	Hexagonal	E:\Programl...
11	Cod 96-411...	63	4111965	Mg2.00	0,501	12	12	13	0	0,224		User I...	Hexagonal	E:\Programl...
12	Cod 96-90...	62	9013059	Mg2.00	0,492	13	13	13	0	0,153		User I...	Hexagonal	E:\Programl...
13	Cod 96-90...	54	9013060	Mg2.00	0,437	12	12	13	0	0,340		User I...	Hexagonal	E:\Programl...
14	Cod 96-90...	48	Periclase	Mg4.00 O4.00	0,048	3	3	4	0	-0,433		User I...	Cubic	E:\Programl...
15	Cod 96-90...	47	Periclase	Mg4.00 O4.00	0,046	3	3	4	0	-0,324		User I...	Cubic	E:\Programl...
16	Cod 96-90...	45	Periclase	Mg4.00 O4.00	0,059	2	2	4	0	-0,815		User I...	Cubic	E:\Programl...
17	Cod 96-90...	45	Periclase	Mg4.00 O4.00	0,062	3	3	5	0	0,012		User I...	Cubic	E:\Programl...
18	Cod 96-90...	44	Periclase	Mg4.00 O4.00	0,047	3	3	5	0	0,328		User I...	Cubic	E:\Programl...
19	Cod 96-90...	44	Periclase	Mg4.00 O4.00	0,055	3	3	5	0	0,236		User I...	Cubic	E:\Programl...
20	Cod 96-90...	44	Periclase	Mg4.00 O4.00	0,055	3	3	5	0	0,248		User I...	Cubic	E:\Programl...
21	Cod 96-90...	44	Periclase	Mg4.00 O4.00	0,057	2	2	4	0	-0,672		User I...	Cubic	E:\Programl...
22	Cod 96-90...	44	Periclase	Mg4.00 O4.00	0,042	3	3	5	0	0,456		User I...	Cubic	E:\Programl...
23	Cod 96-90...	43	Periclase	Mg4.00 O4.00	0,048	2	2	4	0	-0,536		User I...	Cubic	E:\Programl...
24	Cod 96-90...	42	Periclase	Mg4.00 O4.00	0,064	3	3	5	0	-0,136		User I...	Cubic	E:\Programl...
25	Cod 96-90...	39	9013061	Mg2.00	0,342	10	10	13	0	0,274		User I...	Hexagonal	E:\Programl...

Figure 3.16 *Matching the potential compounds based on the peaks. The higher the score, the greater the accuracy of the compound match.*

- Fitting the experimental pattern using the Rietveld *phase fit* function.

Parameter Varied	Min. Shift/ESD	Use	Switch Off
Flat Background	0,1	☑	☐
More background	0,1	☑	☐
Peak Position	0,1	☑	☐
Peak Height	0,1	☑	☐
Peak FWHM	0,1	☑	☐
Peak Shape	0,1	☑	☐
Specimen Displacement	0,1	☑	☐
Lattice Parameters	0,1	☑	☐
Caglioti W	0,1	☑	☐
Caglioti U	0,1	☑	☐
Caglioti V	0,1	☑	☐
Peak Shape Parameter 1	0,1	☑	☐
Peak Shape Parameter 2	0,1	☑	☐

Figure 3.17 *The parameters utilized during the Rietveld refinement process.*

- Visually inspecting the calculated patterns of the different phases to check that the software has achieved a good fit.

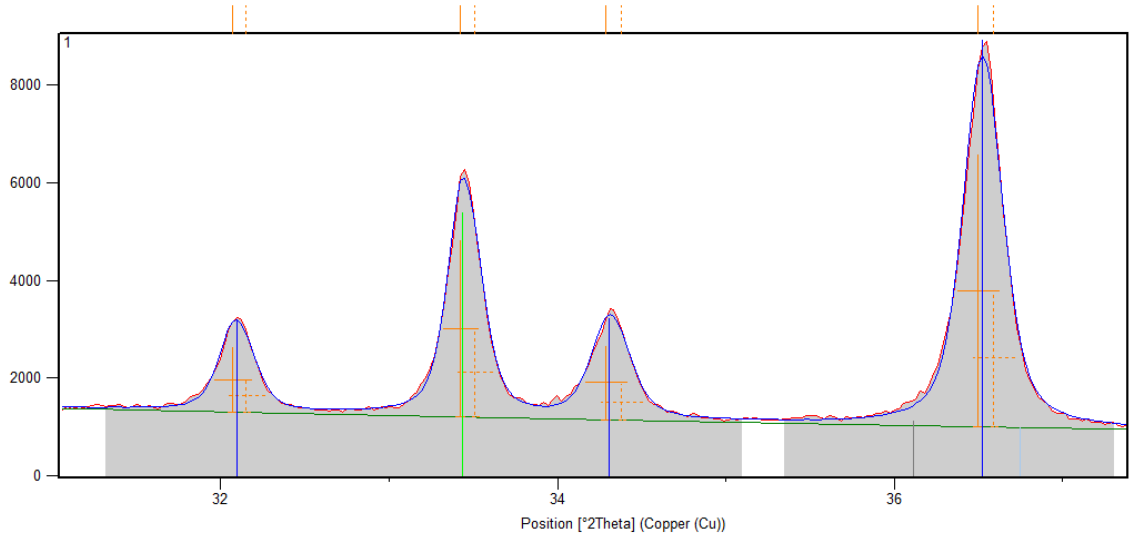

Figure 3.18 *An example of visually inspecting whether the fitting has been successfully completed. The red peak indicates the peak in the data, while the blue peaks represent the fitted peaks.*

While performing phase identification using the PANalytical HighScore Plus software, only Mg, B, and O atoms were included in the analysis, and other atoms were excluded. As a result, the software assigned phases to the peaks extracted from the ICSD database (the reference number for MgB_2 is 1000026) based solely on these three atoms. Instrumental broadening of peaks was corrected using the same Si standard measured under the same

beam optics and scan conditions. The crystallite size, microstrain, and lattice parameters presented in this thesis were obtained using Highscore Plus software.

The errors associated with XRD analysis of MgB_2 powders and bulk samples, as determined through the HighScore Plus analysis method previously described, have been extensively investigated by Dr. Guillaume Matthews [202] within my research group (see **Table 3.3**). The precision of the different parameters was established as half the difference between the maximum and minimum values obtained via Rietveld methods after analysing five nominally identical MgB_2 bulk samples.

Table 3.3 *The accuracy of MgB_2 crystallite size, strain, and lattice parameters determined through Rietveld refinement Reproduced from* [202] *(Copyright © 2020 by IOP Publishing).*

	Crystallite size (nm)	**Microstrain (%)**	***a* axis (Å)**	***c* Axis (Å)**
Precision	± 12	± 0.005	± 0.0002	± 0.0003

All Rietveld refinements presented in this thesis are conducted using the HighScore Plus methodology.

3.3.2 Scanning Electron Microscopy, Energy Dispersive X-ray Spectroscopy and Electron Backscatter Diffraction

When an electron beam interacts with a specimen in Scanning electron microscopy (SEM), it generates secondary electrons (SE), backscattered electrons (BSE) and characteristic X-rays. SE imaging reveals surface details, while BSE imaging penetrates deeper, providing insights into chemical variations. While SE imaging is effective for surface topography, BSE imaging highlights compositional variations. If a BSE image differs from an SE image, it's due to accentuated compositional differences. For comprehensive topographical analysis, SE imaging is preferred. EDX detectors capture characteristic X-rays emitted by excited atoms for elemental composition analysis. Detecting light elements such as Be, B, C, N, O,

and F is challenging due to signal absorption. The analysis of light elements is challenging due to their low photon energies, leading to several issues [203]:

- High absorption in the specimen and detector.
- Low energy peaks close to the electronic noise (around 0 keV).
- Low X-ray yield for light elements.

In contrast, higher atomic number elements produce spectra with more distinct peaks, allowing for alternate peak use in case of spectral overlap [203]. The characteristic K_α X-rays for magnesium, boron, and oxygen are observed at energies of 1.254 keV, 0.183 keV, and 0.525 keV, respectively. An accelerating voltage of 10 kV was chosen in this thesis to ensure full excitation of X-rays from these elements, facilitating quantitative analysis.

SEM and energy dispersive X-ray spectroscopy (EDX) were utilized for microstructural characterization and elemental analysis at the David Cockayne Centre for Electron Microscopy. Microstructural evolution and compositional analysis of bulk samples were performed using a Zeiss Merlin field-emission scanning electron microscope (FE-SEM) equipped with an Oxford Instruments X-Max 150 mm^2 EDX detector, with the accelerating voltage and current set at 10 kV and 2 nA, respectively. For the analysis of joints and wires, a Zeiss EVO microscope outfitted with an Oxford Instruments X-act Silicon drift EDX detector was utilized, with the accelerating voltage and current configured at 10 kV and 200 pA. In some instances where boron detection presents challenges, a 5 kV accelerating voltage and 200 pA current have been utilized to enhance the detection of low-energy X-rays from boron, thereby improving surface sensitivity and minimizing background noise. Both EDX detectors are equipped with polymer windows, which allow efficient transmission of low-energy X-rays, enabling the detection of light elements while

maintaining structural durability under vacuum conditions. These polymer windows were utilized during the EDX analysis conducted in this thesis.

EDX data were analysed using Aztec software. Element maps based on peak selection may overlook peak overlaps and background signals reducing sensitivity to light and minor elements. Trumap corrections were employed to eliminate false data and map artifacts. QuantLine, utilizing Tru-Q routines in the Aztec software was used for providing quantitative element variations. For point analysis, peak positions and shapes were fitted algorithmically to calculate elemental concentrations and the calculation errors were given by the software.

3.3.3 Physical Property Measurement System, PPMS

Magnetic properties were assessed using a Quantum Design physical properties measurement system (PPMS) with a Vibrating Sample Magnetometer (VSM) at the Clarendon Laboratory, Physics Department.

Cuboid MgB_2 samples, approximately 2×2×3 mm in size, were mounted to a non-magnetic brass holder fixed tightly by quartz cylindrical holders. Kapton tape prevents the holder loosening during vibration. MultiVu software was used for VSM automation and control. Samples are cooled under zero field and T_c is measured by moment-temperature sweeping at a fixed applied magnetic field of 5 mT.

Moment-field (M-H) sweeps were conducted at 4.2 K and 20 K to facilitate comparison with existing literature they are the feasible operating temperatures.

When changing samples, the chamber is warmed up to 100 K and the magnetic field set to 0 in oscillate mode, stabilizing the system for at least 16 hours to eliminate residual field in the superconducting magnet.

Hysteresis loops from PPMS are used to determine the J_c, H_c and T_c of the sample. During the measurement, magnetic flux enters from the surface, forming vortices that move inward due to the external field's repulsive force. Vortex pinning opposes this force, creating a flux density gradient and generating a shielding current.

The hysteresis loop in **Figure 3.19**a begins after zero-field cooling (ZFC). Initially, the superconductor is in the Meissner state with the initial slope termed the Meissner slope, dependent only on the sample's geometry, assuming the smallest dimension significantly exceeds the magnetic penetration depth. When the applied field exceeds the lower critical field, H_{c1}, vortices penetrate the superconductor [204].

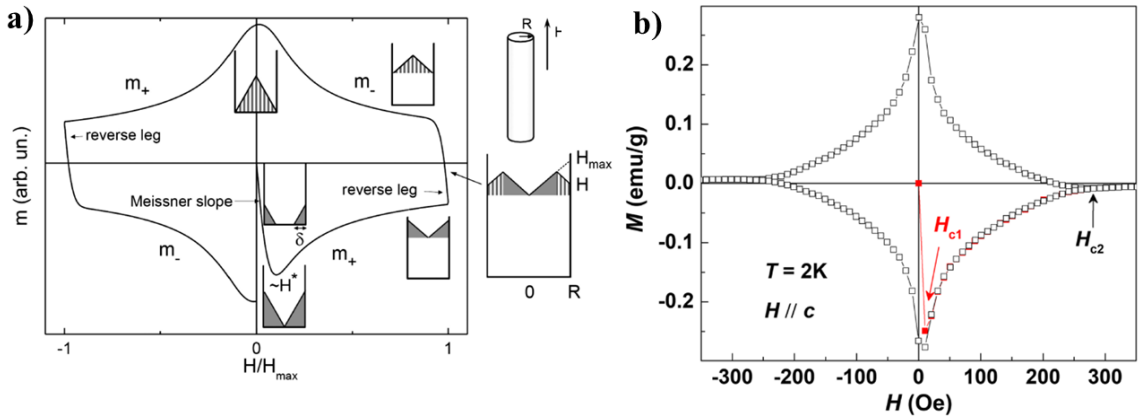

Figure 3.19 *a) Hysteresis loop of a non-reversible Type II superconductor. The insets depict the critical condition within an infinitely long cylinder aligned with the magnetic field. The gradient of the field profiles correlates directly with J_c. The shaded areas, grey and striped, represent magnetic moments with opposing orientations* [204]. *b) An example illustrating the approximate points of H_{c1} and H_{c2}. Reprinted from* [205] *(Copyright © 2021, LLC part of Springer Nature)*

Identifying H_{c1} is difficult since linear behaviour continues as long as the Bean penetration depth, δ, exceeds the sample's dimensions. However, H_{c1} typically marks the point where the diamagnetic Meissner phase, indicated by the negative part of the M(H) curve, deviates from linearity [205] as seen in **Figure 3.19**b. Additionally, H_{c2} is usually the field where the magnetization reaches zero during the increasing field branch of the loop as shown in **Figure 3.19**b [205]. Current density is calculated using Bean's critical state model which is;

$$J_c = \frac{2\Delta M}{a(1 - a/3b)} \tag{3.1}$$

where ΔM is the width of the magnetic hysteresis loops which can be also obtained from the hysteresis loop, *a* and *b* is the cuboid sample dimensions with *a*>*b*.

3.3.4 High current transport measurement

The term '*transport*' denotes a current that is introduced from an external source at one location on the sample and withdrawn at another. For a more precise characterization of a real superconductor sample, it is essential to examine either the current-voltage curve *V*(*I*) or the relationship between current density and electric field, *E*(*J*) [206].

Superconductors are often described as having zero electric field, *E*, below a critical current density, J_c, and normal-state *E* above J_c. In reality, various dissipation mechanisms influenced by material properties and external conditions, result in diverse *E(J)* behaviours. A common trait is non-linearity in the *E(J)* relationship: at low current densities, *E* is minimal and may be undetectable, but it increases non-linearly with current density before stabilizing near the normal-state *E*.

Figure 3.20 illustrates five *V–I* characteristics. They can be described as follows: In **Figure 3.20** (a), a resistive region is observed at low currents due to insufficient separation between the current leads and voltage taps. The transition to the normal conducting state becomes apparent at higher currents, as depicted in **Figure 3.20** (b). Flux creep (see section 2.3.3) manifests at lower currents, while at higher currents, the transition becomes more pronounced as flux flow initiates, as shown in **Figure 3.20** (c).

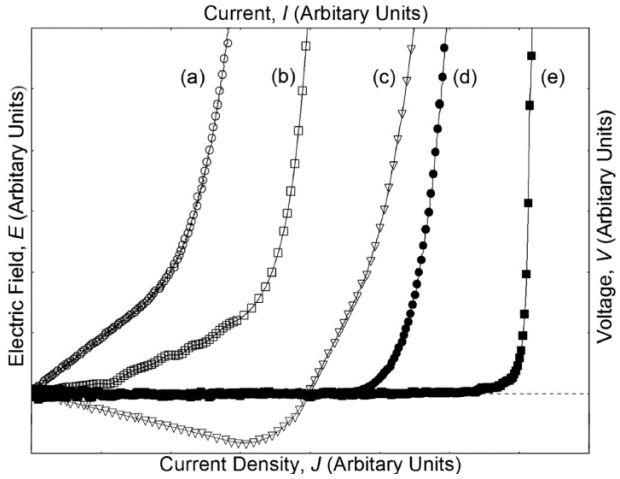

Figure 3.20 *Schematic V–I characteristics illustrating (a) current transfer, (b) flux creep, (c) a thermal voltage followed by current transfer, (d) flux flow and (e) thermal runaway* [207]

Negative thermal voltage may develop at low currents, possibly caused by excessive heating at the current injection point, leading to a notable temperature gradient between the voltage taps. At intermediate currents, the voltage may become net positive due to resistive voltage associated with current transfer in and out of a limited number of damaged filaments. In the flux flow state, depicted in **Figure 3.20** (d) at high currents, there is a zero-resistance region followed by a flux flow transition. Zero resistance persists until a quench occurs in the conductor, leading to heating, as illustrated in **Figure 3.20** (e) [207].

If the *E(J)* curves are not perfectly abrupt, certain standards are required to clearly define J_c or I_c values. Typically, an electric field criterion is utilized, such as defining J_c as the current density producing an electric field E of 10^{-4} V/m. Additionally, specific levels of resistivity, like $\rho_c = 10^{-12}$ Ωm, or dissipated power per unit volume, such as $\rho_c = 104$ W/m^3, are sometimes used as criteria [206]. In short, straight geometries with a measurement distance around 1 cm, a voltage sensitivity under 100 nV is needed to achieve 10 μV m^{-1}. Hence, an electric field criterion of 100 μV m^{-1} or even 1000 μV m^{-1} is often used [208].

The cryostat at Epoch was custom-made, with details published by Baskys et al [209].

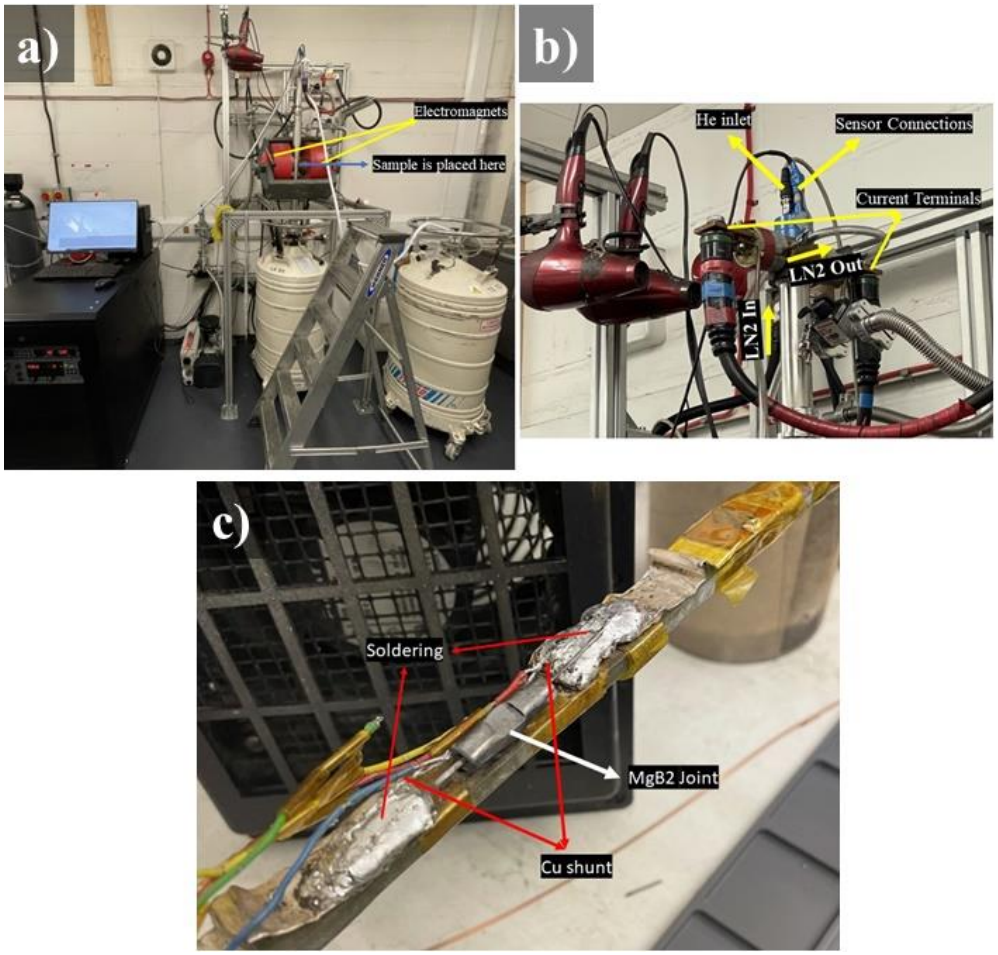

Figure 3.21 *High current transport T_c measurement instrument at Epoch. a) shows the general set up of the instrument, b) shows current terminals, sensor connections and gas inlet/outlet.*

The setup of the instrument is depicted in **Figure 3.21**a-b, while the sample holder rod is illustrated in **Figure 3.21**c. In the sample holder shown in **Figure 3.21**c, the wires of the joint were soldered, and a copper shunt was also soldered in parallel to the joint. The Cu shunt is employed as a precautionary measure in the event of a sudden quench or loss of superconductivity in the joint under test. Its high resistance enables the excess current to bypass the superconducting wire, thereby preventing damage to the measurement equipment. The current taps have been soldered onto this Cu shunt whereas voltage taps were soldered onto the joined wires. However, the image shows the stage prior to their soldering.

3.3.5 Low current transport measurement system

It was important in this work to have a relatively quick way to check if there was a superconducting path between the two wires in a joint before attempting much slower and more complex persistence measurements. The illustration of the cryocooler setup is given in **Figure 3.22.**

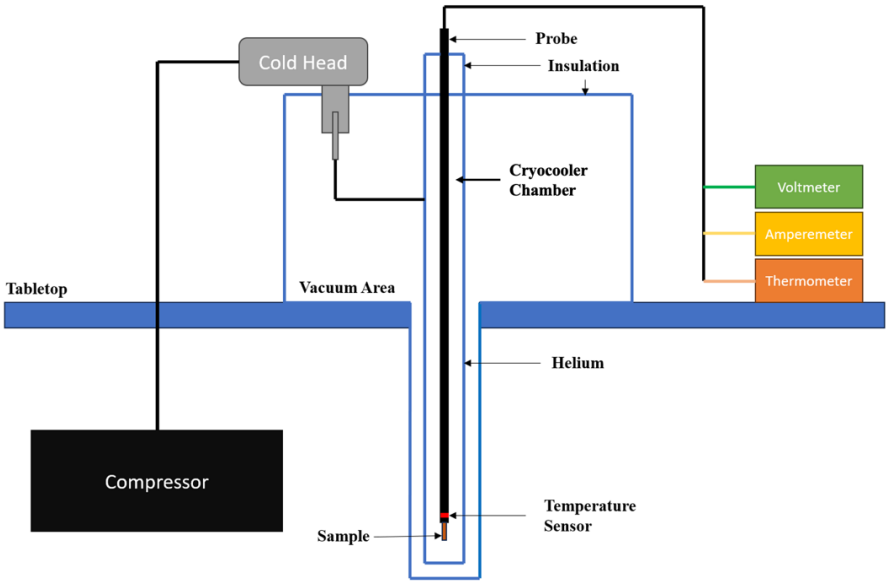

Figure 3.22 *Schematic illustration if the cryocooler setup.*

The sample holder was mounted onto a probe and carefully inserted into the cryocooler chamber. A DC current was supplied by a Keysight E36311A programmable DC Power Supply. The voltage across the two voltage contacts was measured using a Keithley 2000 Digital Multimeter. To monitor the temperature, an SD706 silicon diode temperature sensor was positioned at the end of the probe, just above the sample. A LabView program record both voltage and temperature measurements during the cooling process from room temperature to below the superconducting transition temperature of the sample, as well as during the subsequent natural warming up phase after the cryocooler was switched off. The onset T_c was measured when the resistance was 90% of its value at 40 K, and the ending critical temperature, known as offset T_c, was taken when the resistance was 10% of its value

at 40 K The difference between T_c onset and T_c offset, denoted as ΔT_c, governs the sharpness (abrupt resistance drop) of the T_c transition. A reduced ΔT_c indicates a more abrupt transition.

It was seen that there appears to be a difference in the T_c values measured while cooling and warming for all the samples. For instance, **Figure 3.23**, the disparity between the T_c transition during cooling and warming sequences is depicted and this situation present in all samples. This could be because the temperature sensor is located within the metallic probe, but the sample holder is located at the bottom of the cryostat, meaning the sensor is cooled first. Since it takes longer for the chamber to warm up, there is a smaller temperature difference between the sample and sensor during warming.

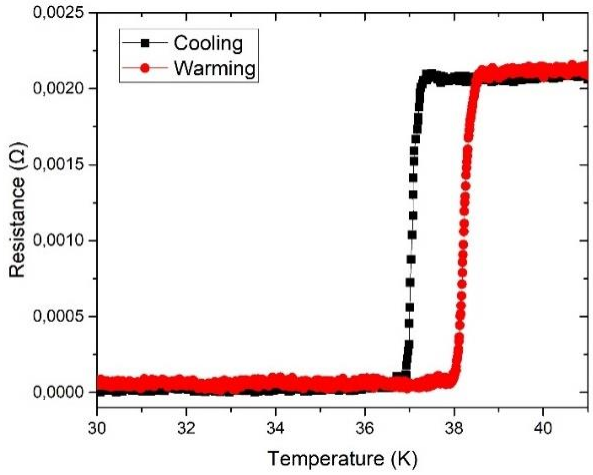

Figure 3.23 *Cooling and warming T_c profile of the sample 1a given in* ***Figure 6.8****.*

Therefore, the temperature when the sample experiences the normal-superconducting transition during warming is higher than during cooling. Thus, it is believed that the warming data will be more accurate than the cooling data. Therefore, only the warming data will be shown from this point onward.

3.3.6 Inductive Resistance Testing, IRT

Inductive Resistance Testing (IRT) [177, 210] has been employed to evaluate the performance of a single-joint closed MgB_2 coil. In terms of I_c determination, the primary distinctions between transport and inductive experiments involve the experimentally accessible range and the configuration of the current path. There are practical constraints on the amplitude of the transport current that can be injected into a sample without encountering significant experimental challenges. These challenges may include ensuring the stability and safety of the experimental setup, managing the heat generated by the high currents, and preventing damage to the sample or the experimental apparatus. In general, transport experiments are better suited for examining lower current densities and higher electric fields, whereas inductive techniques typically entail higher current densities and lower electric fields.

The second key difference between transport and inductive experiments relates to the current path. In transport measurements, the current flows between two contact points, while magnetically induced currents form closed loops confined within the sample or closed coil.

In a uniform sample, both types of currents are governed by the same *E(J)* curve. Consequently, given equivalent conditions (such as magnetic field strength, temperature, and electric field), both experiments will yield identical critical current densities [211]. However, if the sample exhibits inhomogeneity, it is plausible that induced current loops, confined to localized regions with high J_c, might dominate the overall magnetization signal, whereas the transport current is obliged to traverse areas with lower J_c. Consequently, in such scenarios, the measured transport J_c may be lower than that derived from an inductive experiment.

Figure 3.24 depicts the setup of the persistent current measurement, conducted using a 9T/3T vector magnet within an Attodry cryostat. For temperature monitoring, a thermocouple was strategically positioned as close as possible to the test coil, placed at the base of the experimental probe. A Lakeshore HGT-2101 Hall probe was centrally situated within the test coil. To execute an IRT measurement, the external magnet applies a field aligned parallel to the coil axis.

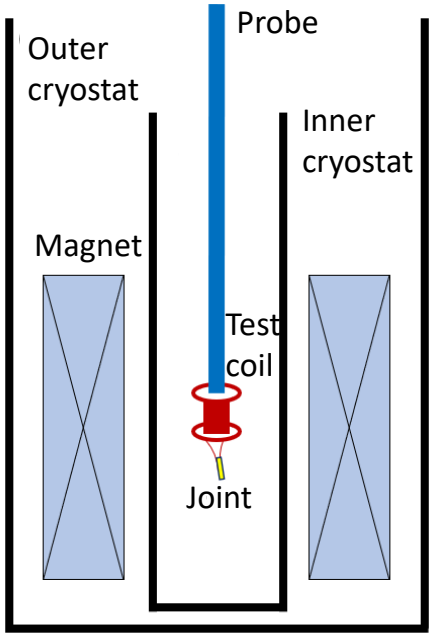

Figure 3.24 *Diagram illustrating the key elements of the IRT experimental setup, including the inner and outer cryostats, the background field magnet, and the experimental probe. The probe consists of a magnetic field sensor, typically a Hall probe, positioned at the tip and inserted into the centre of the jointed test coil.*

In a typical experiment, the applied field is gradually increased to a maximum, such as 1 T, before being gradually decreased (usually at a slower rate to prevent coil instability leading to flux jumps) back to zero or to a preferred background field. As the external magnetic field diminishes, the induced current generated within the coil flows in a manner that produces a magnetic field opposing the decreasing external field as prescribed by Faraday's law of electromagnetic induction. This alteration in flux triggers an electromotive force (EMF) within the coil prompting the flow of current. In accordance with Lenz's law, this induced

current opposes the change in the magnetic field ensuring that the voltage produced attempts to counteract the reduction in field strength. Consequently, if the field decreases slightly, a voltage will be generated to increase the current flowing through the coil, aiming to boost the field again.

The field decay and so the current decay rate can be found with the following equations [32];

$$\frac{\mathrm{B(t)}}{\mathrm{B(0)}} = \mathrm{e}^{\left(\frac{-\mathrm{R}}{\mathrm{L}}\right)\mathrm{t}} \tag{3.2}$$

$$I = \frac{B\sqrt{4r^2 + l^2}}{\mu_0 N} \tag{3.3}$$

where, *B(t)* and the *I* are the induced magnetic field and the circulating current at time, *t*. *B(0)* is the initially induced magnetic field, *R* is the joint resistance, *L* is the coil inductance *t* is the time, *r* is the coil inner radius, *l* is the coil length, μ_0 is the vacuum magnetic permeability and *N* is the number of turns.

Chapter 4 Microstructure and Superconducting Properties of Preliminary Cold-Pressed MgB_2 Bulks

4.1 Introduction

Before starting MgB_2 joint production, I conducted preliminary studies to understand the effects of using different stoichiometric ratios of reactants and heat treatment methods on the crystallographic and superconducting properties of MgB_2. The aim is to understand the reactions that would occur in the filler material added to the joint that will form the superconducting path between the two MgB_2 wires, but without the geometric complexities of the joint design described above.

Recent studies in the literature predominantly concentrate on high-pressure MgB_2 bulk production [212–215], given the correlation between MgB_2 density and its J_c, as discussed with a dense joint structure [193] in 2.6.1. Several examples of high-pressure sintering methodologies comprise cubic anvil high-pressure sintering, 5.5 GPa [213], ultra-high pressure-assisted sintering, 5 GPa [212], hot isostatic pressure, 196 MPa [216] and field assisted sintering [217], 50 MPa continuous pressure during the heat treatment.

In this work, the applied cold pressure before heat treatment is kept relatively low, around 30 MPa, due to die limitations. MgB_2 is characterized by its brittleness as a ceramic material, necessitating higher pressure and the packing ratio to maintain structural integrity [216]. Insufficient pressure risks fracturing the material even during sample removal from the furnace, making it impractical to cut tiny samples for PPMS measurements. To address this, excess Mg was incorporated to preserve mechanical strength during cutting and to investigate MgB_2's properties with excess Mg. The study used temperatures between 700°C and 800°C, as Mg's reaction liquid phase occurs between 650°C and 1100°C (see **Figure**

2.8). Excess Mg expedited the reaction at temperatures above 700°C, preventing unreacted Mg. The 800°C upper limit minimized Mg evaporation as much as possible and avoided forming borides like MgB_4.

In summary, this chapter examines the preliminary processes involved in producing cold-pressed MgB_2 ceramics. It includes using an elevated quantity of Mg as the initial powder, followed by heat treatment at various temperatures and durations. The microstructural and magnetic characteristics of the samples are then analysed.

4.2 Experimental methods of cold-pressed MgB_2 bulks

The synthesis of MgB_2 is pivotal in the fabrication of both wire and joints, and so comprehending the mechanisms and kinetics of reaction is essential for controlling an effective process. Different ratios of Mg and B were prepared in pellet form using a 32 mm diameter steel die and subjected to heat treatment at various temperatures and dwelling times in a tube furnace under Ar atmosphere. Production steps are described in section 3.1.1 Starting powder ratios and heat treatment conditions of four samples are given in **Table 4.1**.

Table 4.1 *The atomic ratio and the applied heat treatments on exceed Mg and B pellets.*

Sample	Mg:B in atomic ratio	Heat Treatment
1	1:0.9	700 °C 1 hour
2	1:0.9	700 °C 5 hour
3	1:0.9	800 °C 5 hour
4	1:1	800 °C 5 hour

Sample 1 and Sample 2 analyse the impact of dwell time of the same heat treatment, whereas Sample 2 and Sample 3 investigate the effects of heat treatment ranging between 700°C and

800°C on samples. Additionally, Sample 3 and Sample 4 also examine the effects of a slightly reduced quantity of magnesium.

4.2.1 Phase identification and quantitative analysis by Rietveld Refinement

The prepared samples were subsequently analysed using X-ray diffraction, and the phases were fitted using Rietveld refinement, following the procedure outlined in Section 3.3.1. The XRD patterns are provided in **Figure 4.1** and quantitative analyses and weight fractions of samples are provided in **Table 4.2**. The reliability of the XRD measurements for the analysed samples varies among the parameters. Precision is derived from mathematical fitting, while the XRD errors are detailed in Section 3.3.1 and presented in **Table 3.3**. The *a*-axis and *c*-axis measurements show high precision, with uncertainties of ± 0.001 Å and XRD errors of ± 0.0002 Å and ± 0.0003 Å, indicating robust data. Similarly, strain values are consistent, with a precision of ±0.055 and XRD error of ±0.005. However, the crystallite size measurements, ranging from 57.24 nm to 97.85 nm, have a high uncertainty of ±12 nm, raising concerns about their reliability.

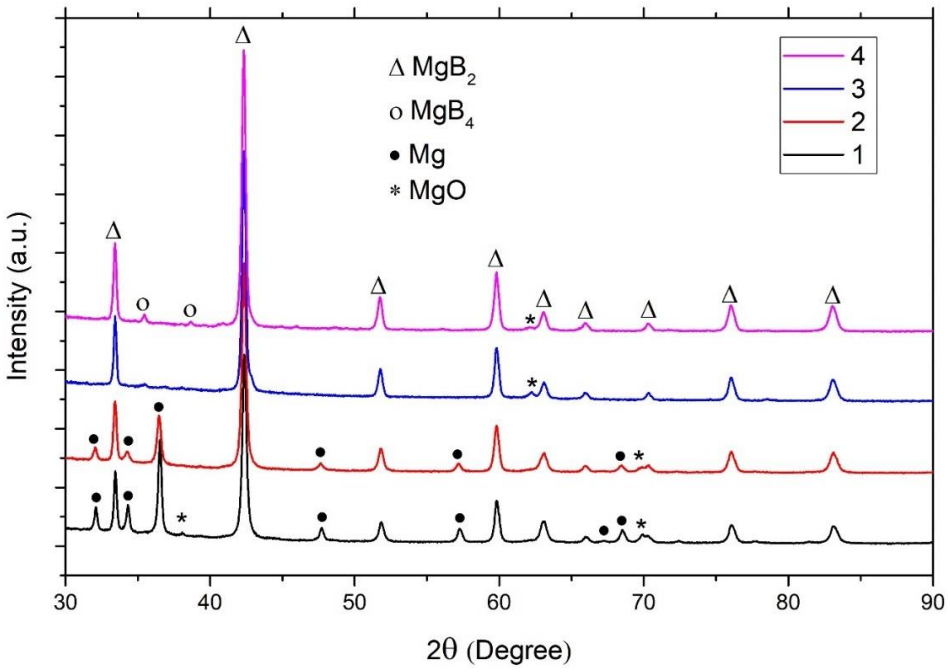

Figure 4.1 *XRD patterns of the bulks.*

This significant precision uncertainty suggests caution in interpreting these results, indicating a need for further investigation to enhance measurement accuracy.

Sample 1 exhibits a high weight fraction of MgB_2 (76.3%), accompanied by minor fractions of unreacted Mg (20.3%) and MgO (3.4%). The MgB_2 lattice parameters (*a*-axis and *c*-axis) are measured at 3.093 Å and 3.524 Å, respectively. A slight level of strain (0.195%) is observed, indicating minimal lattice distortion. The crystallite size is determined to be ~57 nm. It appears that the temperature, 700 ^oC or the dwelling time, 1 hour, is not sufficient for the complete reaction to form MgB_2 in this composition. Due to an excess Mg initially, it is essential to facilitate the evaporation of surplus Mg to achieve a higher yield of MgB_2. Otherwise, as demonstrated here, it is quite typical to observe a significant amount of unreacted Mg.

When the dwell time increased to 5 hours, in Sample 2, the MgB_2 content increased to 83.1%, while Mg and MgO were present in smaller proportions (16.4% and 0.5%, respectively).

Table 4.2 *Weight fractions and quantitative analysis of MgB_2 pellets.*

Sample	**Weight Fractions %**				***a*-axis**	***c*-axis**	**Strain %**	**Crystallite size nm**
	MgB_2	**Mg**	**MgO**	**MgB_4**				
1	76.3	20.3	3.4	-	3.093	3.524	0.195	57
2	83.1	16.4	0.5	-	3.136	3.526	0.218	57
3	97.6	-	2.4	-	3.090	3.528	0.238	97
4	97.4	-	1.5	1.1	3.091	3.530	0.229	77
Precision					±0.001	±0.001	±0.055	±0.001
XRD errors					±0.0002	±0.0003	±0.005	±12

As with Sample 1, no MgB_4 phase was detected since there was still unreacted Mg present. While the *a*-axis significantly increased, the *c*-axis was similar to Sample 1, with a slightly

increased level of strain (0.218%) and a comparable crystallite size of ~58 nm. The increase in the *a*-axis parameter in Sample 2 (3.136 Å) likely results from reduced residual Mg content (16.4%), which decreases lattice constraint. Excess Mg generally resides at grain boundaries or defects, where it exerts compressive stress on the MgB_2 lattice, limiting expansion. In Sample 1, a higher residual Mg content (20.3%) correlates with a smaller *a*-axis (3.093 Å). By decreasing residual Mg in Sample 2, these compressive stresses are alleviated, allowing minor lattice relaxation along the *a*-axis. The longer heat treatment at 700°C for 5 hours further supports Mg redistribution, enhancing this expansion effect.

When the temperature increased to 800°C, sample 3 demonstrated a significantly higher weight fraction of MgB_2 (97.6%), alongside detectable amounts of MgO (2.4%). It is thought that the excess Mg left the bulk and evaporated leaving behind substantial amount of MgB_2 and small amount of MgO. This compositional change results in an increase in the *a*-axis and a decrease in the *c*-axis, with elevated strain (0.238%) indicating greater lattice distortion. Notably, the crystallite size in Sample 3 is significantly larger, measuring at ~98 nm.

Finally, Sample 4 presents the high weight fraction of MgB_2 (97.4%), along with minor amounts of MgB_4 (1.1%) and MgO (1.5%). The initial quantity of Mg was lower than that of previous samples, 1, 2 and 3. It appears that once the volatile Mg escapes from the pellets, the MgB_4 phase begins to be present. The lattice parameters closely resemble those observed in Samples 1 and 2, with a moderate level of strain (0.229%) and a crystallite size of around 77 nm. Dadiel et al. [218] investigated *in-situ* MgB_2 production using the spark plasma sintering method. They prepared *in-situ* (Mg+2B) pellets with the standard stoichiometric ratio of 1:2 and subjected them to various heat treatment conditions ranging from 720°C to 775°C for 15 and 20 minutes separately under an Ar atmosphere. At 775°C for 20 minutes,

they began to observe a significant amount of MgB_4 which can be detected in *in-situ* MgB_2 samples when subjected to heat treatment at temperatures ≥ 775°C, even with short dwell times such as 20 minutes. This observation may be attributed to the accelerated evaporation rate of Mg beyond a certain threshold, around 775°C, in the *in-situ* reaction of MgB_2. This could explain the presence of MgB_4 in sample 4, given the higher duration (5 hours) and temperature (800°C) compared to Dadiel's study.

It is also thought that the increase in the *c*-axis parameter across samples is primarily due to reduced residual Mg, prolonged heat treatments, and improved phase purity, which collectively relax lattice constraints. In Sample 1, treated at 700°C for 1-hour, higher residual Mg and MgO content create compressive stress, yielding a smaller *c*-axis (3.524 Å). Extending the treatment to 5 hours (Sample 2) reduces Mg content, allowing slight *c*-axis expansion (3.526 Å). At 800°C, Samples 3 and 4 show the greatest *c*-axis values (3.528 Å and 3.530 Å, respectively) due to nearly complete Mg diffusion, minimal secondary phases, and enhanced crystallinity, illustrating how optimized conditions promote lattice relaxation and expansion along the *c*-axis.

4.2.2 Microstructural analysis

Microstructural analysis of these samples has been conducted, with SEM images provided in **Figure 4.2**. The specimens underwent a carbon coating process with an 18 nm thickness, as detailed in section 3.2.1. The main purpose of this coating was to reduce surface charging effects and prevent image distortion during SEM and EDX analyses. The carbon data was intentionally obscured in EDX maps due to its substantial impact on the maps.

In Sample 1(a-b), numerous porosities ranging from approximately 100 to 150 μm were observed on the surface, closely resembling the initial Mg powder sizes. This suggests that the voids may have formed either through reaction with B or evaporation from the

environment. To mitigate porosity size, using smaller Mg particles would be advantageous, but this approach is cost-prohibitive, as discussed in section 2.5.

As the presence of Mg diminishes, primarily due to excessive evaporation, the structure becomes increasingly porous and brittle. For instance, Sample 3 demonstrated brittleness, evident from its susceptibility to breakage during sample preparation for PPMS analysis. Notably, Sample 2 exhibited higher surface porosity compared to Sample 1, attributed to the higher levels of evaporated Mg, as corroborated by the weight fraction of unreacted Mg outlined in **Table 4.2**. This resulted in varied sizes and depths of surface voids. However, regions with denser morphology, observed in both Samples 1 and 2, indicate Mg-rich domains, as further evidenced by forthcoming EDX mappings (**Figure 4.3**).

In Sample 3(e-f), at low magnification (e), a reduction in porosity size was observed, with particles exhibiting fusion thereby decreasing overall porosity. At high magnification, (f), the aggregation of small particles into larger grains was evident. This phenomenon may be attributed to the reaction of Mg and B, which commences at around 600°C, accelerating with increased heat.

At a certain point, where all B has reacted and there is no unreacted B in the system, saturation of the bulk material is attained, halting further MgB_2 production, while unreacted Mg persists within the bulk (as observed in Samples 1 and 2). With higher temperatures (800°C in Sample 3), some Mg evaporates, and trace amounts of MgB_2 decompose into $MgB_{4(solid)}$ and $Mg_{(vapor)}$ (as discussed in 2.4.3.2). With residual Mg present, MgB_4 reacts with existing Mg, resulting in fused regions akin to those observed in (f), persisting until complete Mg depletion from the bulk. MgB_4 was not observed in Sample 3, presumably because the Mg in the bulk was not completely depleted by the end of the 1-hour duration.

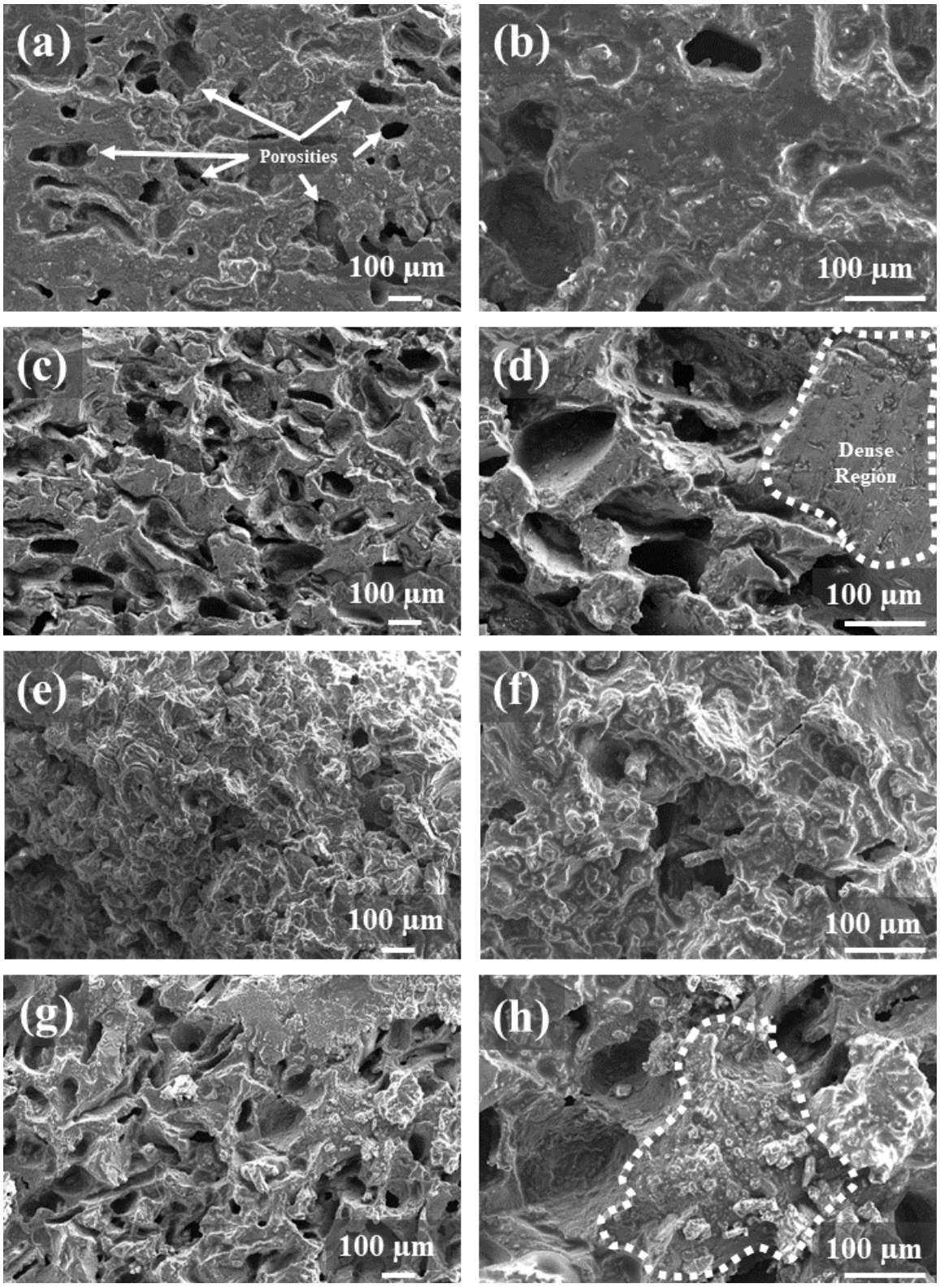

Figure 4.2 *SEM images of the bulk samples. a-b is the sample 1, c-d is the sample 2, e-f is the sample 3 and g-h is the sample 4.*

In Sample 4(g-h), subjected to an extended heat treatment duration of 5 hours, the decomposition of MgB_2 initiates around 800°C and progresses gradually during the dwell

time. Consequently, MgB_2 decomposition product, $Mg_{(vapor)}$, gradually depart from the bulk over time, resulting in the emergence of higher boride phases. This occurrence likely accounts for the trace amounts of MgB_4 detected as evidenced in **Table 4.2**. Furthermore, in (h), a particular region was delineated due to the presence of observed small particles. A thorough examination of these particles was conducted using the BSE and EDX mapping in the following paragraphs.

In **Figure 4.3**, EDX maps and BSE images of the samples are presented. Oxygen-rich regions are indicated by dotted red circles, while magnesium-rich regions are highlighted with dotted light blue circles. Additionally, suspected MgO particles are identified with red arrows.

In Sample 1, **Figure 4.3**a, it is evident that Mg distribution is uneven, with accumulation observed in specific regions, corroborating the findings depicted in **Figure 4.2**a. Furthermore, small MgO particles were identified, one of which is highlighted by a red arrow. Within the region highlighted by a red dotted circle, indicating oxygen-rich areas, Mg displayed a lower concentration relative to oxygen. However, the detection of boron appears to be limited, a common challenge in EDX imaging resulting from signal absorption associated with the low photon energies of boron [203], as discussed in Section 3.3.2. Additionally, the measurement error provided by the Aztec software, amounting to approximately ± 3.8% for this sample, must also be taken into consideration.

In sample 2, **Figure 4.3**b, EDX revealed the presence of small white particles suspected as MgO, with one of them being specifically indicated by an arrow. Within the area shown by a small blue circle, a notable concentration of Mg was observed, contrasting with low levels of oxygen. Nevertheless, the concentration of B remained indistinct.

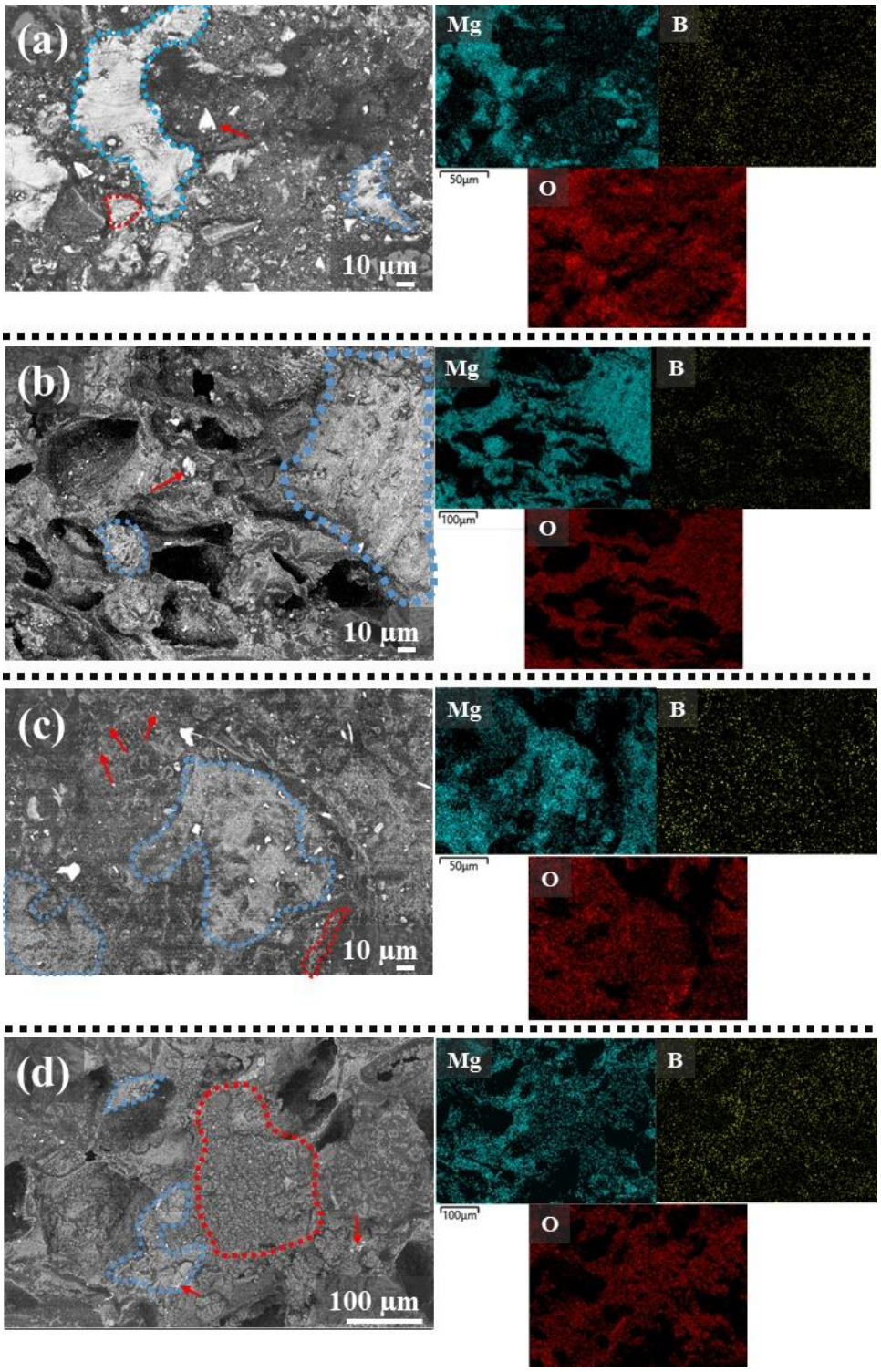

Figure 4.3 *EDX maps of the samples are provided. Mg is blue, B is yellow and O is red colour. Red arrows showing MgO particles, red-dotted area shows oxygen rich regions, blue-dotted area shows Mg rich regions.*

However, within the larger blue circle corresponding to the Mg-rich region, a relatively higher concentration of boron was observed, suggesting the potential presence of MgB_2

compound within that particular area compared to rest of the region. In sample 3, **Figure 4.3**c, the B concentration is notably more pronounced in comparison to the B maps obtained for samples 1 and 2, with a high error margin of 3.66%. In a specified zone marked by a blue circle, there is a noticeable abundance of Mg, whereas areas beyond this boundary exhibit relatively diminished levels of Mg concentration. In contrast, in the region outlined by a red dashed line, there is an abundance of oxygen, yet intriguingly limited Mg concentration is observed. This adds complexity to the analysis as the spectrum of this area reveals the following elemental compositions:

Table 4.3 *The atomic % of the area shown red dotted circle in sample 3,* ***Figure 4.3****c*

Element	Atomic %	Error %
B	18.83	± 3.66
C	55.00	± 2.82
O	9.32	± 1.04
Mg	11.86	± 1.32

The elevated level of carbon observed likely originates from a carbon coating. Examination of the table may suggest the presence of Mg-B-O inhomogeneities, with the size of these inclusions typically ranging within a few micrometres. A similar scenario has been noted in sample 4.

In sample 4, **Figure 4.3**d, the red circle denotes an oxygen-rich region. Similar to Sample 3, the concentration of Mg is not significantly high compared to the blue circle depicted in the same image. However, in contrast to Sample 3, this oxygen-rich area appears more expansive. This may suggest that prolonged treatment duration may have led to an increase in the quantity of Mg-B-O compounds present. The atomic concentration of this region is provided in **Table 4.4**.

Table 4.4 *The atomic % of the area shown red dotted circle in sample 4,* ***Figure 4.3****d.*

Element	Atomic %	Error %
B	18.54	± 1.27
C	63.02	± 1.15
O	16.11	± 0.71
Mg	2.33	± 0.21

The **Table 4.4**. reveals concentration ratios for Sample 4 similar to those in **Table 4.3** for sample 3 with significantly reduced amount of Mg and a lower B error. The corresponding spectra are provided in **Figure 4.4**.

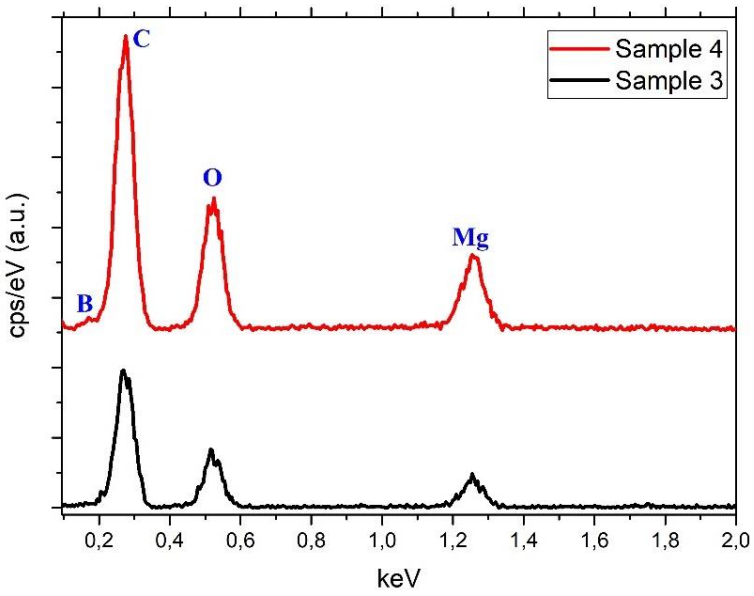

Figure 4.4 *The spectra of the regions, whose details are provided in Table 4-3 and Table 4-4 for the black and red curves, respectively.*

It has seen that there is large C peak and its left tail is overlapping the B spectrum. Which may affect the actual amount of B in corresponding regions. However, Mg peaks are not overlapping with any atoms and its intensity is lower and broader in Sample 3 compared to Sample 4. This may suggest that the onset of non-superconducting inhomogeneities, B-O compound in this point, may occur above a certain temperature threshold. Estimating the compositions of the small precipitates proves challenging due to the overlapping signals of

compounds within the area, which contribute to the EDX analysis. Consequently, the EDX spectrum alone does not provide sufficient data to distinguish these precipitates. Liao et al. [219] prepared Mg+B powder with a 1:1 stoichiometric ratio, deviating from the typical 1:2 ratio without explanation. They applied approximately 500 MPa to form pellets, followed by heat treatment at 900°C for 2 hours under an Ar atmosphere. They identified precipitates ranging from 10-100 nm. Larger precipitates primarily consisted of magnesium and oxygen, while smaller ones included magnesium, boron, and oxygen. As precipitate size increased, oxygen content rose while boron content decreased, indicating boron substitution by oxygen. They concluded that oxygen dissolved in MgB_2 at high temperatures precipitates as $Mg(B,O)_2$ at lower temperatures. Prolonged high-temperature exposure transforms $Mg(B,O)_2$ precipitates into MgO with minimal size change. They proposed that 5-10 nm size precipitates serve as significant pinning centres in MgB_2.

Prikhna et al. [220] noted the occurrence of Mg-B-O nano inclusions during the synthesis of MgB_2. They conducted experiments involving the synthesis of two distinct *in-situ* MgB_2 bulks using a stoichiometric ratio of 1:2 for the Mg and B powder mixture. Each sample was subjected to a pressure of 2 GPa, with one heat-treated at 600°C and the other at 1050°C (the duration of treatment was not specified). They observed that the sample treated at 1050°C exhibited higher J_c under both 0 T and 1 T magnetic fields. This enhancement was attributed to the presence of nano Mg-B-O inclusions observed within the bulk, which were hypothesized to act as pinning centres.

4.2.3 Magnetisation measurements

The sample preparation for this test is detailed in section 3.2.3, while the measurement technique is elaborated upon in section 3.3.3. An example of a cut sample is shown in **Figure 4.5**. This piece underwent moment-field (M-H) and moment-temperature (M-T)

measurements to determine the values of T_c from M-T and J_c from M-H, as illustrated in **Figure 4.7**. The M-H plots were produced using a Python script that I developed (see Appendix C).

Figure 4.5 *An example of an MgB_2 piece cut for magnetisation measurement.*

Regrettably, magnetization tests for Sample 3 could not be performed due to its breakage during attachment to the sample holder. As outlined in Section 2.5, MgB_2 is a brittle ceramic material that demands careful handling during cutting procedures. This illustrates the need to utilize surplus magnesium as an initial powder, as discussed in the introduction. H_{c1} and H_{c2} values of the samples were deduced from their hysteresis loops as discussed in section 3.3.3. H_{c2} is delineated as the point at which the magnetic moment reaches zero (shown as green dots in **Figure 4.6**), while H_{c1} is identified as the value where the Meissner slope starts to deviate from a linear behaviour in **Figure 4.6** shown as red dots.

Figure 4.6 illustrates the magnetic moment's field dependence for samples at 4.2 K (a) and 20 K (b). Notably, pronounced flux jumps were observed subsequent to the low-field Meissner region (H_{c1}). These flux jumps manifest promptly as the field surpasses H_{c1}, a critical threshold where fluxes pinned at defects begin to mobilize, subsequent to crossing a lower critical field, H_{c1}. Under low temperatures (<10 K) MgB_2 exhibits flux jumps due to the low specific heat capacity below these temperature range (<0.2 mJ/mol K^2 at 4.2 K and

~7 mJ/mol K^2 at 20 K [221]), meaning even a slight increase in temperature caused by flux motion can significantly impair the superconducting properties, like J_c, of MgB_2. Additionally, at these low temperatures, the rate of magnetic diffusion surpasses that of thermal diffusion, leading to the rapid movement of magnetic flux, resulting in flux jumps [222].

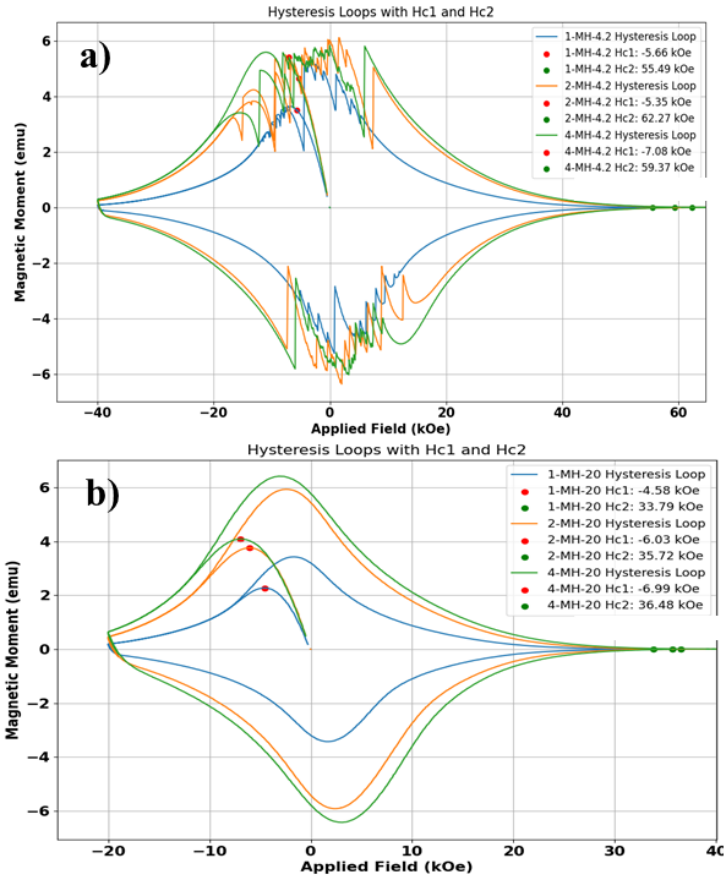

Figure 4.6 *The magnetization hysteresis loops of the samples at 4.2 (a) and 20 K (b), showing the estimated H_{c1} and H_{c2} values.*

Furthermore, the weakly pinned fluxes at defects under increasing applied fields contribute to flux jumping. When assessing the size of flux jumps across the samples, it becomes evident that sample number 1 demonstrated smaller jumps, while samples 2 and 4 exhibited larger ones.

Figure 4.7a-b shows the critical current values of samples using the equation (3.1) at 20 K and 4.2 K respectively while **Figure 4.7**c shows the moment values of samples as a function of temperature is given to determine the T_c values.

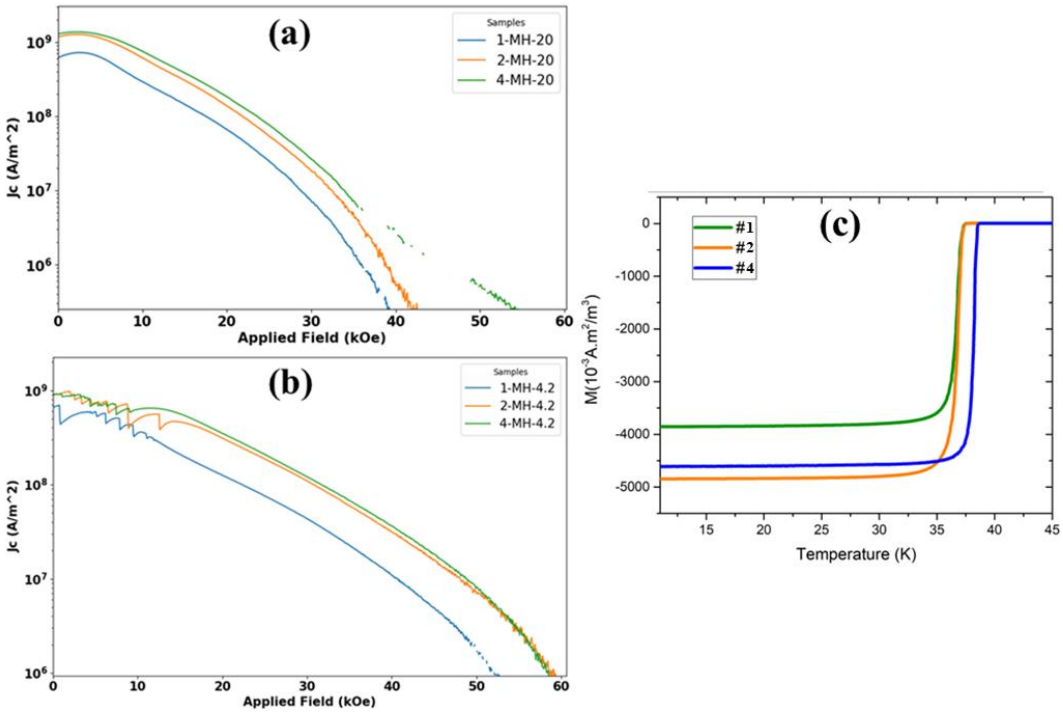

Figure 4.7 *Critical current densities and T_c values of the bulk samples extracted from the magnetisation measurements. The relationship between J_c and the applied field at a) 4.2 K and b) 20 K are shown. Figure c) displays the T_c values of the samples.*

The J_c, T_c, and H_{c2} values of the bulk samples are provided in **Table 4.5**.

Table 4.5 *J_c, T_c and H_{c2} values of bulk samples.*

Sample	**4.2 K**			**20 K**			**T_c (K)**
	J_c (0 T), (10^4Acm^{-2})	J_c (1 T), (10^4Acm^{-2})	H_{c2} (T)	J_c (0 T), (10^4Acm^{-2})	J_c (1 T), (10^4Acm^{-2})	H_{c2} (T)	
1	6.81	3.48	5.55	6.4	2.89	3.38	37.5
2	9.08	4.92	6.23	11.8	5.81	3.57	37.6
4	9.02	6.32	5.94	12.9	7.53	3.65	38.7

It is clear, as expected, that higher proportions of MgB_2 lead to elevated values of J_c. However, when subjected to an external 1 T field, the critical current density values dropped

by a ratio at both 20 K and 4.2 K as shown in **Figure 4.8**. The analysis indicates that the reduction in J_c is less pronounced in Sample 4 at both temperatures (4.2 K and 20 K) compared to samples 1 and 2. This observation may suggest that Samples 1 and 2 are more susceptible to the influence of applied magnetic field, resulting in a more pronounced effect on J_c due to flux penetration, leading to reduced J_c, in contrast to Sample 4. This observation may also suggest the potential presence of submicron Mg-B-O precipitations act as flux pinning centres in Sample 4, as previously speculated.

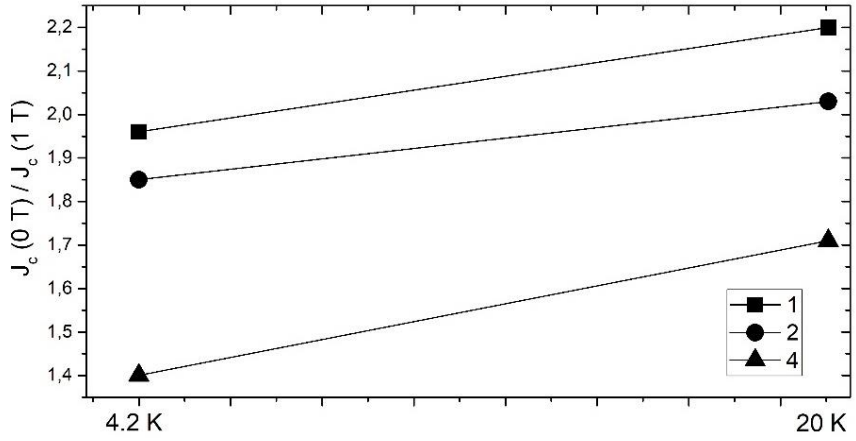

Figure 4.8 *The ratio of the J_c at 0 T to that measured at 1 T for the samples at temperatures of 4.2 K and 20 K.*

Samples 1 and 2 exhibited lower T_c values compared to sample 4, possibly due to unreacted Mg and trace MgO between MgB_2 grains, especially noticeable in sample 1. Smaller crystallite sizes are also known to correlate with reduced T_c values in MgB_2 [223, 224]. Sample 4, with the largest crystallite size, displayed the highest T_c, while sample 1, with the smallest crystallite size, showed the lowest T_c as demonstrated in **Table 4.2** and **Table 4.5**.

Higher strain levels below 20 K inversely affected both J_c and T_c values, whereas larger crystallite sizes demonstrated enhanced superconducting behaviour. The impact of strain and crystallite size on H_{c2} warrants further investigation. Serquis et al. [225] noted that strains below 0.5% in the MgB_2 lattice have minimal impact on T_c, with strains exceeding

1% resulting in a decrease of only 2 K in T_c. They also claimed that effect of strain on T_c reduction is to be less significant than that of crystallite size.

Table 4.6 *Literature studies and their J_c and T_c results. All samples were in-situ synthesized MgB_2 and no doping elements.*

Ref.	**Sintering**		**T_c onset (K)**	**J_c (10^4A cm^{-2}) at 20 K**	
	Condition, ^{o}C	**Duration**		**Self-field**	**1 T**
[226]	775	1h	38.5	27	-
	775	5h	38.5	23	-
	780	3h	38.7	19	-
[227]	1200	30 min	38	8	2.5
[228]	800	6h	38.2	10	5.5
[229]	850	30 min	37	-	2.9
[230]	775	2h	38	30	10
This study	**700**	**1h**	**37.5**	**6.4**	**2.9**
	700	**5h**	**37.6**	**11.8**	**5.8**
	800	**5h**	**38.7**	**12.9**	**7.5**

Here in this study, increased strain levels adversely affect J_c and T_c as Serquis et al. suggested, indicating the persistent sensitivity of superconductivity to mechanical lattice perturbations. Conversely, larger crystallite sizes maintain a positive correlation with J_c and T_c, highlighting the crucial role of grain size in determining superconducting behaviour, even at low temperatures.

Table 4.6 presents various studies and their outcomes from the literature. All the samples listed here were produced via *in-situ* synthesis methods and are in pellet forms. The production methods and applied pressures varied from study to study. Additionally, none of them contain doping elements for comparison with the results provided in this chapter.

Sample 4's results seem favourable compared to the literature, with a notably high T_c, one of the highest among the samples listed. Regarding the J_c under self-field, it falls around the average of literature values and even surpasses some studies. Looking at J_c under a magnetic field of 1 T, it appears notably higher. This could potentially be attributed to the pre-suggested Mg-B-O inclusions acting as pinning centres. However, further research efforts are needed to validate this theory.

4.3 Conclusions

In conclusion, the investigation of the cold pressed MgB_2 study clarifies the complex interplay between strain, crystallite size, and key superconducting parameters, namely J_c, T_c and H_{c2}, at both 20 K and 4.2 K. This preliminary study focused on understanding the effects of different stoichiometric ratios of reactants and heat treatment methods on the crystallographic, structural and superconducting properties of MgB_2 formed by the kinds of reaction processes that might be used to process joints. The magnetization measurements provided useful insights into the superconducting behaviour of bulk samples, that can help explain what is happening in joints processed in similar temperature ranges. The observed trends in J_c and T_c values highlighted the significant influence of MgB_2 fraction and crystallite size on superconducting performance. Particularly noteworthy was the inverse relationship between strain and J_c/T_c, indicating the detrimental effects of mechanical perturbations on superconductivity. At both 20 K and 4.2 K, increased strain levels correlated with decreased J_c and T_c, while achieving a larger crystallite size enhanced these superconducting properties.

Chapter 5 Microstructure and Superconducting Properties of joints in Epoch's Monofilament MgB_2 Wire

5.1 Introduction

As the significance and application scope of superconductors expand, companies are directing their efforts towards the development of technological advancements across various forms, including wires, tapes, films, and bulk materials. Concerning MgB_2, prominent market players such as ASG Superconductor in Italy, Hitachi in Japan, Sam Dong in South Korea, and American Superconductors (AMSC) and Hyper Tech Research Inc. in the U.S. stand out. Additionally, emerging enterprises like Epoch Wires Ltd. in the UK, project partner in my research, are making strides.

Epoch Wires Ltd. has been manufacturing MgB_2 wires since 2019, focusing on enhancing technological capabilities. They aim to develop MgB_2 joints, particularly for reacted wires, for magnet production. While they have succeeded in producing joints between unreacted wires, ensuring reproducibility remains challenging. Achieving consistent, high-performance, and cost-effective joints for reacted wires is crucial for the react and wind method, as there is a recognized demand from magnet producers to adopt this method to reduce energy consumption and other factors discussed in section 3.1.2.2. To address this, Epoch is dedicated to developing reproducible, mass-production suitable methods for MgB_2 joints between reacted wires. A series of studies conducted in partnership with Epoch labs outline approaches for developing these joints.

The chapter starts by explaining the experimental procedures in detail, followed by a section about the important wire characteristics needed for joint fabrication. Then, it describes how the joints were analysed using SEM and EDX. Following this, high-current transport

measurements are conducted to ascertain the I_c of the joints, alongside low-current transport measurements aimed at determining the T_c of the joints.

5.2 Experimental details

The process of creating joints was initially attempted at Epoch Wires laboratories in Cambridge, UK, involving the following steps:

i. Familiarizing with the wire and comprehending its specifications, delineating its superconducting properties and physical dimensions.

ii. Investigating the pre-matured joint technology between unreacted wires developed by Epoch, including learning manufacturing steps, observing challenges, and assessing pros and cons, as detailed in section 3.1.2.1.

iii. Examining heat treatment procedures and rationale, testing various regimes for both reacted and unreacted joints. Despite efforts, optimal ranges remain elusive with joint reproducibility and performance inconsistency. The actual mechanism behind the applied heat treatment procedures is unknown, and no systematic study has been conducted. Details of the applied heat treatment for this investigation are explained in the following section.

iv. Replicating joint technology between unreacted wires and initiating preliminary efforts to produce joints between reacted wires. These joints undergo high-current transport measurements to ascertain their transport I_c, detailed in section 5.2.3.

v. Acquiring I_c values for each joint and transporting them to CfAS for characterization of interface quality. The microstructure properties of the joints are outlined in section 5.2.2.

In the Epoch study, twelve joints were fabricated using the method outlined in section 3.1.2.1, with detailed descriptions provided in **Table 5.1**. One example of a short joint is illustrated in **Figure 5.1**. Samples 5 and 11 depict joints between unreacted wires, while the rest involve joints between reacted wires. The decision to include unreacted wires allows for comparison with reacted counterparts, aiding in the understanding of the reaction mechanism. Additionally, samples 7, 9, and 12 are doped with 5% SiC within the core, aiming to evaluate performance under high external fields for flux pinning, though no significant outcomes were observed.

Table 5.1 *Specifications used during joint production of the joints. SS stands for stainless steel.*

Sample Number	Wire Pressure (Tons)	Wire Composition	Outer sheath	Drilling Hole Diameter
1	4	MgB_2	SS	1.25mm
2	3	MgB_2	SS	1.25mm
3	1	MgB_2	SS	1.25mm
4	2	MgB_2	SS	1.25mm
5	0	Mg+B	SS	1.25mm
6	3	MgB_2	SS	0.9mm
7	0	MgB_2+ 5% SiC	SS	1.25mm
8	1	MgB_2	Monel	0.9mm
9	4	MgB_2+5% SiC	SS	1.25mm
10	0	MgB_2	Monel	1.25mm
11	0	Mg+B	SS	1.25mm
12	2	MgB_2+5% SiC	SS	1.25mm

Notably, samples 8 and 10 feature Monel as an outer sheath, introduced to investigate potential impacts on the joints' I_c and interface quality. Furthermore, some wires were

pressed under different loads (tons) (as described in section 3.1.2.1) to assess whether the pressure on the wire before joining affects the results.

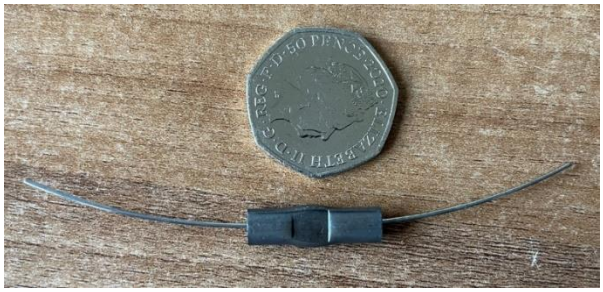

Figure 5.1 *One of EPOCH's short joint.*

Drilling hole diameter was another observed factor presenting a challenge. Given the wire diameter of 0.75 mm, a diameter of 1.25 mm seems too large, making it challenging to maintain wire stability during pressure application as seen in **Figure 5.2**. Therefore, it was reduced to 0.9 mm (it is 0.9 mm since it was the smallest drilling bit in the lab.) in some cases (sample 6 and 8).

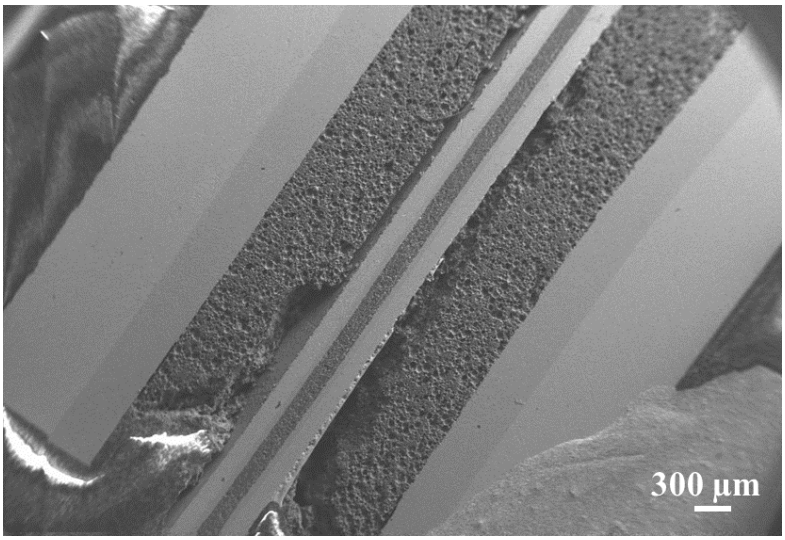

Figure 5.2 *SEM image of one of the joints, illustrating the drilling hole (1.25 mm) resulting in wire looseness.*

Heat treatments to the joints were conducted in a tube furnace under a 10 PSI Ar atmosphere. SEM characterizations were performed in Oxford, CfAS while high current transport measurements were carried out in Epoch.

5.2.1 Wire characteristics used in the joints

All wires used here were produced by Epoch Wires Ltd using the classical PIT method with a stoichiometric ratio of Mg:B at 1:2. Their wire manufacturing technology can be found in [231–233] and specifications are given **Table 5.2**.

Table 5.2 *Reacted and unreacted wire specifications*

Wire	Outer Sheath	Barrier material	Heat Treatment under Ar	Diameter (mm)	Core Diameter (mm)	Thickness of the barrier (mm)	Thickness of the outer sheath (mm)
#1	Low C steel	Titanium	700 ^{o}C 15 Minutes	0.75	0.38	0.085	0.1
#2	Monel	Titanium	700 ^{o}C 15 Minutes	0.75	0.38	0.085	0.1
#3	Low C steel	Titanium	unreacted	0.75	0.38	0.085	0.1
#4	Monel	Titanium	unreacted	0.75	0.38	0.085	0.1

Wires were prepared with a heat treatment, 700 ^{o}C for 15 minutes, under an Ar atmosphere, and some of them may contain 5%at SiC, as detailed in **Table 5.1**. This heat treatment regime was preferred because based on their experiences, it yielded the best heat treatment results for their wire, particularly in terms of exhibiting high I_c (206 A at 20 K, 1 T) shown in **Figure 5.6**. Additionally, for research purposes, some of the wires were also pressed under a certain amount of load as shown in the same table.

SEM images and EDX elemental maps of a typical monofilament reacted MgB_2 wire produced by Epoch are shown in **Figure 5.3**. Joint studies conducted using reacted wires were performed using this treated wire, while joint studies involving unreacted wires utilized the wire in its unreacted form.

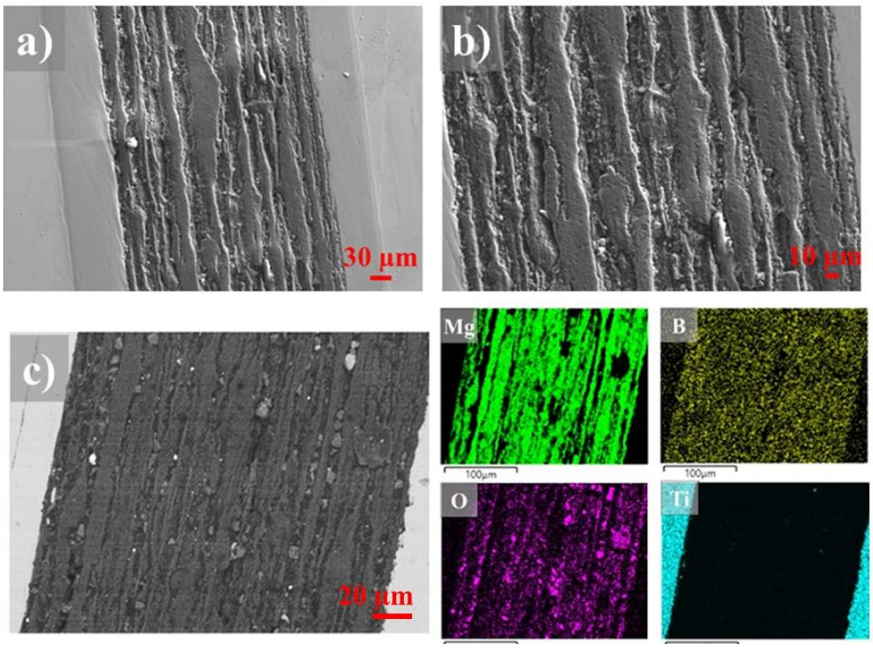

Figure 5.3 *Longitudinal cross-section SEM (a-b) and BSE image along with its EDX images obtained in the Trumap mode of the reacted MgB_2 wire*

The wire, with outer and inner diameters of 0.75 mm and 0.38 mm respectively, features an inner sheath of Ti to minimize core reactions and an outer layer of mild steel for easier drawing. Mg and B EDX maps indicate uniform element distribution post-heat treatment, though impurities, particularly oxygen, were found within the core, likely from surface oxidation during grinding. The impact of this impurity on properties is discussed in section 2.4.4. The transverse cross-section surface area percentage of core area is 27.4%. The wire's cross-section reveals an elongated fibrous macrostructure, a result of magnesium particle elongation during wire drawing.

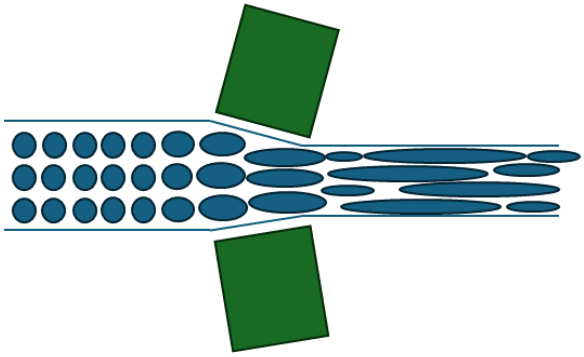

Figure 5.4 *The visualization of the elongation process of magnesium particles during wire drawing.*

Subsequent heat treatment causes migration of the magnesium macrostructure towards the B layers, creating aligned porosity and leaving voids behind, as schematised in **Figure 5.4**.The same effect has also been demonstrated in the literature by Shi et al.[234] (**Figure 5.5**a) and Uchiyama et al. [235] (**Figure 5.5**b).

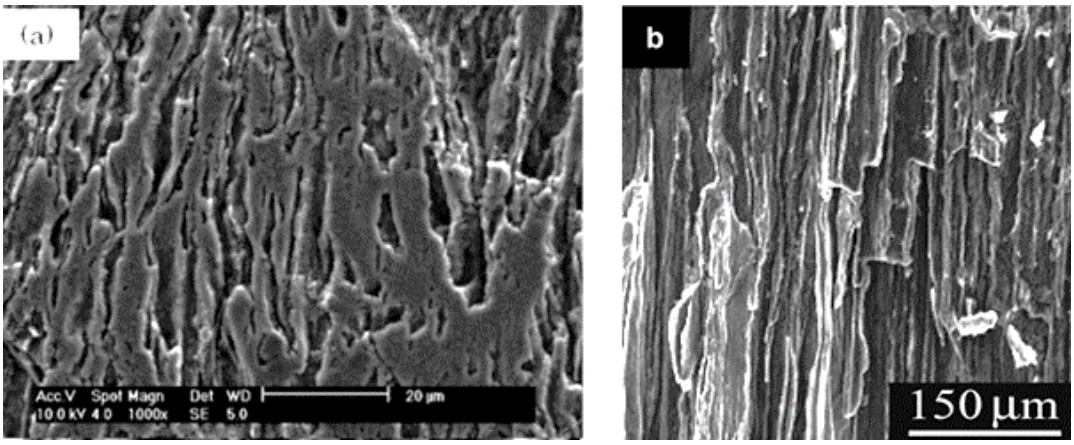

Figure 5.5 *The fibrous structure of in-situ PIT-reacted MgB_2 wires from the literature. a) Shi et al. [234] and b) Uchiyama et al. [235] (Copyright © 2010 IOP Publishing and 2007 Elsevier Ltd.)*

Figure 5.6 depicts the critical current of the wire as a function of temperature when subjected to a background field of 1 T. Obtaining the I_c value below 20 K proved challenging because of excessive heating in the copper wire employed as a shunt.

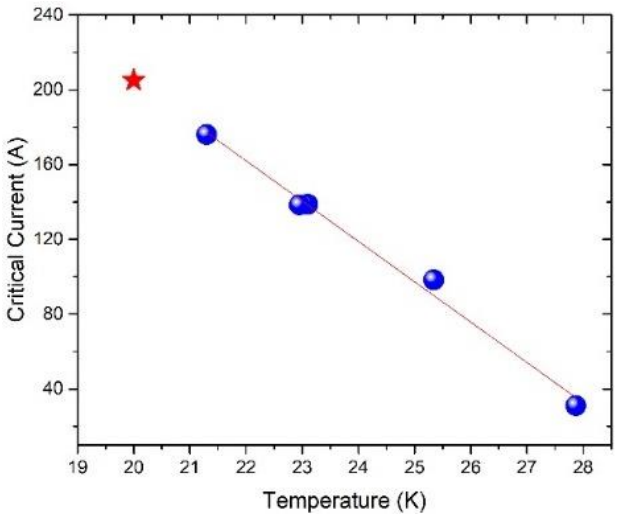

Figure 5.6 *The relationship between the I_c of the wire and measurement temperature in a 1 T background magnetic field. Extrapolating the fitted line enables an estimation of the I_c value at 20 K, denoted by the star.*

Nevertheless, by extrapolating the linear trend observed in the graph, an estimated I_c value of 206 A has been determined for the wire at 20 K under 1 T. Given the known surface area of the wire, the engineering J_c is calculated as 4.7×10^4 A/cm^2.

Table 5.3 *The J_e values of PIT monocore in-situ MgB_2 wires reported in the literature and the wire utilized in this study.*

Ref.	Wire	J_e (A cm^{-2})	Environment
Wang et al.[236]	PIT in-situ monocore	3.5×10^5	20 K, 0 T
Pradhan et al.[193]	PIT in-situ monocore	1.9×10^4	20 K, 0 T
Patel et al.[237]	PIT in-situ monocore	6.9×10^4	20 K, 1 T
Choi et al. [238]	PIT in-situ monocore	2.3×10^4	20 K, 2 T
Martinez et al. [239]	PIT in-situ monocore	2×10^5	20 K, 1 T
This wire	**PIT in-situ monocore**	**4.7×10^4**	**20 K, 1 T**

Table 5.3 presents the engineering critical current density values of PIT monocore *in-situ* MgB_2 wires in the literature. The J_c value of the wire utilized in this study is marginally higher than the literature average and notably superior to some instances.

5.2.2 Effect of heat treatment on wire/case interface

All joints presented in this chapter underwent heat treatment at 900°C for 30 minutes and 650°C for 1 hour (see **Figure 5.7**). The reason for specifically utilizing this heat treatment is that Epoch previously conducted similar studies at different temperatures, as discussed in the introduction, without achieving tangible positive results. Therefore, exploration of alternative heat treatment regimens is warranted since existing literature indicates a lack of consensus regarding the optimal heat treatment for joints between reacted wires (see section 2.6.1).

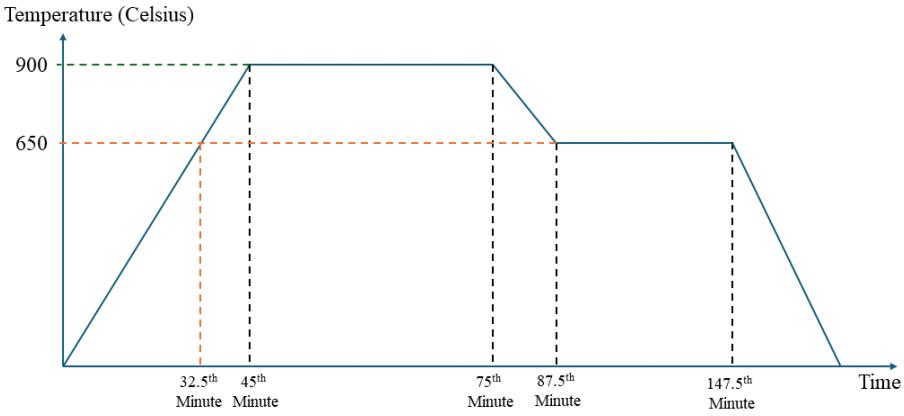

Figure 5.7 *Heat treatment procedure.*

It is thought that it is imperative to leverage the decomposition property of MgB_2 at elevated temperatures to trigger the chemical reaction between wires and the case. As demonstrated previously in section 2.4.3.2, and as also suggested by Dancer et al. [89], Peng et al.[240] and Chen et al. [159], the onset of MgB_2 decomposition effectively occurs at temperatures of 900°C-1000 °C for both *in-situ* and *ex-situ* MgB_2. The joint system presented here also consist of both *ex-situ* (because the wire is reacted) and the *in-situ* (because the case is unreacted) MgB_2 prior to joint heat treatment. Therefore, in order to fulfil the requirement (decomposing the MgB_2 into $Mg+MgB_4$ and creating new MgB_2 grains between wire and the case interface), it is inevitable to create MgB_4 in both parts. Thus, to minimize reactions within the core-barrier-steel structure, a maximum temperature of 900°C is deemed optimal. Furthermore, the duration of the treatment is minimized to 30 minutes to mitigate the risk of unintended side reactions and to control Mg evaporation. At this temperature, it is postulated that MgB_2 decomposes into MgB_4 + Mg, as expounded upon in section 2.4.3.2. Notably, the encapsulation of wire tips within the case confines evaporated Mg within the joint, while allowing its release from the case ends. However, it is anticipated that Mg vapor emanating from the innermost regions of the case, near the wire ends (since they are close to mid-section of the case), may persist within the case to some extent. Prolonged treatment

durations may exacerbate this expectation, potentially leading to the accelerated loss of Mg vapor from deep within the case to its ends.

The second stage of the heat treatment involves reaching the melting point of Mg, which occurs at 650°C for a duration of 1 hour. This temperature is selected to facilitate the reversion of vapor Mg to its liquid state and thereby reverse the reaction leading to MgB_4 + Mg → $2MgB_2$ as Peng et al. [240] suggested. Their findings indicate that MgB_2 can be synthesized through the MgB_4 + Mg reaction occurring during the heat treatment process of *ex-situ* MgB_2, with a content of MgB_4, at a temperature of 650°C. Temperatures lower than 650 °C would maintain Mg in its solid state, prolonging the solid-state reaction excessively. Conversely, temperatures higher than 650°C may impede control over Mg migration, allowing continued escape from the case. The 1-hour duration is chosen to afford sufficient time for Mg to react with MgB_4 and yield new-born MgB_2. It is anticipated that this reaction will predominantly occur near the wire ends, as evaporated Mg within the wire may migrate towards the case and create MgB_2 by reacting MgB_4. Additionally, the study conducted by Yan et al. [241] demonstrated that the reaction between MgB_4 and Mg may occur in its solid, liquid, and gaseous states. Their XRD results confirm that the reaction MgB_4 + Mg = $2MgB_2$ takes place regardless of the physical state of Mg. In Differential Scanning Calorimetry (DSC) measurements of their sample, initially composed of MgB_4 and Mg and subsequently heat-treated, the first endothermic peak appears at approximately 650°C. This peak is attributed to the potential activation of a solid–solid reaction between MgB_4 and Mg. SEM observations further reveal that the MgB_2 samples synthesized from MgB_4 + Mg mixtures exhibit a denser microstructure compared to those synthesized directly from Mg + B mixtures. To understand the reaction process, they proposed a simple model involving spherical Mg and MgB_4 particles. Initially, it is assumed that Mg particles (45 μm) are surrounded by smaller MgB_4 particles (5–10 μm). At temperatures below Mg's melting

point, the solid-state reaction $Mg(s) + MgB_4(s) = 2MgB_2(s)$ begins at the Mg/MgB_4 interface. The reaction progresses as Mg diffuses through the newly formed MgB_2 layer toward the MgB_4 particles. However, diffusion experiments suggest that solid Mg diffusion through the MgB_2 layer is slow, as indicated by their XRD results, which show only limited MgB_2 formation, even after prolonged annealing. When the temperature exceeds Mg's melting point, the reaction $Mg(l, g) + MgB_4(s) = 2MgB_2(s)$ occurs more rapidly, as Mg in liquid or gaseous form can diffuse more easily into MgB_4 grains, significantly increasing the reaction rate. However, at temperatures above 720°C, excessive Mg vapor pressure can lead to Mg loss through evaporation, limiting the maximum effective temperature for MgB_2 synthesis. This reaction chain ($MgB_4 + Mg \rightarrow 2MgB_2$) proposed to occur within the joint is further supported by other literature studies [240–243].

This carefully devised heat treatment protocol is implemented to attain a comprehensive understanding of its underlying mechanisms and to identify avenues for potential enhancement.

SEM images of selected samples were conducted to assess the quality of the wire-joint interface, **Figure 5.8** and their transport I_c results are given in **Table 5.4**, section 5.2.3. An investigation is carried out to identify the underlying issues and explore possible solutions to address drawbacks. Consequently, I focused on samples 1, 5, 6, 7 and 11, as samples 5, 6, and 11 exhibited I_c while samples 1 and 7 did not. The purpose of this specific focus is to understand why one sample exhibited high current compared to others and why another did not exhibit any current. In the following section, from the samples previously shown in **Table 5.1**, sample 1 is referred to as J1, sample 5 as J5, sample 6 as J6, sample 7 as J7 and sample 11 as J11.

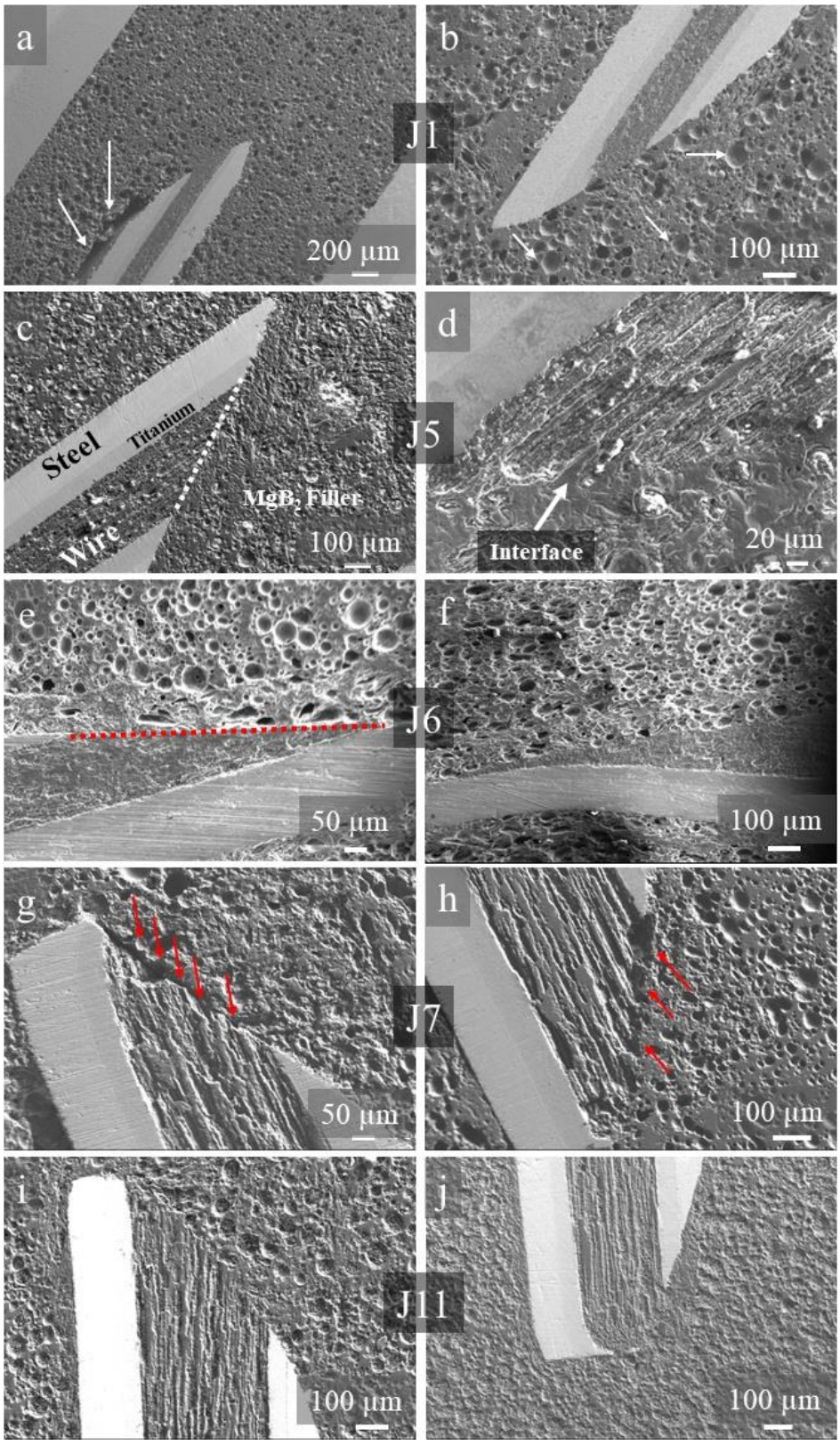

Figure 5.8 *SEM Images of the samples I produced at Epoch. The bright white colour represents steel, grey indicates titanium, and dark grey denotes MgB_2. Dark grey regions located between the two grey colours (Ti) represent MgB_2 inside the wire, while the remaining dark grey regions are MgB_2 filler from the case, and some of the porosities shown by white arrows as examples in (b).*

The images are organized as follows: the first line (a-b) depicts J1, the second line (c-d) showcases J5, the third line (e-f) J6, the fourth line (g-h) presents J7 and the fifth line (i-j) shows J11. Each set of images portrays two wire ends, which is why there are 2 images in every line. In J1 (images a-b), a higher load of 4 metric tonnes weight was applied to the unreacted wire and then the wire was heat treated under 700 ^{o}C for 15 minutes under Ar. The primary objective was to minimize the presence of voids within the reacted wire through the application of load. After joint making procedure, the joint was reacted using the heat treatment procedure showed in **Figure 5.7**.

In J1, large and deep voids indicated by white arrows in **Figure 5.8**b suggest the initial case powder may contain sizable Mg fragments. These voids could potentially hinder the current path. A drawback of this joint orientation (continuous joint) is the greater distance between the two wire ends compared to termination joints. Along the current path, numerous voids of varying sizes are present, which is not conducive to optimal current flow.

Furthermore, as depicted by arrows in **Figure 5.8**a, there is mechanical fracture adjacent to the wire ends, potentially rendering the joint susceptible to external damage and manipulation.

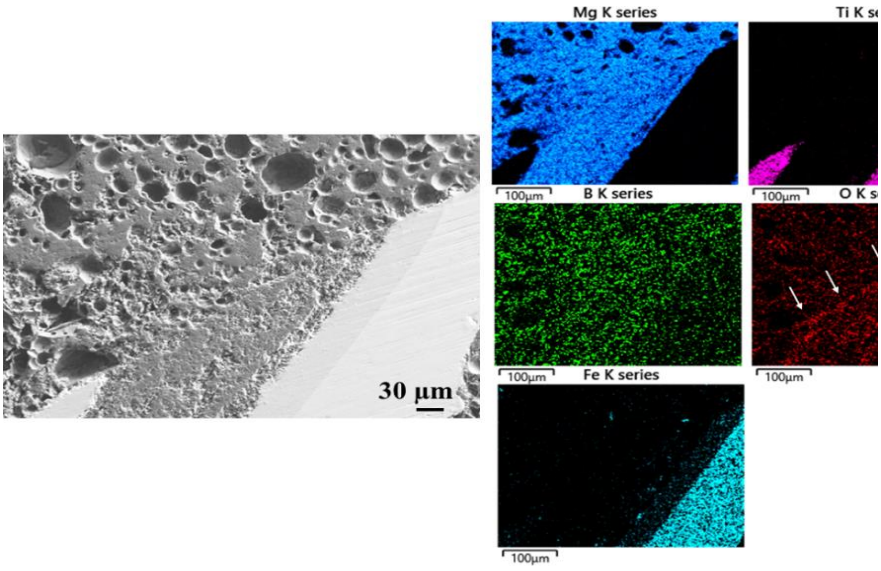

Figure 5.9 *EDX mapping of the interface of sample J1.*

The EDX maps displaying the elemental composition of sample J1 are presented in **Figure 5.9**. The magnesium distribution at the interface appears relatively uniform; however, it is noted that a line along the interface, indicated by the white arrow in the oxygen map, is visible. The concentration of oxygen within the wire is higher than in the filler material, and the possible presence of MgO at the interface, identified as an insulator, may significantly impact the conductivity of the current path.

In J5, both the wire and the case were in an unreacted state before joint assembly, and no load was applied to the wire. The heat treatment process for the joint followed the same procedure as previous samples. Compared to J1, the interface in J5 exhibited significantly smoother characteristics at both wire ends. The calculated I_c value of the joint without a Cu shunt was 181 A at 20 K and 1 T field, resulting in an 83% CCR. The disparity in the measured I_c values between J1 and J5 can be attributed to differences in heat treatment procedures. The smoother interface in J5 is believed to be due to the unreacted state of the wires and the case, resulting in nicely fused interfaces. During the heat treatment process of J5, gradual solid-state reactions between Mg and B initiated around 600 °C, reaching a peak at 650°C (at the 32nd minute, see **Figure 5.7**), the melting point of Mg. Limited production of MgB_2 began within this temperature window, leading to porosity due to volume reduction described in section 2.5.1. As the temperature reached 650°C, the increasing mobility of molten Mg accelerated the formation of MgB_2 but also generated porosity. Between the 45th and 75th minutes, some Mg dissociated from decomposing MgB_2, likely in gaseous form, initiating the reaction $MgB_2 \rightarrow MgB_4 + Mg$ as discussed above. After the 75th minute, some of vapor-phase Mg trapped within the wire or case, unable to escape, likely resided in the porosities at the wire-case interface and within the filler. From the 87th minute onwards, the trapped Mg return back its liquid phase and reacted with nearby MgB_4 to form newly synthesized MgB_2, potentially contributing to a well-fused structure at the interface.

In **Figure 5.8** e-f, SEM results for J6, fabricated with a 3-tonne load applied to the wire, are presented. As depicted in **Figure 5.2** and discussed previously, securely holding the wires in place during pressure application posed a challenge due to the diameter mismatch between the wire (0.75mm) and the hole (1.25mm). To mitigate this issue, the hole diameter was reduced to 0.9mm. Initially, the unreacted wires underwent a 3-tonne load before insertion into the case. Heat treatment was then conducted at 700°C for 15 minutes under an argon atmosphere, followed by the joint-making procedure. While some voids at the interface persisted, the transport critical current was measured to be 26 A at 20 K and 1 T.

In sample J7 (g-h), the wires underwent pre-heat treatment following the procedure used in previous joints involving reacted wires. The heat treatment of the joint followed the same procedure as the other samples. However, the interface at both wire ends is poor, leading to no connection, likely explaining the measured I_c of zero.

In J11 (i-j), both the wire and the joint case were unreacted Mg+2B before assembly into the joint. The joint underwent heat treatment at 900 ^{o}C for 30 minutes and 650 ^{o}C 1 hour. The resultant I_c was 22 A at 20 K and 1 T external magnetic field. Further investigation has been conducted to understand the reason behind this low I_c.

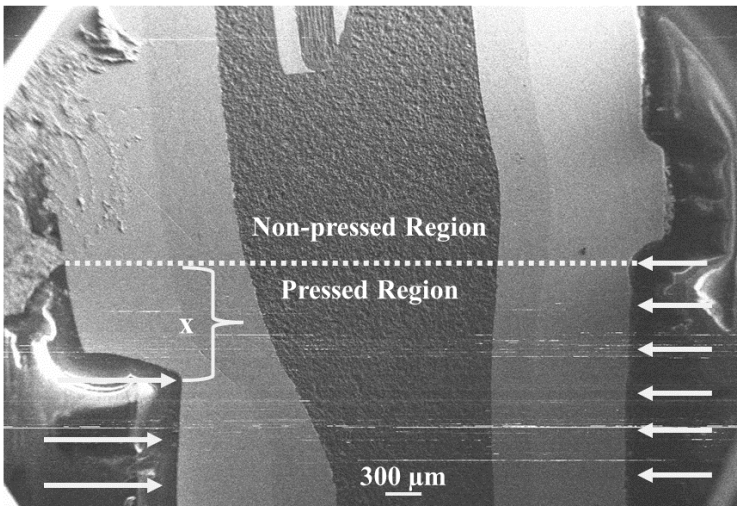

Figure 5.10 *Low magnification joint cross-section. White arrows indicate pre-applied load direction on the joint.*

In **Figure 5.10**, the area marked by 'x' indicates a misalignment of the tool bits used to apply load in the upper and lower parts, preventing a homogeneous load application to the joint. Despite the intention to increase density around the wire ends, challenges in the joint-making process hindered this goal. While not the primary reason for the low I_c, this misalignment underscores the difficulty in controlling load application on the joint.

Figure 5.11 depicts the EDX maps and linescan analysis of the interface. It's notable that voids within the case are larger than those within the wire, attributed to differences in Mg particle sizes and shapes. Despite significant voids at the interface, fused connections between the wire and filler remain sufficiently intact.

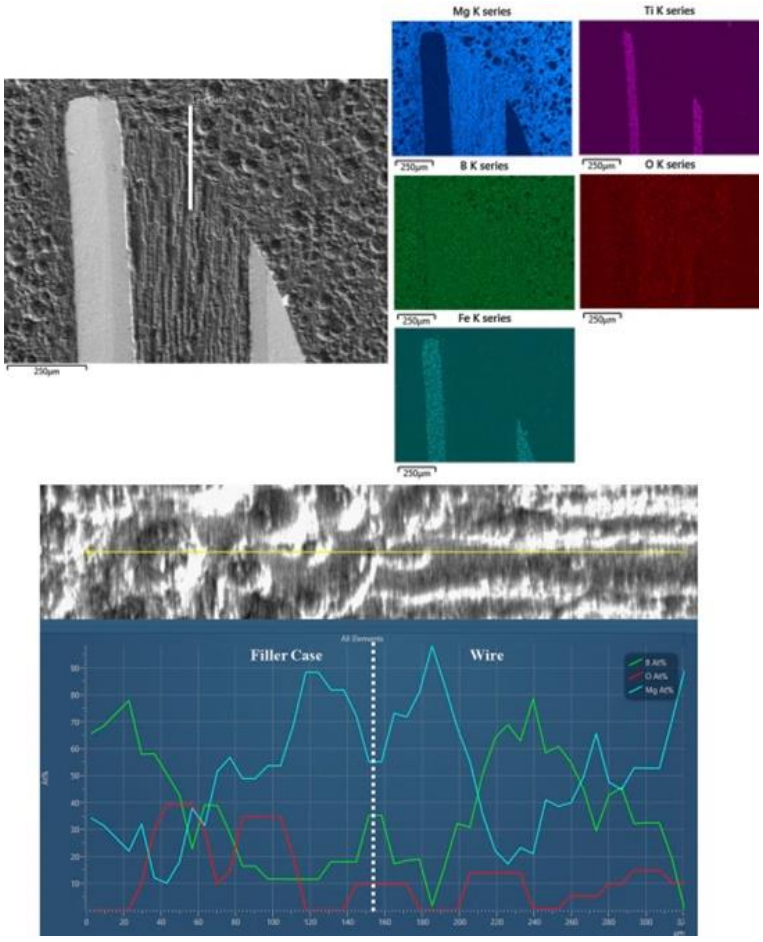

Figure 5.11 *EDX maps and linescan analysis of the interface.*

Linescan analysis indicated that the presence of oxygen at the interface is not problematic, and the presence of Mg and B along the wire appears satisfactory. Regarding interface

quality, no specific explanation has been identified for the low I_c obtained. It is considered that there may be another underlying cause.

Some potential factors could include significant voids that may have formed in specific regions within the wire, such as discontinuities, cracks, or fractures occurring in either or both wires. At times, identifying cracks or broken segments of the wire through SEM analysis cannot be straightforward, as occurred in sample 4 from **Table 5.1**, depicted in **Figure 5.12**. The joint, situated between reacted wires, underwent a load of 2 tonnes before undergoing wire heat treatment.

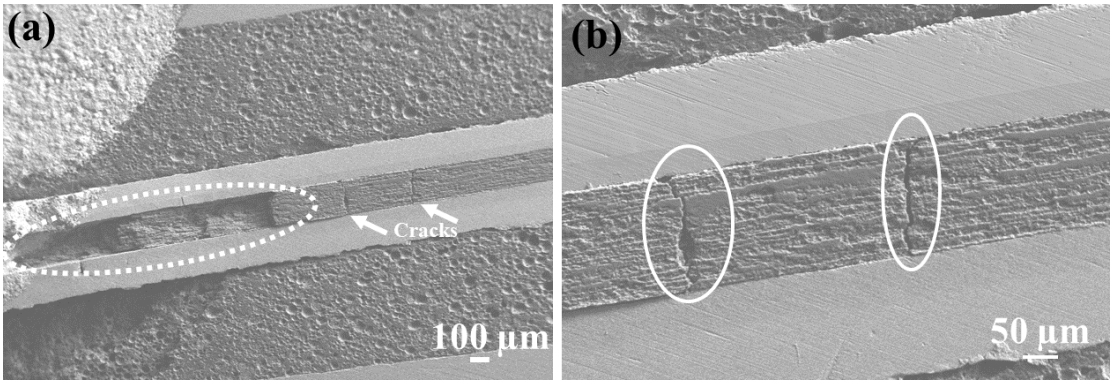

Figure 5.12 *A broken/cracked wire was observed in the joint of sample 4.*

Following the standard joint-making procedure and joint heat treatment, vertical cracks and a missing MgB_2 section (**Figure 5.12**, indicated by the dotted line circle) were observed within the wire, particularly in the part located inside the joint case. These cracks may have occurred either during heat treatment or during handling.

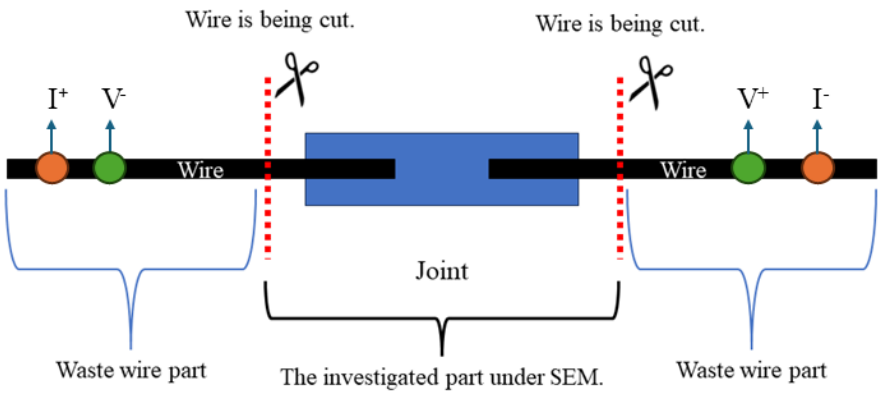

Figure 5.13 *Illustrating how joint samples are prepared for SEM analysis.*

If the crack had occurred in the section of the wire positioned outside the joint case, referred to as the waste wire part (depicted in **Figure 5.13**), which encompasses the area near where the voltage tap (green) and current tap (orange) were situated, it would have been impossible to detect it via SEM. This is because the wire was cut before SEM imaging, as depicted in **Figure 5.13**, to conform to the size required by the rubber mold.

5.2.3 High current transport I_c measurements to the joints

High-current transport measurements were conducted according to the procedure detailed in section 3.3.4. The electric field criterion was established as 100 μV/cm, consistent with the standard employed by Epoch for characterizing their wires and joints and all measurements carried out under 1 T background field to limit the externally applied current. The results of the joints under various temperatures are given in **Table 5.4**

Table 5.4 *I_c results of the joints were obtained at different temperatures, with magnetic field set at 1 T.*

Joint No	**I_c[A]**		
	20 K	**25 K**	**30 K**
1	0	0	0
2	0	0	0
3	21	9	0
4	0	0	0
5	143/**181**	91	36
6	32/**26**	18	4.7
7	0	0	0
8	0	0	0
9	0	0	0
10	0	0	0
11	22	15	8.8
12	0	0	0

Among the tested joints, numbers 5 and 6 showed promising results, with I_c values of 143 A and 32 A at 20 K, respectively. These values were calibrated to accommodate the presence of a Cu shunt. In contrast, the directly measured values for sample 5 were 181 A and 26 A at 20 K, without using a Cu shunt as shown in **Table 5.4**. The V-I measurement in **Figure 5.14** facilitated the determination of the 20 K value through linear extrapolation. The CCR value for sample 5 was calculated at 88% at 20 K and 1 T field. Notably, sample 5 exhibited a higher I_c compared to its shunted version, while sample 6 displayed a lower I_c under similar conditions. This difference could be due to potential issues with current tap connections during the second round of testing, potentially resulting from residual soldering from previous assessments. These complications necessitated additional preparation time for sample retesting, during which mechanical damage to the wire joints' interface may have occurred due to excessive manipulation.

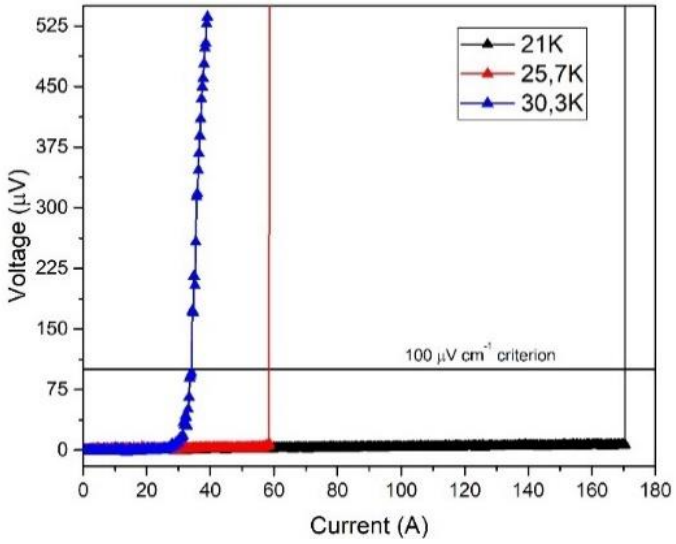

Figure 5.14 *I-V measurement of the sample under different cooling temperatures.*

As evident from the **Table 5.4**, there is inconsistency in the joint results in both between reacted and unreacted wires. While high I_c joints between unreacted wires can be produced using this method and procedure (e.g., sample 5), they may not be reliable from a reproducibility standpoint.

5.2.4 Low current transport T_c measurements

To assess the T_c values of Epoch design joints (**Figure 5.15**A), three joints were produced using the same method as Epoch, and their T_c values were measured. Additionally, to evaluate the effect of the distance between wire ends on T_c, one joint was produced with a modified design (**Figure 5.15**B), reducing the joint's length from 2.2 cm to 2 cm. This modification decreased the distance between wire ends from 0.4 cm to 0.2 cm, potentially reducing the presence of MgB_4 along the current path. Comparing the T_c performance between the standard Epoch joint design and the modified design was thus introduced.

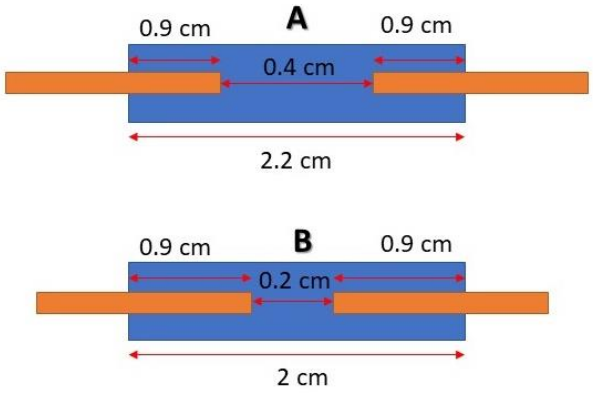

Figure 5.15 *Schematic of Epoch joint design. a) the classical design introduced earlier, b) the modified design tested in this section.*

T_c measurements were conducted using a cryocooler, as described in section 3.3.5. **Figure 5.16** demonstrates the normal state resistance and superconducting transition of joints between unreacted wires made using Epoch's method. Sample number 1 and 2 were produced using the standard method (**Figure 5.15**A), while sample number 3 was created by reducing the length of the case from 2.2 cm to 2 cm (**Figure 5.15**B). This modification led to a reduction in the normal state resistance. Samples 1 and 3 exhibited a broad ΔT_c and two-stage transition behaviours, indicating that there is some material in the current path possessing a lower T_c. Given the low current in this test, which would easily be carried by a

small cross section of superconductor, this indicates the absence of a fully continuous pathway of the MgB_2.

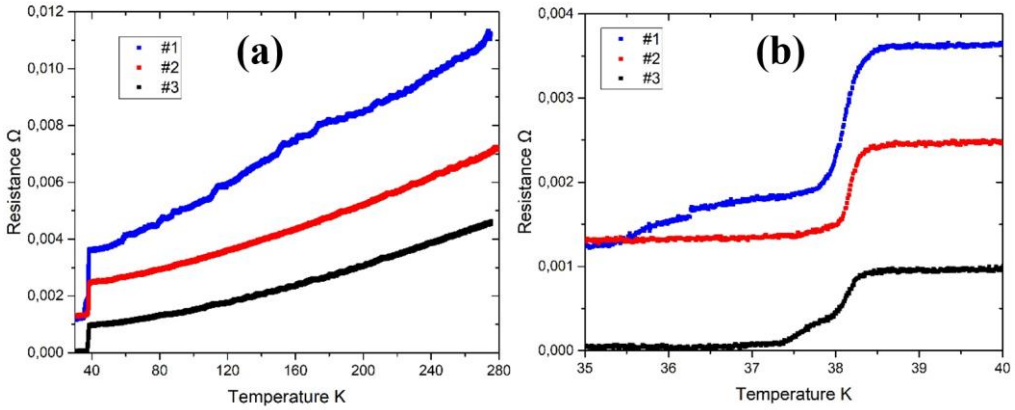

Figure 5.16 *R-T plots of Epoch joint designs (#1-2) and modified joint (#3) are depicted with an applied current of 0.1 A. (a) illustrates the variances in normal state resistances and transitions, while (b) showcases the T_c performances of the joints.*

The interpretation of these *R/T* plots can be complex. In **Figure 5.17**, two different scenarios of the current pathway might be suggested. In the first scenario, if the wire exhibits a higher T_c compared to the filler material, then just below this temperature the current could follow multiple pathways.

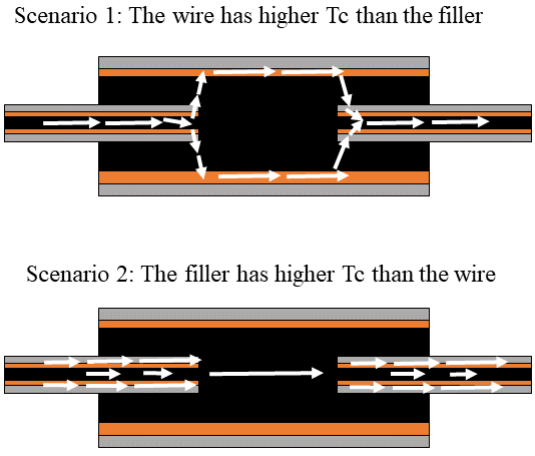

Figure 5.17 *The current path in different scenarios is illustrated. White arrows indicate the current path.*

These pathways may include traversing the superconducting wire to the wire tips, and then dispersing to pass through the normal state MgB_2 present in the filler material. However, if

the wire exhibits a lower T_c compared to the filler, the current will flow through the normal metallic sheath to the wire tip, and subsequently pass through the superconducting filler.

In both scenarios, only at a lower temperature will both regions of MgB_2 be superconducting. However, it is evident that the residual resistance of the original Epoch design is significantly higher compared to the modified design. This observation suggests the presence of non-superconducting (MgO or/and high borides) materials or/and high number of voids along the current path, which contributes to the increased resistance.

The high current transport I_c measurements to the Epoch standard joints at 20 K are far below the various drops in resistance measured in the T_c measurement, but they might still provide some indication of the performance at 20 K. In the high current transport I_c measurements, if there is no physical or mechanical problem in the joint according to the tests conducted, and yet the I_c remains zero, it can be observed from the T_c test that even at low currents, there is a significant residual resistance below T_c. This may suggest that at higher currents, higher resistances may have been generated, leading to the loss of the superconductivity of the joint. The resistance generated here could be due to phases such as MgB_4 and exceed porosities which may be present between the two wire ends and among MgB_2 grains along the current path. The high current transport I_c measurement of the modified joint was not carried out for these samples, as it should have been done as further work to compare the results and ensure whether there are any supercurrent passes through the joint.

The experimental results emphasize the difficulties in achieving high I_c in MgB_2 wire joints, especially with reacted wires. Key observations include superior I_c in joints between unreacted wires due to solid-state reactions during heat treatment, which produced well-bonded interfaces. In contrast, joints between reacted wires showed poor interfaces with large voids, resulting in low or zero I_c. Design modifications, such as reduced drill hole

diameter, improved stability but did not eliminate voids. Heat treatment was critical, with unreacted wires bonding effectively, whereas reacted wires needed high-temperature decomposition, which was hard to control. The findings reveal reproducibility as a major challenge, addressed in the next chapter through a novel method with promising outcomes.

5.3 Conclusions

The experimental results underscore the challenges in achieving high I_c values for MgB_2 wire joints, particularly those involving pre-reacted wires. Here are the key findings:

- Unreacted wire joints (J5 and J11) exhibited significantly higher I_c values at 20 K and 1 T field compared to joints made with reacted wires. This superior performance is attributed to solid-state reactions during heat treatment, resulting in well-fused interfaces between the unreacted wires and filler material.
- For the joint made with reacted wire (J1) under a high load of 4 metric tonnes, a poor interface with large voids was observed, leading to an immeasurably low I_c.
- Reducing the drilling hole diameter in J6 improved wire stability during assembly, but some voids persisted, limiting I_c. The joint made with reacted wire and 5% SiC doping (J7) exhibited a complete lack of connection at the wire ends, resulting in zero I_c.
- Misalignment of tool bits during load application led to non-uniform pressure distribution on the joint. Additionally, a broken/cracked MgB_2 was found in one joint (sample 4), adversely affecting current transport.
- The heat treatment procedure crucially determined interface quality and I_c performance. Unreacted wires underwent reactions during heat treatment, leading to well-fused interfaces.

- T_c measurements on joints made with unreacted wires using a modified design showed variations in normal state resistance and superconducting transitions. Positioning wires deeper into the case aimed to reduce MgB_4 presence and number of voids along the current path compared to the standard design.

The results indicated that the reproducibility of this technique is a significant challenge that needs to be addressed in joints between both reacted and unreacted wires. In the next chapter, a novel method is proposed, and promising results have been obtained.

Chapter 6 Microstructure and Superconducting Properties of Novel Reacted Monofilament MgB_2 Wire Joints

6.1 Introduction

As discussed in Chapter 5, it is feasible to achieve high I_c and CCR performances by connecting unreacted wires using the Epoch standard method. However, challenges remain in achieving high I_c with reacted wire connections. Given the reproducibility issues in both joint types, distinct investigations are necessary to address these concerns. Therefore, this chapter will focus on developing a novel connection design for reacted MgB_2 wires, inspired by the Epoch standard design.

Joints between reacted wires are crucial for R&W magnets, as discussed in sections 2.5.2 and 2.6. Current methods involve coiling unreacted wires and sintering them into coils (as outlined in Chapter 2), which raises costs and scrap rates [246]. The lack of efficient technology for joining reacted MgB_2 complicates magnet repairs and makes predicting component expansion during heat treatment challenging. Therefore, developing an effective method for connecting reacted MgB_2 conductors is essential for advancing applications like MRI scanners. This study presents a promising jointing technique for MgB_2 reacted monofilament wires, detailed in this chapter.

The chapter begins by outlining the experimental details, followed by a section on the wire characteristics essential for joint fabrication. Subsequently, an explanation is provided regarding the characterization and test results, encompassing SEM, XRD, joint I_c, and resistance, each introduced separately.

6.2 Experimental Details

MgB_2 joints have been produced utilizing the method introduced in section 3.1.2.2. A number of joint samples have been fabricated between reacted wires, with 15 of them being discussed in this chapter. The remaining samples largely replicate the 15 discussed samples. In order to minimise the excess consumption of expensive MgB_2 wire, the first step was to measure resistance and T_c transition data of short joints through low current transport measurements in order to select a process for preparing jointed coils.

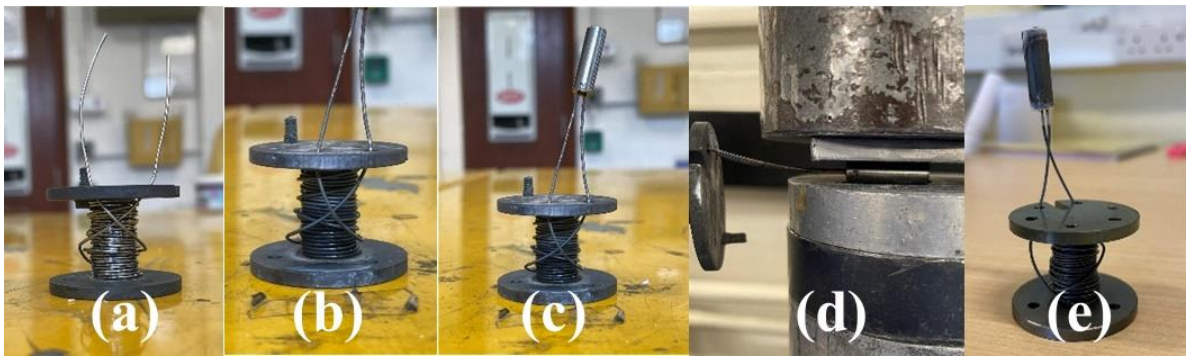

Figure 6.1 *MgB_2 coil making steps. a) MgB_2 coil before the initial heat treatment (700 °C for 15 minutes), b) after heat treatment, c) joining the wire tips, d) mechanical pressing of the joint e) after heat treatment (900 °C for 30 minutes and 650 °C for 1 hour) of the joint.*

Figure 6.1 illustrates the sequential steps involved in coil fabrication: a) depicts the MgB_2 coil prior to the initial heat treatment at 700°C for 15 minutes, b) presents the coil subsequent to the initial heat treatment, c) demonstrates the wire tip joining process, d) indicates the mechanical pressing of the joint and e) displays the coil following the heat treatment of the joint.

6.2.1 Wire characteristics used in joint

All the wires used in this chapter were produced by Epoch via the powder-in-tube method, and their specifications are previously detailed in **Table 5.2**. Cross-sectional SEM image of the wire is shown in **Figure 6.2**. The first factor that I needed to explore was the response of wire reacted with the Epoch standard process to a second heat treatment. This is because

when reacted wires are to be joined, at least some of the wire length will be subjected to a second heat treatment in the joint.

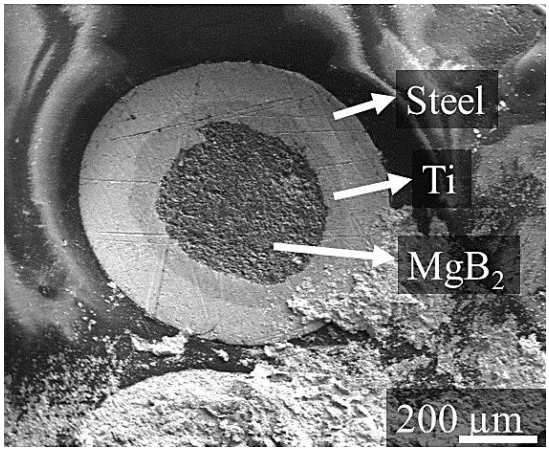

Figure 6.2 *Cross sectional SEM image of the reacted MgB_2 wire, whose specifications are given in* ***Table 5.2*** *#1.*

I carried out the heat treatments listed in **Table 6.1** to explore the effect of this second heat treatment, and the same treatment applied to unreacted wire. Therefore, W2 and W3 were trimmed into 2-cm pieces before the heat treatment. The low current transport measurement results, which provide the resistivity versus temperature plot of the wire under different heat treatments, are presented in **Figure 6.3**.

Table 6.1 *The thermal treatments applied to wires. #1 and #3 are the wires whose specifications are already given in* ***Table 5.2****. The T_c values of W2 and W3 represent the T_c after the second heat treatment.*

Wire	When it is received from EPOCH	Heat treatment after obtaining the wire	T_c (K)
W1	Reacted, #1	-	37.8
W2	Reacted, #1	900 °C 30 mins + 650°C 1h	38.2
W3	Unreacted, #3	900 °C 30 mins + 650°C 1h	37.4

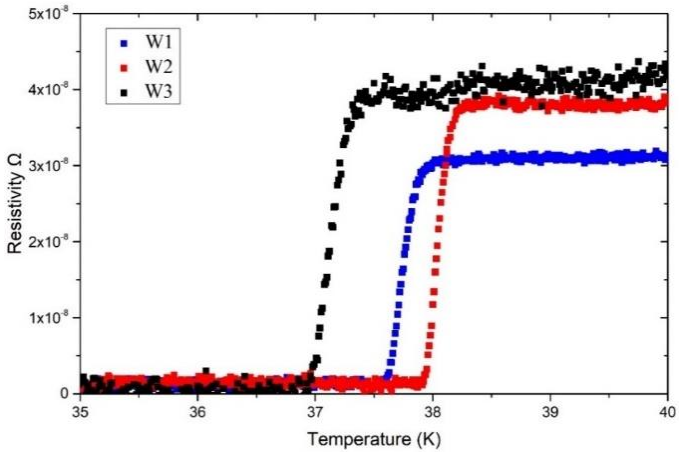

Figure 6.3 *Resistivity versus temperature plots of monofilament MgB_2 wires heat-treated under different conditions.*

W1 displays a moderate T_c value, while W2 demonstrates the highest T_c. Conversely, W3 exhibits the poorest T_c performance. The two-stage heat treatment applied to reacted MgB_2 yields superior results compared to the unreacted wire under identical heat treatment conditions.

The disparity between W2 and W3 may suggest that Mg vaporization commences earlier in W3, leading to a higher concentration of MgB_4 within W3 compared to W2. It may also imply that the decomposition of MgB_2 initiates at higher temperatures in W2 than in W3 as suggested in 2.4.3.2. Further insights into the mechanism are elucidated in Section 6.2.3.

6.2.2 Effect of heat treatment on wire/case interface

The procedures for making the joint between reacted wires with the modified design are detailed in section 3.1.2.2. The joint was then subjected to heat treatment at 900°C for 30 minutes and 650°C for 1 hour and the rationale behind this heat treatment has been previously discussed in Chapter 5. Subsequently, the joint underwent testing for its T_c, with results provided in section 6.2.4. Following testing, the joint was sectioned according to the procedure outlined in section 3.2.5.

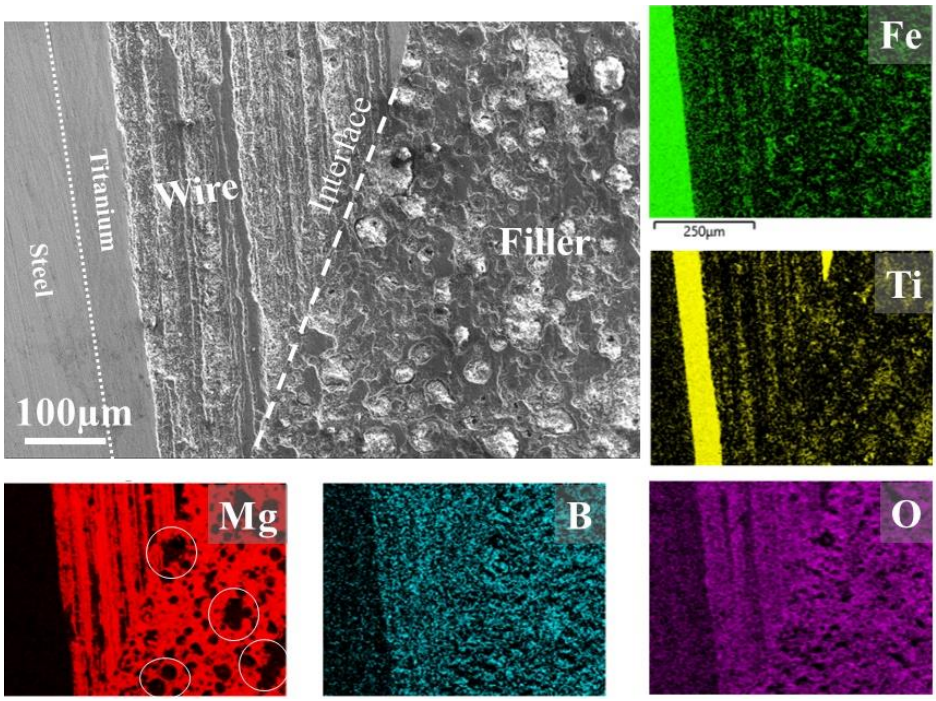

Figure 6.4 *SEM picture and elemental dispersion showcasing the boundary between the MgB_2 wire and the MgB_2 filler in the joint case by the heat treatment (900 °C 30 mins + 650°C 1h). The dashed line denotes the interface and circles in Mg maps shows big pores.*

As depicted in **Figure 6.4**, the MgB_2 microstructures in the wire and case regions differ due to their formation at distinct temperatures. However, the MgB_2 phase forms a continuous pathway across the interface, free of discernible pores or fractures. Oxygen mapping reveals significant MgO in both regions, likely due to air entrapment during joint pressing and exposure of the polished surface to air before analysis. Additionally, some Ti and Fe counts are noticeable within the MgB_2 joint filler, likely from the softer sheath metals transferring into MgB_2 pores during polishing.

6.2.3 Effect of heat treatment on the microstructure of the filler and wire

In the fabrication of jointed coils, reacted MgB_2 within the wires and Mg+2B powders contained in the joint case are subjected to a sequence of heat treatments. Expected reactions are outlined in **Table 6.2**. The wire undergoes three thermal treatment phases: initially at 700 °C for 15 minutes before assembly as a joint, followed by 900 °C for 30 minutes, and finally at 650 °C for 1 hour during the jointing process.

Table 6.2 *Summary of the heat treatment steps and expected reactions.*

Heat treatment	**First**	**Second**	**Third**
	700 °C 15 min	**900 °C 30 min**	**650 °C 1h**
Wire	$Mg + B \rightarrow MgB_2$	$2MgB_2 \rightarrow MgB_4 + Mg$	$MgB_4 + Mg \rightarrow 2MgB_2$
Joint case	-	$Mg + B \rightarrow MgB_2$ $2MgB_2 \rightarrow MgB_4 + Mg$	$MgB_4 + Mg \rightarrow 2MgB_2$

In contrast, the Mg+B powders within the case experience only the last two stages: 900 °C for 30 minutes and 650 °C for 1 hour. The rationale for this multistep process has been previously discussed, and the expected reactions at each stage are detailed in section 5.2.2.

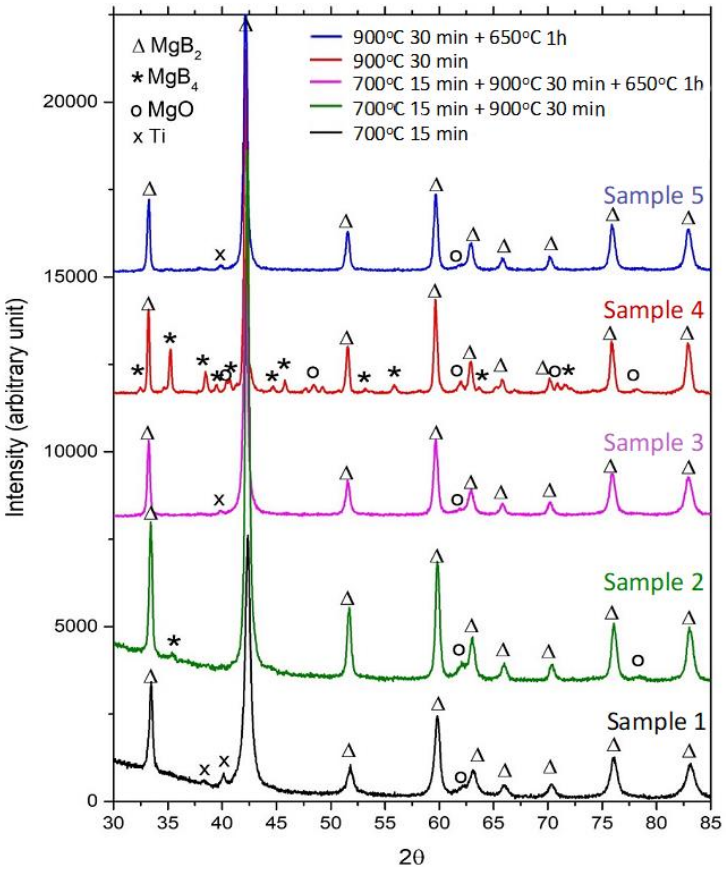

Figure 6.5 *X-ray diffraction scans showing the effect of heat treatment on the phase composition of case filler material.*

To characterize the phase transformations during these thermal stages, five Mg+2B filled joint cases (2 cm in length and 5.5 mm in diameter) underwent different heat treatment procedures, and the reacted material was extracted for XRD analysis. The sample

preparation method for XRD analysis is described in Section 3.2.2. Characterization was performed using the PANalytical Empyrean diffractometer, as detailed in Section 3.3.1, and phase identification was carried out utilizing PANalytical HighScore Plus software. The assumptions made during phase identification and the errors associated with assessing the phase content of the materials are also discussed in the same section.

No wires were inserted into the cases for this preliminary study. The specifics of the heat treatment methods and the proportions by weight of various phases, analysed by Rietveld refinement of the XRD patterns illustrated in **Figure 6.5**, are shown in **Table 6.3**. **Table 6.4** presents the crystallographic properties of the MgB_2 phase in these samples. Samples 1, 2, and 3 underwent heat treatments mirroring those encountered by the MgB_2 wires in the different stages of the jointed coil manufacturing process mentioned in the section 3.1.5.1. Samples 4 and 5 provide insights into the phases developed within the joint at each phase of the heat treatment.

Table 6.3 *The proportions of phases present in the wire core and the cases subsequent to each individual heat treatment stages analysed by Rietveld refinement. Dashes indicate that the corresponding compound is not present in detectable volume fraction at that stage of the heat treatment.*

Sample number	Heat treatment	Weight fraction (%)				Received by
		MgB_2	MgB_4	MgO	Ti	
1	700 °C 15 min	99.4	-	<1	trace	wires
2	700 °C 15 min + 900 °C 30 min	98.1	<1	1.4	-	wires in joint
3	700 °C 15 min + 900 °C 30 min + 650 °C 1h	99.0	-	<1	trace	wires in joint
4	900 °C 30 min	68.9	29.6	1.5	-	joint filler
5	900 °C 30 min + 650 °C 1h	98.9	-	<1	trace	joint filler

Table 6.4 *Quantitative results of MgB_2 lattice parameters, crystallite size and strain*

Sample Number	Heat treatment	*a*-axis	*c*-axis	Strain %	Crystallite size nm
1	700 ºC 15 min	3.086	3.524	0.34	40
2	700 ºC 15 min + 900 ºC 30 min	3.089	3.534	0.20	38
3	700 ºC 15 min + 900 ºC 30 min + 650 ºC 1h	3.121	3.567	0.16	24
4	900 ºC 30 min	3.101	3.543	0.23	112
5	900 ºC 30 min + 650 ºC 1h	3.085	3.526	0.21	50
Precision		±0.002	±0.002	±0.07	±0.005
XRD Errors		±0.0002	±0.0003	±0.005	±12

The precision and XRD errors in the table provide important insights into the reliability of the measured values for the *a*-axis and *c*-axis lattice parameters, strain, and crystallite sizes. As mentioned earlier, precision is obtained through mathematical fitting, whereas the XRD errors are outlined in Section 3.3.1 and displayed in **Table 3.3**. The precision values of ± 0.002 Å for the lattice parameters and ± 0.005 nm for crystallite size reflect a high degree of measurement consistency, supported by the XRD errors of ± 0.0002 Å and ± 0.0003 Å for the *a*-axis and *c*-axis, respectively. In contrast, the ± 12 nm uncertainty in the crystallite size measurements indicates substantial variability.

In addition, some samples detected a trace amount of Ti, likely originating when the reacted material was extracted from the Ti sheath.

Sample 1, which underwent a heat treatment at 700 °C for 15 minutes, exhibits the smallest lattice parameters (*a*=3.086 Å, *c*=3.524 Å), closely aligning with the theoretical values provided in section 2.4.1, alongside the highest weight fraction of MgB_2 (99.4%). This suggests that the relatively low thermal energy resulted in minimal atomic movement,

maintaining a stable lattice structure, although the presence of defects is suggested by a strain of 0.34%.

Subsequent thermal treatment at 900 °C for 30 minutes (sample 2) results in a slight elevation in the MgO fraction, coupled with the emergence of a small quantity of MgB_4. This aligns with our expectation that some of the pre-existing MgB_2 undergoes partial decomposition into MgB_4 and Mg vapor at this temperature, with the vaporized Mg reacting with incidental oxygen to generate extra MgO. This decomposition may introduce trace magnesium and oxygen, slightly affecting the lattice dimensions. The reaction representing this decomposition, as discussed in 5.2.2, is as follows:

$$2MgB_2 \rightarrow MgB_4 + Mg$$

Differentiating between MgB_2 and MgO poses a challenge due to the limited number of prominent peaks in the MgO spectrum. Notably, the most significant peak at $2\theta = 42.92°$ is only 0.5° away from the dominant peak of MgB_2 at $2\theta = 42.41°$. Additionally, the second strongest MgO peak at $2\theta = 62.30°$, overlaps with the left tail of the MgB_2 at $2\theta = 63.17°$. Quantifying compositions through X-ray diffraction can be complicated, as peaks from minor phases may be indistinguishable from the baseline. Furthermore, various factors, such as texture, strain, instrumental broadening, and misalignment, can influence peak positions and intensities. Therefore, interpreting the MgO peaks has consistently posed a challenge throughout the thesis. Sample 2 also exhibits a slight increase in lattice parameters (a = 3.089 Å, c = 3.534 Å), which can be attributed to enhanced thermal vibrations and atomic mobility. The reduced strain (0.20%) indicates that the elevated temperature has facilitated lattice relaxation through defect healing, resulting in improved crystallinity, even in the presence of minor distortions from the secondary phases.

Sample 3 underwent a sequential combination of heat treatments: the first at 700 °C for 15 minutes (as in Sample 1), followed by 900 °C for 30 minutes (as in Sample 2), and concluding with a treatment at 650 °C for 1 hour. Each treatment step uniquely contributes to the properties of the lattice and the overall phase composition of the material. The effects of Samples 1 and 2 have been discussed previously. In the final heat treatment, which extends Sample 2 to 650 °C for 1 hour, the magnesium produced from *ex-situ* reaction during the second heat treatment (as discussed in Sample 2) plays a crucial role. In the absence of sufficient oxygen, it is highly plausible that the liberated magnesium generated during the second heat treatment (900 °C for 30 minutes) can interact with the nearby MgB_4 formed during the same treatment to regenerate MgB_2 during the third heat treatment step at 650 °C for 1 hour. This has also been previously discussed in the work of Peng et al [240] and Yan et al. [241], as presented in Section 5.2.2. This transformation enhances the weight fraction of MgB_2 to 99.0% while also resulting in increased lattice parameters of a = 3.121 Å and c = 3.567 Å. The nucleation of new MgB_2 grains during this reaction likely restricts their growth, contributing to the observed smaller crystallite size of 24.46 nm. Despite the observed decrease in strain, the increase in lattice parameters at this stage remains incompletely understood, even after accounting for precision and XRD-related errors. This phenomenon may therefore warrant further investigation to clarify the underlying mechanisms responsible for this behaviour.

Sample 4 underwent a single heat treatment at 900 °C for 30 minutes, which reflects the conditions present within the case at the outset, as it contained unreacted Mg and B. This treatment represents the initial heat treatment step encountered by the case, facilitating the transformation of the unreacted materials. It reveals that executing the reaction between Mg and B solely at the higher temperature of 900 °C, excluding the preceding 700 °C stage, leads to a notably increased fraction of MgB_4. The reason for this could be that since all the

tested powders mentioned were extracted from within the cases, it is probable that during the heat treatment at 900°C, there was a significant loss of Mg at both ends of the short lengths of case, resulting in a higher quantity of MgB_4 at these points compared to the interior. The analysis of the powders revealed the presence of MgB_4 from the case ends and the enriched region, likely contributing to the higher observed MgB_4 ratio. During the first heat treatment (900°C for 30 minutes), Mg and B in sample 4 begin reacting to form MgB_2 (*in situ* reaction) starting from around 600°C. Since the ramp-up rate of the heat treatment is 20°C/min, it takes only 15 minutes to reach 900°C, which is relatively fast and may accelerate Mg evaporation. At temperatures above 700°C, Mg not only liquefies but also vaporizes in an argon atmosphere at ambient pressure [247]. Consequently, MgB_2 formation occurs more slowly compared to the rapid evaporation of Mg, leading to significant Mg loss. This likely results in the large amount of MgB_4 observed in sample 4. The resulting lattice parameters for Sample 4, a = 3.101 Å and c = 3.543 Å, are elevated relative to the values seen in lower-temperature treatments (such as Sample 1) due to the high atomic mobility and thermal expansion experienced at 900 °C. The presence of MgB_4 and MgO may also slightly distort the lattice, resulting in a strain of 0.23%. Additionally, Sample 4 shows the largest crystallite size of 112.26 nm, likely due to increased atomic diffusion at high temperatures, which can promote crystal growth.

Finally, in Sample 5, an additional heat treatment (650°C for 1 hour) following the treatment applied to Sample 4 results in a notably higher amount of MgB_2 compared to Sample 4. However, Sample 4 exhibited significant Mg loss, which indicates that all the MgB_4 present may not simply recombine with Mg to reform MgB_2. This finding suggests that the Mg vapor released during the initial *in-situ* reaction between Mg and B at 900°C in Sample 5 does not fully escape from the joint cases. Alternatively, there may be alternative mechanisms leading to the binding of B in other compounds, such as through reactions with

Ti forming TiB_x. Further investigation is recommended to determine whether side reactions are indeed binding the B in unintended compounds. Sample 5 also exhibits a slightly lower MgO fraction than sample 4. This is important because if a substantial volume of MgO is generated during the joint manufacturing process, it might generate unwanted insulating phases within the joint region. Moreover, further heat treatment of 650 °C for 1 hour resulted in lowered lattice parameters of *a*-axis: 3.085 Å and *c*-axis: 3.526 Å. Furthermore, it reduced the strain to 0.207% and the crystallite size to 50.28 nm. Similar to Sample 1, this sample primarily consisted of MgB_2, with trace amounts of MgO. It is believed that a similar effect observed in sample 2 (forming small MgB_2 grains from MgB_4) may also be occurring here, as the reduction in crystallite size and the increased presence of MgB_2 can be attributed to this phenomenon.

The decomposition reaction proposed in this study, $MgB_4 + Mg \rightleftharpoons 2MgB_2$, occurs under non-equilibrium conditions and cannot be explained by the phase diagram previously presented in **Figure 2.8**. Initial studies of Mg–B phase diagrams by Okamoto et al. [248] identified three intermediate phases—MgB_2, MgB_4, and MgB_7. Subsequently, Liu et al. [249] used the CALPHAD approach to update the phase diagram, incorporating these phases. Building on this work, Balducci et al. [76] included the boron-rich phase MgB_{20}, and Kim et al. [72] further refined the Mg–B phase diagram using CALPHAD software, as depicted in **Figure 2.8**. Despite these advancements, a fully validated and reliable experimental phase diagram for the Mg–B system remains unavailable in the literature. This limitation arises due to the high sensitivity of phase formation to Mg vapor pressure, which has thus far complicated efforts to establish a definitive experimental phase diagram for this system [241]. Thus, the challenging-to-predict localized vaporization behaviour of Mg within the case and wire may have induced non-equilibrium reactions between Mg and B at specific points in the wire and case. Consequently, the behaviour observed in this study

could differ from that outlined in equilibrium phase diagrams reported in the literature. As further work, to understand the fundamental mechanism of the decomposition reaction under the non-equilibrium conditions presented here, an experimental setup could be developed with meticulous control and monitoring of Mg vaporization under these temperature ranges. This would allow for a detailed investigation of potential non-equilibrium reaction presented here.

In conclusion, these XRD findings indicate that by the conclusion of the two-stage joint-making process, a substantial fraction (>98%) of the superconducting MgB_2 phase is expected in both constituents of the joint – the wire and the filler. Leveraging the decomposition property of MgB_2 at high temperatures and manipulating the heat treatment accordingly can achieve a smooth and well-fused surface between the wire and joint filler. By initiating MgB_4 production through the first heat treatment step, triggering Mg vaporization from both the joint and the wire, and then transitioning Mg from the gas phase back to the liquid phase at 650°C, it is possible to react the initially formed MgB_4 to produce new MgB_2 with smaller crystallite sizes. This new MgB_2 formation at the wire-filler interface is believed to result in a smooth particle fusion.

6.2.4 Low current transport T_c measurements on short joints

In this section, the T_c results of the short joints between reacted wires are measured via low transport measurement system outlined detailed in section 3.3.5. The term "short joint" refers to the joined state of two short lengths of superconducting wire, each measuring 2 cm in these experiments as shown in **Figure 6.6**. The purpose of using a short joint in this test is twofold: to conserve MgB_2 wire and to facilitate testing in the cryocooler, given its small sample holder.

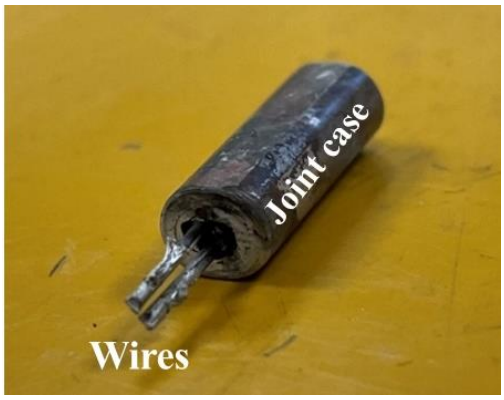

Figure 6.6 *One of the short joint example. The wires, each measuring 2 cm in length, were placed into two holes, each 1 cm deep, drilled into the compressed Mg+B powder contained within the case.*

Results obtained here can be transferred to coil after optimizing production for speed and cost, as demonstrated later in this study.

This section aims to obtain T_c values and interface structures of joints heat-treated under different conditions, as shown in **Table 6.5**.

Table 6.5 *Heat treatment procedures and resistance-temperature values of joints. A stands for heat treatment 900 ^oC -30min + 650 ^oC -1h and B stands for 700 ^oC-15min.*

Sample	***HT - Case***	***HT – Joint***	***T_c onset***	***T_c Offset***	***ΔT_c***
1a	Unreacted	A	37.8	37.5	0.3
1b	Unreacted	A	37.7	37.5	0.3
1c	Unreacted	A	37.8	37.3	0.5
1d	Unreacted	A	37.8	37.6	0.2
2*	Unreacted	A	37.6	29.9	7.7
3	B	A	37.6	32.3	5.3
4a	Unreacted	B	37.4	32.5	4.9
4b	Unreacted	B	37.2	33.9	3.3

*In this sample, wire tips positioned in the case as looking each other rather than looking upwards like others (**Figure 6.7**, bottom).

The breadth of the superconducting transition (ΔT_c) in the R/T plot reflects the uniformity and purity of the MgB_2 sample. A narrower transition indicates a more consistent and purer sample, while a broader transition suggests impurities or flaws.

Sample 2 in **Table 6.5**, was produced with a different wire orientation compared to samples 1, 3, and 4, in order to observe the effect of pressure on joint ends and to examine the interface between the wire ends and the filler, along with its impact on T_c. The wire orientation inside the case is depicted in **Figure 6.7** (note that the case is not depicted in these illustrations). The pressing direction after the wires have been introduced to the case has also been indicated.

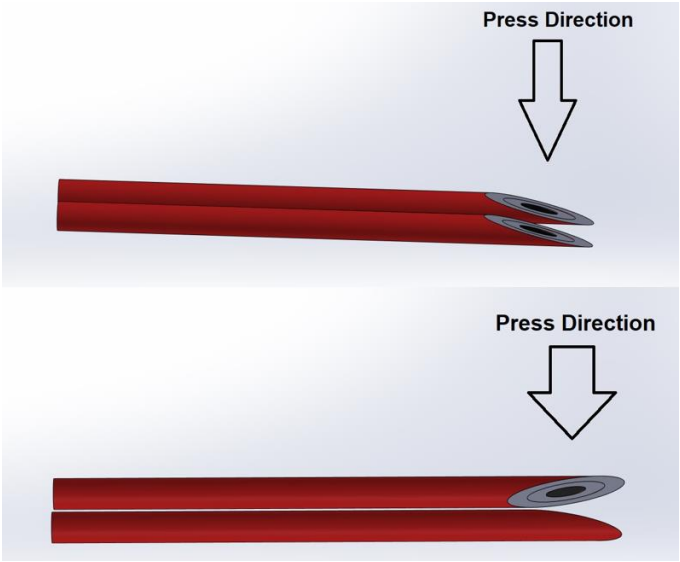

Figure 6.7 *The wire orientations inside the case of samples 1, 3, and 4 is depicted at the top, whereas sample 2 is illustrated at the bottom.*

Figure 6.8a presents resistance versus temperature plots for the reacted joint samples and **Figure 6.8**b represents the interface between the joint tips and the core within the case of samples 1a and 1b given in **Table 6.5**. It is evident that groups 1 (a, b, c, and d) and 4 (a and b) exhibit lower residual resistance below T_c than samples 2 and 3. Sample 2 has the wire orientation shown in **Figure 6.7** (bottom), and when prepared for SEM analysis it was clear that there was a large void next to the scarfed wire end, **Figure 6.9**. This may be a result of pressing the case with the cut surfaces of the wires positioned face to face.

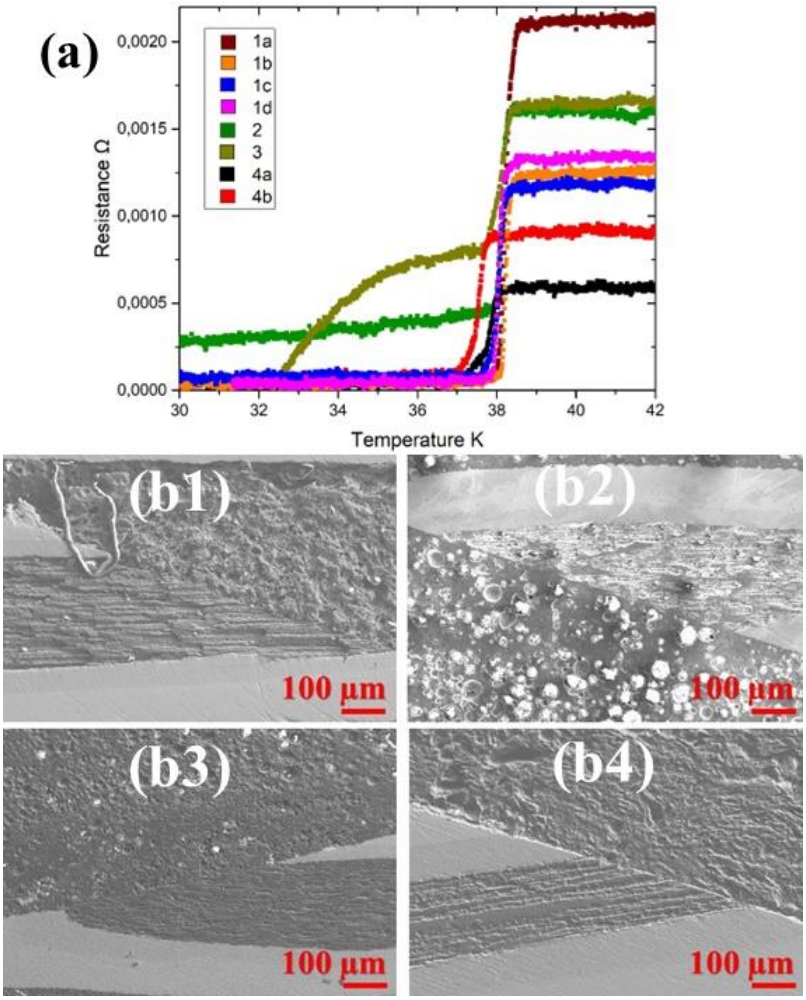

Figure 6.8 *a) Resistance-Temperature plot of the samples and b) the interface quality of the sample #1a (b1, b2) and #1b (b3, b4)*

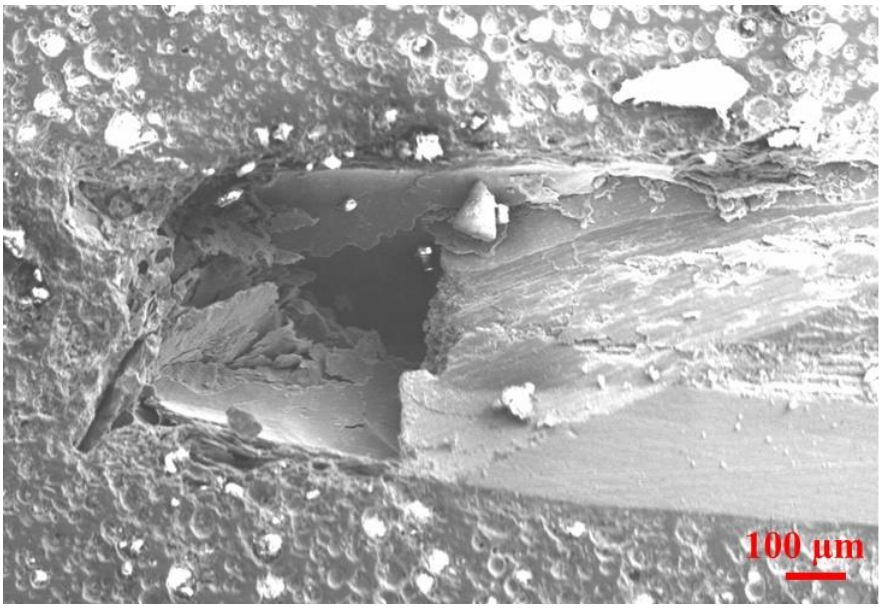

Figure 6.9 *SEM image showing the interface void found at the wire end in sample 2.*

The presence of residual resistance might be explained by the current path introduced previously in scenario one shown in **Figure 5.17**. If the wires were superconducting, it is most likely that the Ti and the steel of the case are contributing resistance below the measured T_c of MgB_2.

Sample 3 was prepared in a slightly different manner. Unlike the other cases, the case of this sample was heat-treated at 700°C for 15 minutes (since the wire previously showed superior T_c performance at this temperature) before the wires were inserted into it. Subsequently, one end of the case was drilled twice to accommodate the wires. Once the wires were inserted, the same pressure (same pressure that applied other joints) was applied to the joint. It was inevitable that numerous cracks would be present inside the joint filler due to the applied pressure. The purpose of this step was to observe the effect of the applied heat treatment on interface between reacted wires and the reacted filler.

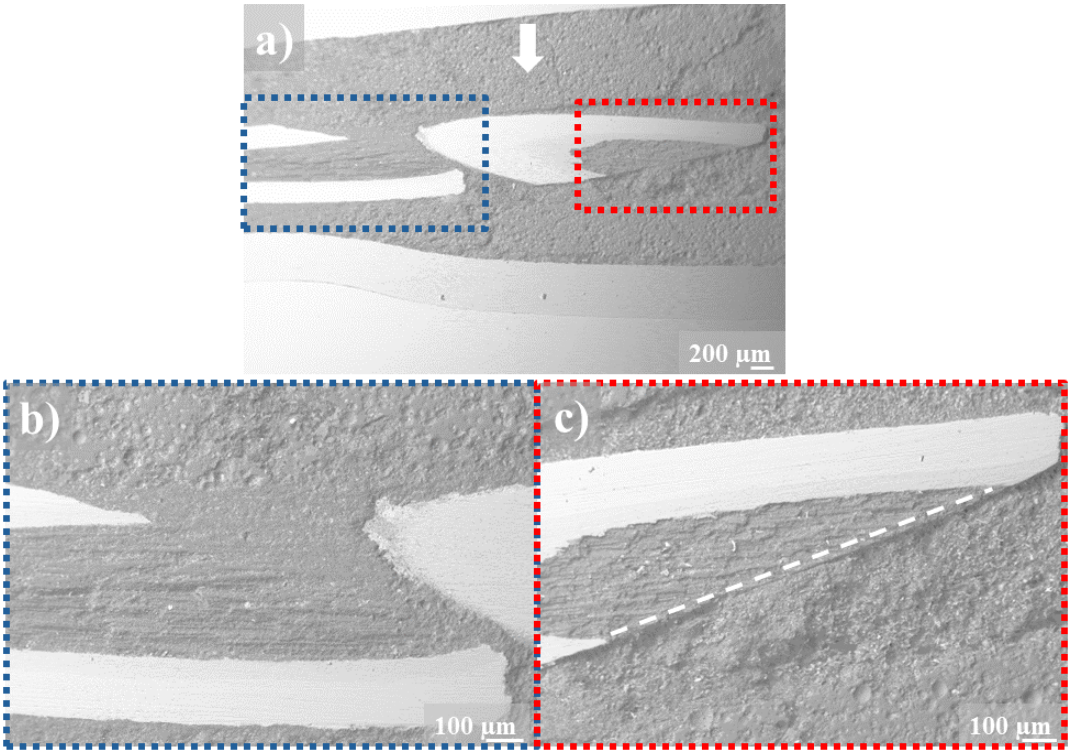

Figure 6.10 *The BSE images of sample 3: a) show lower magnification of wire/filler interfaces, and high magnification of wire/filler interfaces given in b) and c). The white arrow in "a" represents the direction of pressure applied on the joint before the heat treatment.*

Figure 6.10 displays the BSE images of sample 3. Drilling the core of the already-reacted case was challenging due to its hard ceramic nature, making proper wire insertion difficult and resulting in improper placement. The wire in (c) originates from beneath the wire in (b). Examining the interfaces, (b) shows a smooth interface with noticeable particle fusion, while (c) has a poor interface with a distinct line between the filler and the wire. Additionally, the scarfed wire ends show different orientations: in (b), the scarfed surface faces upward, while in (c), it faces downward. This discrepancy suggests wire shifting during insertion or pressure application (as indicated by the white arrow in **Figure 6.10**a). The wire in (c) likely did not receive effective pressure distribution.

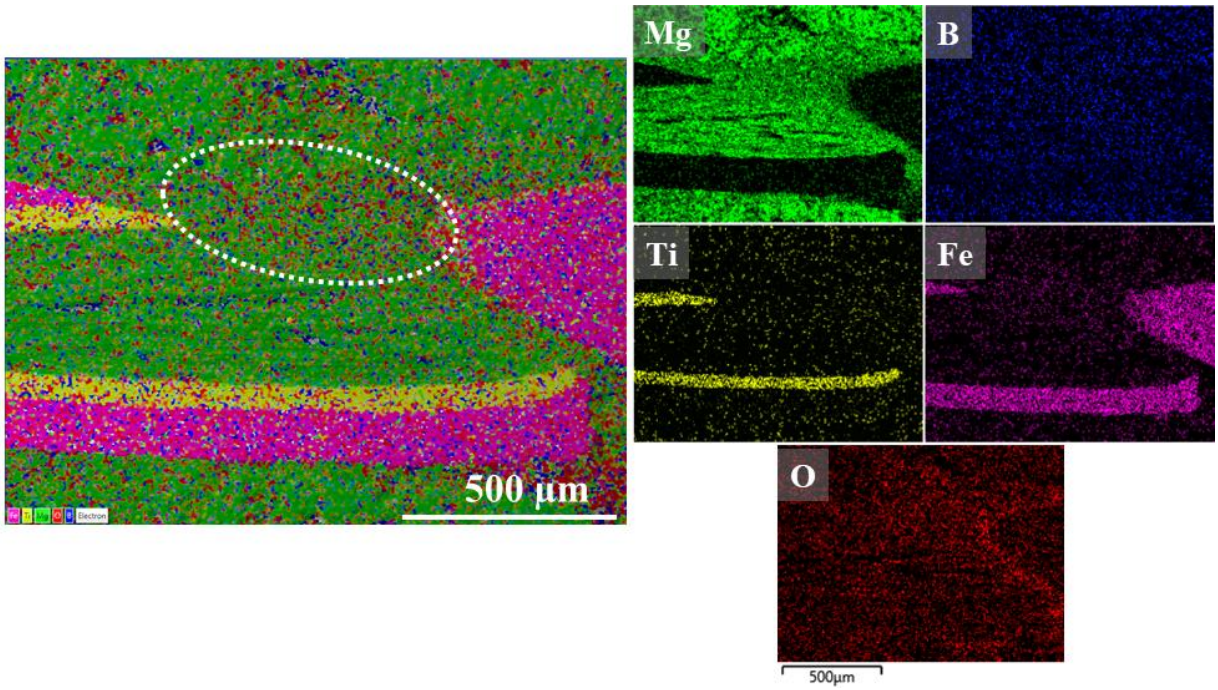

Figure 6.11 *EDX maps of the interface of sample 3.*

Figure 6.11 illustrates the EDX maps of the interface of the wire from joint sample 3, as shown in **Figure 6.10**b. The interface appears smooth, with some oxygen-rich regions delineated by a dotted circle around the interface along the current path. This smooth interface suggests that the applied heat treatment was sufficient for the decomposition of MgB_2 and its recombination into MgB_4 and Mg in both the reacted wire and the reacted

filler. This fused interface scenario aligns with other joints between reacted wires and unreacted cases. However, the joint exhibited a two-stage superconducting transition (**Figure 6.8**a), likely due to the poor connection of the other wire end shown in **Figure 6.10**c.

Figure 6.12a compares the performance of joints formed between reacted wires using heat treatments at 700, 800, and 900 °C, and the fourth one by a two-stage heat treatment at 900 °C and subsequently at 650 °C. The joint heat-treated at 700°C exhibits an onset T_c value of 37.8 K with a relatively broad transition, characterized by a significant tail before reaching zero resistance. Both the onset T_c and the sharpness of the transition improve when the joint is heat treated at 800°C, likely due to the higher reaction temperature leading to better stoichiometry, reduced disorder within the MgB_2 lattice, and enhanced uniformity of the material through which the current flows.

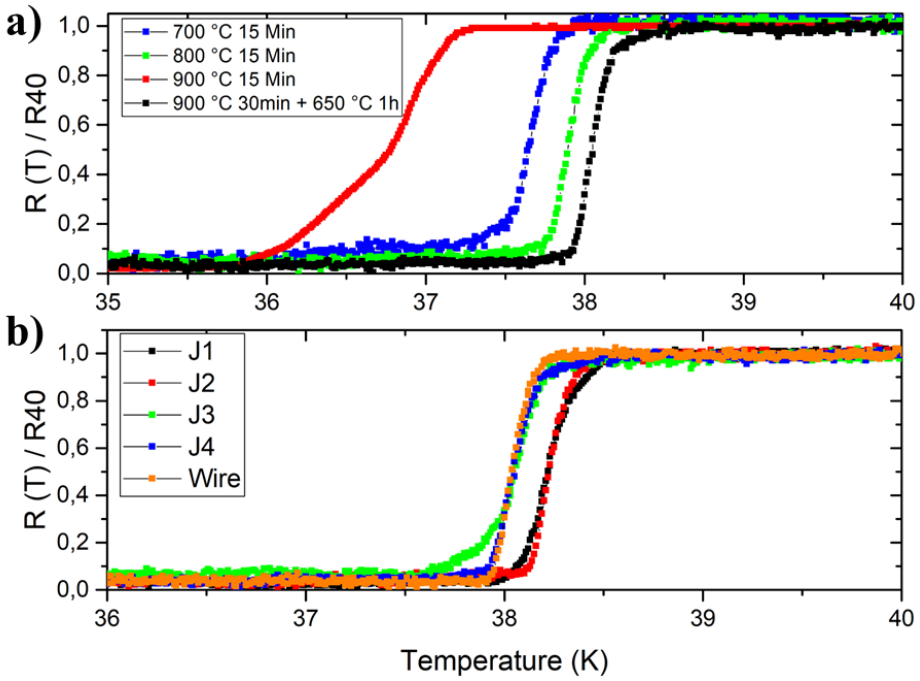

Figure 6.12 *(a) Resistance-to-temperature (R/T) data for joints subjected to different processing temperatures, and (b) the assessment of four joints, ostensibly identical, processed through the two-step heat treatment (900 °C for 30 mins and 650 °C 1 hour) method and the wire.*

Raising the temperature to 900 °C notably diminishes the joint performance. This decline is likely due to the well-documented thermal breakdown of MgB_2 into non-superconducting

MgB_4 and $Mg_{(vapor)}$, expected to occur at such a high temperature under standard pressures. However, an additional heat treatment at 650 °C significantly enhances the superconducting characteristics of joints initially reacted at 900 °C because the decomposition reaction can be reversed through annealing at a lower temperature. Given that the two-stage heat treatment at 900 °C followed by 650 °C yields the sharpest superconducting transition and the highest T_c value of 38.2 K, I chose these conditions to manufacture jointed coils for persistence measurements.

To assess the reproducibility of this process, R/T curves were plotted for four ostensibly identical samples (J1, J2, J3, and J4) heat-treated 900 °C for 30 minutes and 650 °C for 1 hour using a current of 0.1 A and self-field. For comparison, the wire's T_c data is also presented. The reacted wire (obtained from Epoch in its reacted form) was heat-treated at 900°C for 30 minutes and 650°C for 1 hour under an Ar atmosphere to replicate the entire reaction sequence. **Figure 6.12**b displays the R/T curves of all four joints along with the wire. All four joints exhibit very similar T_c values (onset values ranging between 38.1 K and 38.4 K) and the wire exhibited almost same with J4's (38.1 K of T_c and 0.2 of ΔT_c). Sample J3 displays a slightly broader transition than the other three, hinting at potential inhomogeneity within the MgB_2 constituting the continuous path. However, no evidence of any ohmic series resistance below the transition is observed in any of the samples. This underscores the reproducibility of the joint preparation process in consistently achieving a continuous superconducting pathway from one wire to another across the joint, capable of supporting at least the low current of 0.1 A employed in these measurements.

In addition to the measurements on the steel/Ti/Mg+2B composite cases, another joint has been produced using a Ti case and shown in **Figure 6.13**. The outer diameter of the Ti tube was 6 mm, and the wall thickness 0.5 mm. Initially, the wire ends were ground, and the Ti

tube was filled with Mg and B powder in a stoichiometric ratio of 1:2. The powder was then hand-pressed using a metal rod and drilled twice, followed by the insertion of pre-ground reacted wires into the holes. Approximately 200 kPa of pressure was applied using a hydraulic pressing machine for 10 minutes, slightly lower than the previous method to prevent wire and case breakage. The heat treatment remained consistent at 900°C for 30 minutes and 650°C for 1 hour.

Figure 6.13 *The short joint comprises reacted wires encased within a titanium tube filled with a mixture of Mg and B (stoichiometric ratio of 1:2) powder.*

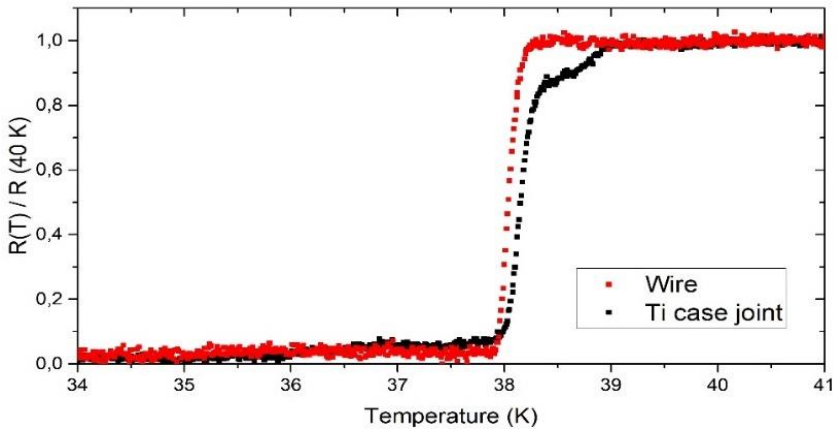

Figure 6.14 *R/T curves of the wire (the wire shown in* ***Figure 6.12*** *(b)) and the joint shown in* ***Figure 6.13****.*

Figure 6.14 depicts the R/T curves of the wire (red), given in **Figure 6.12**, and the joint prepared using a Ti tube (black), as shown in **Figure 6.13**. The plot suggests the feasibility of implementing this heat treatment regimen using a basic Ti tube as a case, even though its T_c appears slightly higher (38.3 K) and ΔT_c looks slightly worse (0.4) than the wire.

6.2.5 Resistance and I_c measurements of the coil

In this section, the coil introduced in the method section underwent testing to determine its resistance and critical current using the field decay method, as outlined in section 3.1.5. Wire #1 from **Table 6.1** was initially intended for use in short joints. However, during the coil-making process, it proved impractical to wind this wire onto the small former we employed, given the bending radius of the reacted wires, which was approximately 12 cm. Consequently, the decision was made to use the unreacted wires (**Table 6.1**, #3) for winding onto this coil without jointing, followed by heat treatment at 700°C for 15 minutes. Subsequently, the joint was positioned and heat treated, as previously detailed. The specifications of the coil are listed in **Table 6.6** and shown in **Figure 6.1**.

Table 6.6 *Specifications of the coil: The inductance has been determined utilizing the long solenoid approximation.*

Coil inner radius	*r*	6 mm
Coil outer radius	*R*	7 mm
Number of turns	*N*	29
Coil length	*l*	20 mm
Inductance	*L*	2.8 x 10^{-5} H

Due to the monofilament nature of the MgB_2 wire, flux jumping behaviour becomes severe at lower temperatures [125, 236] as also discussed in 4.2.3, so the results presented here are from experiments conducted at 20 K.

To establish the connection between the circulating current (I) and trapped magnetic field (B), the previously introduced Biot-Savart law (equation (3.3)) equation was used to derive the field expected in the centre of the coil as a function of current, incorporating the geometry and parameters specific to the test coil outlined in **Table 6.6**. The field is initially applied to a level of H_{max}, the energizing field, before being reduced back to zero or to a desired

background field (1 T). The resulting drop (ΔB) in field induces a current in the superconducting coil, effectively trapping the applied field within the coil, provided that the joint is operating according to specifications.

Figure 6.15 (a) depicts a standard energization profile of a 1 T background field measurement, where a peak field of 1.4 T was utilized to energize the coil.

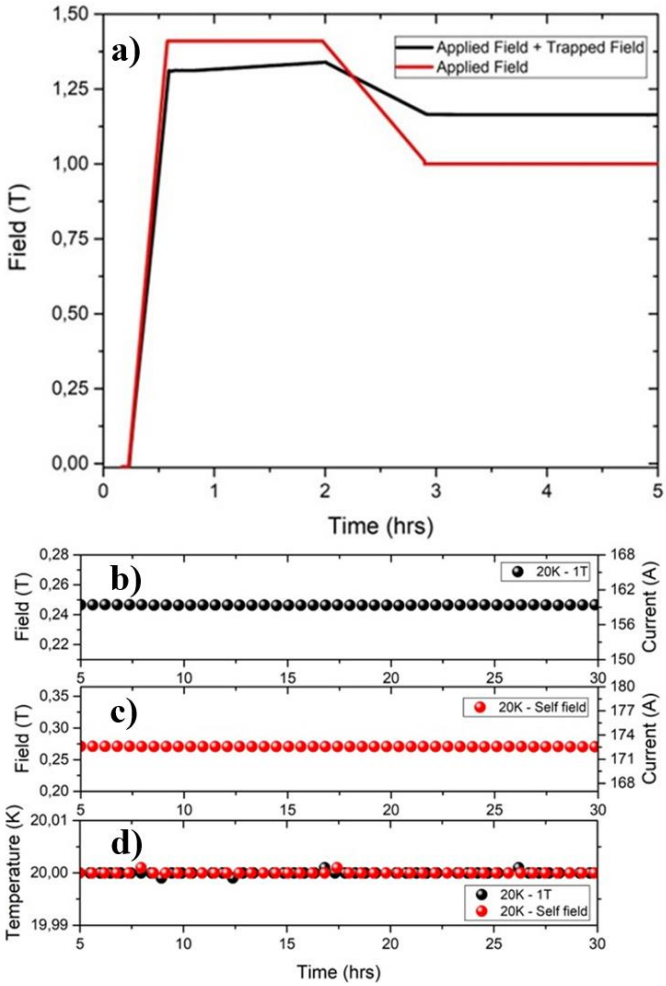

Figure 6.15 *(a) An exemplar energization profile from a 1 T background field experiment. The recorded field and the current obtained from equation (3.3) (b) 20 K with a 1 T field, (c) 20 K with self-field, and (d) the recorded temperature throughout the measurement.*

The rate chosen during the decrease in field strength was deliberately slower than the ascent rate to mitigate the impact of flux jumping, an issue arising from the decay curves of the coil, tested at 20 K and in 1 T background field or in self-field, are shown in **Figure 6.16** and the resistance of the circuit was calculated using the equation (3.2). The circles on the

graph represents the decay profile that would be observed if the coil had a resistance of 10^{-12} Ω. It is evident in both cases that the joint exhibits a resistance lower than 10^{-12} Ω under these conditions. In both scenarios, the resistance remained below 10^{-12} Ω (**Figure 6.16**), satisfying the persistence criterion unequivocally. Once persistence had been reached, the trapped fields stabilized at 0.27 T and 0.25 T in self-field and a 1 T background field, respectively, equating to trapped currents of 172 A and 160 A calculated from equation (3.3). The computed resistance after stabilization for both the self-field and the 1 T decay measured 5.5×10^{-14} Ω and 5.6×10^{-14} Ω, respectively. These currents result in a critical current ratio (CCR) of 78% at 20 K within a 1 T background field, based on a wire I_c of 206 A (**Figure 5.6**).

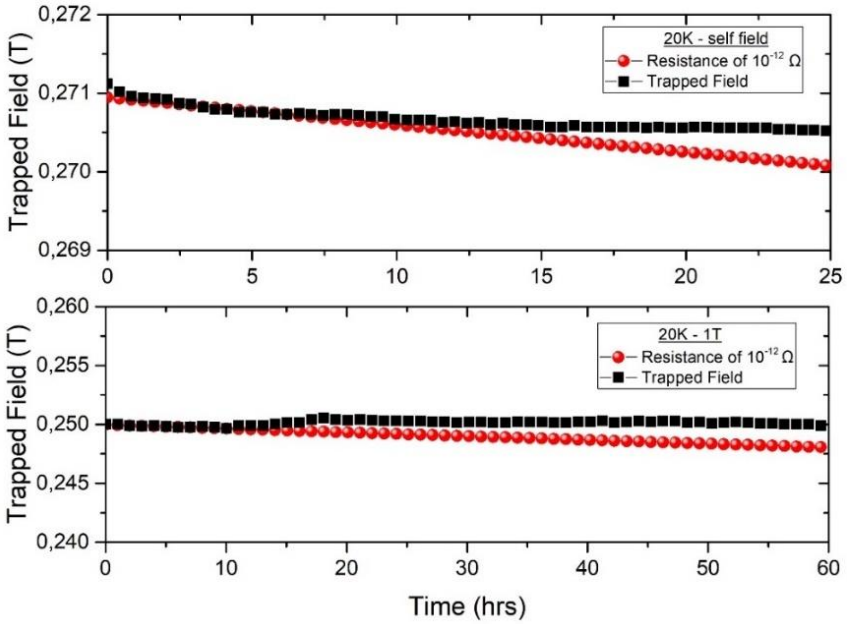

Figure 6.16 *Typical decay curves in self-field (top) and 1 T background field (bottom), alongside the corresponding decay curves that would be observed if the coil had a resistance of 10^{-12} Ω (red-circles).*

However, as the wire I_c is unknown under self-field conditions, the CCR value in zero background field cannot be computed. The I_c of the wire at persistent mode value is also unknown. It is expected to be significantly lower than the I_c established by standard transport measurement. If the I_c of the wire at 20 K and 1 T field were determined using the IRT

method, it would be less than 206 A. Consequently, the actual CCR value exceeds 78%. The primary reason for this is that, in a homogeneous sample, both types of currents (transport current and induced current) follow the same *E(J)* relationship. Thus, under identical conditions (e.g., magnetic field intensity, temperature, and electric field), both experiments will yield matching critical current densities [211]. However, in the presence of sample non-uniformity, localized regions with high J_c may dominate the overall magnetization signal through induced current loops, while the transport current must traverse regions with lower J_c. Consequently, in such cases, the measured transport J_c may be lower than that determined from an inductive experiment.

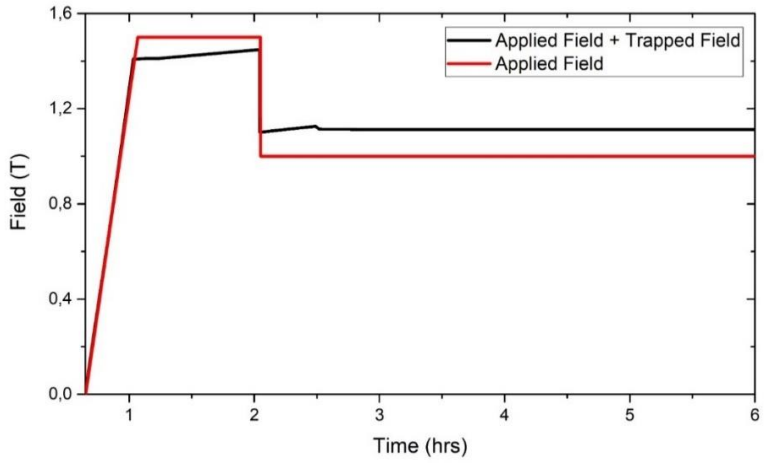

Figure 6.17 *A second example of the energisation of a coil showing, after initial settling, similar behaviour as in* ***Figure 6.15****a.*

The energisation process was repeated twice and find that the coil can be warmed and cooled and re-energised without any signs of performance degradation. **Figure 6.17** shows a second energisation with a very similar performance.

This chapter presents a novel process for fabricating persistent-grade joints in monofilament reacted MgB_2 wires. The resulting wire-joint interface demonstrates excellent connectivity, yielding residual resistances below 10^{-13} Ω and achieving trapped persistent currents of 172 A in self-field and 160 A in a 1 T background field. The critical current ratio (CCR) of at

least 78% in a 1 T field at 20 K represents the highest reported CCR for reacted MgB_2 wire joints. The subsequent step involves fabricating a joint between reacted multifilament wires. The applicability of the method introduced in this chapter has been analysed and is presented in the following chapter.

6.3 Conclusions

A novel joint making process has been demonstrated for introducing persistent grade joints into monofilament reacted MgB_2 wires. The key stages of the joining process include inserting reacted monofilament wires into pre-drilled holes in unreacted Mg + B powder in a joint case, followed by a pressing operation designed to place the exposed wire ends into close mechanical contact with the powder. Subsequently, a final two-step heat treatment process is employed to achieve good density and connectivity, as well as a low fraction of non-superconducting impurity phases.

Additionally, this joint fabrication method results in a well-connected interface between wire and joint filler, leading to residual resistances below 10^{-13} Ω. Trapped persistent currents of 172 A and 160 A are obtained in self-field and 1 T background field, respectively. The critical current ratio (CCR) is calculated as at least 78% under a 1 T background field at a temperature of 20 K, which represents the highest value reported to date for joints made between reacted MgB_2 wires. These results suggest the feasibility of a robust jointing process suitable for manufacturing persistent mode react-and-wind MgB_2 magnets capable of operating at temperatures as high as 20 K.

For future research, a detailed investigation is recommended into the observed increase in lattice parameters of Sample 3 despite the reduction in strain, as the mechanisms behind this phenomenon are not yet fully understood. Further studies could also examine whether side reactions contribute to the unintended binding of boron into compounds such as TiB_x in

Samples 4 and 5, as this could affect phase formation and reduce the available boron content. Additionally, to explore the fundamental mechanisms driving the decomposition reaction, $MgB_4 + Mg \rightarrow 2MgB_2$ under non-equilibrium conditions, an experimental setup could be developed for precise control and monitoring of Mg vaporization within the relevant temperature range. This approach would facilitate a detailed investigation into potential reaction behaviours, providing insights into the underlying processes of the system.

Chapter 7 Microstructure and Superconducting Properties of Novel Reacted Multifilament MgB_2 Wire Joints

7.1 Introduction

Multifilament superconducting wires are favoured over monofilament wires in certain applications due to their higher current-carrying capacity and reduced screening current-induced fields (SCIFs), especially crucial for MRI magnets where uniform magnetic fields are essential [32]. Unlike monofilament wires, multifilament wires offer greater uniformity in magnetic field distribution [32]. Hence, for the advancement of MgB_2 MRI magnet technology, the adoption of multifilament wires is strongly recommended [250, 251].

The number of filaments within a wire can vary widely, ranging from a few dozen to as many as 100,000 [252], depending on specific application requirements such as filament diameter and critical current. This variation facilitates the dissipation of heat and helps mitigate changes in magnetic fields, which can arise from mechanical energy release or the onset of the flux jump.

On the contrary, the incorporation of multifilament wire in persistent mode MRI magnets alone does not resolve the issue. The process of joining reacted MgB_2 multifilament wires, with a resistance of $<10^{-12}$ Ω, and attaining high CCR presents challenges due to their smaller filament size. Establishing a seamless interface between fine filaments and the filler material proves challenging in comparison to monofilament MgB_2 conductors [77]. The more filaments there are, the more filament-case filler interfaces need to be managed. Consequently, despite its significant relevance in MRI magnet applications, there have been limited successful joining outcomes reported thus far with multifilament MgB_2 conductors [77, 253, 254] as also discussed in Chapter 2.

In this chapter, following the successful creation of a joint between reacted monofilament MgB_2 wires presented at the previous chapter, the exploration of whether these joint-making strategies and the heat treatment regime can be applied to MgB_2 multifilament wires is undertaken. The chapter starts with detailing the experimental procedures, followed by a section discussing the wire characteristics used for joint fabrication. Then, an explanation is given regarding the characterization and test results, which include SEM, EDX, T_c, and joint resistance, each introduced separately.

7.2 Experimental details

The procedure for fabricating joints between reacted multifilament MgB_2 wires is detailed in Section 3.1.3. Initially, unreacted wires were heat-treated at 700°C for 15 minutes for comparison with previously used monofilament reacted wires. After joining, the wires underwent a heat treatment at 900°C for 30 minutes followed by 650°C for 1 hour, a regime chosen for its superior results in previous reacted monofilament MgB_2 joints, allowing for potential result comparison.

To avoid wasting multifilament wires, the first step involved conducting T_c transition measurements of short joints using low current transport measurements, as detailed in Chapter 6. This process aimed to identify an optimal procedure before preparing jointed loop coils. The resistance and T_c data of the joints were carefully analysed, as well as inductive resistance testing, which was performed on the coil.

7.2.1 Wire characteristics used in the joint

The 6-filament MgB_2 wire used was manufactured via the PIT method by Dr. Doğan Avci at Abant Izzet Baysal University in Bolu, Türkiye. **Figure 7.1** depicts the multifilament MgB_2 wire cross section utilized in this experiment.

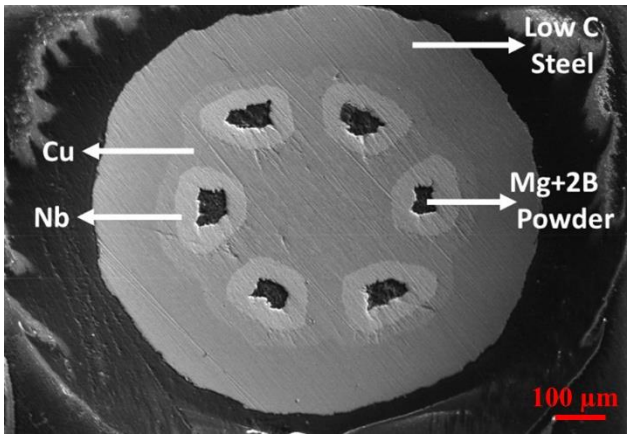

Figure 7.1 *SE1 SEM image of the MgB_2 Multifilament wire cross-section.*

Further details about the wire production procedure and its specifications can be found elsewhere [255]. They produced the monofilament MgB_2 wire, encased in Cu/Nb sheaths, by mixing amorphous nano-boron powder (98% purity, <250 nm size) and magnesium powder (99% purity, 74–144 µm size) in a stoichiometric ratio (Mg+2B) of 1:2. The I_c data of the wire is presented in **Table 7.1**, with measurements conducted at 25 K and a 4 T background field. However, there is an absence of data for the 20 K and 1 T background field, hindering comparative analysis with the results outlined in Chapter 6.

Table 7.1 *The transport I_c data of the wire used here were measured at 25 K and a 4 T background field. The field criterion was 1 µV/cm. Data was obtained from* [255].

Heat Treatment to the wire	**Transport I_c (A)**
650 °C - 15 min	0.65
650 °C - 30 min	0.55
650 °C - 45 min	0.5
650 °C - 60 min	0.66
650 °C - 240 min	0.58
700 °C - 60 min	0.7

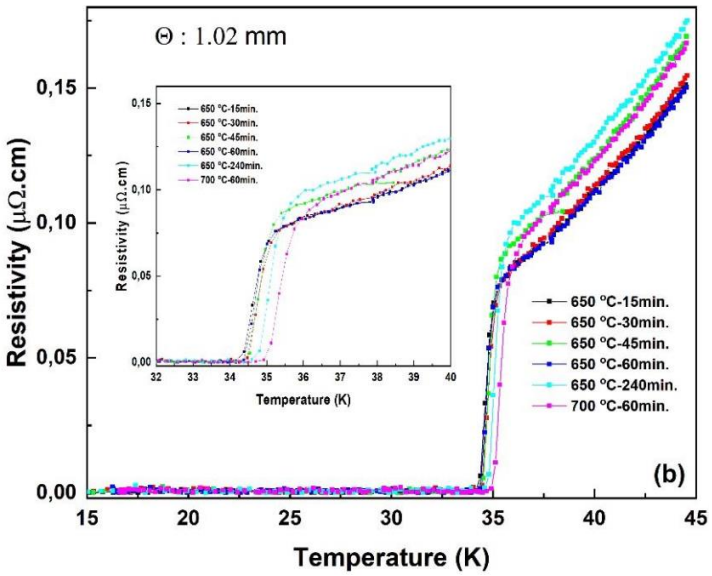

Figure 7.2 *The low current transport measurement that gives resistivity vs temperature plot of wires heat treated under various conditions. Reprinted from* [255].

Figure 7.2 displays the superconducting transition profiles of wires subjected to heat treatment at various temperatures. Notably, it exhibits a well-defined transition even at 650°C for 15 minutes and at 700 °C for 60 min. To facilitate comparison with the joint between monofilament wires utilized in Chapter 6, the heat treatment protocol was adjusted to 700°C for 15 minutes.

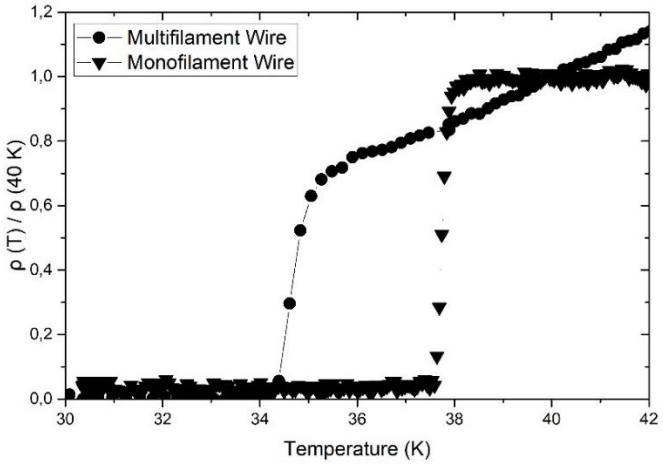

Figure 7.3 *Low current transport measurement critical temperature transition profiles of wires. Their unreacted forms were heat treated under 700°C for 15 minutes.*

In **Figure 7.3**, the comparison between the T_c values of the Epoch monofilament wire utilized in preceding chapters and the multifilament MgB_2 wire from [255] is presented. The

applied heat treatment for both wires is identical: 700°C for 15 minutes. The Epoch monofilament wire demonstrates superior performance in terms of T_c onset, T_c offset, and ΔT_c values when compared to the multifilament wire.

The preparation of the joint and coil for the multifilament wires is described in section 3.1.3 and 3.1.5.1 respectively

7.2.2 Effect of heat treatment on wire/case interface

Following joint fabrication with reacted multifilament wires, the next step involved heat treating the joints using similar parameters from Chapter 6. A comparative analysis was aimed, given the superior results seen with reacted monofilament wire under the same heat treatment (900°C for 30 minutes and 650°C for 1 hour). The prescribed heat treatment was applied, and microstructural examination (**Figure 7.4**) revealed an absence of discernible interface between filaments and filler material. Notably, wire end observations were highlighted in specified areas denoted by blue and red dotted rectangles in **Figure 7.4**b and **Figure 7.4**c, respectively, prompting further investigation. In **Figure 7.4**b, it is observed that Cu is present until a certain point indicated by the white arrow, beyond which the presence of Cu is inconsistent. Additionally, Nb suddenly appears, as indicated by a white dotted circle in Nb map, although it should have been continuous since it is the filaments barrier. However, before reaching the end of the white arrow, Nb is not visible, suggesting that the remaining Nb embedded in Cu, or there appears to be a lack of connection between Nb and Cu, indicating potential filament breakage. Furthermore, the region indicated by the dotted white rectangular area in **Figure 7.4**b, there seems to be a void that was filled with grinding powder during the polishing process, as evidenced by the presence of carbon (not shown here) from the epoxy. However, this region was meant to be Cu, as it constitutes the

matrix. This void may suggest that Cu in that region diffused into the filler material, leaving a void behind.

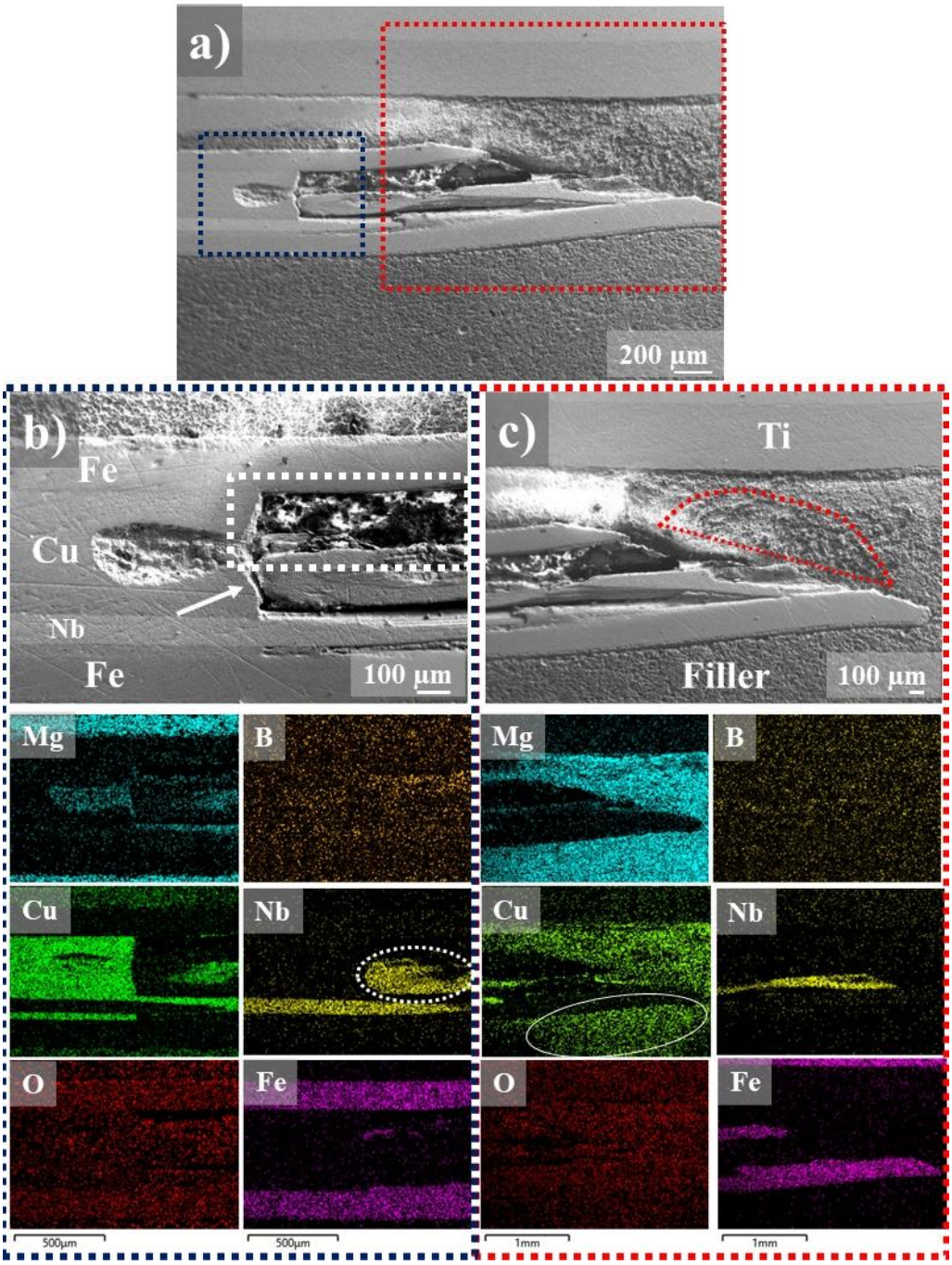

Figure 7.4 *The cross-sectional SEM image of the joint interface depicts its various regions (b and c), along with corresponding EDX maps of those regions.*

The Cu map of **Figure 7.4**c may support this theory, as it shows the presence of Cu within the filler, extending even below the wire ends as indicated by the solid circle in Cu map.

This presence of Cu was unexpected, considering that there is steel between the Cu matrix and the filler material. Determining whether Cu has dissolved into MgB_2 or precipitated is challenging due to the significant quantity of Cu present. Both scenarios are plausible. The reaction between MgB_2 and Cu has been previously discussed in section 0. If Cu has dissolved into MgB_2, it could detrimentally impact the superconducting properties of MgB_2 by potentially reducing the amount of magnesium through reaction.

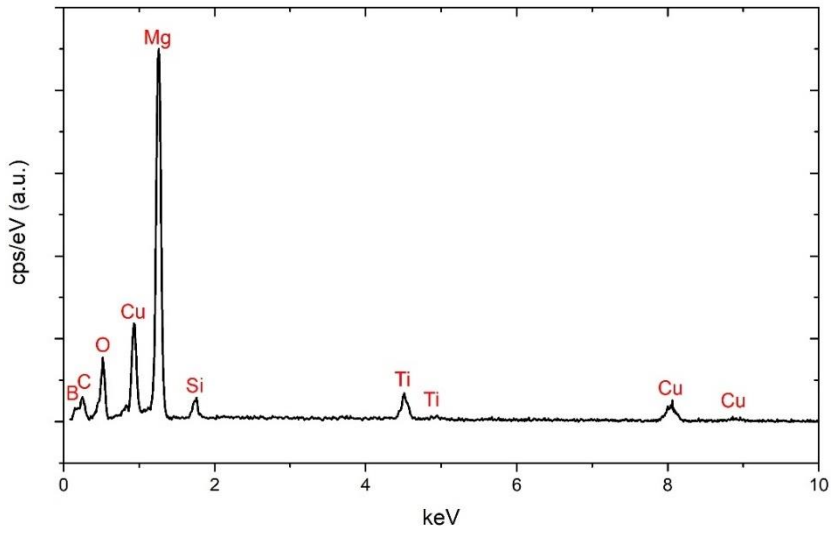

Figure 7.5 *EDX spectrum of the region shown by a red dotted area in* ***Figure 7.4****c*

Figure 7.5 displays the EDX spectrum from the red region in **Figure 7.4**c, revealing prominent Cu peaks alongside Si, Ti, O, and C peaks. Si and C likely stem from the polishing process, while Ti may have transferred from the case barrier during polishing. According to the binary phase diagram (**Figure 7.6**), Mg-Cu reaction likely initiates around 460°C with approximately 33% Cu content, forming $MgCu_2$. Kario et al. [97] studied the impact of heat treatment temperature on *ex-situ* MgB_2 and copper sheath efficiency. They found that 750°C treatment yielded optimal results, with minimal Mg-Cu reaction, showcasing 90 wt% MgB_2 and only 1 wt% Mg-Cu secondary phase. However, at 800°C, MgB_2 content decreased to 88 wt%, while Mg-Cu secondary phases increased to 2 wt%. Zhou et al. [158] investigated different sheath materials' effects on wire J_c properties. They observed adverse impacts on

Cu-sheathed tapes above 800°C, leading to significant bubbling and tape damage, resulting in J_c loss. Chen et al. [159] examined copper incorporation in both *in-situ* and *ex-situ* settings. They found significant Mg-Cu reaction above 800°C in samples heat treated between 600 and 900°C for one hour.

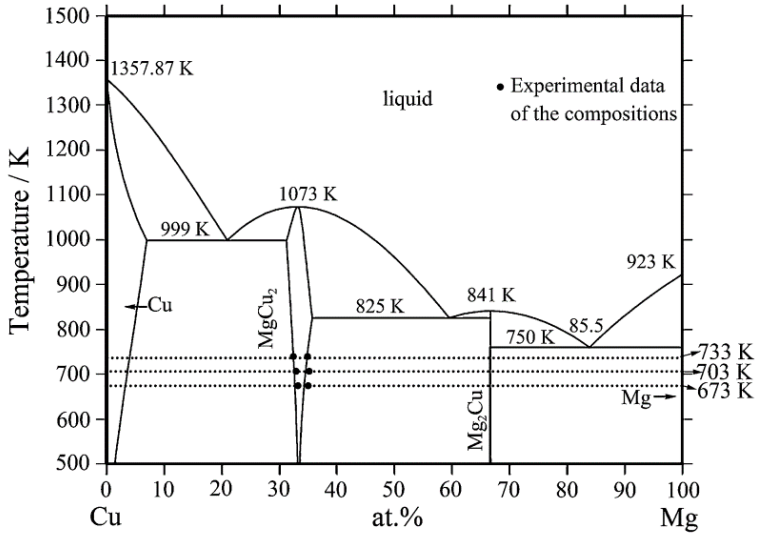

Figure 7.6 *Binary Cu-Mg phase diagram* [256]

Therefore, it was hypothesized that the mobility of copper occurred during the initial heat treatment, conducted at 900°C for 30 minutes, which is close to the melting point of copper (1085°C). Thus, it was deemed prudent to explore another joint-making approach by eliminating the copper at the end of the wire intended for placement within the case. Consequently, the wire ends were etched using a 35% concentrated HNO_3 solution for 10 minutes. After the etching process, both the steel and Cu were removed, leaving behind six Nb-encased Mg+2B powder filaments, as depicted in **Figure 7.7**a.

Figure 7.7 *a) Etched MgB_2 multifilament, and b) short joint made using the etched wire.*

The wire depicted in **Figure 7.7**a was heat treated at 700°C for 15 minutes under an Ar atmosphere following which the tips of the filaments were carefully ground using a large grinding wheel. Subsequently, the wires were inserted into the predrilled holes of the joint and pressure was applied on it. Then, resulting joint is shown in **Figure 7.7**b. Afterwards, the joint underwent heat treatment at 900°C for 30 minutes and 650°C for 1 hour under tube furnace and Ar atmosphere. The main purpose of this heat treatment is to determine whether the pre-worked procedure for joints between monofilament MgB_2 wires would also be effective for joints between multifilament MgB_2 wires.

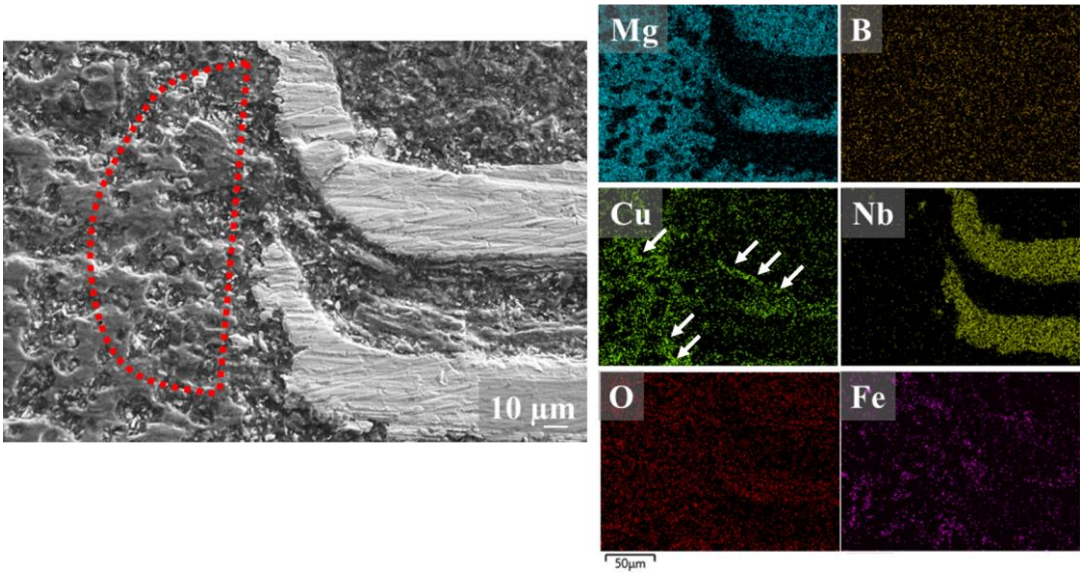

Figure 7.8 *SEM and EDX images of the interface between the end of one filament and the filler material of the joint.*

The sample preparation for SEM analysis was previously introduced in section 3.2.5 and the interface between the filament and filler is depicted in **Figure 7.8**. Inside the case, there were six different filaments, making it challenging to obtain their interfaces without damaging them during the polishing process. Nevertheless, it was observed that there is a small connection between one filament and the case filler.

As indicated by the SEM image, the interface appears quite smooth and well-connected. The EDX spectrum of the red circular area (the current path) shown in **Figure 7.8** is given in

Figure 7.9. The presence of C, Si, and Ti is also evident in this spectrum, mirroring observations from the preceding analysis (**Figure 7.5**).

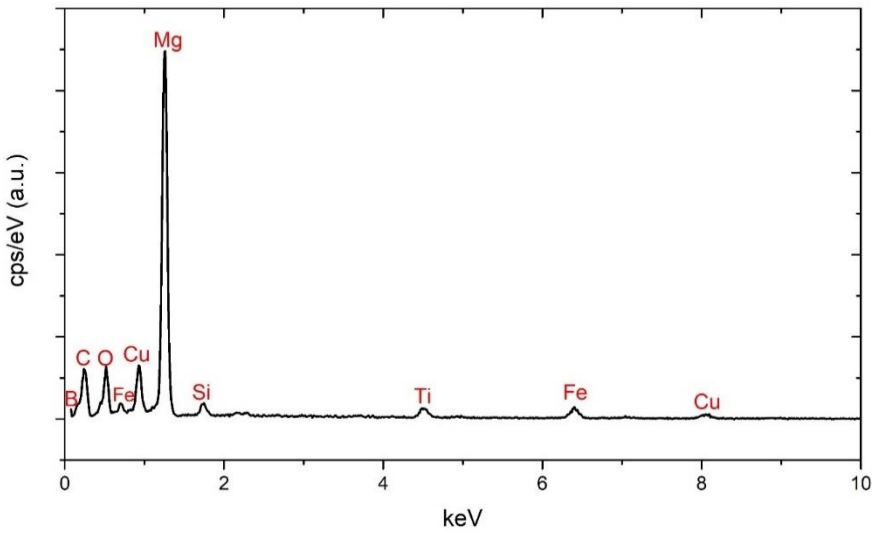

Figure 7.9 *The EDX spectrum of the red dotted circular area given in* ***Figure 7.8***

Additionally, Fe is detected here, contrasting with the spectrum provided in **Figure 7.5**. This presence can be attributed to the inadvertent smearing of steel from the outer sheath of the case during the polishing process, as indicated by the Fe accumulation shapes depicted in **Figure 7.8**, where Fe particles appear to fill voids and manifest as localized clusters. In contrast to **Figure 7.5** the intensity of Cu peaks is notably diminished in this spectrum thanks to the etching. However, the persistence of Cu after etching suggests that the 10-minute etching duration may have been insufficient. Discrete localizations of Cu may indicate the presence of Cu precipitations at the interface. Conversely, continuous Cu presence, particularly inside and outside the wire as highlighted by arrows, may suggest Cu diffusion. Nevertheless, this observation is pivotal in assessing the efficacy of the heat treatment regime in achieving a smooth interface between the smaller filaments and the filler material using same joint making methodology discussed in Chapter 6. Additionally, an amount of oxygen is evident as seen at the other MgB_2 interfaces presented previously, likely stemming

from the polishing and the etching process, which could lead to oxidation on the outside of the Nb barrier.

Subsequently, a coil was produced in accordance with the procedure outlined in section 3.1.5, followed by etching the wire with 35% concentrated HNO_3 for 20 minutes. The remaining steps of the procedure remained consistent with those outlined in the corresponding method section. Upon completion of coil measurements (outlined in the next section), the joint was deliberately ripped off from the coil and subsequently sectioned for SEM investigation.

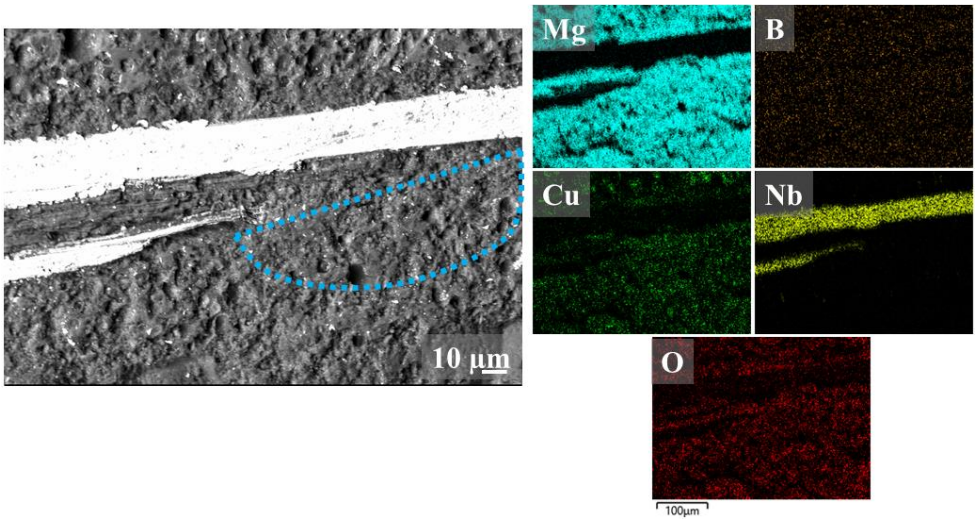

Figure 7.10 *The interface BSE image and EDX maps of the joint which was detached from the coil.*

Figure 7.10 displays the interface of the joint detached from the coil and a smooth interface, akin to that observed in **Figure 7.8**, is evident. However, despite the 20-minute etching process, traces of copper persist, albeit with significantly reduced peak intensities, as depicted in **Figure 7.11**, corresponding to the blue circular region highlighted in **Figure 7.10**.

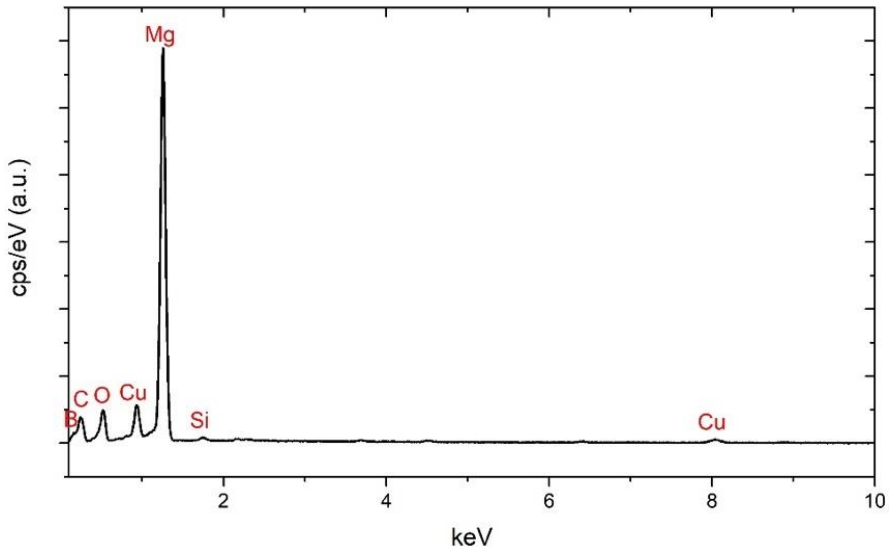

Figure 7.11 *EDX spectrum of the area highlighted in* ***Figure 7.10***

A homogeneous presence of Cu at the interface may indicate that Cu has diffused into MgB_2. Additionally, the presence of small Cu clusters suggests the possibility of local Cu precipitations. While one of the filament/filler interfaces exhibited a smooth interface, the status of the remaining interfaces between the filaments and the filler are unknown. Therefore, if these interfaces were poor, they could potentially affect the T_c profile (resulting in high ΔT_c) and contribute to residual resistance, as investigated in subsequent section.

7.2.3 Low current transport T_c measurements on short joints

After implementing the jointing process devised for the reacted monofilament wires outlined in Chapter 6 to join the reacted multifilament wires, low current transport measurements was conducted to those joints using a current of 0.1 A, following the procedure outlined in section 3.3.5. **Figure 7.12** illustrates the normalized resistance versus temperature plots of the joints. The red and blue curves represent the joints between reacted multifilament wires, while the black curve depicts the T_c transition of the joint between reacted monofilament wires, sample 1a shown in **Figure 6.8**. Specifically, the red data curve corresponds to the joint showcased in **Figure 7.4**, exhibiting minimal transition compared to other samples. However, two small transitions are faintly discernible shown by arrows.

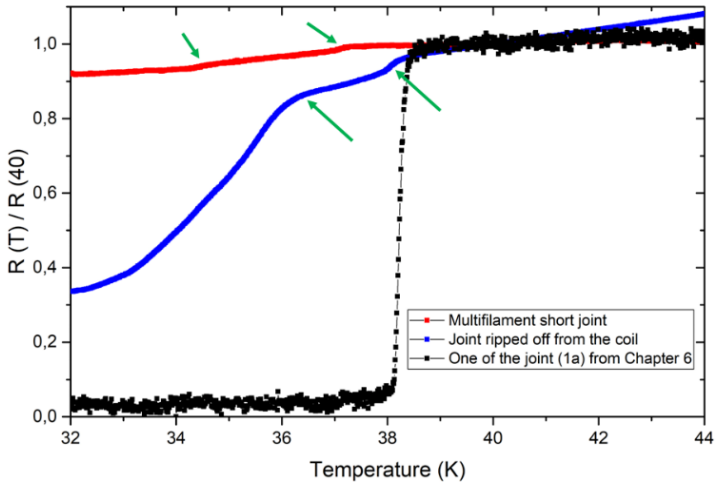

Figure 7.12 *The low-current transport measurement results of the joints are as follows: the red data points represent the short joint produced by the reacted multifilament wires, with its SEM image provided in* ***Figure 7.4****; the blue data points depict the joint that was detached from the coil, accompanied by its SEM image in* ***Figure 7.10****; and the black curve correspond to the joint between reacted monofilament wires introduced in Chapter 6, as shown in* ***Figure 6.8****. Green arrows are showing the transitions.*

Reason for the elevated resistance is evident from its SEM image (**Figure 7.4**), revealing a lack of connection between filaments and the filler. Conversely, the blue curve corresponds to the sample featured in **Figure 7.10**. Its transition is superior to the red curve, indicating a connection between the wire and the filler. However, residual resistance persists below the T_c, and the ΔT_c is broader (~5.6) compared to the black curve. Two transitions may arise from differences in manufacturers: the multifilament wire has a T_c of approximately 35 K, while the Epoch wire (representing the case filler) has a T_c of about 38 K as illustrated in **Figure 7.3**. Therefore, the first transition may signify the superconducting state of the case, while the wires remain non-superconducting. Regarding residual resistance, if the connection between the filaments of one wire and the filler is inadequate, additional resistance may occur, increasing the residual resistance. Managing all filaments effectively poses a significant challenge in joints made with multifilament wires, compounded by the inability to individually inspect each filament.

7.2.4 Resistance and I_c measurements of the coil

After the completion of the short joint production and low current transport measurements, the subsequent procedure involved the fabrication of a coil, as detailed in section 3.1.5 and as shown in **Figure 7.13**. The SEM images and EDX maps of the interface between the filament and the filler is depicted in **Figure 7.10** and its low current transport measurement performance is given in **Figure 7.12** with blue curve.

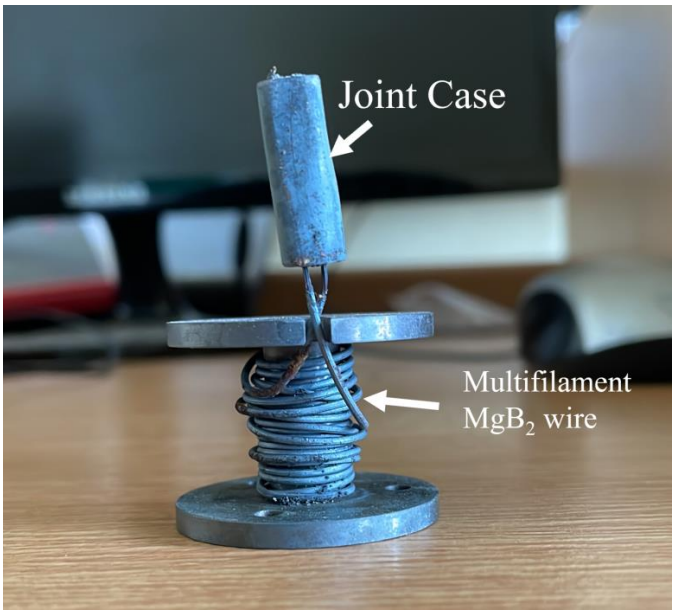

Figure 7.13 *A jointed loop coil prepared by MgB_2 multifilament wire.*

Initially, the unreacted wire was wound around the coil and subjected to heat treatment at 700°C for 15 minutes. The rationale for this action was previously discussed in Chapter 6, specifically concerning the limited bending radius of the reacted wires. Following this, the wire ends underwent etching with 35% concentrated HNO_3 for 20 minutes. Subsequently, the filaments were gently scarfed and inserted into the pre-drilled holes of the case, followed by a gentle pressing for 10 minutes. The joint was then subjected to heat treatment at 900°C for 30 minutes, followed by 650°C for 1 hour. Thereafter, the coil underwent testing utilizing the IRT measurement outlined in section 3.3.6. The specification of the coil is given in **Table 7.2**.

Table 7.2 *The specifications of the coil include the determination of inductance using the long solenoid approximation.*

Coil inner radius	*r*	6 mm
Coil outer radius	*R*	7 mm
Number of turns	*N*	20
Coil length	*l*	20 mm
Inductance	*L*	2.8 x 10^{-5} H

The result of this test is presented in **Figure 7.14**.

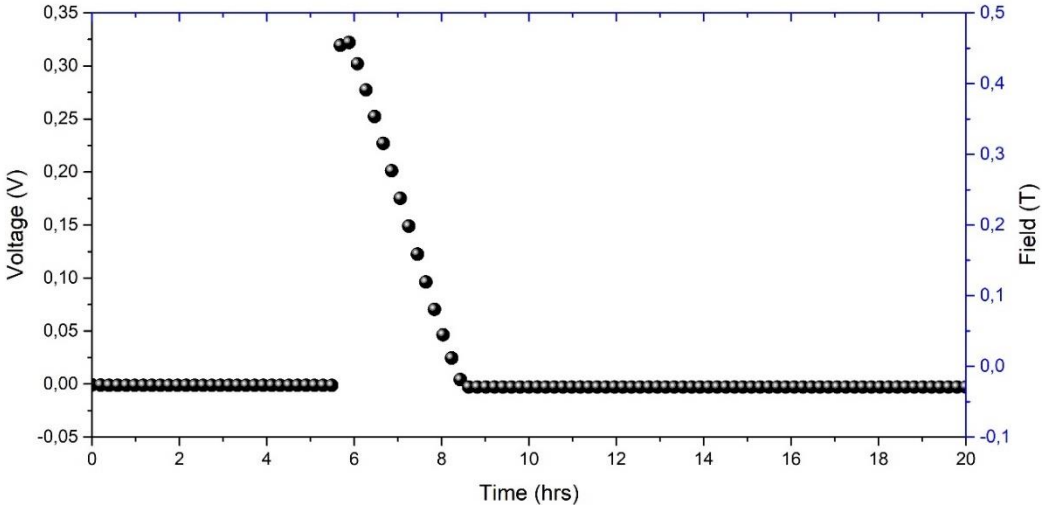

Figure 7.14 *Inductive resistance testing data of the coil under 20 K and self-field.*

Approximately 0.5 T of external magnetic field was applied to the coil using the MFM under 20 K, as outlined in section 3.3.6. The temperature was set to 20 K for the purpose of comparing the potential results with the joint introduced in Chapter 6. The voltage was then measured using a Hall probe situated inside the cryostat. Subsequently, the results were assessed and analysed using equation (3.3). Unfortunately, no trapped current was detected, as the voltage dropped to zero upon removal of the external field.

Although one of the interfaces appears satisfactory, it is evident that excessive resistance persists in the joint, likely due to poor quality of the interfaces between other filaments and the filler. Additionally, as evident in the blue curve depicted in **Figure 7.12**, two T_c

transitions and a considerable amount of residual resistance are observed. The dual transitions may be attributed, as previously discussed, to mismatches between the case and wire materials. Therefore, ensuring similarity in the characteristics of the case and wire in the joint to be made may be important. Further research into this procedure is warranted, as it shows promise but requires additional investigation.

This chapter provides key insights into the interfaces and performance of joints and coils made from reacted multifilament MgB_2 wires. Microstructural analysis revealed challenges in achieving smooth interfaces, with residual copper and voids affecting uniformity. Consequently, copper was significantly reduced through etching, leading to improved material compatibility. Low-current transport tests on non-etched joints indicated high resistance and poor superconducting transitions, whereas etched joints showed improved performance with lower resistance and dual T_c transitions, suggesting partial connectivity.

7.3 Conclusions

The experimental results provided key insights into the joints' interfaces and the performance of coils fabricated using reacted multifilament MgB_2 wires. Microstructural analysis revealed challenges in achieving smooth interfaces between filaments and filler material, with residual copper and voids indicating issues with uniformity and continuity. Efforts to remove copper through etching significantly reduced its presence.

Low-current transport measurements on short joints (without etching) showed minimal transition and elevated resistance, suggesting poor filament-filler interface quality and incomplete superconducting behaviour. Joints using etched wires displayed improved performance with residual resistance and dual T_c transitions, indicating some successful filament connections but also material mismatches between the case and wire.

These findings highlight the need for optimization in the joint-making process, particularly in enhancing filament-filler interface integrity and material compatibility. As part of further work, it may be considered to create joints using MgB_2 fillers with wires made from the same material. Specifically, it is advisable that if a wire is produced with a particular Mg+B composition under specific conditions, the filler material inside the case should also be manufactured under the same conditions. Otherwise, as observed in this study, two different critical transition temperatures may be encountered.

Chapter 8 Bi-2212 - MgB_2 Dissimilar Joint Production Processes

8.1 Introduction

Heine et al. [257] produced the first high-temperature superconductor wire in 1989, Bi-2212 ($Bi_2Sr_2CaCu_2O_8$). However, it was not suitable for high-field applications until 2014 when the Bi-2212 processing technology under hyperbaric oxygen pressure was developed by Larbalestier et al.[258], making it suitable for high-field (> 30 T) magnet applications. Bi-2212 is particularly well-suited for high-field magnets because it can be manufactured as round wire, which is preferred by magnet designers and builders. Unlike other high-temperature superconductors like YBCO ($YBa_2Cu_3O_7$) and Bi-2223 ($Bi_2Sr_2Ca_2Cu_3O_{10}$), which are available only as flat tapes, Bi-2212 round wire offers greater versatility in terms of architectural configurations, ease of cabling, and isotropic electromagnetic properties along its length [259].

Bi-2212 round wire manufacturing begins with a precursor powder, which is shaped into wire using the PIT process. Silver is chosen for the tube material due to its non-reactivity with Bi-2212 components, resistance to oxidation at high temperatures (900°C), and permeability to oxygen, optimizing the oxygen content in the superconducting phase. The as-drawn PIT Bi-2212 wire is not superconducting and requires heat treatment to form aligned, connected grains capable of carrying supercurrent. Coils made with this wire undergo a "wind-and-react" process, where they are wound with the as-drawn wire and then heat treated due to wire brittleness post-treatment, preventing direct coil winding.

Bi-2212 round wires hold promise for MRI/NMR applications like MgB_2 and Nb-Ti. Yet, creating low-resistance joints between Bi-2212 wires poses a significant challenge. In MRI scanners, the entire magnetic circuit requires resistance values below 10^{-12} Ω for persistent

mode operation. Several methods, such as soldering with PbBi [260] and Pb-free solders [261, 262], as well as powder-in-tube melting processing [263], are explored for achieving low-resistance joints between Bi-2212 wires.

In this chapter, I explored the possibility of using MgB_2 as a filler joint material between Bi-2212 wires, a novel approach not found in existing literature. The primary focus was to investigate the chemical compatibility of the interface between Bi-2212 and MgB_2 during joint heat treatment. Additionally, I examined whether the joint-making strategy introduced in Chapter 6 could be applied to Bi-2212 multifilament wires using an MgB_2 case. The chapter begins with a detailed overview of the experimental procedures, followed by a discussion on the wire characteristics used for joint fabrication. Subsequent sections cover the characterization and test results, including SEM, EDX, T_c, and joint resistance analyses.

8.2 Experimental details

The experimental procedure for fabricating joints between reacted multifilament Bi-2212 wires follows a methodology similar to that used in previous chapters (Chapter 6 and Chapter 7), as outlined in section 3.1.4. Initially, wires obtained in a reacted form were scarfed at the ends. Pre-drilled holes in unreacted MgB_2 cases were partially loaded with Mg+B powders in a 1:2 stoichiometric ratio to ensure contact with the filaments' ends and MgB_2. Scarfed Bi-2212 wires were then inserted into these holes, and a pressure of 1.7 MPa, similar to MgB_2 joints, was applied. The assembly underwent heat treatment at 700°C for 15 minutes, based on prior optimization for Epoch-made MgB_2. Resistance and T_c transition measurements were conducted on short joints through low current transport measurement to determine the optimal method before preparing jointed loop coils, ensuring efficient wire usage.

In the coil making process, the wire was initially obtained in its unreacted state and wound around the former, as detailed in section 3.1.5.2. It then underwent heat treatment under a box furnace, using the W&R method. This method was applied to prevent wire breakage or damage during winding, considering the brittleness of the reacted Bi-2212 wire and the smaller diameter of the former used. After that, the wire ends were gently polished using a grinding wheel. Mg+2B powder was added into the holes, and wires were inserted into the pre-drilled case and subjected to heat treatment using a tube furnace at 700°C for 15 minutes. Following this, two short joints were acquired, one of which was detached from the coil, while the other was created as a short joint utilizing the thermal treatments described above. The samples underwent characterization, followed by analysis of their resistance and T_c data. Subsequently, inductive resistance testing was performed.

8.2.1 Wire characteristics used in the joint

The winding of a small Bi-2212 superconducting coil and the fabrication of the short joint utilized Bi-2212 multifilament round wire obtained from Bruker-OST. The specifications of the wire are detailed in **Table 8.1** and a cross-sectional SEM image of the reacted Bi-2212 round wire is provided in **Figure 8.1**. The optimized heat treatment procedure for the unreacted Bi-2212 wire involves heating to 895°C for 0.5 h, followed by final annealing at 835°C for 60 h in an oxygen flow of 600 cm^3 min^{-1}. This heat treatment procedure provided the best J_c performance according to the literature [264, 265].

Table 8.1 *Bi-2212 wire specifications* [266].

Number of Filaments	55 × 18
Stabiliser	Ag
Diameter of the wire	~ 0.9 mm
Filament size	~ 12 μm
J_e (4.2 K, 5 T)	~ 1400 A mm^{-2}

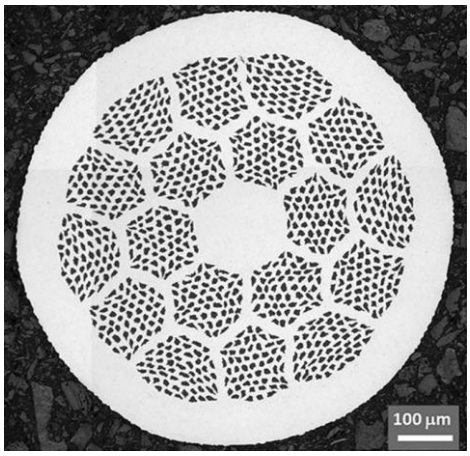

Figure 8.1 *The cross-sectional SEM image depicts the reacted 55 × 18 (it indicates there are 18 bundles each containing 55 filaments) filament Bi-2212 manufactured by Bruker-OST* [266] *(Copyright © 2023, IEEE). White regions are Ag and blacks are Bi-2212.*

To prepare the short joint, the wires were first cut into small pieces, each measuring 2 cm in length. Subsequently, the steps for joint fabrication were carried out in accordance with the procedures detailed in section 3.1.4. In the preparation of the coil, the wind and react method was employed. The joint was positioned within the reacted coil using the procedure delineated in section 3.1.5, followed by the heat treatment.

8.2.2 Effect of heat treatment on wire/case interface

The primary focus is on assessing the suitability of applying this heat treatment method (700°C for 15 minutes) to Bi-2212 joints. As a result, samples underwent microstructural analysis following the transport measurements. The sample preparation procedures for the SEM characterisation followed the same guidelines outlined for previously introduced joints.

Figure 8.2 illustrates the wire-filler interface of the short joint at low magnification. The area marked by white dots represents a part of the drilled section of the case, which was filled with Mg+2B powder just before the heat treatment and prior to inserting the wires into the holes. It was observed that the wire did not fit snugly into the hole completely, and the powder in that area was not as compact as the MgB_2 filler.

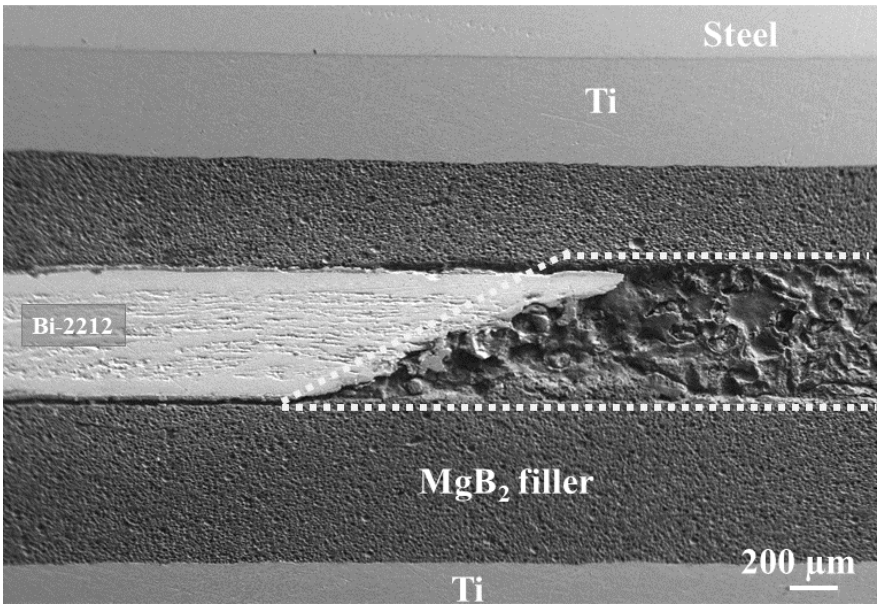

Figure 8.2 *SEM image of a typical region of the interface between MgB_2 filler and the Bi-2212 wire.*

Thoroughly compacting the Mg+2B powders subsequently poured into the holes and firmly inserting the Bi-2212 wires into the holes can enhance the connection between the wire and the MgB_2 filler. Upon examining the wire-case interface, **Figure 8.3** displays SEM (a-b), BSE (c-d) images, and EDX maps of two distinct regions. **Figure 8.3**c corresponds to the BSE image of a, while **Figure 8.3**d corresponds to the BSE image of b. Demonstrating both imaging modes is crucial, especially since voids may not be readily discernible in BSE images. However, distinguishing between phases can be challenging in SEM images. The presence of Bi, Sr, and Cu outlines the position of the Bi-2212 filaments, as indicated by solid white arrows in the Cu map of **Figure 8.3**a-c. Yet, direct evidence of the filament-case filler interface is lacking due to the need for higher magnification. Oxygen abundance at the interface is notable, as depicted in the O maps of both regions. During heat treatment, Mg+2B powder is susceptible to oxygen, as Mg readily reacts with oxygen even at low temperatures as discussed in section 2.4.3.1. A small oxygen cluster highlighted in **Figure 8.3**a-c indicates this susceptibility. An EDX spectrum of this area revealed 43.94% B, 32.81% O, and 21.39% Mg suggesting the presence of Mg-B-O compounds at the interface (as previously seen in section 4.2.2).

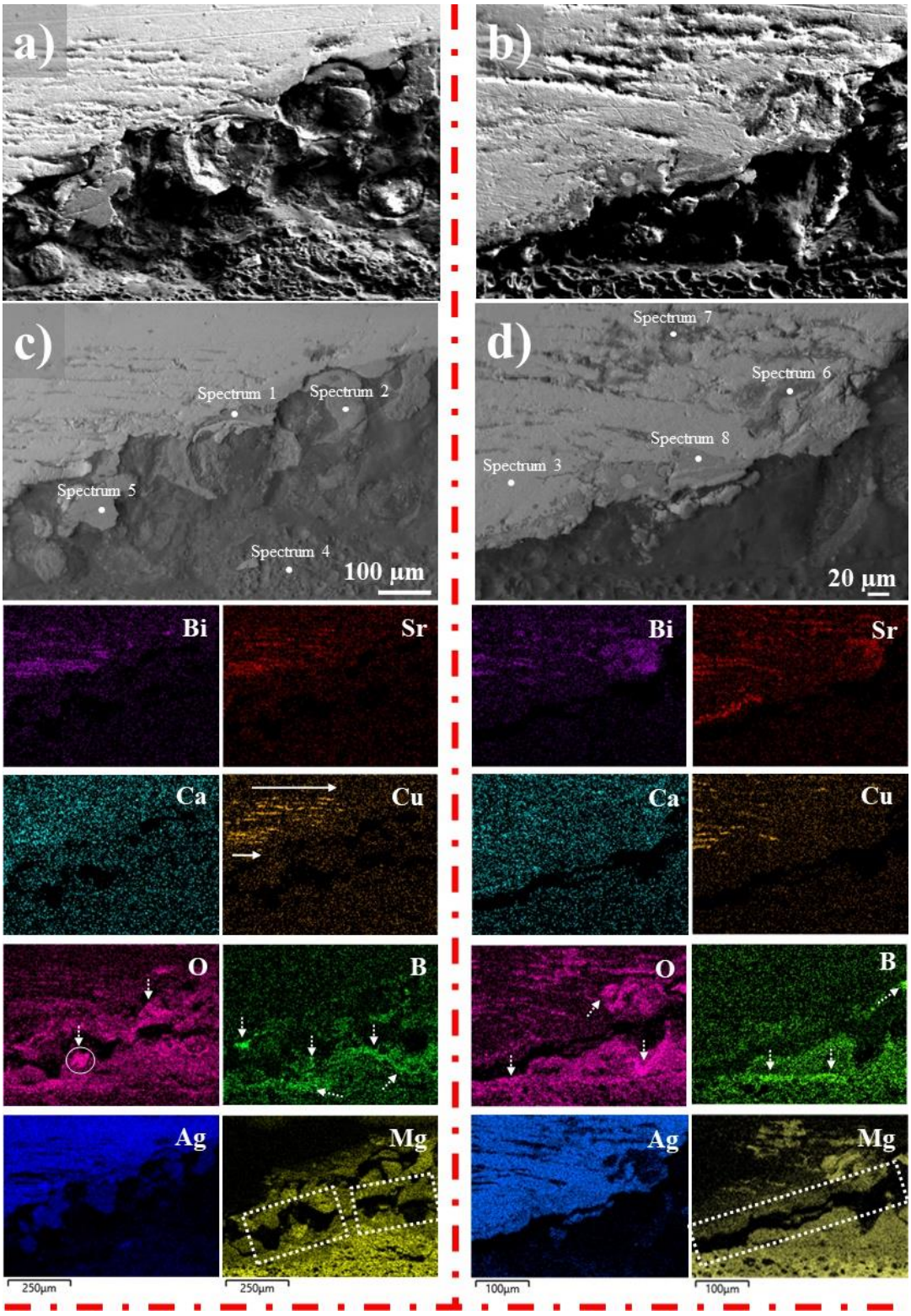

Figure 8.3 *SEM (a-b) and BSE images (c-d) of two distinct interface regions, accompanied by EDX maps of these interfaces. In BSE images, white represents Ag, dark blacks denote voids, black indicates MgB_2, and greys represent different phases (refer to the text for details). Solid arrows indicate the position of Bi-2212 filaments, dashed arrows denote clusters of corresponding atoms and dashed rectangles showing gaps.*

The dashed rectangles shown in the Mg maps signify voids, a feature discernible upon inspection of the SEM images (a-b). Additionally, these voids imply either incomplete insertion of the wire due to the narrow-drilled hole or hindrance from the added Mg+2B powder preventing further wire insertion. Pushing the wire further into the holes to compress the powder may serve as potential solutions to address this issue.

When considering the various phases observed in the BSE images in both images c and d, the point analysis spectra were labelled as 1, 2, 3, 4, 5, 6, 7 and 8, and their EDX spectrums are provided in **Figure 8.4**. The rationale behind specifically selecting these regions is that Spectrum 1 represents the interface, while Spectrums 2 and 5 are located inside the filler close to the interface, Spectrums 3 and 4 are control points for Ag sheath of the wire and the MgB_2 filler inside the case respectively. Spectrums 6, 7 and 8 are located slightly further inside the wire. Therefore, gaining insight into these distinct regions could elucidate potential reactions that occurred between the wire and the filler.

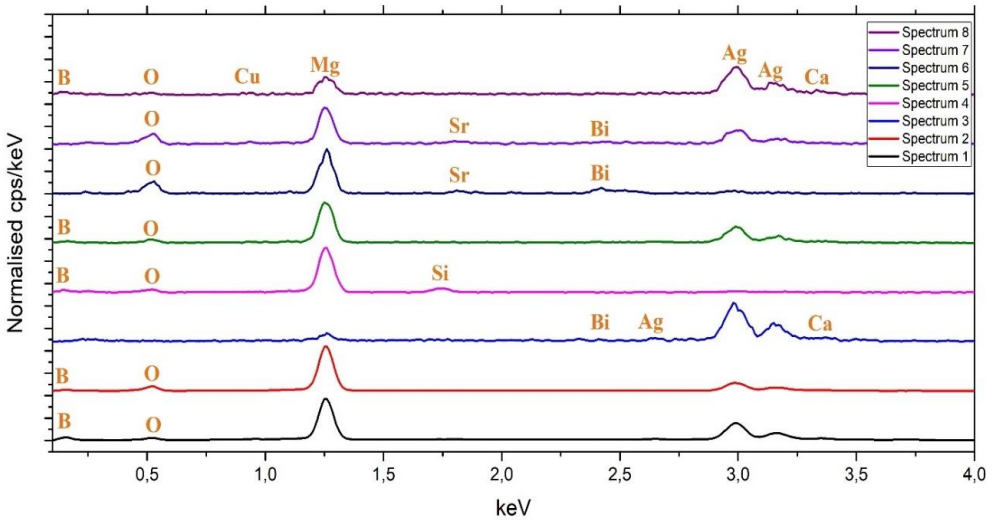

Figure 8.4 *The spectrum of elements obtained from EDX point analyses of the regions depicted in* ***Figure 8.3****a-b*

The atomic percentages of those elements that were obtained from the Aztec software is given in **Table 8.2**. Additionally, the software-reported error for each element in each spectrum for this sample is less than ± 0.20% and is not indicated in the table.

Table 8.2 *Atomic fractions of the spectrums. Note that impurities such as C and Si were detected but not included to the table.*

Spectrums	Atomic %							
	Bi	**Sr**	**Ca**	**Cu**	**O**	**B**	**Mg**	**Ag**
1	0.17	0.1	0.36	0.37	9.8	50.7	27.4	11.2
2	-	-	0.1	-	23.6	28	40.3	7.8
3	-	-	0.2	-	18.6	-	13.8	67.4
4	-	-	-	-	8.3	64.6	25.8	1.3
5	0.13	-	0.13	0.6	15.3	43	30	11
6	2.77	1.77	0.6	0.21	49.8	-	42.1	2.76
7	0.44	1.2	0.9	1.9	48.7	-	34,7	12.2
8	1.1	1	-	2.9	21	-	32.8	41.2

In spectrum 1, prominent peaks of B and Mg are evident, accompanied by observable Ag peaks alongside O, suggesting the significant presence of MgB_2 with oxygen. However, the structure lacks the typical porous appearance of MgB_2 and appears dense, indicating a potential Mg-Ag reaction.

In spectrum 2, there's a notable presence of Mg and approximately half the quantity of B compared to spectrum 1. Oxygen concentration appears elevated, while Ag quantity is slightly diminished. The region appears slightly darker, possibly due to lower Ag presence. The reduced B quantity and increased Mg, along with oxygen, may suggest a reaction between Mg and O.

Spectrum 3 serves as the control point, representing the silver sheath. Oxygen presence may result from both polishing and Bi-2212 filaments. Notably, Mg is present, possibly due to Mg diffusion into Ag, forming an Mg-Ag alloy. Mg comprises approximately 18% of the

region's atomic composition, while Ag constitutes around 82%. Consulting the Mg-Ag phase diagram (**Figure 8.5**) suggests the plausible formation of the Ag_3Mg. Despite monovalent Ag's limited solubility in divalent Mg, divalent Mg exhibits greater solubility in Ag favoured by the atomic size alignment, albeit constrained by valency differences.

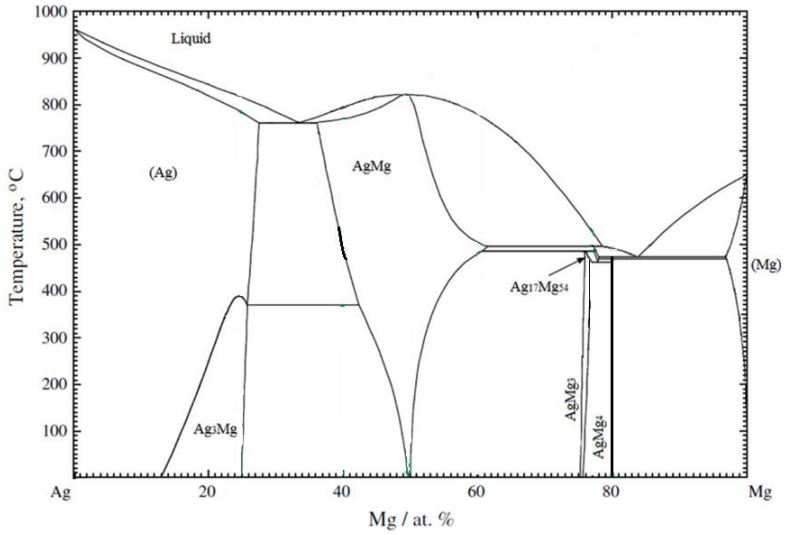

Figure 8.5 *Binary phase diagram of Mg-Ag* [267] *(Copyright © 2021, Elsevier Ltd.)*

Spectrum 4, like Spectrum 3, serves as a control, originating from the MgB_2 filler inside the case. Expectedly, it exhibits notable amounts of Mg and B, alongside oxygen. Oxygen presence within the filler is inevitable due to trapped air during powder pouring into holes and oxygen introduced during polishing.

Spectrum 5, dominated by B and Mg, also shows noticeable Ag presence, alongside oxygen. This suggests the presence of MgB_2 accompanied by silver. However, the topography differs from typical porous MgB_2 regions, as seen in Spectrum 2, hinting at a denser structure possibly containing an Ag-Mg compound.

Spectrums 6 and 7 stand out as the darkest regions within the wire in the BSE image (d). Spectrum 6 reveals notably high levels of Mg alongside oxygen, with ratios of 42% and 50%, respectively. Similarly, spectrum 7 shows significant levels of Mg and O, with a notably higher presence of Ag compared to spectrum 6. Oxygen levels remain consistent,

while magnesium concentration decreases discernibly, with no overlap of peaks observed. SEM examination of the region in **Figure 8.3**b reveals that spectrums 6 and 7 are within voids. Trace amounts of Bi and Sr suggest these voids may have been filaments originally, possibly losing powder during polishing. While these voids may have been filled with MgB_2 during polishing, the absence of B in those regions is noteworthy. Detection of Mg in inner wire regions, especially in these areas, is significant.

Spectrum 8 indicates another region suggesting potential formation of a Mg-Ag alloy, with an atomic percentage of 41% for Ag and 32.8% for Mg. Referring to the binary phase diagram of Mg-Ag in **Figure 8.5**, it's plausible that an AgMg alloy may have formed in that region.

Subsequently, the joint detached from the coil was examined. Significantly, less additional Mg+2B powder was used, with wires inserted into the holes to maximize powder compression. Following prescribed joint-making procedures and the designated heat treatment regimen, a detailed examination of the interface microstructure was conducted.

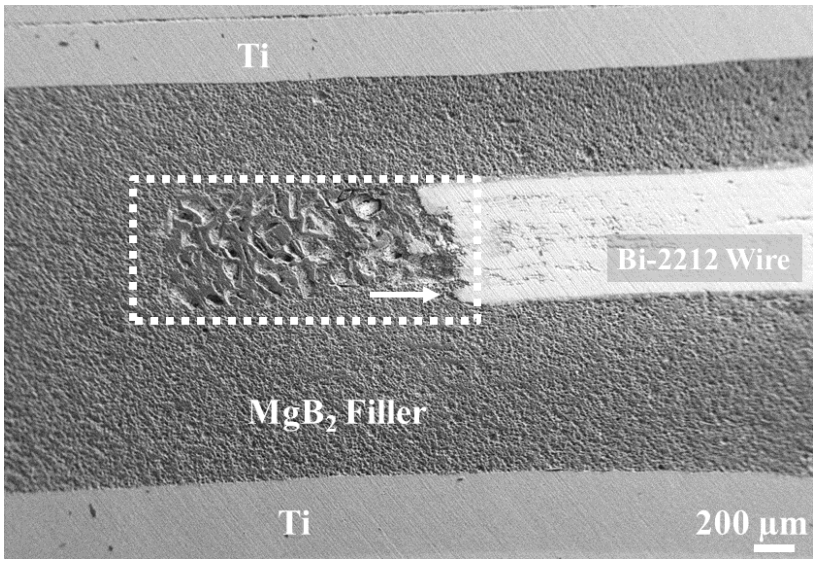

Figure 8.6 *SEM image of the joint that was ripped off from the coil.*

Figure 8.6 shows the wire placement within the pre-drilled case. The area with pre-added Mg+2B powder, marked by dashed rectangles, appears slightly denser compared to the

preceding joint in **Figure 8.2**. However, it seems that the wire did not fully penetrate the final segment of the hole due to the hump indicated by the white arrow. To address this issue, slight expansion of the holes could facilitate wire insertion.

Figure 8.7 displays the interface of the joint detached from the coil, showcasing its SEM(a) / BSE(b) images and EDX maps. Compared to the short joint in **Figure 8.3**, this interface demonstrates improvements in powder compaction and a reduction in large voids. Notably, there is no significant cliff-like feature observed at the interface, unlike in the previous joint.

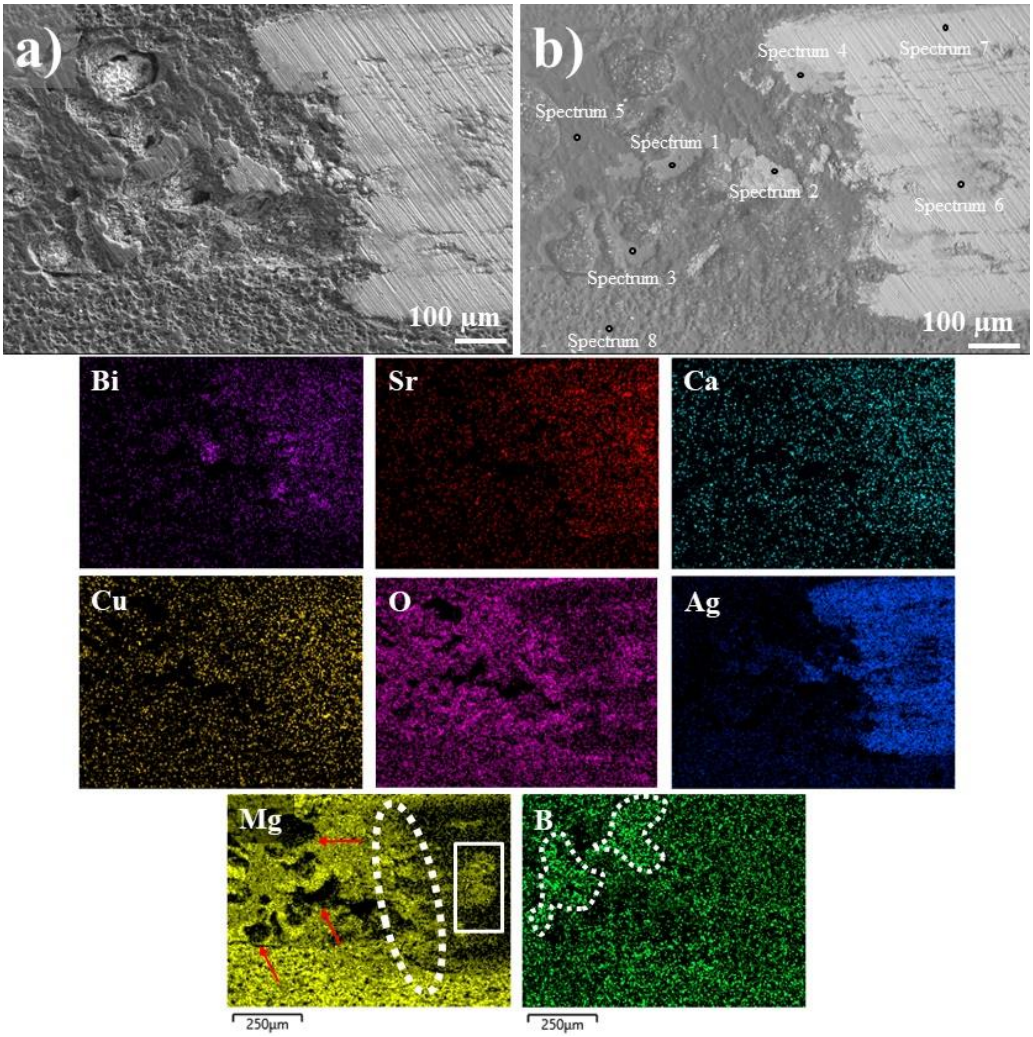

Figure 8.7 *SEM (a) and BSE (b) images illustrating the interface of the joint detached from the coil, accompanied by EDX maps.*

However, local voids within the MgB_2 filler are noticeable, and a notable amount of Mg is detected just inside the wire, suggesting potential Mg diffusion. Additional phases are also

present, warranting further investigation to identify any deviations from the previous joint. Point spectrums were marked on the BSE image to facilitate detailed analysis. Control points, identified as Spectrums 7 and 8, represent the Ag sheath and MgB_2 filler, respectively. Spectrums 1, 2, 3, and 5 are positioned within the filler, with 1, 2, and 3 closers to the interface. Spectrums 4 and 6 are situated within the wire, showcasing noticeable differences. Further details on the spectrums can be found in **Figure 8.8**, while corresponding atomic fractions are listed in **Table 8.3** for each spectrum. The error rates for B are notably high across several spectra. These elevated error levels indicate significant measurement uncertainty for B, which could compromise the accuracy of its detected concentration.

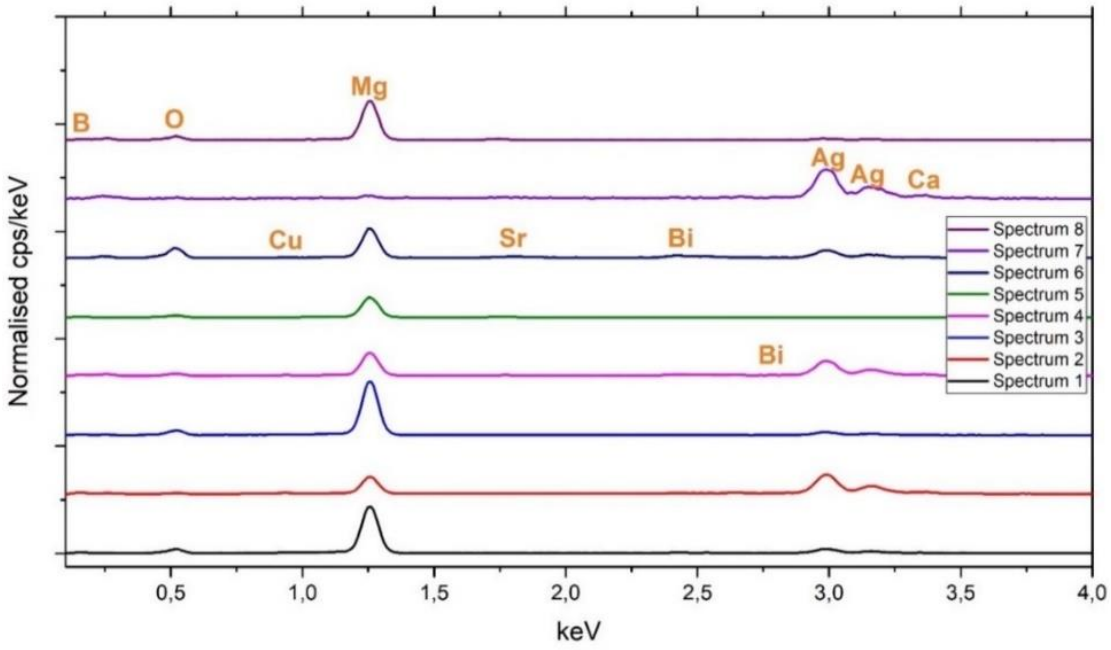

Figure 8.8 *Atomic fractions of the point analysis shown in* ***Figure 8.7***

In spectrum 1, positioned within the MgB_2 filler and in proximity to the interface, a notable contrast difference is observed, appearing denser compared to its surroundings. It reveals an atomic percentage of 50.4% for Mg, 22.36% for B, 21% for O, along with 5% for Ag. This spectrum bears resemblance to Spectrum 2 previously depicted in **Figure 8.3**, suggesting consistency of this phase at the interface.

In spectrum 2, an atomic percentage of 34% for Mg, 15.4% for B, and 14.7% for O is observed, along with a notably high amount of Ag at 33.4% atomic concentration, contributing to the region's brighter appearance.

Table 8.3 *Atomic fractions of the spectrums of the joint that ripped off from the coil. Note that impurities such as C and Si were detected but not included to the table.*

Spectrums	**Atomic %**							
	Bi	**Sr**	**Ca**	**Cu**	**O**	**B**	**Mg**	**Ag**
1	-	-	-	0.3	21.28	22.36	50.4	5.3
***Error* ± %**	-	-	-	*0.24*	*0.73*	*3.35*	*1.92*	*1.02*
2	0.6	-	-	2.0	14.7	15.4	33.9	33.4
***Error* ± %**	*0.29*	-	-	*0.21*	*0.3*	*0.93*	*0.23*	*0.8*
3	-	-	0.1	0.3	25.9	7.8	61.4	4.38
***Error* ± %**			*0.12*	*0.26*	*0.95*	*4.4*	*2.75*	*1.01*
4	1.0	-	0.2	0.9	27.9	-	43.8	26.2
***Error* ± %**	*0.4*	-	*0.11*	*0.25*	*0.4*	-	*0.28*	*0.52*
5	-	-	0.17	-	18.2	37.8	43.8	-
***Error* ± %**	-	-	*0.2*	-	*1.5*	*5.7*	*4.4*	-
6	1.33	0.57	0.6	0.5	53.9	-	34	9.1
***Error* ± %**	*0.5*	*0.3*	*0.13*	*0.3*	*0.5*	-	*0.4*	*0.5*
7	0.9	0.24	0.18	0.5	23	-	6.3	68.9
***Error* ± %**	*0.21*	*0.3*	*0.13*	*0.2*	*0.41*	-	*0.52*	*0.32*
8	-	-	0.37	-	21.2	16.6	58.5	2.7
***Error* ± %**	-	-	*0.21*	-	*0.43*	*2.5*	*0.62*	*0.23*

This point is situated relatively close to the wire, which likely accounts for the elevated Ag content. Spectrum 2 can be compared to Spectrum 5 in **Figure 8.3**; however, the Ag content here exceeds that of Spectrum 5. Interestingly, this region appears as an isolated island, indicating no direct connection to the wire sheath, the primary source of Ag. It is conceivable that this portion may have been transferred to the interface from the wire during the polishing process, given its similarity in Mg and Ag concentrations to Spectrum 4 in **Figure 8.7**b, which was obtained from the wire. As proximity to the wire increases, the Ag content is observed to rise as expected. Additionally, it is noteworthy that Mg is also present along with Ag to a certain extent within the wire, as indicated by the solid white rectangle in the Mg map.

In spectrum 4, located within the wire and close to the interface, a distinct contrast is evident. It bears resemblance to a Mg-Ag alloy, akin to spectrum 8 observed in **Figure 8.3**, given the substantially higher concentrations of Ag and Mg at 26.2% and 43.8% atomic percentages, respectively. This observation may suggest that at the very ends of the wire, Mg reacts with the Ag sheath, resulting in the formation of various Ag-Mg alloy configurations contingent upon the concentration of these atoms.

In spectrum 5, located within the MgB_2 filler and notably distant from the interface, an intriguing observation is made: the topography appears dense, lacking the typical porous nature associated with MgB_2. These regions with denser appearance exhibit elevated concentrations of B, as highlighted by the white dashed regions in B map along with O. This may suggest that nonstoichiometric Mg-B-O may be the primary compound in this region. As discussed in Chapter 4, an increase in the amount of Mg typically corresponds to an increase in porosity; however, in this case, the denser regions with higher B concentrations display fewer pores.

Spectrum 6 is positioned within the wire, displaying a distinct contrast compared to its surroundings. A notable presence of oxygen is detected at 54% atomic concentration, while Mg comprises almost 34% atomic concentration, with no detection of B. Interestingly, the concentration of silver is remarkably low, even within the wire. This observation may indicate that Mg located at the interface potentially diffused through the filaments and reacted with oxygen. Additionally, Bi, Sr, Ca, and Cu were identified with deviated ratios. The presence of a specific quantity of oxygen could potentially originate from the Bi-2212 ceramic.

Spectrums 7 and 8 serve as the control points for the Ag wire sheath and the MgB_2 filler, respectively. They have demonstrated atomic fractions approximately in line with the expected values for their respective locations.

In summary, various phases have been observed, particularly in the vicinity of the interface. Additionally, it is evident that at the initial segments of the Bi-2212 wire ends, Ag reacts with Mg, resulting in distinct contrasts in BSE images. The formation of these alloys depends on the atomic concentrations present during these specific reactions.

8.2.3 Low current transport T_c measurements on short joints

The low current transport measurement of both the short joint and the joint ripped off from the coil is conducted to determine their T_c properties. The short joint, illustrated in **Figure 8.9**a, is situated on the sample holder as depicted in **Figure 8.9**b. Subsequently, it undergoes measurement in accordance with the procedures delineated in Section 3.3.5. The resulting transport measurement outcomes are presented in **Figure 8.9**c-d. The lines represent the approximate T_c transitions of the samples determined as the first deviation of the curves. The 1st and the 2nd lines indicate the first T_c transitions of the short joint and the joint detached from the coil with values approximately 84 K and 80 K, respectively.

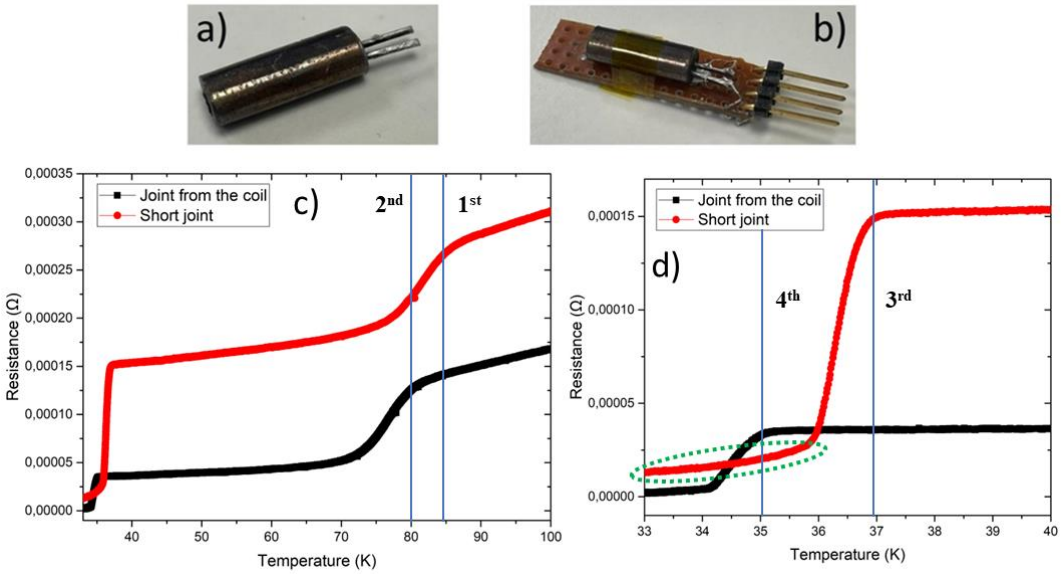

Figure 8.9 *Bi-2212-MgB_2 joint making attempt: a) reacted Bi-2212 wires inserted inside pre-drilled holes in the MgB_2 case, b) the joint mounted to the sample holder for low current transport measurement, c) transport measurement results showing T_c transitions, d) T_c transitions of the MgB_2 fillers.*

The 3rd and 4th lines denote the second stage T_c values of the short joint and the detached joint from the coil, with values approximately 37 K and 35 K, respectively. The reason for the resistance drops in both the 1st and the 2nd lines are attributed to the high T_c value of the Bi-2212 wires. As a result, when the system reaches the T_c of the MgB_2 filler material, its resistance diminishes, and the remaining resistance typically arises from non-superconducting compounds at corresponding temperature, along with voids that impede the flow of supercurrent along the current path. The most probable location for these insulating phases is the Bi-2212/MgB_2 interface, as discussed in the previous section.

As observed in **Figure 8.9**d, the residual resistance of the short joint below the T_c of the MgB_2 is higher than that of the joint detached from the coil as highlighted by green dashed circle. This difference may be attributed to the significant cliff at the interface and the additional by-products in the short joint, as discussed in **Figure 8.3**. Conversely, similar by-products have been observed in the cut joint, yet the residual resistance is nearly zero, indicating the successful establishment of a superconducting current path between Bi-2212

filaments and the MgB_2 filler. It is crucial to emphasize that the voltage sensor's sensitivity in the low-current transport measurement system is not exceedingly high. It can detect the voltage corresponding to a minimum resistance of approximately 10^{-6} Ω (see section 3.3.5). As a result, immeasurably low resistances may still remain undetected. IRT measurements provide a more accurate insight into the resistance levels. Further details about this measurement are outlined in the subsequent section.

8.2.4 Resistance and I_c measurements of the coil

Despite the presence of residual resistance below T_c of MgB_2, it was deemed worthwhile to fabricate a coil for testing the persistence of the joint. Consequently, a coil was prepared using the method described earlier in Section 3.1.5.2 and coil's geometry and dimensions outlined in **Table 8.4**. The measurement was conducted within the MFM, as introduced in section 3.3.6, under conditions of 20 K and self-field.

Table 8.4 *The specifications of the coil include the determination of inductance using the long solenoid approximation.*

Coil inner radius	*r*	6 mm
Coil outer radius	*R*	7 mm
Number of turns	*N*	15
Coil length	*l*	20 mm
Inductance	*L*	1.6 x 10^{-6} H

At the outset, the externally applied field is set to a magnitude of 0.5 T, serving as the energizing field, and is subsequently diminished to zero. This decreases (ΔB) in the field induces a current within the superconducting coil, effectively confining the applied field within the coil, provided that the joint operates within specified parameters.

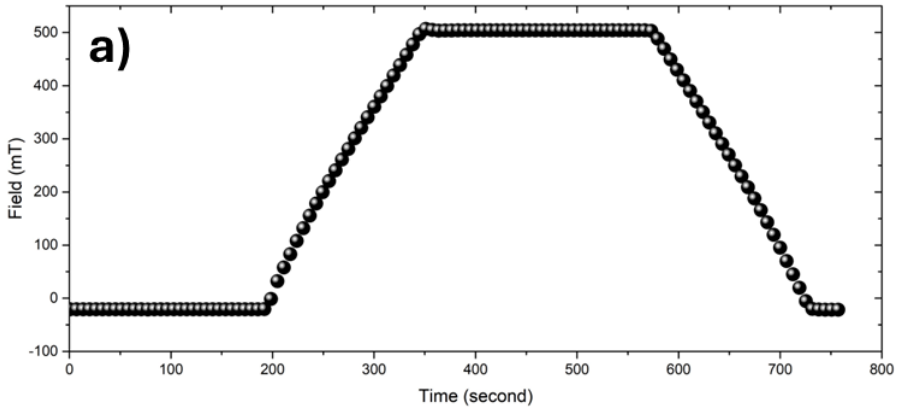

Figure 8.10 *Field decay measurement test. a) measured field as a function of time at 20 K and self-field.*

Figure 8.10 depicts the energization profile utilized for the self-field measurement, wherein a peak field of 0.5 T was utilized to energize the coil. The measurement was halted after the 760th second upon noticing that there was no significant current trapped within the coil. This implies that the shielding current generated in the coil in response to the decay of the external field dissipated rapidly.

The experimental results revealed significant challenges, with residual resistance observed in the joints due to the formation of non-superconducting compounds at the interface. EDX maps and point analyses indicated the presence of Mg and Ag compounds at the interface, suggesting the formation of non-superconducting or low T_c superconducting compounds. Overall, while the use of MgB_2 as a filler joint material shows promise, further optimization of the jointing process is necessary to minimize residual resistance of Bi-2212-MgB_2 dissimilar joints in future work.

8.3 Conclusions

In conclusion, this chapter examined the production processes and experimental outcomes of dissimilar joints between Bi-2212 and MgB_2 wires. Furthermore, the feasibility of utilizing MgB_2 as a filler joint material between Bi-2212 wires was investigated. The

experimental results highlighted significant challenges, with residual resistance detected in the joints due to the formation of non-superconducting compounds at the interface.

Future work may focus on ensuring proper fitting of Bi-2212 wires into the MgB_2 case holes to improve interface quality, as indicated by microstructural analysis. EDX mapping and point analyses have revealed Mg and Ag compounds at the interface, suggesting the formation of non-superconducting or low-T_c superconducting compounds in line with the Mg-Ag phase diagram. Refining the heat treatment process could help reduce the formation of these unwanted Mg-Ag compounds. At this stage, introducing additive elements, such as nano Ni [268], using Mg-based precursors [293], and ball milling pretreatment [294] in the initial powder may lower the melting temperature of Mg, thereby reducing the reaction temperature needed for MgB_2 formation and potentially minimizing the Mg-Ag reaction. If necessary, further studies could investigate the reaction mechanism in an Ag-free environment containing only Bi-2212 and MgB_2, under various thermal conditions.

Chapter 9 Nb-Ti - MgB_2 Dissimilar Joint Production Processes

9.1 Introduction

Niobium-titanium (Nb–Ti) alloys have been pivotal in superconducting applications since the early 1960s. Their appeal lies in their remarkable balance of strength, ductility, and capacity to carry high currents in magnetic fields—essential for many practical uses. Particularly within the 2–8 T operational magnetic field range, Nb–Ti alloys offer these advantages at a lower cost in materials and manufacturing compared to other superconductors. Noteworthy applications include MRI magnets [20], nuclear magnetic resonance (NMR) [269], particle accelerators [270], and superconducting magnetic energy storage (SMES) [271]. The demand for Nb–Ti in MRI magnets alone requires approximately 4000 tons of wire annually [272]. A significant advantage of Nb–Ti superconductors is the ability to apply heat treatments for enhancing in-field performance before cable, winding, and magnet assembly processes, with minimal impact on mechanical toughness.

Effective flux pinning plays a crucial role because achieving a strong overall current-carrying capacity, particularly up to fields of about 8 T, is the primary technological advantage of Nb–Ti. As the pinning force increases, so does the critical current, which is a significant factor to consider. Importantly, the cost of magnet conductors decreases as flux pinning strength increases because the total amount of conductor needed to produce a specific magnetic field decreases proportionally to the current-carrying capacity.

Achieving a high J_c hinges on a significant factor: the Ti-rich α phase in Nb–Ti is non-superconducting at typical operating temperatures. This allows for the creation of numerous flux-pinning sites by precipitating α-Ti during moderate temperature heat treatments [273]. Compositions are typically denoted by mass fraction, such as $Nb_{47}Ti$ indicating the standard

commercial alloy containing 47% Ti by mass [274]. A notable feature of the Nb–Ti phase diagram, depicted in **Figure 9.1**, is that the β phase begins decomposing well below the melting temperature.

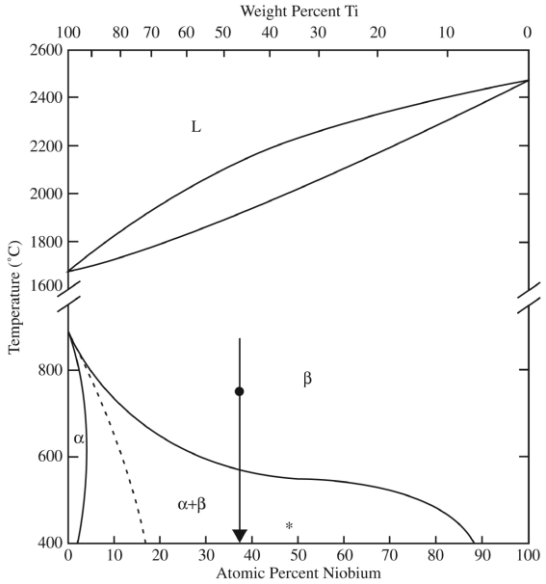

Figure 9.1 *Equilibrium phase diagram of Nb-Ti adapted from* [275] *(Copyright © 1981, Springer)*

The composition of Nb-Ti stands out as the most pivotal factor influencing the superconducting performance of this alloy, as emphasized in the introduction and illustrated in **Figure 9.2**. This figure highlights the variations of T_c, resistivity (ρ), and the upper critical field (H_{c2}) across different alloy compositions.

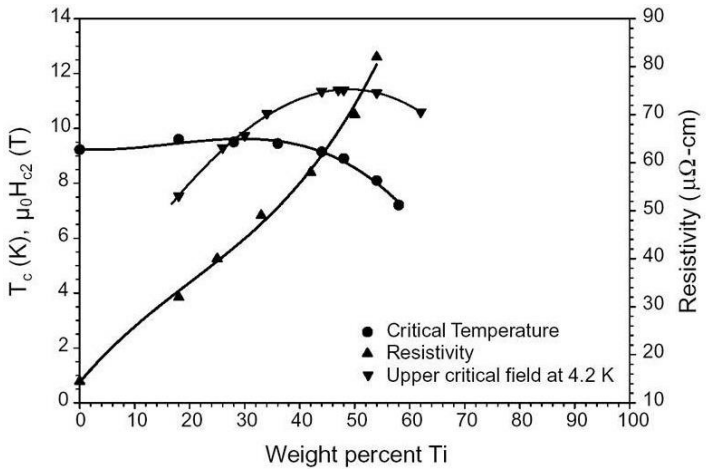

Figure 9.2 *The critical temperature, upper critical field at 4.2 K, and resistivity at 293 K are plotted as functions of the mass fraction of Ti across the binary Nb-Ti alloy system. Reprinted from* [273] *and the data shown in the plot was obtained from* [276] *and* [277].

The T_c experiences a subtle change from pure Nb (9.23 K) to Nb50Ti (8.5 K), with a slight peak around Nb30Ti (9.8 K). However, introducing Ti has a more pronounced effect in lowering T_c for alloys containing over 50% Ti by mass. The H_{c2} displays a broad, dome-like curve, reaching a peak of approximately 11.6 T at Nb44Ti composition. For compositions ranging from approximately Nb40Ti to about Nb52Ti, the upper critical field remains above 11 T.

Flux-pinning centres are generated through a sequence of heat treatment and wire drawing steps. The heat treatments may involve fixed times at the same temperature, or may vary widely in both time and temperature, depending on the desired precipitate structure. Employing aggressive heat treatments, ranging from 10 to 160 hours at temperatures between 405°C and 435°C, resulted in significant enhancements in J_c compared to the standard industry heat treatment of 40 hours at 375°C [278].

Figure 9.3a presents an optical cross-sectional image of Nb-Ti wire, while **Figure 9.3**b depicts a transmission electron microscopy (TEM) image showcasing the α-Ti ribbons inside the Nb-Ti alloy.

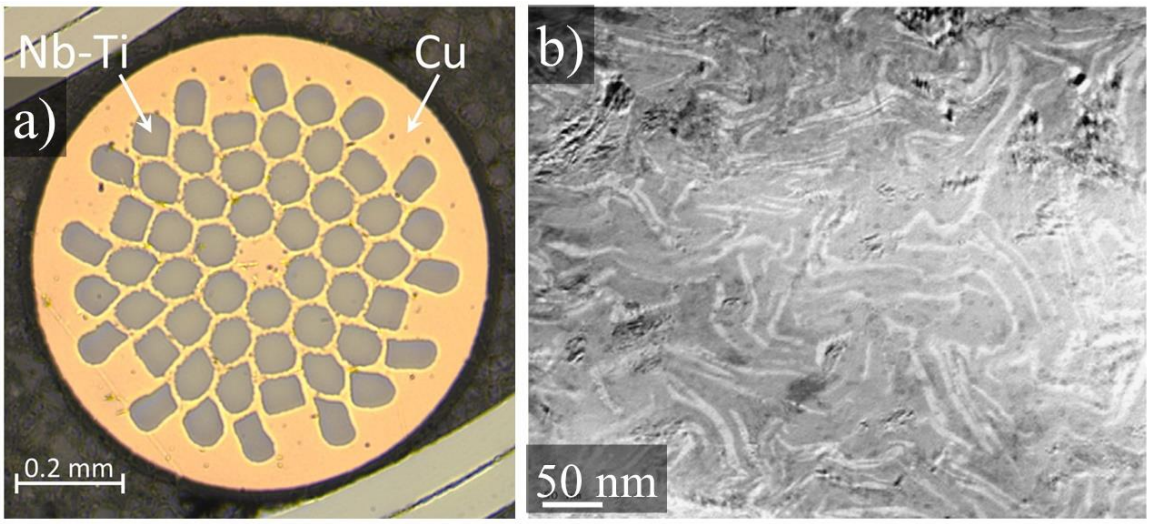

Figure 9.3 *a) An optical image of a multifilament Nb-Ti wire's cross section* [279] *and b) high magnification TEM image of an Nb-Ti sample. The thin, light gray ribbons are a-Ti phases while the darker areas show the β-Nb-Ti grains* [280] *(Copyright © 2008 Elsevier B.V.)*

Creating genuinely superconducting persistent joints is crucial to fulfil the highly demanding field stability criteria of MRI magnets [281]. However, achieving this goal is made complex by the wire's geometry, wherein delicate Nb-Ti filaments are encased within a copper matrix [282]. Several methods are employed for producing joints, including solder matrix replacement [283], ultrasonic welding [284], diffusion welding [285], cold pressing [269], and spot welding [286]. All these joint techniques have matured considerably over the years, attaining resistance values as low as 10^{-14} Ω at 4.2 K and in relatively high fields like 5 T. However, in the soldering methods, which are widely favoured in the industry, superconducting Pb-based solders, known for their high toxicity, are commonly employed.

In some applications, joining two different superconducting conductors is necessary, and the existing methods may not be suitable. Consequently, additional jointing techniques are required. For instance, Banno et al. [200] investigated joints between Nb-Ti and Nb_3Sn for NMR devices, which need superconducting joints due to their use in high-frequency NMR magnets. These magnets typically employ an outer coil of Nb-Ti and an inner coil of Nb_3Sn, requiring effective magnetic field sharing and cost efficiency. Similar needs may arise for MgB_2 as its use expands in NMR, MRI devices, and power transmission lines in the near future. However, research on MgB_2/Nb-Ti joints is limited. Only one documented study in the literature discusses MgB_2/Nb-Ti joint technology. Takashi et al. [162] conducted measurements on their MgB_2 coil operating in persistent current mode to determine resistance and trapped current. They successfully fabricated a small single-loop coil using MgB_2 and Nb-Ti conductors. However, the study lacks comprehensive information on the joint-making procedure, leading to uncertainty about the exact method of joint formation. Nonetheless, the authors observed that their MgB_2/Nb-Ti joint exhibited a resistance value of less than 10^{-13} Ω for around 2.5 hours.

Consequently, there exists a notable gap in the study of wire joining techniques between these two technological superconductors. Thus, the primary objective of the experiment conducted in this chapter was to study Pb-free, easily manufacturable, and cost-effective joints between Nb-Ti wires utilizing a MgB_2 filler. Additionally, the study aimed to investigate the behaviour of the MgB_2/Nb-Ti combination and any reactions they would exhibit at the interface at different temperatures.

9.2 Experimental details

The procedure for fabricating joints between monofilament Nb-Ti wires is detailed in Section 3.1.4. Initially, monofilament wires were scarfed by rough polishing and washed with ethanol. The unreacted MgB_2 case, pre-drilled and partially filled with Mg+B powders (1:2 ratio), accommodated the wire diameter difference to minimize interface gaps. The scarfed Nb-Ti wires were inserted, and 3.4 MPa pressure was applied for 10 minutes. This higher pressure, compared to previous 1.7 MPa, is suitable due to the ductility of Nb-Ti wires unlike MgB_2 wires, improving the interface without risking damage to the case.

Subsequent to this, the assembly underwent various heat treatments to find optimum temperature, commencing at 600°C, followed by 650°C and 700°C, each for a duration of 15 minutes. The reason for this is primarily because the mechanism required to form MgB_2 below 600°C is a solid-state reaction, which necessitates prolonged heat treatment. However, the reaction to form MgB_2 happens faster in the temperature range of 650 °C-700 °C as discussed in section 2.5.1. Keeping the heat treatment duration short is crucial because it can accelerate the dissolution of previously precipitated α-Ti particles within the Nb-Ti wire, leading to a decrease in pinning effect and potential reversion of the Nb-Ti to the β phase. To minimize this effect, the heat treatment temperature is kept as low as possible, and the duration of heat treatment is kept short.

To minimise wire wastage, the initial step, as previously carried out in earlier joint studies detailed in Chapter 6-8, entailed performing T_c transition measurements on short joints. Following this, the assembly underwent individual heat treatments at 600°C, 650°C, and 700°C for 15 minutes each, within a tube furnace under an argon atmosphere. This process also aims to determine the optimal thermal treatment approach before preparing jointed loop coils.

During the coil fabrication process, the monofilament wire was initially obtained and wound around the former and then standard joint making procedures given above were applied. Then, optimised heat treatment temperature from the short joint was applied to the coil's joint.

Five short joints were produced, with two detached from the coil, and the other created as a short joint using the thermal treatments described earlier. The samples underwent characterization, followed by analysis of their resistance and T_c data. Due to the limitations of the cryostat, it was not feasible to measure the T_c of Nb-Ti via low current transport measurement, which will be below the base temperature of 20 K. However, the short joints were tested as it enables the observation of the MgB_2 T_c transition. Subsequently, inductive resistance testing was conducted.

9.2.1 Wire characteristics used in the joint

The conductor employed in this study was the Supercon Inc. T48BG monofilamentary NbTi/Cu wire. This particular wire variant consists of a central filament with a nominal diameter of 200 μm, composed of Nb with 46 wt.% Ti, embedded within a copper matrix measuring 100 μm in thickness. Moreover, a 15 μm layer of Formvar (polyvinyl acetal resin) insulation is pre-applied around the wire. The essential specifications of the Nb-Ti wire utilized in this investigation are presented in **Table 9.1**.

Table 9.1 *Nb-Ti wire specifications*

Number of Filaments	1
Protecting layer	Formvar
Stabiliser	Cu
Diameter of the wire	0.43 mm
Diameter of the Nb-Ti	0.2 mm

9.2.2 Effect of heat treatment on wire/case interface

The primary objective is to assess the superconducting performance and interface qualities between the wire and the filler by applying various heat treatment regimes to the joints. These heat treatment regimes are of 600°C, 650°C, and 700°C for a duration of 15 minutes. Subsequently, after the heat treatments and superconducting measurements, the samples underwent microstructural analysis.

In **Figure 9.4**, typical regions of interfaces found in dissimilar joints are presented. **Figure 9.4**a, b, and c illustrate the interfaces of the joints that were heat treated at 600°C, 650°C, and 700°C for 15 minutes each, respectively.

In **Figure 9.4**a, the interface between the Nb-Ti and the filler appears very smooth. Visible porosities are indicated by white arrows within the MgB_2 filler, consistent with characteristic MgB_2 voids observed in all MgB_2 cases used throughout this thesis. White dashed rectangles indicate void-like regions, which are presumed to be Cu, but in the one shown at the bottom, it has completely disappeared, likely due to the polishing/grinding process causing it to be ripped off somehow. Interestingly, in the top one, Cu has lost some parts, containing a high concentration of Mg. Point analysis, represented as Spectrum 1, showed 64.6%at Mg and 35.4%at Cu with the relatively minor error given by the software is ± 2.57 % for both Mg and Cu. Referring to the Mg-Cu phase diagram (**Figure 9.5**), this may suggest Mg_2Cu

formation, with a Mg-rich eutectic at 750 K (477ºC). Further discussion on the reaction dynamics between Mg and Cu has been provided in section 0.

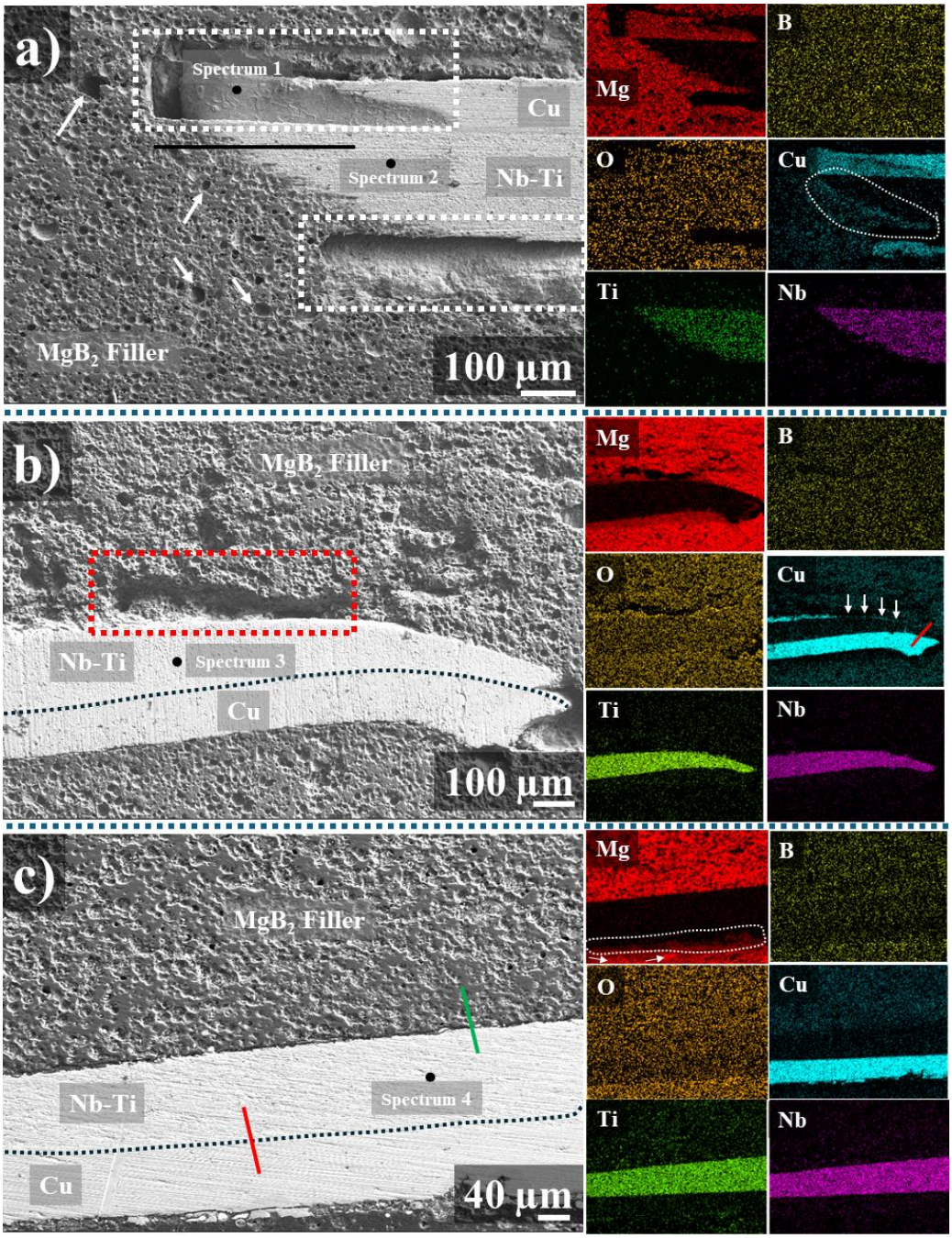

Figure 9.4 *SEM images and EDX maps of dissimilar joints that heat treated at a) 600 °C, b) 650 °C and c) 700 °C for 15 minutes each.*

Spectrum 2, a control point, displayed 51.9%wt Nb and 48.1%wt Ti corresponding to the β phase of Nb-Ti (**Figure 9.1**). The error given by the software is ± 2.2 % for both Nb and Ti. Given this error margin, the Ti content measured in Spectrum 2 is consistent with the

nominal composition of the β phase, and no significant deviation is observed. Examination of the interface revealed a homogenous Cu strip indicating Cu dissolution as seen in the Cu map.

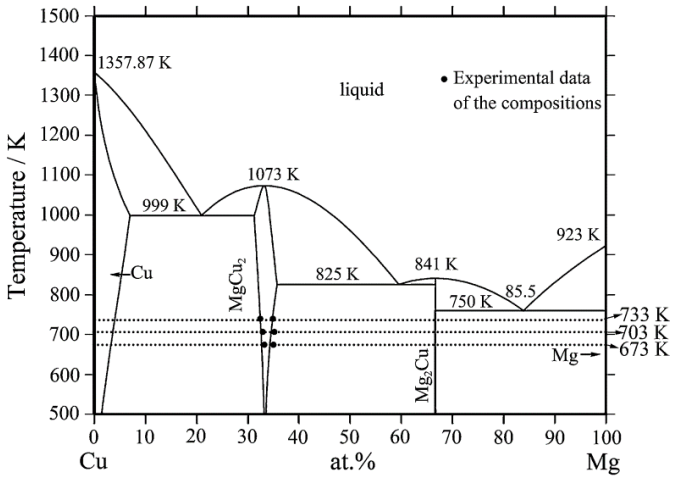

Figure 9.5 *Binary Cu-Mg phase diagram* [256] *(Copyright © 2015, ASM International)*

Linescan analysis of **Figure 9.4**a (black line) shown in **Figure 9.6** and highlighted Cu peaks by brown arrows suggesting potential reactions involving Cu, Mg, and O. The initial Cu peak observed between 50-75 µm coincides with a small O peak alongside Cu and nearby Mg detection hinting at a potential reaction involving Cu, Mg, and O.

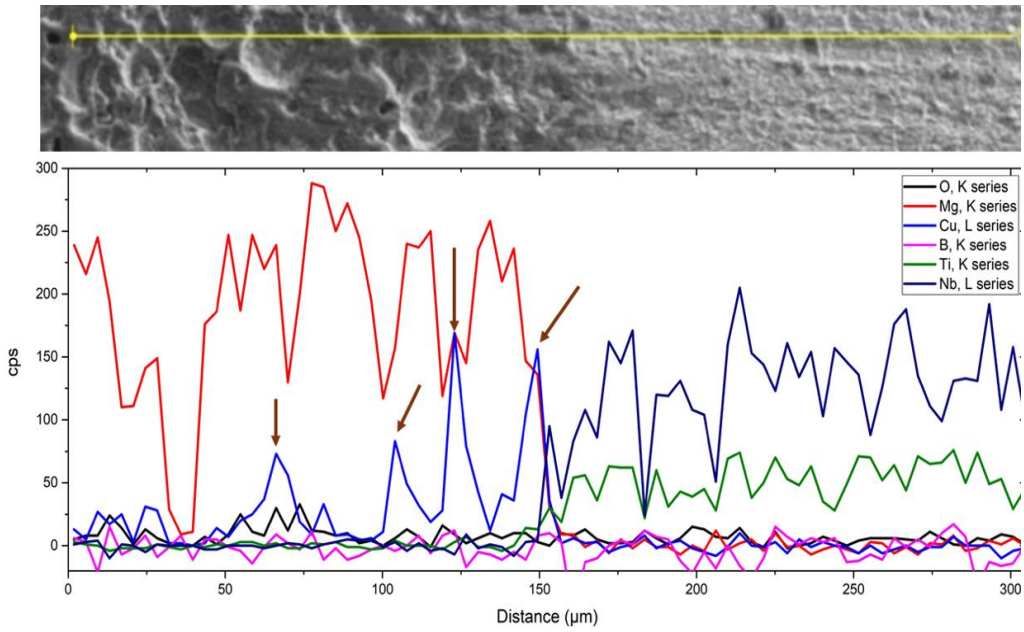

Figure 9.6 *The linescan analysis of the interface of the joint, subjected to heat treatment at 600°C for 15 minutes.*

Additionally, at the second Cu peak, it aligns with the Mg trough suggesting possible Cu precipitation. Similarly, at the third Cu peak around 125 µm, a Mg peak accompanies the Cu peak indicating potential Cu-Mg reaction. It appears that copper is undergoing both dissolution and precipitation within the MgB_2.

Figure 9.4b depicts the interface of the dissimilar joint after heat treatment at 650°C for 15 minutes. Spectrum 3 indicates Nb and Ti atomic percentages of 52.4%wt and 47.6%wt, respectively. The software indicates an error of ± 0.9 % for both Nb and Ti. Considering this margin, the slight reduction in Ti content compared to Spectrum 2 falls within the error range and is thus not a meaningful difference. The red dashed rectangle highlights a void at the interface, potentially resulting from insufficient or inhomogeneous pressure applied to the joint. Nevertheless, there is a well-defined interface between Nb-Ti and MgB_2. However, as depicted in its Cu map, a Cu strip is observed along the interface, indicated by white arrows in **Figure 9.4**b.

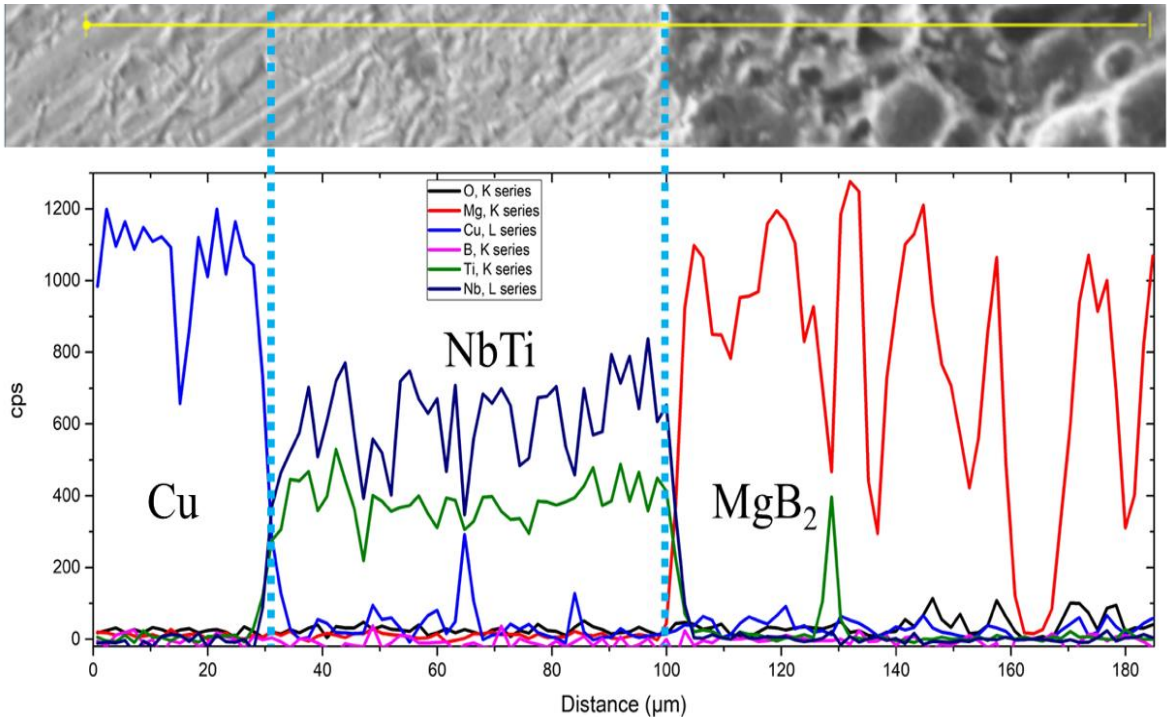

Figure 9.7 *The linescan analysis of the interface of the joint heat treated at 650°C for 15 minutes*.

This is presumably due to insufficient grinding of the wire during scarfing, suggesting the presence of Cu at the surface. However, the area around the red line in the map exhibits a smooth interface with relatively less Cu strip. The linescan analysis (red line) of that interface is shown in **Figure 9.7**. It appears that the presence of Cu in relatively well-scarfed region (the region around the linescan) has diminished. However, there are some Cu peaks suggesting the precipitation inside the Nb-Ti which may disrupt the superconducting properties of Nb-Ti. Interestingly, there's a significant Ti peak within the MgB_2 interface, around 128 µm, along with Mg through, suggesting possible Ti precipitation. In the MgB_2 filler region, there are no significant Cu peaks observed, and there is a lack of obvious oxide layer at the interface.

In **Figure 9.4**c, the joint underwent heat treatment at 700°C for 15 minutes. Spectrum 4 indicates a composition of 47.2%wt Ti and 52.8%wt Nb, with the software reporting an error of ± 1.3% for both Nb and Ti. This error range overlaps with the values observed in Spectrum 2 and Spectrum 3. Consequently, the observed reduction in Ti content in Spectrum 4 is within the measurement error and therefore does not represent a statistically significant compositional change. A white dashed region in the Mg map suggests Mg presence within the Cu layer.

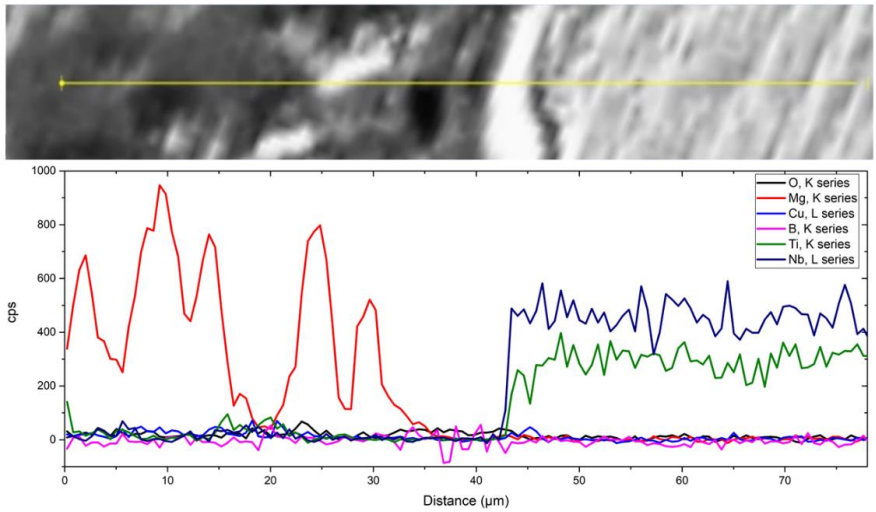

Figure 9.8 *The linescan analysis of the interface of the joint heat treated at 700°C for 15 minutes.*

However, examining the same location in the Cu map reveals restricted Cu beneath the Cu layer within the MgB_2 filler, hinting at Mg diffusion into Cu. Bright Mg clusters, akin in brightness to the MgB_2 filler, are highlighted by white arrows, suggesting Mg consumption via diffusion into Cu. The interface appears smooth without significant voids, ensuring uninterrupted current path. Line scan analysis (green line in **Figure 9.4c**) of the interface is detailed in **Figure 9.8**. In contrast to the interfaces of the previous two joints, the presence of Cu at the interface is nearly negligible. This could be attributed to the well-scarfed wire ends, as no Cu layer was observed in Cu map above the Nb-Ti layer. Additionally, there is a lack of significant oxide layer, as evidenced by the small oxygen peaks.

Scheuerlein et al. [287] extensively studied the temperature-induced degradation of Nb-Ti/Cu composite wire, observing evolving mechanisms through *in-situ* synchrotron X-ray diffraction measurements during heat treatment. Heat treatments ranging from 200°C to 700°C revealed the emergence of Cu_4Ti_3, Cu_4Ti, Cu_2Ti, and Cu_3Ti_2 phases, with Cu diffusion into the Nb-Ti filaments and Ti diffusion into the Cu matrix observed. Exposure to temperatures below 400°C for 5 minutes notably reduced the J_c under external fields.

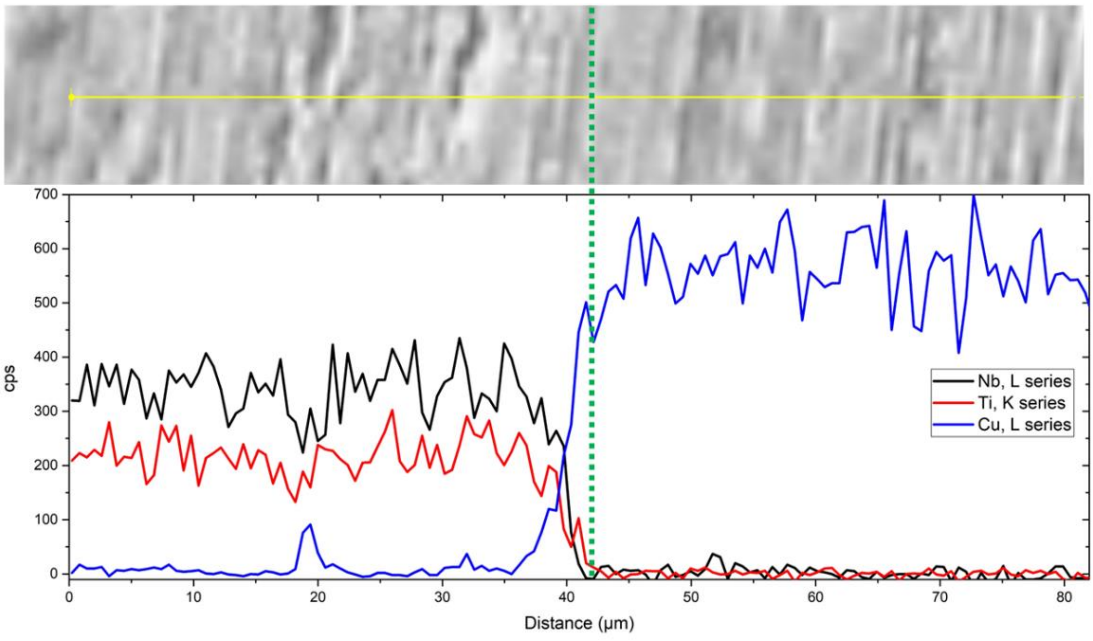

Figure 9.9 *Nb-Ti/Cu interface line scan analysis.*

This reduction was attributed to alterations in the size of α-Ti precipitates, resulting in a loss of flux pinning force. Their findings align with the increased copper count in Nb-Ti observed in **Figure 9.9**, suggesting analogous conclusions regarding Ti diffusion into Cu, consistent with Scheuerlein's study. The elevated temperatures employed (600°C, 650°C, and 700°C) here significantly exceed 400°C, facilitating the dissolution of α-Ti precipitates within Nb-Ti.

Consequently, this phenomenon inevitably leads to a reduction in the J_c. Furthermore, the researchers noted that temperatures exceeding 550°C facilitated Ti diffusion leading to the formation of CuTi intermetallic compounds. This phenomenon was found to degrade the mechanical properties of the composite. Notably, prolonged heating above 600°C induced brittle behaviour in the composite, ultimately resulting in a complete loss of load-carrying capacity.

Thus, the next step was to eliminate Cu before creating a coil. The Cu around the Nb-Ti wire ends were placed into MgB_2 filler case was removed by chemical etching using an iron (III) chloride solution with a ratio of 60 g $FeCl_3$ to 100 ml H_2O. The $FeCl_3$ reacts with Cu to form $CuCl_2$, which is soluble in water. After etching the Cu, a coil with a termination joint was produced with Nb-Ti wire as shown in **Figure 9.15**a. The applied heat treatment to the joint was set at 700°C for 15 minutes instead of 600°C and 650°C due to the superior T_c and residual resistance data obtained from this heat treatment compared to others. This will be discussed in section 9.2.3. The coil was subsequently tested using IRT as discussed in 9.2.4. Following this, the joint was detached from the coil for T_c measurement and microstructural characterization.

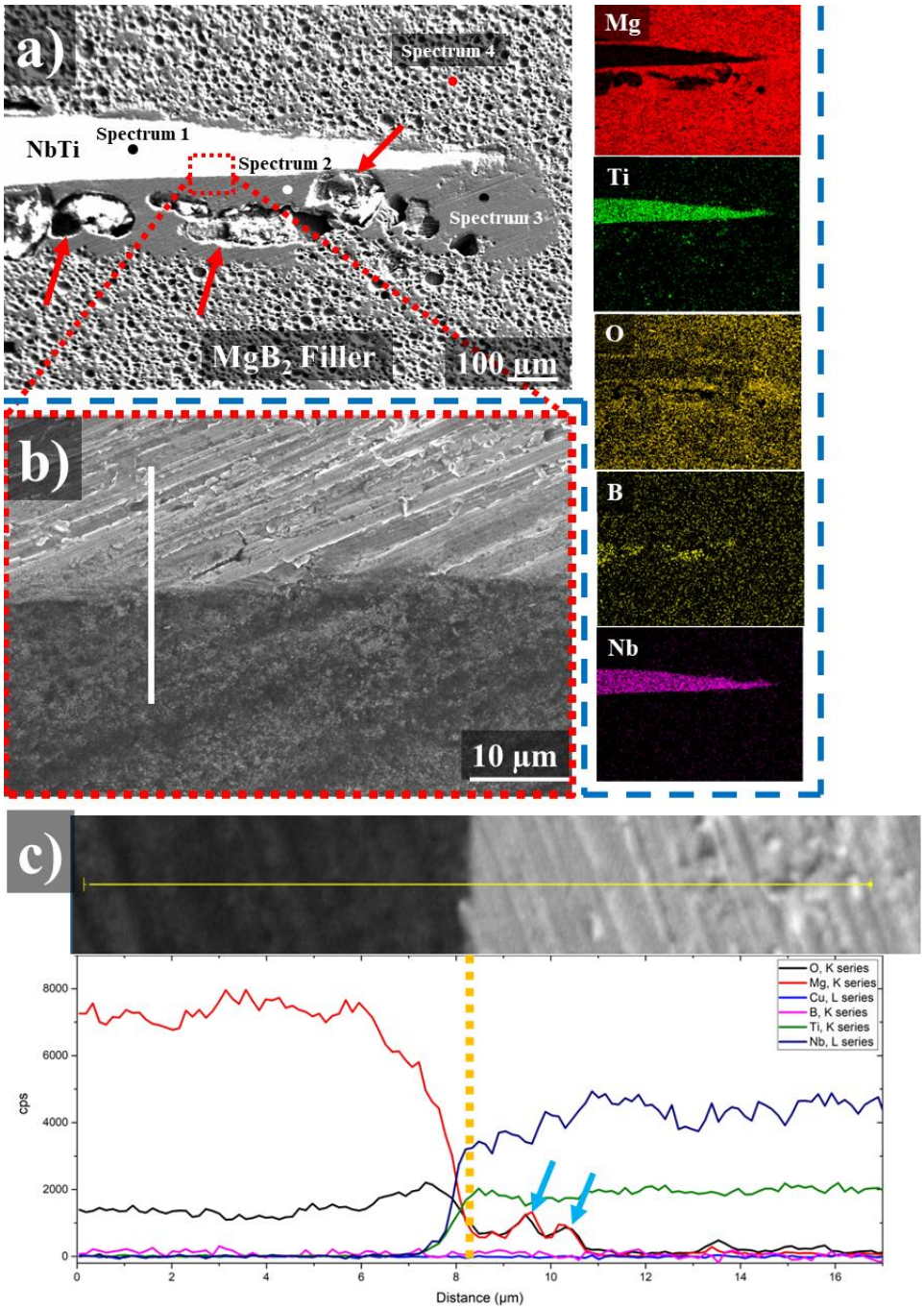

Figure 9.10 *SEM images of the interface of the joint with wire etched. a) interface with its EDX maps, b) the area showing the interface in a high magnification and the location of the linescan, c) the spectrum of the linescan.*

The SEM image of the interface, along with its corresponding EDX maps, are presented in **Figure 9.10**a, while the linescan analysis of the interface is illustrated in **Figure 9.10**b and **Figure 9.10**c.In **Figure 9.10**a, the interface between the wire and the MgB_2 filler appears smooth and uniform at many regions. However, there are noticeable voids highlighted by

red arrows. These voids may have formed due to inadequate mixing of Mg inside the powder that was poured into the holes, resulting in the presence of Mg clusters within the powder.

Consequently, these clusters may have left giant voids (>100 μm) behind upon reacting with B and O. The point analyses were conducted at various locations and results are given in **Table 9.2**. Spectrum 1 serves as the control point within the Nb-Ti wire, revealing the expected ratios of Nb and Ti (see the phase diagram in **Figure 9.1**). Spectrum 2, located beneath the wire in a dense region exhibited a high concentration of oxygen as indicated by the oxygen map in **Figure 9.10**a. This suggests the possibility of an Mg-B-O reaction further supported by the linescan in **Figure 9.10**c.Spectrum 3, in another dense region near the wire tip, showed similar characteristics to Spectrum 2, indicating a potential Mg-B-O reaction in these regions. Excessive oxygen trapped between powder particles during pouring into the holes likely reacted with Mg. Additionally, the chemical etching process may have contributed to an oxygen layer at the wire surface.

Table 9.2 *Point analyses spectrums of the elements in atomic ratio.*

Spectrum	Mg%at	B%at	O%at	Nb%at	Ti%at
1	-	-	-	51	49
2	31.7	50	18.3	-	-
3	29.4	47.7	22.9	-	-
4	36.7	53.6	9.7	-	-
Error %	± 1.8	± 2.5	± 0.7	± 1.7	± 1.7

The denser regions observed, unlike typical MgB_2 filler regions, may result from an excess reaction of Mg with oxygen. Spectrum 4, another control point within the MgB_2 filler, exhibited less oxygen, supporting the idea of oxygen trapping within the pre-added powders. Further oxygen analysis at the interface with Nb-Ti is detailed in the line scan analysis in **Figure 9.10**c.

The linescan analysis revealed that the interface between Nb-Ti and MgB_2 is free from Cu, and there is a smooth interface between the Nb-Ti filament and the filler material. However, the presence of homogenous oxygen peaks alongside Mg peaks may suggest the dissolution of oxygen into MgB_2. Additionally, there are two obvious Mg-O peaks observed and highlighted with blue arrows in **Figure 9.10**c. The presence of O is slightly increased at the interface compared to previous samples. It can be observed that there is no significant diffusion from filler to Nb-Ti and vice versa.

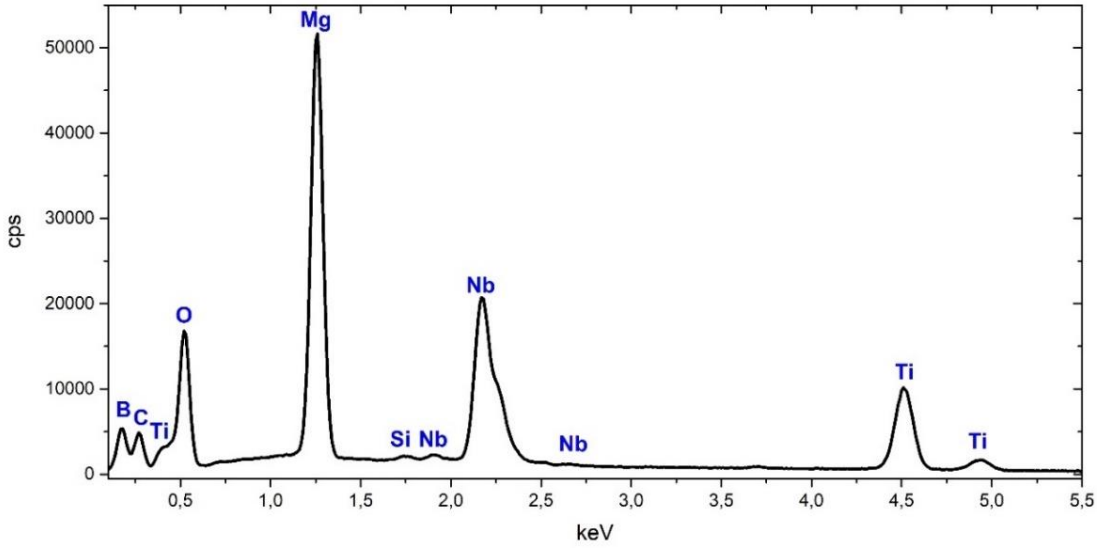

Figure 9.11 *The spectrum of the linescan given in* ***Figure 9.10****c.*

However, inevitably oxygen is apparent at the interface. When the pre-poured powder was placed into the holes, a significant amount of oxygen must have been trapped in the interface and inside the filler. **Figure 9.11** shows that the oxygen K-α peak overlaps with the Ti peak (observed in the left tail) and it is distinct from the Mg peak. Additionally, it appears that significant quantity of Mg diffuses into the Nb-Ti, but there is limited diffusion of Nb and Ti into the MgB_2 filler. Any non-superconducting layer at the interface, or a layer consisting of a low T_c superconductor (lower than operating temperature), has the potential to impede macroscopic supercurrent flow.

Additionally, alterations in the crystallographic properties of Nb-Ti can also impact its superconducting characteristics. According to Mousavi et al. [288], as the grain size increases, the critical temperature of Nb-Ti decreases, while the upper critical field increases. Furthermore, the potential diffusion of Cu, as discussed for the **Figure 9.9** into the Nb-Ti lattice during heat treatment can also lead to lattice distortion, changes in strain, and grain growth [289, 290] thereby influencing the crystallographic properties and consequently affecting the superconducting properties. Therefore, crystallographic properties of the Nb-Ti in the wires were thoroughly investigated by XRD characterization using the technique outlined in section 3.3.1.

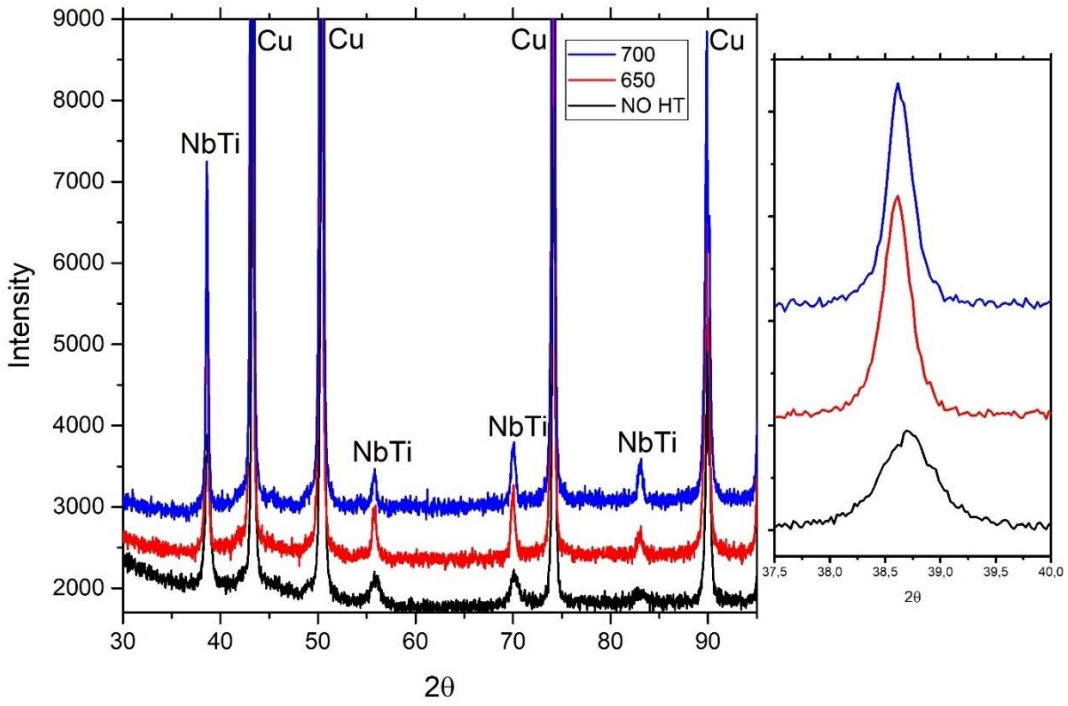

Figure 9.12 *XRD patterns of Nb-Ti wires. Black: wires as obtained, Red: wire heat treated 650 °C for 15 minutes, Blue: wire heat treated 700 °C for 15 minutes.*

Figure 9.12 shows the X-ray diffraction patterns of the Nb-Ti wires under different conditions and results are given in **Table 9.3**. While the precision of the mathematical fitting error is included, XRD device-related errors have not been characterized for Nb-Ti. It is recommended to consider this in future work.

Table 9.3 *XRD characterisation results of the Nb-Ti wires.*

Sample	Lattice parameter, Å	Strain %	Crystallite size (nm)
NO HT	3.286	0.426	24
650 °C 15 min	3.292	0.140	33
700 °C 15 min	3.290	0.201	50
Precision	± 0.0008	± 0.014	± 2

Samples were prepared by heat treating the wires first, cutting them into small pieces, and then moulding them with epoxy as previously introduced in section 3.2.4. Subsequently, the moulded wires were ground using a grinding wheel, starting from 240, 400, 800, 1200, and 2500 grit sandpapers.

When examining the peak located at 2θ, 38.7°, it is evident that the wire in its as-obtained state without heat treatment (black curve), displays a broad peak and lower peak intensity. Upon the application of thermal treatment, the peak narrows and intensifies. This can be attributed to the reduction of strain, the coarsening of the crystallite size and/or dissolving the α-Ti precipitations. For the reference sample without heat treatment, the lattice parameter was measured at 3.286 Å, with a corresponding strain percentage of 0.426% and a crystallite size of 24.58 nm.

Upon subjecting the wires to a thermal treatment regime of 650°C for 15 minutes, notable changes in crystallographic parameters were observed. The lattice parameter experienced a modest increase to 3.292 Å, suggesting a degree of lattice expansion may induce the effect of dissolving the α-Ti precipitations. Concurrently, the strain percentage exhibited a significant reduction to 0.140%, indicative of a relaxation of lattice distortion or internal stresses within the material. This relaxation is further supported by the observed decrease in lattice strain, indicative of the annealing out of lattice defects within the material. Moreover, the modest increase in lattice parameter suggests a change in the composition of the matrix induced by the thermal treatment.

Subsequent heat treatment at 700°C for the same duration elicited further alterations in the crystallographic characteristics of the Nb-Ti wires. The lattice parameter, although marginally decreased compared to the 650°C treatment, remained elevated relative to the reference sample, indicating continued lattice expansion. However, the strain percentage experienced a slight increment to 0.201%, suggesting a nuanced response to the heightened thermal exposure.

The next step involved minimizing Cu presence to prevent potential reactions with Nb-Ti and assess its impact on joint superconducting properties. Initially, a nearly 1-meter Nb-Ti wire was etched with HNO_3 until no visible Cu remained. Although complete elimination was challenging, efforts were made to minimize the presence of Cu. Standard coil manufacturing procedures followed, and the wire was jointed as before. The coil was tested via IRT, showing minimal resistance and retaining persistent trapped current for at least 20 hours. Further details are provided in section 9.2.4.

Figure 9.13a presents the SEM image and EDX maps of the interface between the MgB_2 filler and the Nb-Ti wire. The interface appears smooth, with localized oxygen particles evident in the filler and the presence of voids, consistent with observations in previous samples. **Figure 9.13**b provides a line scan analysis of the interface, demonstrating a Cu-free interface and indicating the absence of an oxide layer or any substantial reactions at the interface. As no Cu has been observed, it has been excluded from the analysis.

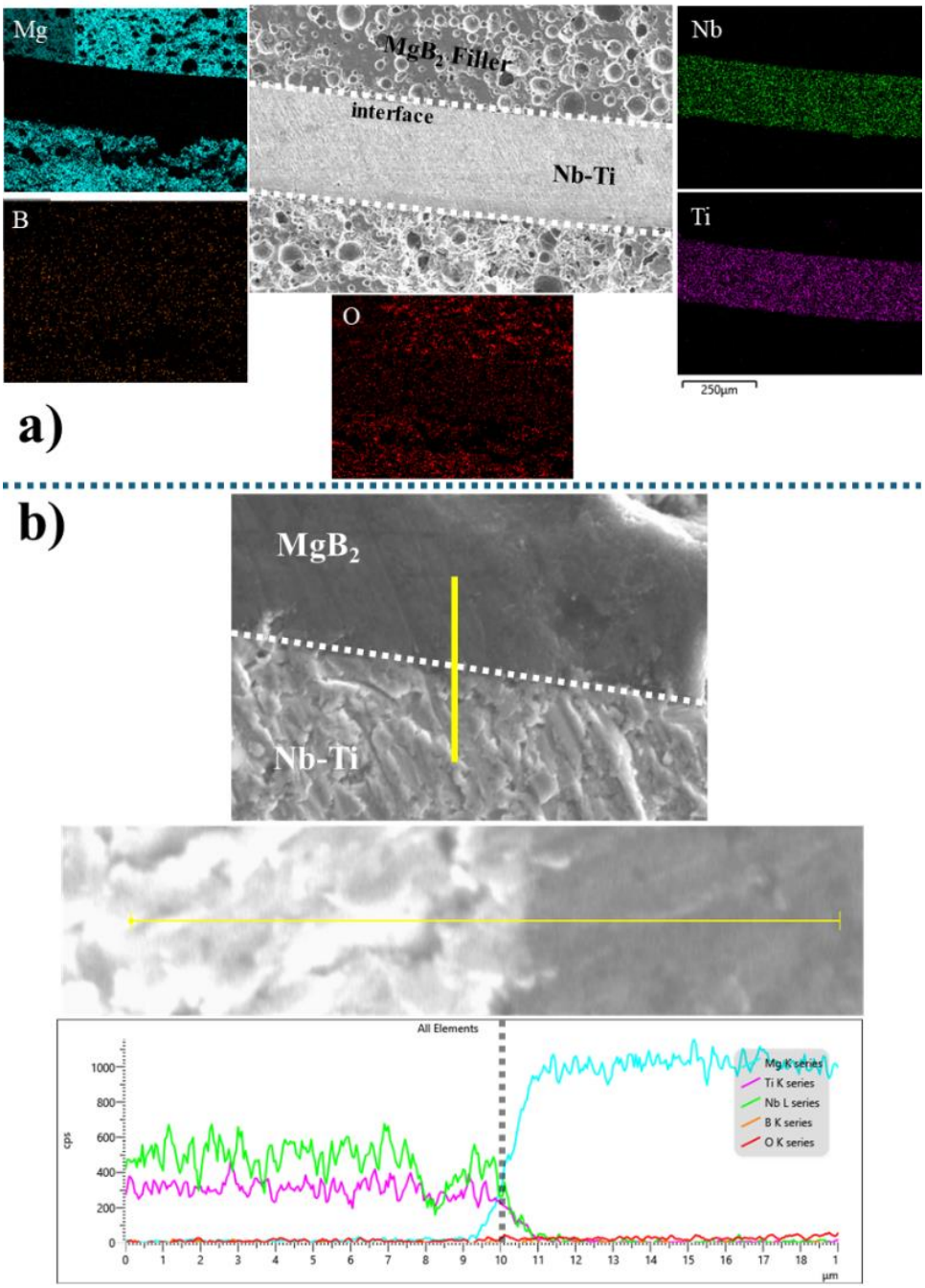

Figure 9.13 *a) SEM image and EDX maps of the interface between the MgB_2 filler and Nb-Ti wire, b) line scan analysis of the interface.*

9.2.3 Low current transport T_c measurements on short joints

The low current transport measurement tests were conducted on three dissimilar joints that underwent heat treatment at 600°C, 650°C, and 700°C for 15 minutes each, with their

microstructures discussed in detail in the previous section. The T_c results for these first three short joints are presented in **Figure 9.14**.

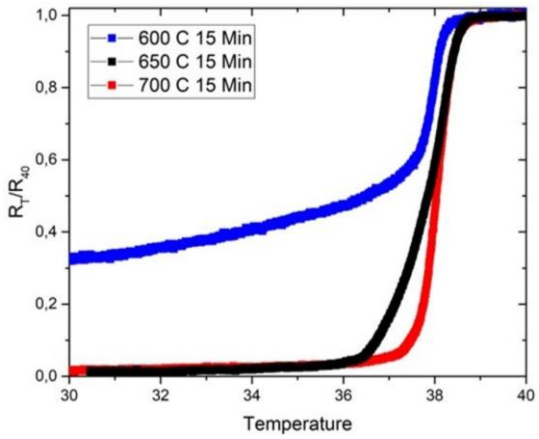

Figure 9.14 *Transport measurements of short joints heat-treated at 600 °C, 650 °C and 700 °C for 15 mins each.*

It is worth noting that as the heat treatment temperature was increased from 600 °C to 700 °C, the superconducting transition became steeper, which suggests that the current is passing through more homogeneous or better reacted MgB_2. In all 3 cases, some residual resistance can be seen below the MgB_2 transition at around 38 K, originating from the ohmic resistance of the Nb-Ti wire which is not superconducting at this temperature.

The blue curve displayed suboptimal performance concerning residual resistance and onset T_c as well as ΔT_c. This observation is potentially linked to the presence of copper along the interface, as depicted in **Figure 9.4**a. Despite the apparently smooth surface, analysis through a linescan at the interface, as depicted in **Figure 9.6**, revealed the possible existence of Cu-based by-products that could impede the supercurrent flow at the interface.

The second joint, subjected to a heat treatment at 650°C for 15 minutes, demonstrated the second-best performance in terms of the sharpness of the T_c but not as pronounced as the idealized black curve, suggesting the potential presence of compounds at the interface with lower T_c. This phenomenon could be attributed to the presence of a copper strip along the interface as shown in its Cu map in **Figure 9.4**b, likely resulting from insufficient scarfing

during wire preparation. Notably, a well-polished small interface devoid of Cu strip, as evidenced by the linescan in **Figure 9.7**, exhibited a favourable interface condition. Nevertheless, the presence of Cu elsewhere along the interface may introduce additional resistance, consequently influencing the T_c behaviour.

The final sample, subjected to heat treatment at 700°C for 15 minutes, displayed a sharper transition in T_c and exhibited a more favourable T_c onset value compared to the black curve. This improvement can be attributed to the presence of a substantial Cu-free interface in this sample, in contrast to the blue and black curves, as evidenced by their respective EDX maps. The interface and corresponding EDX maps of the red curve are presented in **Figure 9.4**c, along with the linescan analysis depicted in **Figure 9.8**. Notably, the interface appears to be devoid of oxygen and copper, further enhancing its suitability for superconducting applications.

In summary, among the heat treatment regimes investigated, the joint subjected to heat treatment at 700°C for 15 minutes demonstrated the most favourable sharpness in the transition of T_c. Consequently, this specific heat treatment condition was identified as the optimized temperature setting. Subsequently, the coil fabricated in the next step was produced under this optimized heat treatment regime, ensuring enhanced reliability.

9.2.4 Resistance and I_c measurements of the coil

To evaluate the superconducting performance, two coils were constructed (**Figure 9.15**a-c) using Nb-Ti wires, as detailed in section 3.1.5.2. Additionally, MgB_2 joint cases, as exampled in **Figure 9.15**b, were employed. A heat treatment of 700°C for 15 minutes was applied to the coil joints, as the short joint demonstrated superior performance compared to the others. The measurements were conducted within the MFM under conditions of 4.7 K and self-field. The coil, with etched wire ends as shown in **Figure 9.15**a exhibited no

significant trapped fields or currents, suggesting that the shielding current induced in the coil by the change of external field decayed very quickly. Therefore, its graphs are not included in this section. In contrast, the coil shown in **Figure 9.15**c exhibited an amount of trapped current and ultra-low resistance. This coil was wound with entirely etched Cu-free Nb-Ti wire as discussed previously, and the rest of the coil and joint-making procedures mirrored those of previous samples. Its microstructure is given in **Figure 9.13**.

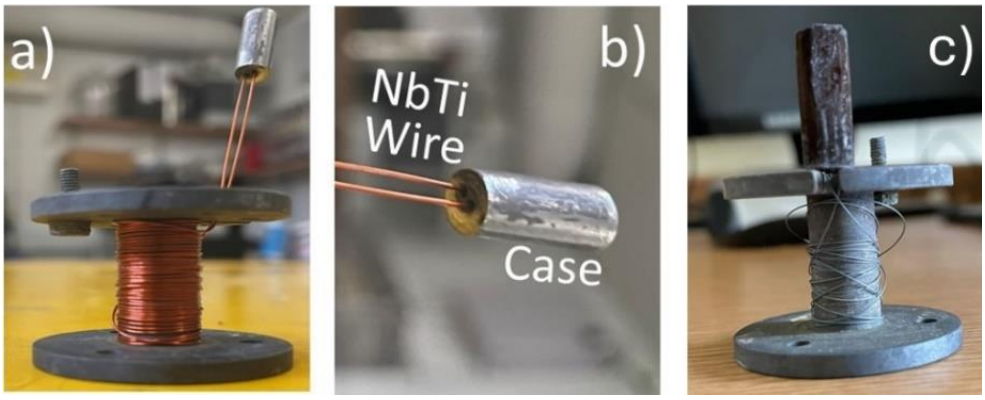

Figure 9.15 *a) the coil made of Nb-Ti wire and MgB_2 case, b) the joint structure, c) the coil made of Cu-free Nb-Ti wire.*

Figure 9.16 illustrates the energization profile (a) for the coil shown in **Figure 9.15**c under self-field measurement, wherein a peak field of 5 mT was employed to energize the coil and subsequently decreased to zero. This reduction (ΔB) in field induces a current within the coil, thereby trapping the applied field within the coil (**Figure 9.16**b), assuming that the joints are functioning within specified parameters. To correlate the circulating current with the trapped magnetic field, the Biot-Savart law (equation (3.3)) was used to predict the field and the current at the coil's centre, considering the test coil's geometry and parameters detailed in **Table 9.4**. The trapped current was calculated to be about 7 A under 4.7 K and self-field as shown in **Figure 9.16**d and the magnet quenching is performed by externally increasing the heat of the magnet.

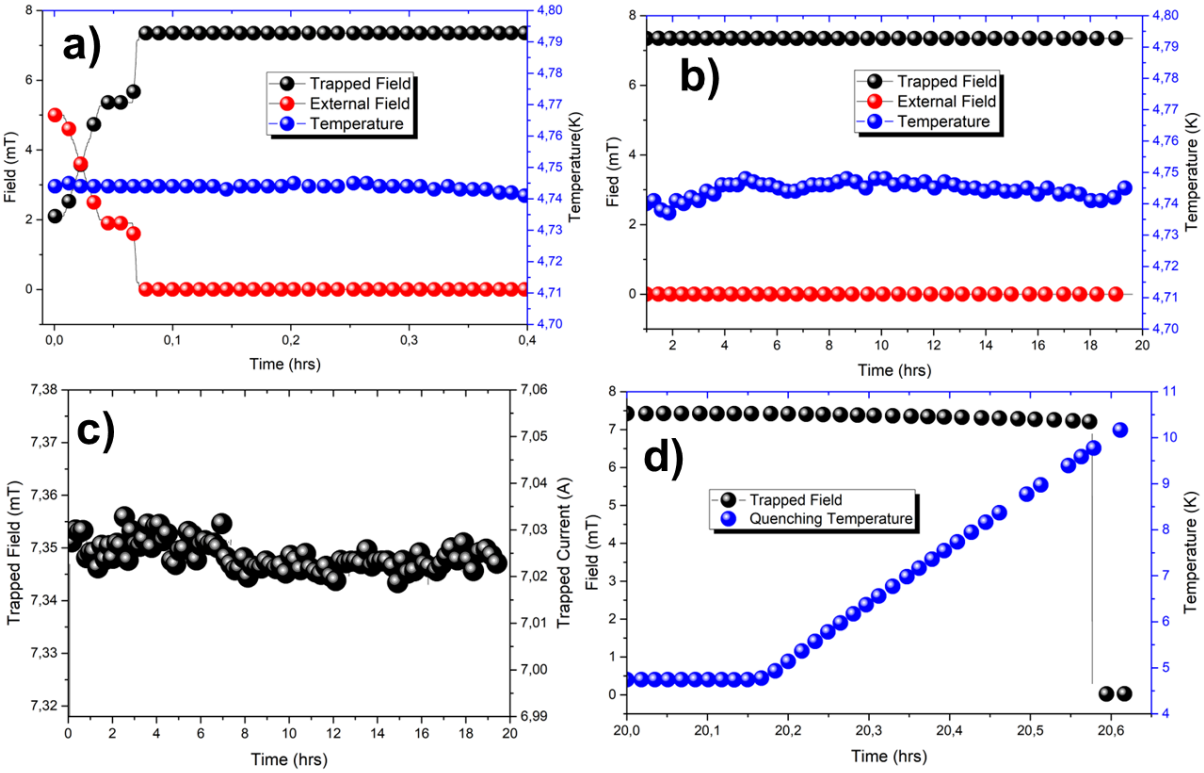

Figure 9.16 *Field decay measurement test. a) measured field as a function of time, b) field decay between 1st and 20th hours at 4.7 K and self-field, c) the trapped field and corresponding trapped field by time and d) shows the magnet quenching by increasing the magnet temperature.*

The magnet quenched at approximately 9.7 K, indicating that the Nb-Ti switched off effectively.

Table 9.4 *The specifications of the coil that the inductance has been calculated using the long solenoid approximation method.*

		Coil with Cu-Nb-Ti wire	**Coil with Cu-free Nb-Ti wire**
Coil inner radius	*r*	6 mm	6 mm
Coil outer radius	*R*	7 mm	7 mm
Number of turns	*N*	40	16
Coil length	*l*	20 mm	15 mm
Inductance	*L*	1.1 x 10^{-5} H	2.42 x 10^{-6} H

To estimate the overall resistance of the coil, equation (3.2) was used, yielding approximately 4.3 x 10^{-15} Ω. This ultra-low resistance has not been achieved even in some

joints between similar superconducting wires reported in the literature. The relatively low current value may be attributed to the dissolution of α-Ti particles, which reduces the J_c of Nb-Ti. It is believed that reducing the heat treatment applied to the joint could improve the Ic value. Further investigation on this matter is warranted.

As a summary, it is speculated that copper from the Nb-Ti wire reacts with Nb-Ti at elevated temperatures, degrading its superconducting properties. Consequently, copper was completely removed from the Nb-Ti wire, which was then wound around a small former and joined using non-reacted Mg + 2B filler powder. The joint was reacted and tested, achieving an ultra-low resistance of approximately 4.2×10^{-15} Ω and a trapped current of 7 A under 4.7 K and self-field conditions. For future research, it is recommended that efforts be made to significantly reduce the MgB_2 composition temperature, as this could enable the minimization of joint heat treatment and thereby better preserve the J_c of the Nb-Ti wire, along with the retention of α-Ti particles. Furthermore, conducting comprehensive transmission electron microscopy (TEM) analysis of Nb-Ti wires following heat treatments would yield critical insights into the behaviour of α-Ti particles under these thermal conditions.

9.3 Conclusions

The feasibility of creating joints between Nb-Ti wires using MgB_2 filler materials has been investigated. It was found that copper from the Nb-Ti wire reacts with Nb-Ti at elevated temperatures, degrading its superconducting properties. Consequently, copper was completely removed from the Nb-Ti wire, and Cu-free Nb-Ti wire was wound around a small former and joined using non-reacted Mg+2B filler powder. The joint was then reacted and tested, yielding an ultra-low resistance of approximately 4.2×10^{-15} Ω and a trapped current of 7 A under 4.7 K and self-field conditions.

A similar study by Tanaka et al. [162] was conducted, but the precise joint structure was not disclosed, making it unclear whether MgB_2 wires were joined to Nb-Ti or vice versa Therefore, direct comparison of results is not possible.

Copper is crucial for quench protection in Nb-Ti coils, making the complete removal of copper impractical for large-scale applications. In this study, the small former size caused the applied heat treatment to affect the entire Nb-Ti wire wound around it, resulting in the loss of J_c properties throughout the wire. The applied temperature of 700°C for 15 minutes exceeds the 400°C threshold, leading to a reduction in J_c due to changes in the size of α-Ti precipitates, which in turn diminishes flux pinning force, as observed by Scheuerlein et al. [287]. To mitigate this effect, the MgB_2 reaction temperature should be minimized as much as possible, potentially through the use of alternative dopants, such as nano Ni particles [288].

In practical applications for larger magnets, the region of the Nb-Ti wire to be joined inside the MgB_2 filler case could be selectively etched using HNO_3 and heat-treated separately from the rest of the coil. The remainder of the coil could be kept cool to prevent the heat treatment effects from degrading the Nb-Ti wires. This approach allows the Nb-Ti wire to wound around the coil to retain its copper. However, the J_c property of the Nb-Ti segment inside the case may still be partially compromised, potentially affecting the overall J_c of the wire. This is the main concern with this technique. If the synthesis temperature of MgB_2 can be significantly reduced, for instance, through the use of additive elements such as Ag [291] and Sn [292], Mg-based precursors [293] and ball milling pretreatment [294] methods, the joint heat treatment process could be minimized. This would help preserve the J_c of the Nb-Ti within the casing to a certain extent.

In conclusion, this study is the first of their kind to demonstrate ultra-low resistance and persistent current in joints between Nb-Ti wires using MgB_2 filler, and it shows promise for further research in this field.

Chapter 10 Conclusions and Suggestion for Future Work

10.1 Conclusions

The most prevalent commercial application of superconductivity is in MRI, a medical diagnostic tool requiring ultra-stable superconducting magnets, which are the costliest component of the system. Currently, Nb-Ti is used for most MRI systems, but alternatives like MgB_2, ReBCO, and BSCCO are being considered. Adhering to MRI standards, such as achieving minimum circuit resistance, poses challenges for some materials. For example, BSCCO's use of silver increases costs, while Nb-Ti's low critical temperature of 9.2 K necessitates expensive liquid helium cooling. MgB_2 is a promising alternative, being cost-effective and maintaining superconductivity at 20 K with cryocoolers in liquid hydrogen and helium environments. Since 2005, MgB_2 joints have been increasingly studied in academia and industry, driven by growing demand and the study presented in this thesis contributes to the current literature and advances the development of MRI scanners using persistent reacted MgB_2 wires.

Table 10.1 *Joint studies in the literature between reacted MgB_2 wires.*

Reacted wires	Environment	Superconducting Properties			Ref.
		I_c, A	CCR, %	Resistance, Ω	
12-filament twisted tape 0.65 × 3.65 mm	20 K, self-field	300	43	$<10^{-14}$	[254]
Monofilament 0.5mm ⌀	20 K, self-field	40	<70	-	[295]
19-filament tape 0.71 × 3.10 mm	20 K, 0.46 T	48	<17	$<10^{-11}$	[296]
18-filament wire 0.83 mm ⌀	20 K, 0.5 T	17.9	<18.5	-	[297]
Monofilament 0.75mm ⌀	***20 K, 1 T***	***160***	***<78***	***$<10^{-14}$***	***This study***

Table 10.1 presents the findings from literature studies on joints between different forms of reacted MgB_2 wires. It is noteworthy that this study demonstrates the most favourable CCR and resistance values reported in the literature to date. For the joint study between reacted multifilament MgB_2 wires presented here, the main challenge was managing all interfaces between the filaments and the filler material. Due to limitations, not all filament-filler interfaces could be examined simultaneously. Consequently, while some interfaces were satisfactory, the status of others remained uncertain. Additionally, copper's reactivity with magnesium led to Mg-Cu compound formation within the filler material, and its high diffusion propensity significantly impacted the joint's superconducting properties. To address this, copper was removed using HNO_3, which also removed steel from the wire. However, trapped current could not be obtained in IRT measurements, and a sharp T_c transition was not observed in short-joint R/T tests. This may be due to the non-industrial, custom-made nature of the wires.

Upon successfully establishing a joint between monofilament reacted MgB_2 wires, extending this achievement to multifilament MgB_2 reacted wires and applying a similar methodology to other technological superconductors, such as Nb-Ti and Bi-2212, was considered. Jointing Bi-2212 wires through the MgB_2 filler was deemed intriguing and worthwhile, despite the joint needing to operate below approximately 38 K. Transport measurements indicated a two-stage superconducting transition of Bi-2212 and MgB_2 respectively with a low residual resistance obtained through T_c measurement, suggesting both wire and case exhibiting superconductivity in some extent. However, when a coil was built for IRT measurements, high resistance led to no trapped current. Investigation uncovered severe side reactions at the interface notably between magnesium and silver. The applied heat treatment (700°C for 15 minutes) to create MgB_2 was deemed too high, exacerbating unwanted reactions.

The strategic approach was extended to another technological superconductor, Nb-Ti, yielding promising initial T_c performance results. Increased heat treatment temperature (700°C for 15 minutes) amplified MgB_2 formation, enhancing superconducting transition. Microstructural analysis revealed copper reacting with filler material and Nb-Ti itself. Chemical etching removed Cu from wire ends, ensuring a smooth Nb-Ti/MgB_2 interface. Despite this, elevated resistance hindered trapped current, attributed to Cu diffusion into Nb-Ti, forming disruptive Cu-Ti compounds. Cu removal along the wire partly resolved this issue, facilitating jointing via Mg+2B filler. IRT measurements showed 7 A trapped current and 4.3×10^{-15} Ω resistance. This low amount was attributed to the reduced J_c of the Nb-Ti wire due to the applied heat treatment, which triggered the dissolution of α-Ti particles.

10.2 Suggestion for Future Work

Future research should concentrate on several key areas to enhance the understanding and performance of superconducting joints.

In terms of the study in Chapter 6, joint between reacted monofilament MgB_2 wires, future research could focus on comprehensively investigating the observed increase in lattice parameters of Sample 3, which occurs despite a reduction in strain, as the mechanisms underlying this behaviour remain unclear. Additional studies might also explore the possibility that side reactions lead to unintended boron incorporation into compounds like TiB_x in Samples 4 and 5, potentially influencing phase formation and reducing available boron content. Moreover, to examine the fundamental mechanisms behind the decomposition reaction $MgB_4 + Mg \rightleftharpoons 2MgB_2$ under non-equilibrium conditions, an experimental setup allowing for precise control and monitoring of Mg vaporization within the relevant temperature range could be developed. This setup would enable a thorough

investigation into potential reaction behaviours, providing valuable insights into the system's underlying processes.

Regarding the joints between multifilament MgB_2 wires, it is crucial to optimize filament-filler interfaces and ensure material compatibility to advance joint fabrication techniques. It is recommended that further studies be conducted in a more controlled environment, where both the joint case material and the wires being joined are produced using the same method, materials, and conditions.

Secondly, when considering the joints between Bi-2212 wires utilizing MgB_2 filler, this approach shows promise for specific applications, such as power transmission cables that incorporate hybrid conductor systems like MgB_2 and Bi-2212 wires. This would facilitate a seamless transition between cables. Although this scenario has yet to be implemented in practice, it has potential for future developments. Further optimization of the jointing process is essential to reduce residual resistance and enhance superconducting properties. Investigating the reaction mechanics between Mg and Ag may also yield insights into minimizing reactions, particularly at the interface. Refining the heat treatment process may have a beneficial effect in reducing the formation of the undesirable Mg-Ag reaction. At this stage, introducing additive elements (such as nano Ni [268], Ag [291] and Sn [292]) into the initial powder within the case, and ball milling pretreatment to the powder [294] could lower the melting temperature of Mg and decrease the reaction temperature for MgB_2 formation, which may help reduce the Mg-Ag reaction to some extent. Furthermore, the reaction mechanism between MgB_2 and Bi-2212 could be examined directly in the absence of silver. Additionally, ensuring that Bi-2212 wires are fully embedded within the Mg+B powder is vital, as eliminating any gaps between the powder and wire filaments is of utmost importance.

In relation to the joints between Nb-Ti wires utilizing MgB_2 filler, it is critical to explore methods for significantly reducing the MgB_2 composition temperature possibly by incorporating alternative dopants/additives as suggested above. The temperature of 700°C applied for 15 minutes surpasses the 400°C limit, resulting in a decrease in J_c due to alterations in the size of α-Ti precipitates. This change subsequently reduces the flux pinning force, as noted by Scheuerlein et al. [284]. Therefore, it is important to develop low-temperature synthesis methods for MgB_2 in the joint case. Several approaches have been employed to facilitate the processing of MgB_2 at lower temperatures and reduce processing time. These include the use of various Mg-based precursors [293], assisted sintering with different metal or alloy additions such as Ag [291] and Sn [292], and ball milling pretreatment of the original precursor powders [294]. Such methods could minimize joint heat treatment, thereby preserving the J_c of Nb-Ti wires in some extent, while retaining α-Ti particles and improving overall joint performance. Furthermore, conducting comprehensive transmission electron microscopy (TEM) analyses on Nb-Ti wires after heat treatments would provide valuable insights into the behaviour of α-Ti particles under varying thermal conditions. Understanding these mechanisms could lead to the development of more effective dissimilar joint fabrication techniques.

Finally, additional studies should evaluate the scalability of the proposed methods for large-scale applications, ensuring that the advancements achieved in laboratory settings can be effectively translated into practical uses for superconducting magnets, persistent coils and power transmission systems.

References

[1] D. Leroy, “Review of the R&D and supply of the LHC superconducting cables,” *IEEE Trans. Appl. Supercond.*, vol. 16, no. 2, pp. 1152–1159, Jun. 2006, doi: 10.1109/TASC.2005.864273.

[2] E. W. Collings *et al.*, “Interstrand Coupling Properties of LARP High Gradient Quadrupole Cables in Response to Variations in Cable Design and Heat Treatment Condition,” *IEEE Trans. Appl. Supercond.*, vol. 27, no. 4, Jun. 2017, doi: 10.1109/TASC.2016.2645235.

[3] Y. Lvovsky, E. W. Stautner, and T. Zhang, “Novel technologies and configurations of superconducting magnets for MRI,” *Supercond. Sci. Technol.*, vol. 26, no. 9, p. 093001, Jul. 2013, doi: 10.1088/0953-2048/26/9/093001.

[4] J. Bascuñán, H. Lee, E. S. Bobrov, and Y. Iwasa, “A low- and high-temperature superconducting NMR magnet: Design and performance results,” *IEEE Trans. Appl. Supercond.*, vol. 13, no. 2 II, pp. 1550–1553, Jun. 2003, doi: 10.1109/TASC.2003.812771.

[5] W. Buckles and W. V. Hassenzahl, “Superconducting magnetic energy storage,” *IEEE Power Eng. Rev.*, vol. 20, no. 5, pp. 16–20, 2000, doi: 10.1109/39.841345.

[6] H. H. J. Ten Kate, “Superconducting magnet system for the ATLAS detector at CERN,” *IEEE Trans. Appl. Supercond.*, vol. 9, no. 2 PART 1, pp. 841–846, 1999, doi: 10.1109/77.783428.

[7] H. Bai *et al.*, “The 40 T Superconducting Magnet Project at the National High Magnetic Field Laboratory,” *IEEE Trans. Appl. Supercond.*, vol. 30, no. 4, Jun. 2020, doi: 10.1109/TASC.2020.2969642.

[8] T. Kiyoshi *et al.*, “Development and operation of superconducting NMR magnet beyond 900 MHz,” *IEEE Trans. Appl. Supercond.*, vol. 11, no. 1 II, pp. 2347–2350, Mar. 2001, doi: 10.1109/77.920332.

[9] Y. Lvovsky, E. W. Stautner, and T. Zhang, “Novel technologies and configurations of superconducting magnets for MRI,” *Supercond. Sci. Technol.*, vol. 26, no. 9, 2013, doi: 10.1088/0953-2048/26/9/093001.

[10] M. T. HyperTech, “Commercial Rules for Making Money with Superconducting Applications (Does it pass the $ test).” https://www.nist.gov/system/files/documents/pml/high_megawatt/Tomsic-DOE-NIST-Motor-Workshop-Sept-8-Mike-Tomsic-Hyper-Tech.pdf (accessed Apr. 03, 2024).

[11] H. Kamerlingh, “Further experiments with Liquid Helium. D. On the change of Electrical Resistance of Pure Metals at very low Temperatures, etc. V. The Disappearance of the resistance of mercury,” pp. 113–115, 1911.

[12] R. C. Jaklevic, J. Lambe, A. H. Silver, and J. E. Mercereau, “Quantum interference effects in Josephson tunneling,” *Phys. Rev. Lett.*, vol. 12, no. 7, pp. 159–160, 1964, doi: 10.1103/PhysRevLett.12.159.

[13] H. Matsuo, Y. Mori, H. Ezawa, S. Ariyoshi, and C. Otani, “Submillimeter-wave camera using SIS photon detectors,” *IRMMW-THz 2006 - 31st Int. Conf. Infrared Millim. Waves 14th Int. Conf. Terahertz Electron.*, p. 28, 2006, doi: 10.1109/ICIMW.2006.368237.

[14] X. Zhu *et al.*, “Coherent coupling of a superconducting flux qubit to an electron spin ensemble in diamond,” *Nature*, vol. 478, no. 7368, pp. 221–224, Oct. 2011, doi: 10.1038/nature10462.

[15] J. Clarke and F. K. Wilhelm, “Superconducting quantum bits,” *Nature*, vol. 453, no. 7198. Nature Publishing Group, pp. 1031–1042, Jun. 2008, doi: 10.1038/nature07128.

[16] T. Wu *et al.*, “Magnetic-field-induced charge-stripe order in the high-temperature superconductor YBa 2Cu 3O y,” *Nature*, vol. 477, no. 7363, pp. 191–194, Sep. 2011, doi: 10.1038/nature10345.

[17] J. F. Schenck *et al.*, “Superconducting open-configuration MR imaging system for image-guided therapy,” *Radiology*, vol. 195, no. 3, pp. 805–814, 1995, doi: 10.1148/radiology.195.3.7754014.

[18] L. Evans and P. Bryant, “LHC Machine,” *J. Instrum.*, vol. 3, no. 8, 2008, doi: 10.1088/1748-0221/3/08/S08001.

[19] C. A. Luongo *et al.*, “Next generation more-electric aircraft: a potential application for hts superconductors,” in *IEEE Transactions on Applied Superconductivity*, Jun. 2009, vol. 19, no. 3, pp. 1055–1068, doi: 10.1109/TASC.2009.2019021.

[20] M. Parizh, Y. Lvovsky, and M. Sumption, “Conductors for commercial MRI magnets beyond NbTi: requirements and challenges,” *Supercond. Sci. Technol.*, vol. 30, no. 1, p. 014007, Nov. 2016, doi: 10.1088/0953-2048/30/1/014007.

[21] P. J. Lee *et al.*, “Development of high performance Nb-Ti(Fe) multifilamentary superconductor for the LHC insertion quadrupoles,” *IEEE Trans. Appl. Supercond.*, vol. 9, no. 2 PART 2, pp. 1559–1562, 1999, doi: 10.1109/77.784692.

[22] W. A. Fietz, C. D. Henning, and R. M. Scanlan, “Muxtifilamentary NB3SN conductor for fusion research magnets,” *IEEE Trans. Magn.*, vol. 11, no. 2, pp. 299–302, 1975, doi: 10.1109/TMAG.1975.1058680.

[23] D. Ciazynski, “Review of Nb3Sn conductors for ITER,” *Fusion Eng. Des.*, vol. 82, no. 5–14, pp. 488–497, Oct. 2007, doi: 10.1016/J.FUSENGDES.2007.01.024.

[24] L. Ozyuzer *et al.*, “Emission of Coherent THz Radiation from Superconductors,” *New Ser.*, vol. 318, no. 5854, pp. 1291–1293, 2007, doi: 10.1126/science.ll46764.

[25] C. M. Friend *et al.*, “The development of high field magnets utilizing Bi-2212 wind react insert coils,” *IEEE Trans. Appl. Supercond.*, vol. 20, no. 3, pp. 583–586, Jun. 2010, doi: 10.1109/TASC.2010.2043237.

[26] T. Tsurudome *et al.*, “Reliability of Bi-2223/AgAu current leads for cryocooled superconducting magnet,” *IEEE Trans. Appl. Supercond.*, vol. 23, no. 3, 2013, doi: 10.1109/TASC.2013.2245282.

[27] G. N. Gol’tsman *et al.*, “Picosecond superconducting single-photon optical detector,” *Appl. Phys. Lett.*, vol. 79, no. 6, pp. 705–707, Aug. 2001, doi: 10.1063/1.1388868.

[28] S. Y. Lee and B. Oh, “Recent progress in microwave HTS technologies in Korea and Japan,” *J. Supercond. Nov. Magn.*, vol. 16, no. 5, pp. 823–831, 2003, doi: 10.1023/A:1026202901726.

[29] V. S. Vyatkin, M. Kiuchi, E. S. Otabe, and T. Matsushita, “Design of practical superconducting DC power cable with REBCO coated conductors,” *IEEE Trans. Appl. Supercond.*, vol. 25, no. 4, Aug. 2015, doi: 10.1109/TASC.2015.2427357.

[30] A. C. Smith, A. Oliver, X. Pei, M. Husband, and M. Rindfleisch, “Experimental testing and modelling of a resistive type superconducting fault current limiter using MgB2 wire,” *Supercond. Sci. Technol.*, vol. 25, no. 12, Dec. 2012, doi: 10.1088/0953-2048/25/12/125018.

[31] D. Cunnane *et al.*, “Characterization of MgB2 superconducting hot electron bolometers,” *IEEE Trans. Appl. Supercond.*, vol. 25, no. 3, Jun. 2015, doi: 10.1109/TASC.2014.2369353.

[32] B. H. Yoo, J. C. Kim, Y. G. Kim, D. Y. Hwang, J. H. Lee, and H. G. Lee, “Investigation of multifilament MgB2 superconducting joint technique for development of MRI magnets,” *Rev. Sci. Instrum.*, vol. 89, no. 9, 2018, doi: 10.1063/1.5040549.

[33] L. Rossi, O. Brüning, C. Ats-Do, and G. Switzerland, “PROGRESS WITH THE HIGH LUMINOSITY LHC PROJECT AT CERN*,” 2019, doi: 10.18429/JACoW-IPAC2019-MOYPLM3.

[34] R. Warner, “Ultra-high field magnets for whole-body MRI,” *Supercond. Sci. Technol.*, vol. 29, no. 9, Aug. 2016, doi: 10.1088/0953-2048/29/9/094006.

[35] W. B. Reinhold Kleiner, *Superconductivity: An Introduction*, 3rd Editio. Wiley, 2015.

[36] W. Meissner and R. Ochsenfeld, “Ein neuer Effekt bei Eintritt der Supraleitfähigkeit,” *Naturwissenschaften*, vol. 21, no. 44, pp. 787–788, Nov. 1933, doi: 10.1007/BF01504252.

[37] R. Wesche, *Physical Properties of High-Temperature Superconductors*, 1st Editio. Wiley, 2015.

[38] S. R. Foltyn *et al.*, “Materials science challenges for high-temperature superconducting wire,” *Nature Materials*, vol. 6, no. 9. Nature Publishing Group, pp. 631–642, 2007, doi: 10.1038/nmat1989.

[39] T. Boutboul, S. Le Naour, D. Leroy, L. Oberli, and V. Previtali, “Critical current

density in superconducting Nb - Ti strands in the 100 mT to 11 T applied field range," in *IEEE Transactions on Applied Superconductivity*, Jun. 2006, vol. 16, no. 2, pp. 1184–1187, doi: 10.1109/TASC.2006.870777.

[40] V. Braccini *et al.*, "Properties of recent IBAD-MOCVD coated conductors relevant to their high field, low temperature magnet use," *Supercond. Sci. Technol.*, vol. 24, no. 3, pp. 35001–35010, Dec. 2011, doi: 10.1088/0953-2048/24/3/035001.

[41] G. Z. Li *et al.*, "Effects of carbon concentration and filament number on advanced internal Mg infiltration-processed MgB2 strands," *Supercond. Sci. Technol.*, vol. 26, no. 9, p. 095007, Sep. 2013, doi: 10.1088/0953-2048/26/9/095007.

[42] J. A. Parrell, "Nb3Sn Conductor Development for Fusion and Particle Accelerator Applications," in *AIP Conference Proceedings*, Jul. 2004, vol. 711, no. 1, pp. 369–375, doi: 10.1063/1.1774590.

[43] National High Magnetic Field Laboratory, "Engineering Critical Current Density vs. Applied for Superconductors Available in Long Lengths," *National MagLab*, 2018. https://nationalmaglab.org/magnet-development/applied-superconductivity-center/plots/.

[44] G. Giunchi and B. Coppi, "MgB2 coil options for fusion poloidal magnets," *IEEE Trans. Appl. Supercond.*, vol. 20, no. 3, pp. 1610–1613, Jun. 2010, doi: 10.1109/TASC.2010.2043664.

[45] A. A. Amin *et al.*, "Mechanical Analysis of MgB2 Based Full Body MRI Coils under Different Winding Conditions," *IEEE Trans. Appl. Supercond.*, vol. 27, no. 4, Jun. 2017, doi: 10.1109/TASC.2017.2654349.

[46] T. Baig *et al.*, "Conceptual designs of conduction cooled MgB2 magnets for 1.5 and

3.0 T full body MRI systems," *Supercond. Sci. Technol.*, vol. 30, no. 4, Mar. 2017, doi: 10.1088/1361-6668/AA609B.

[47] A. Ballarino *et al.*, "The BEST PATHS Project on MgB2 Superconducting Cables for Very High Power Transmission," *IEEE Trans. Appl. Supercond.*, vol. 26, no. 3, Apr. 2016, doi: 10.1109/TASC.2016.2545116.

[48] G. Sarmiento *et al.*, "Design and Testing of Real-Scale MgB2 Coils for SUPRAPOWER 10-MW Wind Generators," *IEEE Trans. Appl. Supercond.*, vol. 26, no. 3, Apr. 2016, doi: 10.1109/TASC.2016.2524460.

[49] A. K. Jha and K. Matsumoto, "Superconductive REBCO thin films and their nanocomposites: The role of rare-earth oxides in promoting sustainable energy," *Front. Phys.*, vol. 7, no. JUN, p. 449335, Jun. 2019, doi: 10.3389/FPHY.2019.00082/BIBTEX.

[50] Y. Iwasa, D. C. Larbalestier, M. Okada, R. Penco, M. D. Sumption, and X. Xi, "A round table discussion on MgB2 toward a wide market or a niche production? - A summary," *IEEE Trans. Appl. Supercond.*, vol. 16, no. 2, pp. 1457–1464, Jun. 2006, doi: 10.1109/TASC.2006.873235.

[51] J. Nagamatsu, N. Nakagawa, T. Muranaka, Y. Zenitani, and J. Akimitsu, "Superconductivity at 39 K in magnesium diboride," *Nature*, vol. 410, no. 6824, pp. 63–64, Mar. 2001, doi: 10.1038/35065039.

[52] I. I. Mazin and V. P. Antropov, "Electronic structure, electron-phonon coupling, and multiband effects in MgB 2," *Phys. C Supercond. its Appl.*, vol. 385, no. 1–2, pp. 49–65, Mar. 2003, doi: 10.1016/S0921-4534(02)02299-2.

[53] D. G. Hinks, H. Claus, and J. D. Jorgensen, "The complex nature of

superconductivity in MgB2 as revealed by the reduced total isotope effect," *Nat. 2001 4116836*, vol. 411, no. 6836, pp. 457–460, May 2001, doi: 10.1038/35078037.

[54] J. M. An and W. E. Pickett, "Superconductivity of MgB2: Covalent Bonds Driven Metallic," *Phys. Rev. Lett.*, vol. 86, no. 19, pp. 4366–4369, Feb. 2001, doi: 10.1103/PhysRevLett.86.4366.

[55] H. J. Choi, D. Roundy, H. Sun, M. L. Cohen, and S. G. Louie, "The origin of the anomalous superconducting properties of MgB2," *Nat. 2002 4186899*, vol. 418, no. 6899, pp. 758–760, Aug. 2002, doi: 10.1038/nature00898.

[56] J. C. Loudon, S. Yazdi, T. Kasama, N. D. Zhigadlo, and J. Karpinski, "Measurement of the penetration depth and coherence length of MgB2 in all directions using transmission electron microscopy," *Phys. Rev. B - Condens. Matter Mater. Phys.*, vol. 91, no. 5, 2015, doi: 10.1103/PhysRevB.91.054505.

[57] P. C. Canfield, S. L. Bud'ko, and D. K. Finnemore, "An overview of the basic physical properties of MgB 2," *Phys. C Supercond. its Appl.*, vol. 385, no. 1–2, pp. 1–7, Mar. 2003, doi: 10.1016/S0921-4534(02)02328-6.

[58] Z. Wang, J. M. Van Oort, and M. X. Zou, "Development of superconducting magnet for high-field MR systems in China," *Phys. C Supercond. its Appl.*, vol. 482, no. 2012, pp. 80–86, 2012, doi: 10.1016/j.physc.2012.04.027.

[59] C. Shekhar, R. Giri, R. S. Tiwari, D. S. Rana, S. K. Malik, and O. N. Srivastava, "Effect of la doping on microstructure and critical current density of MgB2," *Supercond. Sci. Technol.*, vol. 18, no. 9, pp. 1210–1214, Sep. 2005, doi: 10.1088/0953-2048/18/9/011.

[60] X. X. Xi, "Two-band superconductor magnesium diboride," *Reports Prog. Phys.*,

vol. 71, no. 11, Nov. 2008, doi: 10.1088/0034-4885/71/11/116501.

[61] Y. Zhu *et al.*, “MgO platelets and high critical field in MgB2 thin films doped with carbon from methane,” *Supercond. Sci. Technol.*, vol. 22, no. 12, p. 4, Oct. 2009, doi: 10.1088/0953-2048/22/12/125001.

[62] C. G. Zhuang *et al.*, “Significant improvements of the high-field properties of carbon-doped MgB2 films by hot-filament-assisted hybrid physical-chemical vapor deposition using methane as the doping source,” *Supercond. Sci. Technol.*, vol. 21, no. 8, p. 082002, Aug. 2008, doi: 10.1088/0953-2048/21/8/082002.

[63] W. Dai *et al.*, “High-field properties of carbon-doped MgB2 thin films by hybrid physical-chemical vapor deposition using different carbon sources,” *Supercond. Sci. Technol.*, vol. 24, no. 12, pp. 125014–125026, Dec. 2011, doi: 10.1088/0953-2048/24/12/125014.

[64] J. M. Rowell, “The widely variable resistivity of MgB2 samples,” *Supercond. Sci. Technol.*, vol. 16, no. 6, 2003, doi: 10.1088/0953-2048/16/6/201.

[65] R. C. Dynes and J. P. Garno, “Metal-Insulator Transition in Granular Aluminum,” *Phys. Rev. Lett.*, vol. 46, no. 2, p. 137, Jan. 1981, doi: 10.1103/PhysRevLett.46.137.

[66] P. A. Sharma *et al.*, “Percolative Superconductivity in Mg1-xB2,” *Phys. Rev. Lett.*, vol. 89, no. 16, pp. 167003/1-167003/4, Oct. 2002, doi: 10.1103/PHYSREVLETT.89.167003.

[67] Y. Eltsev *et al.*, “Anisotropic superconducting properties of MgB2 single crystals probed by in-plane electrical transport measurements,” *Phys. Rev. B - Condens. Matter Mater. Phys.*, vol. 65, no. 14, pp. 1–4, Jan. 2002, doi: 10.1103/PhysRevB.65.140501.

[68] A. Yamamoto and R. Flükiger, “Processing of Low Tc Conductors: The Compound MgB2,” *Handb. Supercond.*, pp. 308–323, Jul. 2022, doi: 10.1201/9780429183027-22.

[69] T. Matsushita, M. Kiuchi, A. Yamamoto, J. I. Shimoyama, and K. Kishio, “Essential factors for the critical current density in superconductingMgB2: connectivity and flux pinning by grain boundaries,” *Supercond. Sci. Technol.*, vol. 21, no. 1, p. 015008, Nov. 2007, doi: 10.1088/0953-2048/21/01/015008.

[70] A. Yamamoto, J. I. Shimoyama, K. Kishio, and T. Matsushita, “Limiting factors of normal-state conductivity in superconductingMgB2: an application of mean-field theory for a site percolation problem,” *Supercond. Sci. Technol.*, vol. 20, no. 7, p. 658, Jun. 2007, doi: 10.1088/0953-2048/20/7/012.

[71] D. C. Larbalestier *et al.*, “Strongly linked current flow in polycrystalline forms of the superconductor MgB2,” *Nature*, vol. 410, no. 6825, pp. 186–189, Mar. 2001, doi: 10.1038/35065559.

[72] S. Kim, D. S. Stone, J. I. Cho, C. Y. Jeong, C. S. Kang, and J. C. Bae, “Phase stability determination of the Mg–B binary system using the CALPHAD method and ab initio calculations,” *J. Alloys Compd.*, vol. 470, no. 1–2, pp. 85–89, Feb. 2009, doi: 10.1016/J.JALLCOM.2008.02.099.

[73] M. W. Chase, *NIST-JANAF Thermochemical Tables*, 4th Editio. American Institute of Physics, -1, 1998.

[74] L. P. Cook, R. Klein, W. Wong-Ng, Q. Huang, R. A. Ribeiro, and P. C. Canfield, “Thermodynamics of MgB2 - By calorimetry and Knudsen thermogravimetry,” *IEEE Trans. Appl. Supercond.*, vol. 15, no. 2, pp. 3227–3229, Jun. 2005, doi: 10.1109/TASC.2005.848809.

[75] J. H. Kim, S. X. Dou, D. Q. Shi, M. Rindfleisch, and M. Tomsic, “Study of MgO formation and structural defects in in situ processedMgB2/Fe wires,” *Supercond. Sci. Technol.*, vol. 20, no. 10, p. 1026, Sep. 2007, doi: 10.1088/0953-2048/20/10/023.

[76] G. Balducci *et al.*, “Thermodynamics of the intermediate phases in the Mg–B system,” *J. Phys. Chem. Solids*, vol. 66, no. 2–4, pp. 292–297, Feb. 2005, doi: 10.1016/J.JPCS.2004.06.063.

[77] D. Patel *et al.*, “Tailored joint fabrication process derived ultra-low resistance MgB2 superconducting joint,” *Scr. Mater.*, vol. 178, pp. 198–202, 2020, doi: 10.1016/j.scriptamat.2019.11.020.

[78] D. K. Singh, B. Tiwari, R. Jha, H. Kishan, and V. P. S. Awana, “Role of MgO impurity on the superconducting properties of MgB2,” *Phys. C Supercond. its Appl.*, vol. 505, pp. 104–108, Oct. 2014, doi: 10.1016/j.physc.2014.06.004.

[79] C. H. Jiang, H. Hatakeyama, and H. Kumakura, “Effect of nanometer MgO addition on the in situ PIT processed MgB 2/Fe tapes,” *Phys. C Supercond. its Appl.*, vol. 423, no. 1–2, pp. 45–50, Jun. 2005, doi: 10.1016/j.physc.2005.03.022.

[80] R. F. Klie *et al.*, “Observation of coherent oxide precipitates in polycrystalline MgB2,” *Appl. Phys. Lett.*, vol. 80, no. 21, pp. 3970–3972, May 2002, doi: 10.1063/1.1481239.

[81] X. Z. Liao *et al.*, “Mg(B,O)2 precipitation in MgB2,” *J. Appl. Phys.*, vol. 93, no. 10, pp. 6208–6215, May 2003, doi: 10.1063/1.1568528.

[82] R. F. Klie, J. C. Idrobo, N. D. Browning, K. A. Regan, N. S. Rogado, and R. J. Cava, “Direct observation of nanometer-scale Mg- and B-oxide phases at grain

boundaries in MgB2," *Appl. Phys. Lett.*, vol. 79, no. 12, pp. 1837–1839, Sep. 2001, doi: 10.1063/1.1404127.

[83] H. Fujii, H. Kumakura, and K. Togano, "Influence of MgB2 powder quality on the transport properties of Cu-sheathed MgB2 tapes," *Phys. C Supercond.*, vol. 363, no. 4, pp. 237–242, Dec. 2001, doi: 10.1016/S0921-4534(01)01094-2.

[84] A. Serquis *et al.*, "The influence of structural defects on intra-granular critical currents of bulk MgB2," *IEEE Trans. Appl. Supercond.*, vol. 13, no. 2 III, pp. 3068–3071, Jun. 2003, doi: 10.1109/TASC.2003.812093.

[85] J. M. Rowell *et al.*, "Critical current density and resistivity of MgB2 films," *Appl. Phys. Lett.*, vol. 83, no. 1, pp. 102–104, Jul. 2003, doi: 10.1063/1.1590734.

[86] C. B. Eom *et al.*, "High critical current density and enhanced irreversibility field in superconducting MgB2 thin films," *Nat. 2001 4116837*, vol. 411, no. 6837, pp. 558–560, May 2001, doi: 10.1038/35079018.

[87] R. K. Singh, Y. Shen, R. Gandikota, C. Carvalho, J. M. Rowell, and N. Newman, "Effect of oxygen incorporation on normal and superconducting properties of MgB2 films," *Appl. Phys. Lett.*, vol. 93, no. 24, Dec. 2008, doi: 10.1063/1.3049618/336267.

[88] S. Brutti, G. Balducci, G. Gigli, A. Ciccioli, P. Manfrinetti, and A. Palenzona, "Thermodynamic and kinetic aspects of decomposition of MgB2 in vacuum: Implications for optimization of synthesis conditions," *J. Cryst. Growth*, vol. 289, no. 2, pp. 578–586, Apr. 2006, doi: 10.1016/J.JCRYSGRO.2005.12.105.

[89] C. E. J. Dancer, P. Mikheenko, A. Bevan, J. S. Abell, R. I. Todd, and C. R. M. Grovenor, "A study of the sintering behaviour of magnesium diboride," *J. Eur.*

Ceram. Soc., vol. 29, pp. 1817–1824, 2009, doi: 10.1016/j.jeurceramsoc.2008.09.025.

[90] G. Grasso *et al.*, “Fabrication and properties of monofilamentary MgB2 superconducting tapes,” in *Superconductor Science and Technology*, Feb. 2003, vol. 16, no. 2, pp. 271–275, doi: 10.1088/0953-2048/16/2/325.

[91] C. Dancer, “Ceramic processing of magnesium diboride,” dissertation, Thesis (D.Phil.)--University of Oxford, 2008., 2008.

[92] H. Kumakura, A. Matsumoto, H. Fujii, and K. Togano, “High transport critical current density obtained for powder-in-tube-processed MgB2 tapes and wires using stainless steel and Cu–Ni tubes,” *Appl. Phys. Lett.*, vol. 79, no. 15, pp. 2435–2437, Oct. 2001, doi: 10.1063/1.1407856.

[93] P. Lezza, R. Gladyshevskii, H. L. Suo, and R. Flükiger, “Quantitative study of the inhomogeneous distribution of phases in Fe-sheathed exsitu MgB2 tapes,” *Supercond. Sci. Technol.*, vol. 18, no. 5, p. 753, Apr. 2005, doi: 10.1088/0953-2048/18/5/030.

[94] D. Eyidi, O. Eibl, T. Wenzel, K. G. Nickel, S. I. Schlachter, and W. Goldacker, “Superconducting properties, microstructure and chemical composition of MgB2 sheathed materials,” *Supercond. Sci. Technol.*, vol. 16, no. 7, p. 778, Jun. 2003, doi: 10.1088/0953-2048/16/7/307.

[95] C. R. M. Grovenor, L. Goodsir, C. J. Salter, P. Kovac, and I. Husek, “Interfacial reactions and oxygen distribution inMgB2 wires in Fe, stainless steel and Nb sheaths,” *Supercond. Sci. Technol.*, vol. 17, no. 3, p. 479, Jan. 2004, doi: 10.1088/0953-2048/17/3/030.

[96] B. Birajdar, V. Braccini, A. Tumino, T. Wenzel, O. Eibl, and G. Grasso, “MgB2 multifilamentary tapes: microstructure, chemical composition and superconductingproperties,” *Supercond. Sci. Technol.*, vol. 19, no. 9, p. 916, Jul. 2006, doi: 10.1088/0953-2048/19/9/006.

[97] A. Kario *et al.*, “Ex situ MgB2 barrier behaviorof monofilament in situ MgB2 wires with Glidcop® sheath material,” *Supercond. Sci. Technol.*, vol. 23, no. 11, p. 115007, Oct. 2010, doi: 10.1088/0953-2048/23/11/115007.

[98] W. Mickelson, J. Cumings, W. Q. Han, and A. Zettl, “Effects of carbon doping on superconductivity in magnesium diboride,” *Phys. Rev. B - Condens. Matter Mater. Phys.*, vol. 65, no. 5, pp. 1–3, 2002, doi: 10.1103/PhysRevB.65.052505.

[99] S. Soltanian, J. Horvat, X. L. Wang, P. Munroe, and S. X. Dou, “Effect of nano-carbon particle doping on the flux pinning properties of MgB2 superconductor,” *Phys. C Supercond. its Appl.*, vol. 390, no. 3, pp. 185–190, Jul. 2003, doi: 10.1016/S0921-4534(03)00960-2.

[100] W. K. Yeoh *et al.*, “Control of nano carbon substitution for enhancing the critical current density in MgB2,” *Supercond. Sci. Technol.*, vol. 19, no. 6, pp. 596–599, Jun. 2006, doi: 10.1088/0953-2048/19/6/030.

[101] W. K. Yeoh and S. X. Dou, “Enhancement of Hc2 and Jc by carbon-based chemical doping,” *Physica C: Superconductivity and its Applications*, vol. 456, no. 1–2. pp. 170–179, Jun. 2007, doi: 10.1016/j.physc.2007.01.024.

[102] M. Paranthaman, J. R. Thompson, and D. K. Christen, “Effect of carbon-doping in bulk superconducting MgB2 samples,” *Phys. C Supercond. its Appl.*, vol. 355, no. 1–2, pp. 1–5, Jun. 2001, doi: 10.1016/S0921-4534(01)00424-5.

[103] X. L. Wang *et al.*, “Significant enhancement of critical current density and flux pinning in MgB2 with nano-SiC, Si, and C doping,” in *Physica C: Superconductivity and its Applications*, Aug. 2004, vol. 408–410, no. 1–4, pp. 63–67, doi: 10.1016/j.physc.2004.02.030.

[104] C. H. Cheng *et al.*, “Doping effect of nano-diamond on superconductivity and flux pinning in MgB2,” *Supercond. Sci. Technol.*, vol. 16, no. 10, pp. 1182–1186, Oct. 2003, doi: 10.1088/0953-2048/16/10/310.

[105] J. L. Wang, R. Zeng, J. H. Kim, L. Lu, and S. X. Dou, “Effects of C substitution on the pinning mechanism of MgB2,” *Phys. Rev. B - Condens. Matter Mater. Phys.*, vol. 77, no. 17, May 2008, doi: 10.1103/PhysRevB.77.174501.

[106] R. H. T. Wilke, S. L. Bud’ko, P. C. Canfield, D. K. Finnemore, R. J. Suplinskas, and S. T. Hannahs, “Systematic effects of carbon doping on the superconducting properties of Mg(B1-xCx)2,” *Phys. Rev. Lett.*, vol. 92, no. 21, May 2004, doi: 10.1103/PhysRevLett.92.217003.

[107] S. X. Dou, W. K. Yeoh, J. Horvat, and M. Ionescu, “Effect of carbon nanotube doping on critical current density of MgB2 superconductor,” *Appl. Phys. Lett.*, vol. 83, no. 24, pp. 4996–4998, Dec. 2003, doi: 10.1063/1.1634378.

[108] M. Kodama *et al.*, “High-performance dense MgB2 superconducting wire fabricated from mechanically milled powder,” *Supercond. Sci. Technol.*, vol. 30, no. 4, Mar. 2017, doi: 10.1088/1361-6668/aa5f36.

[109] S. Choi *et al.*, “Evaluation and control of residual amorphous phases in carbon-doped MgB2 superconductors,” *J. Alloys Compd.*, vol. 864, May 2021, doi: 10.1016/j.jallcom.2021.158867.

[110] Y. Yang, M. D. Sumption, and E. W. Collings, “Influence of Metal Diboride and Dy2O3 Additions on Microstructure and Properties of MgB2 Fabricated at High Temperatures and under Pressure,” *Sci. Rep.*, vol. 6, no. July, pp. 1–11, 2016, doi: 10.1038/srep29306.

[111] S. X. Dou *et al.*, “Nanoscale-SiC doping for enhancing J c and H c2 in superconducting MgB 2,” *J. Appl. Phys.*, vol. 96, no. 12, pp. 7549–7555, Dec. 2004, doi: 10.1063/1.1814415.

[112] S. X. Dou *et al.*, “Superconductivity, critical current density, and flux pinning in MgB 2-x(SiC)x/2 superconductor after SiC nanoparticle doping,” *J. Appl. Phys.*, vol. 94, no. 3, pp. 1850–1856, Aug. 2003, doi: 10.1063/1.1586467.

[113] G. Serrano *et al.*, “SiC and carbon nanotube distinctive effects on the superconducting properties of bulk MgB2,” *J. Appl. Phys.*, vol. 103, no. 2, 2008, doi: 10.1063/1.2832463.

[114] S. X. Dou *et al.*, “Enhancement of the critical current density and flux pinning of MgB 2 superconductor by nanoparticle SiC doping,” *Appl. Phys. Lett.*, vol. 81, no. 18, pp. 3419–3421, Oct. 2002, doi: 10.1063/1.1517398.

[115] A. Matsumoto, H. Kumakura, H. Kitaguchi, and H. Hatakeyama, “Effect of SiO2 and SiC doping on the powder-in-tube processed MgB2 tapes,” *Supercond. Sci. Technol.*, vol. 16, no. 8, pp. 926–930, Aug. 2003, doi: 10.1088/0953-2048/16/8/317.

[116] D. Tripathi and T. K. Dey, “Effect of nano-AlN addition on the critical current density of MgB 2 superconductors,” *J. Supercond. Nov. Magn.*, vol. 27, no. 7, pp. 1647–1658, 2014, doi: 10.1007/s10948-014-2508-1.

[117] C. H. Jiang, T. Nakane, and H. Kumakura, “JC enhancement in nano-Si3N4 doped

MgB2/Fe tapes prepared by a short pre-annealing and intermediate rolling process," in *IEEE Transactions on Applied Superconductivity*, Jun. 2007, vol. 17, no. 2, pp. 2818–2821, doi: 10.1109/TASC.2007.897917.

[118] K. Vinod, N. Varghese, R. G. A. Kumar, U. Syamaprasad, and S. B. Roy, "Influence of Mg particle size on the reactivity and superconducting properties of in situ MgB2," *J. Alloys Compd.*, vol. 464, no. 1–2, pp. 33–37, Sep. 2008, doi: 10.1016/J.JALLCOM.2007.10.030.

[119] J. Zhou and P. Bai, "A review on the methods of preparation of elemental boron," *Asia-Pacific J. Chem. Eng.*, vol. 10, no. 3, pp. 325–338, May 2015, doi: 10.1002/APJ.1892.

[120] X. Xu *et al.*, "Effect of boron powder purity on superconducting properties ofMgB2," *Supercond. Sci. Technol.*, vol. 19, no. 6, p. 466, Mar. 2006, doi: 10.1088/0953-2048/19/6/009.

[121] J. N. Wang, "Prediction of Peierls stresses for different crystals," *Mater. Sci. Eng. A*, vol. 206, no. 2, pp. 259–269, Feb. 1996, doi: 10.1016/0921-5093(95)09982-4.

[122] J. D. DeFouw and D. C. Dunand, "Superplastic compressive flow in MgB2," *Acta Mater.*, vol. 57, no. 16, pp. 4745–4750, Sep. 2009, doi: 10.1016/j.actamat.2009.06.033.

[123] M. Tomsic *et al.*, "Overview of MgB2 Superconductor Applications," *Int. J. Appl. Ceram. Technol.*, vol. 4, no. 3, pp. 250–259, Jul. 2007, doi: 10.1111/j.1744-7402.2007.02138.x.

[124] D. Wang *et al.*, "Enhancement of Jc B properties for binary and carbon-doped MgB2 tapes by hot pressing," *Supercond. Sci. Technol.*, vol. 25, no. 6, Jun. 2012,

doi: 10.1088/0953-2048/25/6/065013.

[125] A. V. Pan, S. Zhou, H. Liu, and S. Dou, “Properties of superconducting MgB2 wires: In situ versus ex situ reaction technique,” *Supercond. Sci. Technol.*, vol. 16, no. 5, pp. 639–644, May 2003, doi: 10.1088/0953-2048/16/5/317.

[126] M. Kodama, Y. Ichiki, K. Tanaka, K. Okamoto, A. Yamamoto, and J. I. Shimoyama, “Mechanism for high critical current density in in situ MgB2 wire with large area-reduction ratio,” *Supercond. Sci. Technol.*, vol. 27, no. 5, p. 9, Mar. 2014, doi: 10.1088/0953-2048/27/5/055003.

[127] Y. Yamada, M. Nakatsuka, A. Nitta, K. Tachikawa, and H. Kumakura, “Superconducting properties and structure of in-situ MgB2 tapes with SiC and TiC addition prepared by hot pressing,” in *IEEE Transactions on Applied Superconductivity*, Jun. 2007, vol. 17, no. 2, pp. 2911–2914, doi: 10.1109/TASC.2007.899479.

[128] P. Kováč *et al.*, “Properties of hot pressed MgB2/Ti tapes,” *Phys. C Supercond. its Appl.*, vol. 469, no. 13, pp. 713–716, Jul. 2009, doi: 10.1016/j.physc.2009.03.007.

[129] H. Yamada *et al.*, “Improvement of the critical current properties of in situ powder-in-tube-processed MgB2 tapes by hot pressing,” *Supercond. Sci. Technol.*, vol. 23, no. 4, 2010, doi: 10.1088/0953-2048/23/4/045030.

[130] C. H. Jiang, T. Nakane, H. Hatakeyama, and H. Kumakura, “Enhanced Jc property in nano-SiC doped thin MgB2/Fe wires by a modified in situ PIT process,” *Phys. C Supercond. its Appl.*, vol. 422, no. 3–4, pp. 127–131, Jun. 2005, doi: 10.1016/j.physc.2005.03.014.

[131] I. Hušek and P. Kováč, “ Mechanical properties, interface reactions and transport

current densities of multi-core MgB 2 / Ti / Cu / SS wire ," *Supercond. Sci. Technol.*, vol. 23, no. 7, p. 075012, Jul. 2010, doi: 10.1088/0953-2048/23/7/075012.

[132] M. S. A. Hossain *et al.*, "The enhanced Jc and Birr of insitu MgB2 wires and tapes alloyed with C4H6O5 (malic acid) after cold high pressure densification," *Supercond. Sci. Technol.*, vol. 22, no. 9, 2009, doi: 10.1088/0953-2048/22/9/095004.

[133] M. Kodama *et al.*, "High-performance dense MgB2 superconducting wire fabricated from mechanically milled powder," *Supercond. Sci. Technol.*, vol. 30, no. 4, p. 044006, Mar. 2017, doi: 10.1088/1361-6668/AA5F36.

[134] C. Li *et al.*, "Significant improvement in superconducting properties of in situ powder-in-tube MgB2 wires through anthracene doping and heat treatment optimization," *Supercond. Sci. Technol.*, vol. 32, no. 10, p. 105004, Aug. 2019, doi: 10.1088/1361-6668/AB3159.

[135] Y. Saito, M. Murakami, A. Matsumoto, and H. Kumakura, "Improvement in microstructure and superconducting properties of single-filament powder-in-tube MgB2 wires by cold working with a swaging machine," *Supercond. Sci. Technol.*, vol. 30, no. 6, p. 065005, May 2017, doi: 10.1088/1361-6668/AA6B48.

[136] Y. C. Zhang, A. Matsumoto, K. Togano, Y. Takano, and H. Kumakura, "Enhancement of the critical current density of in-situ powder-in-tube processed MgB2 wires with both xylene and SiC addition," *Phys. C Supercond. its Appl.*, vol. 551, pp. 5–9, Aug. 2018, doi: 10.1016/J.PHYSC.2018.05.004.

[137] H. Jie *et al.*, "Superior transport Jc obtained in in-situ MgB2 wires by tailoring the starting materials and using a combined cold high pressure densification and hot isostatic pressure treatment," *Scr. Mater.*, vol. 129, pp. 79–83, Mar. 2017, doi:

10.1016/J.SCRIPTAMAT.2016.09.042.

[138] A. Yamamoto, H. Tanaka, J. I. Shimoyama, H. Ogino, K. Kishio, and T. Matsushita, “Towards the realization of higher connectivity in MgB 2 conductors: In-situ or sintered ex-situ?,” *Jpn. J. Appl. Phys.*, vol. 51, no. 1, 2012, doi: 10.1143/JJAP.51.010105.

[139] V. Braccini *et al.*, “MgB2 tapes with non-magnetic sheath: Effect of the sintering temperature on the superconducting properties,” *IEEE Trans. Appl. Supercond.*, vol. 15, no. 2 PART III, pp. 3211–3214, Jun. 2005, doi: 10.1109/TASC.2005.848796.

[140] H. L. Suo, C. Beneduce, M. Dhallé, N. Musolino, J. Y. Genoud, and R. Flükiger, “Large transport critical currents in dense Fe- and Ni-clad MgB2 superconducting tapes,” *Appl. Phys. Lett.*, vol. 79, no. 19, pp. 3116–3118, Nov. 2001, doi: 10.1063/1.1415349.

[141] R. Flükiger, H. L. Suo, N. Musolino, C. Beneduce, P. Toulemonde, and P. Lezza, “Superconducting properties of MgB 2 tapes and wires,” *Phys. C Supercond. its Appl.*, vol. 385, no. 1–2, pp. 286–305, 2003, doi: 10.1016/S0921-4534(02)02307-9.

[142] H. Fujii, H. Kumakura, and K. Togano, “Improved critical current in MgB2 tapes sheathed with carbon steels,” *J. Mater. Res.*, vol. 17, no. 9, pp. 2339–2345, Sep. 2002, doi: 10.1557/JMR.2002.0343/METRICS.

[143] G. Grasso *et al.*, “Large transport critical currents in unsintered MgB2 superconducting tapes,” *Appl. Phys. Lett.*, vol. 79, no. 2, pp. 230–232, Jul. 2001, doi: 10.1063/1.1384905.

[144] V. Braccini, D. Nardelli, R. Penco, and G. Grasso, “Development of ex situ processed MgB2 wires and their applications to magnets,” *Phys. C Supercond.*, vol.

456, no. 1–2, pp. 209–217, Jun. 2007, doi: 10.1016/J.PHYSC.2007.01.030.

[145] M. Capra *et al.*, “Characterization of freeze dried boron nanopowders and parameter optimization in MgB2 ex-situ wire production,” *IEEE Trans. Appl. Supercond.*, 2020, doi: 10.1109/TASC.2020.3014318.

[146] G. Bovone *et al.*, “Synthesis temperature effects on ex-situ manufactured MgB2 wires useful for power applications,” *J. Alloys Compd.*, vol. 660, pp. 342–346, Mar. 2016, doi: 10.1016/J.JALLCOM.2015.11.121.

[147] V. Beilin *et al.*, “Evolution of core connectivity in MgB2 wires and tapes during PIT processing,” *Phys. C Supercond. its Appl.*, vol. 405, no. 1, pp. 70–76, May 2004, doi: 10.1016/j.physc.2004.01.016.

[148] I. Hušek, P. Kováč, A. Rosová, T. Melišek, W. Pachla, and M. Hain, “Advanced MgB2 wire made by internal magnesium diffusion process,” *J. Alloys Compd.*, vol. 588, pp. 366–369, Mar. 2014, doi: 10.1016/j.jallcom.2013.11.101.

[149] G. Giunchi, G. Ripamonti, E. Perini, T. Cavallin, and E. Bassani, “Advancements in the reactive liquid Mg infiltration technique to produce long superconducting MgB2 tubular wires,” in *IEEE Transactions on Applied Superconductivity*, Jun. 2007, vol. 17, no. 2, pp. 2761–2765, doi: 10.1109/TASC.2007.900014.

[150] J. M. Hur, K. Togano, A. Matsumoto, H. Kumakura, H. Wada, and K. Kimura, “Fabrication of high-performance MgB2 wires by an internal Mg diffusion process,” in *Superconductor Science and Technology*, Mar. 2008, vol. 21, no. 3, p. 4, doi: 10.1088/0953-2048/21/3/032001.

[151] H. Kumakura, J. Hur, K. Togano, A. Matsumoto, H. Wada, and K. Kimura, “Superconducting properties of diffusion-processed multifilamentary MgB 2 wires,”

IEEE Trans. Appl. Supercond., vol. 21, no. 3 PART 3, pp. 2643–2648, Jun. 2011, doi: 10.1109/TASC.2010.2100342.

[152] K. Togano, J. M. Hur, A. Matsumoto, and H. Kumakura, "Fabrication of seven-core multi-filamentary MgB2 wires with high critical current density by an internal Mg diffusion process," *Supercond. Sci. Technol.*, vol. 22, no. 1, p. 5, Jan. 2009, doi: 10.1088/0953-2048/22/1/015003.

[153] K. Togano, H. Fujii, T. Takeuchi, and H. Kumakura, "Composite process for the fabrication of MgB2 wire using ductile Mg-Li alloy," *Supercond. Sci. Technol.*, vol. 20, no. 3, pp. 239–243, Mar. 2007, doi: 10.1088/0953-2048/20/3/022.

[154] D. Xu *et al.*, "Properties of multifilamentary MgB2 wires fabricated by internal magnesium diffusion using amorphous and crystalline boron powders," *IEEE Trans. Appl. Supercond.*, vol. 27, no. 4, Jun. 2017, doi: 10.1109/TASC.2016.2637321.

[155] R. G. A. Kumar, K. Vinod, N. Varghese, and U. Syamaprasad, "Reactivity of sheath materials with Mg/B inMgB2 conductor fabrication," *Supercond. Sci. Technol.*, vol. 20, no. 3, p. 222, Jan. 2007, doi: 10.1088/0953-2048/20/3/018.

[156] J. C. Grivel, R. Pinholt, N. H. Andersen, P. Kováč, I. Hušek, and J. Homeyer, "In situ investigations of phase transformations in Fe-sheathedMgB2 wires," *Supercond. Sci. Technol.*, vol. 19, no. 1, p. 96, Dec. 2005, doi: 10.1088/0953-2048/19/1/016.

[157] P. Kováč, I. Hušek, T. Melišek, W. Haessler, and M. Herrmann, "Improvement of current density by texture andIc anisotropy inthin filament MgB2/Fe tapes," *Supercond. Sci. Technol.*, vol. 19, no. 10, p. 998, Aug. 2006, doi: 10.1088/0953-2048/19/10/002.

[158] S. Zhou, A. V. Pan, M. Ionescu, H. Liu, and S. Dou, “Influence of Ag, Cu and Fe sheaths on MgB2 superconducting tapes,” *Supercond. Sci. Technol.*, vol. 15, no. 2, p. 236, Jan. 2002, doi: 10.1088/0953-2048/15/2/310.

[159] S. K. Chen, M. Majoros, J. L. MacManus-Driscoll, and B. A. Glowacki, “In situ and ex situ Cu doping of MgB2,” *Phys. C Supercond.*, vol. 418, no. 3–4, pp. 99–106, Feb. 2005, doi: 10.1016/J.PHYSC.2004.11.011.

[160] I. Barin, “Thermochemical Data of Pure Substances,” *Thermochem. Data Pure Subst.*, Oct. 1995, doi: 10.1002/9783527619825.

[161] J. Ling *et al.*, “Construction and persistent-mode operation of MgB2 coils in the range 10-15 K for a 0.5-T/240-mm cold bore MRI magnet,” *IEEE Trans. Appl. Supercond.*, vol. 25, no. 3, pp. 5–9, 2015, doi: 10.1109/TASC.2014.2370105.

[162] M. Takahashi, K. Tanaka, M. Okada, H. Kitaguchi, and H. Kumakura, “Relaxation of trapped high magnetic field in 100 m-long class MgB 2 solenoid coil in persistent current mode operation,” in *IEEE Transactions on Applied Superconductivity*, Jun. 2006, vol. 16, no. 2, pp. 1431–1434, doi: 10.1109/TASC.2006.869993.

[163] E. A. Young, J. Pelegrin, I. Falorio, J. C. Archer, L. L. Jarvis, and Y. Yang, “Temperature and background field dependence of a compact react and wind MgB2 solenoid coil,” *IEEE Trans. Appl. Supercond.*, vol. 25, no. 3, Jun. 2015, doi: 10.1109/TASC.2014.2361095.

[164] A. Matsumoto and H. Kumakura, “Superconducting joints made with internal-magnesium-diffusion-processed MgB2 wires,” *IEEE Trans. Appl. Supercond.*, vol. 28, no. 3, pp. 1–4, 2018, doi: 10.1109/TASC.2017.2772813.

[165] A. M. Valente-Feliciano, “Superconducting RF materials other than bulk niobium:

A review," *Superconductor Science and Technology*, vol. 29, no. 11. Institute of Physics Publishing, Sep. 2016, doi: 10.1088/0953-2048/29/11/113002.

[166] M. Wózniak, B. A. Glowacki, S. B. Setiadinata, and A. M. Thomas, "Pulsed magnetic field assisted technique for joining MgB2 conductors for persistent mode MRI magnets," *IEEE Trans. Appl. Supercond.*, vol. 23, no. 3, 2013, doi: 10.1109/TASC.2012.2229093.

[167] G. Giunchi, L. Saglietti, G. Ripamonti, A. F. Albisetti, E. Bassani, and E. Perini, "Superconducting joints between MgB2 wires and bulks," *IEEE Trans. Appl. Supercond.*, vol. 20, no. 3, pp. 1524–1527, 2010, doi: 10.1109/TASC.2010.2040260.

[168] W. Luo *et al.*, "MgB2 Superconducting Joint Technique Based on Mg Diffusion Method," *IEEE Trans. Appl. Supercond.*, vol. 29, no. 5, pp. 1–5, 2019, doi: 10.1109/TASC.2019.2905419.

[169] D. Patel *et al.*, "Superconducting Joining Concept for Internal Magnesium Diffusion-Processed Magnesium Diboride Wires," *ACS Appl. Mater. Interfaces*, vol. 13, no. 2, pp. 3349–3357, Jan. 2021, doi: 10.1021/ACSAMI.0C17385/SUPPL_FILE/AM0C17385_SI_002.MP4.

[170] W. Yao, J. Bascuñán, S. Hahn, and Y. Iwasa, "A superconducting joint technique for MgB2 round wires," in *IEEE Transactions on Applied Superconductivity*, Jun. 2009, vol. 19, no. 3, pp. 2261–2264, doi: 10.1109/TASC.2009.2019063.

[171] X. H. Li *et al.*, "High critical current joint of MgB2 tapes using Mg and B powder mixture as flux," *Supercond. Sci. Technol.*, vol. 21, no. 2, Feb. 2008, doi: 10.1088/0953-2048/21/2/025017.

[172] Y. G. Kim *et al.*, “Note: Progress on the use of MgB2 superconducting joint technique for the development of MgB2 magnets for magnetic resonance imaging (MRI),” *Rev. Sci. Instrum.*, vol. 88, no. 8, Aug. 2017, doi: 10.1063/1.4997257.

[173] R. Penco and G. Grasso, “Recent development of MgB2-based large scale applications,” in *IEEE Transactions on Applied Superconductivity*, Jun. 2007, vol. 17, no. 2, pp. 2291–2294, doi: 10.1109/TASC.2007.898519.

[174] D. K. Park *et al.*, “MgB 2 for MRI magnets: Test coils and superconducting joints results,” *IEEE Trans. Appl. Supercond.*, vol. 22, no. 3, pp. 3–7, 2012, doi: 10.1109/TASC.2012.2185472.

[175] Y. Yanagisawa, Y. Xu, X. Jin, H. Nakagome, and H. Maeda, “Reduction of screening current-induced magnetic field of REBCO coils by the use of multi-filamentary tapes,” *IEEE Trans. Appl. Supercond.*, vol. 25, no. 3, Jun. 2015, doi: 10.1109/TASC.2014.2377492.

[176] Y. Koyama *et al.*, “Towards beyond 1 GHz NMR: Mechanism of the long-term drift of screening current-induced magnetic field in a Bi-2223 coil,” *Phys. C Supercond. its Appl.*, vol. 469, no. 13, pp. 694–701, Jul. 2009, doi: 10.1016/j.physc.2009.02.014.

[177] G. D. Brittles, T. Mousavi, C. R. M. Grovenor, C. Aksoy, and S. C. Speller, “Persistent current joints between technological superconductors,” *Superconductor Science and Technology*, vol. 28, no. 9. Institute of Physics Publishing, Sep. 2015, doi: 10.1088/0953-2048/28/9/093001.

[178] Y. I. Kazuhide Tanaka, Motomune Kodama, “MGB2-supraleitende mehradrige Drähte, supraleitende Kabel und supraleitende Magnete - Google Patents,” EP2642543A1, 2012.

[179] K. O. Yota ICHIKI, “Joint Portion of Superconducting Wires and Method of Joining Superconducting Wires - Google Patents,” US20190207331A1, 2017.

[180] T. W. Yota ICHIKI, “Joint for superconducting wire - Google Patents,” US20180012682A1.

[181] M’hamed Lakrimi, “Methods for forming joints between magnesium diboride conductors - Google Patents,” US20140364318A1, 2012.

[182] M. W. M Hamed Lakrimi, Adrian Mark Thomas, “Superconducting jointing process - Google Patents,” GB2523812A, 2014.

[183] K. S. Felicitas Tenbrink, André Aubele, Volker Gluecklich, Bernd Sailer, “Superconducting connection between MgB2 superconducting wires via a compressed element made from HTS powder - Google Patents,” US20100216645A1, 2009.

[184] Y. K. Seungyong Hahn, Yukikazu lwasa, Juan Bascunan, John Peter Voccio, Jiayin Ling, Jungbin Song, “Persistent-Mode MRI Magnet Fabricated From Reacted, Monofilamentary MgB2 Wires And Joints - Google Patents,” US20150018220A1, 2014.

[185] M. L. Mark Blumenthal, “Method for joining superconducting wires, and superconducting joint - Google Patents,” US20140135223A1, 2012.

[186] M. T. Motomune Kodama, Michiya Okada, “Superconducting Circuit, Production Method of Superconducting Joints, Superconducting Magnet, and Production Method of Superconducting Magnet - Google Patents,” US20110028327A1, 2009.

[187] T. W. Motomune Kodama, “Superconducting joint and method for manufacturing same - Google Patents,” US20120021915A1, 2010.

[188] S. J. CALVERT, “Joints with very low resistance between superconducting wires and methods for making such joints - Google Patents,” US20140038828A1, 2011.

[189] M. J. T. David W. Doll, “Low loss joint for superconducting wire - Google Patents,” US20100190649A1, 2010.

[190] S. M. D. Judson SloanMarte, Xianrui Huang, Evangelos Trifon Laskaris, Bruce Alan Knudsen, Thomas Robert Raber, Robert John Zabala, James William Bray, Paul Shadforth Thompson, Sergio Paulo Martins Loureiro, Curtis Alan Johnson, “Methods for making low resistivity joints - Google Patents,” US9287485B2, 2007.

[191] K. T. Yota ICHIKI, Tsuyoshi Wakuda, “Joint of superconducting wires and method for joining superconducting wires - Google Patents,” US20120108435A1, 2010.

[192] M. H. L. Mark David Blumenthal, “Methods of joining superconducting wires - Google Patents,” GB2498961A, 2012.

[193] S. Pradhan, S. K. Das, A. Bano, and A. Kundu, “A Novel Technique Toward Fabricating High-Current-Carrying MgB2-Based Superconducting Joints,” *IEEE Trans. Appl. Supercond.*, vol. 26, no. 8, pp. 1–5, 2016, doi: 10.1109/TASC.2016.2594262.

[194] D. Patel *et al.*, “MgB2 superconducting joints for persistent current operation,” *Supercond. Sci. Technol.*, vol. 28, no. 6, 2015, doi: 10.1088/0953-2048/28/6/065017.

[195] H. Tanaka *et al.*, “An MgB2 Superconducting Joint with its Own Heat-Treatment Schedule,” *IEEE Trans. Appl. Supercond.*, vol. 8223, no. August 2017, pp. 1–5, 2021, doi: 10.1109/TASC.2021.3064517.

[196] D. Avcı *et al.*, “Optimized superconducting MgB 2 joint made by IMD technique,”

2023, doi: 10.1088/1361-6668/accf3f.

[197] M. D. Sumption *et al.*, “Wind and react and react and wind MgB2 solenoid, racetrack and pancake coils,” in *IEEE Transactions on Applied Superconductivity*, Jun. 2007, vol. 17, no. 2, pp. 2286–2290, doi: 10.1109/TASC.2007.898039.

[198] H. Tanaka *et al.*, “Conduction-Cooled MgB2 Coil in Maximum Self-Magnetic Flux Density 2.3 Tesla Made with 300-Meter-Long Multifilamentary MgB2 Wire,” *IEEE Trans. Appl. Supercond.*, vol. 27, no. 4, Jun. 2017, doi: 10.1109/TASC.2016.2643443.

[199] D. Zhang *et al.*, “Instrumentation, cooling, and initial testing of a large, conduction-cooled, react-and-wind MgB2 coil segment for MRI applications,” *Supercond. Sci. Technol.*, vol. 31, no. 8, Jul. 2018, doi: 10.1088/1361-6668/aacae3.

[200] N. Banno, K. Kobayashi, A. Uchida, H. Kitaguchi, A. Takenouchi, and M. Watanabe, “Novel Pb-Free Superconducting Joint between NbTi and Nb3Sn Wires Using High-Temperature-Tolerable Superconducting Nb-3Hf Intermedia,” *IEEE Trans. Appl. Supercond.*, vol. 32, no. 6, Sep. 2022, doi: 10.1109/TASC.2022.3168616.

[201] THE EUROPEAN COMMISSION DELEGATED DIRECTIVE (EU) 2022/1632, “Amending, for the purposes of adapting to scientific and technical progress, Annex IV to Directive2011/65/EU of the European Parliament and of the Council as regards an exemption for the use oflead in certain magnetic resonance imaging devices,” *Off. J. Eur. Union*, p. 245, Sep. 2022.

[202] G. A. B. Matthews, S. Santra, R. Ma, C. R. M. Grovenor, P. S. Grant, and S. C. Speller, “Effect of the sintering temperature on the microstructure and superconducting properties of MgB2 bulks manufactured by the field assisted

sintering technique," *Supercond. Sci. Technol.*, vol. 33, no. 5, May 2020, doi: 10.1088/1361-6668/AB7C53.

[203] L. Ingemarsson and M. Halvarsson, "SEM/EDX ANALYSIS OF BORON A case study."

[204] M. Eisterer, "Magnetic Measurements of Critical Current Density, Pinning, and Flux Creep," *Handb. Supercond.*, pp. 209–227, Jul. 2022, doi: 10.1201/9781003139638-14.

[205] Y. Liu *et al.*, "The Upper Critical Field, Anisotropy, and Critical Current Density of Superconducting LaO1-xBiS2 with x = 0.07," *J. Supercond. Nov. Magn.*, vol. 34, no. 4, pp. 1157–1163, Apr. 2021, doi: 10.1007/S10948-021-05845-7/FIGURES/5.

[206] M. Dhallé, "DC Transport Critical Currents," in *Handbook of Superconductivity*, Second EDİ., B. A. I. Cardwell, David A., Larbalestier David C., Ed. CRC Press, 2022, pp. 141–176.

[207] M. J. Raine, S. A. Keys, and D. P. Hampshire, "Characterisation of the Transport Critical Current Density for Conductor Applications," in *Handbook of Superconductivity Vol III*, Second Edi., B. A. I. Cardwell, David A., Larbalestier David C., Ed. CRC Press, 2022, pp. 177–208.

[208] D. A. Cardwell, D. C. Larbalestier, and A. I. Braginski, "E5.3 Persistent Mode Joints," in *Handbook of Superconductivity - Processing and Cryogenics (Volume II)*, 2022, pp. 480–492.

[209] A. Baskys, S. C. Hopkins, J. Bader, and B. A. Glowacki, "Forced flow He vapor cooled critical current testing facility for measurements of superconductors in a wide temperature and magnetic field range," *Cryogenics (Guildf).*, vol. 79, pp. 1–6,

Oct. 2016, doi: 10.1016/J.CRYOGENICS.2016.07.003.

[210] M. J. Leupold and Y. Iwasa, “Superconducting joint between multifilamentary wires 1. Joint-making and joint results,” *Cryogenics (Guildf).*, vol. 16, no. 4, pp. 215–216, 1976, doi: 10.1016/0011-2275(76)90262-9.

[211] A. D. Caplin, L. F. Cohen, G. K. Perkins, and A. A. Zhukov, “The electric field within high-temperature superconductors: mapping the E-J-B surface,” *Supercond. Sci. Technol.*, vol. 7, no. 6, p. 412, Jun. 1994, doi: 10.1088/0953-2048/7/6/014.

[212] Z. Gao *et al.*, “Microstructures and superconducting properties of MgB2 bulk samples processed by ultra-high pressure-assisted sintering,” *J. Eur. Ceram. Soc.*, vol. 42, no. 16, pp. 7481–7490, Dec. 2022, doi: 10.1016/J.JEURCERAMSOC.2022.09.008.

[213] J. Shao *et al.*, “Superhard MgB2 bulk material prepared by high-pressure sintering,” *J. Phys. Condens. Matter*, vol. 14, no. 44, p. 11181, Oct. 2002, doi: 10.1088/0953-8984/14/44/449.

[214] C. U. Jung *et al.*, “Effect of sintering temperature under high pressure on the superconductivity of MgB2,” *Appl. Phys. Lett.*, vol. 78, no. 26, pp. 4157–4159, Jun. 2001, doi: 10.1063/1.1382632.

[215] Y. Takano *et al.*, “Superconducting properties of MgB2 bulk materials prepared by high-pressure sintering,” *Appl. Phys. Lett.*, vol. 78, no. 19, pp. 2914–2916, May 2001, doi: 10.1063/1.1371239.

[216] A. Murakami, H. Teshima, T. Naito, H. Fujishiro, and T. Kudo, “Mechanical Properties of MgB2 Bulks,” *Phys. Procedia*, vol. 58, pp. 98–101, Jan. 2014, doi: 10.1016/J.PHPRO.2014.09.034.

[217] G. A. B. Matthews, S. Santra, R. Ma, C. R. M. Grovenor, P. S. Grant, and S. C. Speller, “Effect of the sintering temperature on the microstructure and superconducting properties of MgB2 bulks manufactured by the field assisted sintering technique,” *Supercond. Sci. Technol.*, vol. 33, no. 5, p. 054003, Mar. 2020, doi: 10.1088/1361-6668/AB7C53.

[218] J. L. Dadiel *et al.*, “Synthesis of Dense MgB2 Superconductor via In Situ and Ex Situ Spark Plasma Sintering Method,” *Mater. 2021, Vol. 14, Page 7395*, vol. 14, no. 23, p. 7395, Dec. 2021, doi: 10.3390/MA14237395.

[219] X. Z. Liao *et al.*, “Mg(B,O)2 precipitation in MgB2,” *J. Appl. Phys.*, vol. 93, no. 10, pp. 6208–6215, May 2003, doi: 10.1063/1.1568528.

[220] T. Prikhna *et al.*, “Pinning in high performance MgB2 thin films and bulks: Role of Mg-B-O nano-scale inhomogeneities,” *Phys. C Supercond. its Appl.*, vol. 533, pp. 36–39, Feb. 2017, doi: 10.1016/J.PHYSC.2016.08.002.

[221] R. K. Kremer, B. J. Gibson, and K. Ahn, “Heat Capacity of MgB_2: Evidence for Moderately Strong Coupling Behavior,” Feb. 2001, Accessed: Apr. 13, 2024. [Online]. Available: https://arxiv.org/abs/cond-mat/0102432v2.

[222] V. Chabanenko *et al.*, “Flux Jumps and H-T diagram of instability for MgB2,” *J. Low Temp. Phys.*, vol. 130, no. 3–4, pp. 175–191, 2003, doi: 10.1023/A:1022236117354/METRICS.

[223] H. Fujii and H. Kitaguchi, “Superconducting properties of sintered ex situ MgB2 tapes through ball milling process as a function of crystallite size in the as-milled and sintered states,” *Phys. C Supercond. its Appl.*, vol. 583, p. 1353838, Apr. 2021, doi: 10.1016/J.PHYSC.2021.1353838.

[224] B. Lorenz, O. Perner, J. Eckert, and C. W. Chu, “Superconducting properties of nanocrystallineMgB2,” *Supercond. Sci. Technol.*, vol. 19, no. 9, p. 912, Jul. 2006, doi: 10.1088/0953-2048/19/9/005.

[225] A. Serquis, Y. T. Zhu, E. J. Peterson, J. Y. Coulter, D. E. Peterson, and F. M. Mueller, “Effect of lattice strain and defects on the superconductivity of MgB2,” *Appl. Phys. Lett.*, vol. 79, no. 26, pp. 4399–4401, Dec. 2001, doi: 10.1063/1.1428109.

[226] M. Muralidhar *et al.*, “Optimization of sintering conditions in bulk MgB2 material for improvement of critical current density,” *J. Alloys Compd.*, vol. 649, pp. 833–842, Nov. 2015, doi: 10.1016/J.JALLCOM.2015.07.191.

[227] J. H. Durrell *et al.*, “A trapped field of >3 T in bulk MgB2 fabricated by uniaxial hot pressing,” *Supercond. Sci. Technol.*, vol. 25, no. 11, p. 112002, Oct. 2012, doi: 10.1088/0953-2048/25/11/112002.

[228] T. Naito, T. Sasaki, and H. Fujishiro, “Trapped magnetic field and vortex pinning properties of MgB2 superconducting bulk fabricated by a capsule method,” *Supercond. Sci. Technol.*, vol. 25, no. 9, p. 095012, Jul. 2012, doi: 10.1088/0953-2048/25/9/095012.

[229] J. L. Wang, R. Zeng, J. H. Kim, L. Lu, and S. X. Dou, “Effects of C substitution on the pinning mechanism of MgB2,” *Phys. Rev. B - Condens. Matter Mater. Phys.*, vol. 77, no. 17, p. 174501, May 2008, doi: 10.1103/PHYSREVB.77.174501/FIGURES/6/MEDIUM.

[230] B. Savaskan *et al.*, “Bulk MgB2 superconductor for levitation applications fabricated with boron processed by different routes,” *J. Alloys Compd.*, vol. 961, p. 170893, Oct. 2023, doi: 10.1016/J.JALLCOM.2023.170893.

[231] B. A. Glowacki *et al.*, “Comparative Study of the Continuous and Batch Thermal Processing of MgB2 Wires,” *IEEE Trans. Appl. Supercond.*, vol. 29, no. 5, Aug. 2019, doi: 10.1109/TASC.2019.2900351.

[232] M. N. Kutukcu *et al.*, “Composite Superconducting MgB2 Wires Made by Continuous Process,” *IEEE Trans. Appl. Supercond.*, vol. 28, no. 4, Jun. 2018, doi: 10.1109/TASC.2018.2820730.

[233] S. Atamert, M. N. Kutukcu, J. L. Scandella, A. Baskys, Z. Zhong, and B. A. Glowacki, “Novel Superconducting MgB2 Wires Made by Continuous Process,” *IEEE Trans. Appl. Supercond.*, vol. 26, no. 3, Apr. 2016, doi: 10.1109/TASC.2016.2549559.

[234] Z. X. Shi *et al.*, “Anisotropic connectivity and its influence on critical currentdensities, irreversibility fields, and flux creep in in situ processedMgB2 strands,” *Supercond. Sci. Technol.*, vol. 23, no. 4, p. 045018, Mar. 2010, doi: 10.1088/0953-2048/23/4/045018.

[235] D. Uchiyama *et al.*, “Fibrous structure and critical current density of MgB2 superconducting wire,” *Cryogenics (Guildf).*, vol. 47, no. 5–6, pp. 282–286, May 2007, doi: 10.1016/J.CRYOGENICS.2007.03.003.

[236] X. L. Wang *et al.*, “Very fast formation of superconducting MgB2/Fe wires with high Jc,” *Phys. C Supercond.*, vol. 361, no. 3, pp. 149–155, Sep. 2001, doi: 10.1016/S0921-4534(01)00900-5.

[237] D. Patel *et al.*, “A new approach to a superconducting joining process for carbon-doped MgB2 conductor,” *Supercond. Sci. Technol.*, vol. 29, no. 9, p. 095001, Jul. 2016, doi: 10.1088/0953-2048/29/9/095001.

[238] Y. Choi *et al.*, “Persistent-mode operation and magnetization behavior of a solid-nitrogen-cooled MgB2 small-scale test coil towards a tabletop 1.5-T osteoporosis MRI,” *Supercond. Sci. Technol.*, vol. 33, no. 12, p. 125007, Oct. 2020, doi: 10.1088/1361-6668/ABBA07.

[239] E. Martínez, R. Navarro, and J. M. Andrés, “Improvement of the critical current density on in situ PIT processed Fe/MgB2 wires by oleic acid addition,” *Supercond. Sci. Technol.*, vol. 26, no. 12, p. 125017, Nov. 2013, doi: 10.1088/0953-2048/26/12/125017.

[240] J. Peng *et al.*, “Enhancement of critical current density by a ‘MgB2-MgB4’ reversible reaction in self-sintered ex-situ MgB2bulks,” *J. Alloys Compd.*, vol. 694, pp. 24–29, 2017, doi: 10.1016/J.JALLCOM.2016.09.312.

[241] S. C. Yan, G. Yan, C. F. Liu, Y. F. Lu, and L. Zhou, “Experimental Study on Phase Transformation Between MgB2 and MgB4,” *J. Am. Ceram. Soc.*, vol. 90, no. 7, pp. 2184–2188, Jul. 2007, doi: 10.1111/J.1551-2916.2007.01664.X.

[242] H. Zhang, L. Li, Y. Zhao, and Y. Zhang, “The performance improvement of MgB2 prepared by the Mg diffusion method with the MgB4 addition,” *J. Phys. Conf. Ser.*, vol. 871, no. 1, p. 012057, Jul. 2017, doi: 10.1088/1742-6596/871/1/012057.

[243] A. Ito, A. Yamamoto, J. Shimoyama, H. Ogino, and K. Kishio, “Synthesis of denser in situ MgB2 Bulks Using MgB4 precursor,” *IEEE Trans. Appl. Supercond.*, vol. 23, no. 3, 2013, doi: 10.1109/TASC.2013.2240035.

[244] R. Schmitt, J. Glaser, T. Wenzel, K. G. Nickel, and H. J. Meyer, “A reactivity study in the Mg–B system reaching for an improved synthesis of pure MgB2,” *Phys. C Supercond.*, vol. 436, no. 1, pp. 38–42, Apr. 2006, doi: 10.1016/J.PHYSC.2006.01.004.

[245] K. L. Tan, K. P. Lim, A. S. Halim, and S. K. Chen, “Enhanced critical current density in MgB2 prepared by reaction of MgB4 and Mg,” *Phys. status solidi*, vol. 210, no. 3, pp. 616–622, Mar. 2013, doi: 10.1002/PSSA.201228752.

[246] R. Pasquet *et al.*, “Design and test of a small react-and-wind MgB2 double pancake,” *IEEE Trans. Appl. Supercond.*, vol. 25, no. 3, Jun. 2015, doi: 10.1109/TASC.2014.2375514.

[247] Z. Y. Fan, D. G. Hinks, N. Newman, and J. M. Rowell, “Experimental study of MgB2 decomposition,” *Appl. Phys. Lett.*, vol. 79, no. 1, pp. 87–89, 2001, doi: 10.1063/1.1383804.

[248] H. Okamoto, “B−Mg (Boron-Magnesium),” in *Journal of Phase Equilibria and Diffusion 2006 27:4*, vol. 27, no. 4, Springer, 2006, pp. 428–428.

[249] Z. K. Liu, D. G. Schlom, Q. Li, and X. X. Xi, “Thermodynamics of the Mg–B system: Implications for the deposition of MgB2 thin films,” *Appl. Phys. Lett.*, vol. 78, no. 23, pp. 3678–3680, Jun. 2001, doi: 10.1063/1.1376145.

[250] F. Grilli and A. Kario, “How filaments can reduce AC losses in HTS coated conductors: a review,” *Supercond. Sci. Technol.*, vol. 29, no. 8, p. 083002, Jul. 2016, doi: 10.1088/0953-2048/29/8/083002.

[251] Y. Koyama *et al.*, “Towards beyond 1 GHz NMR: Mechanism of the long-term drift of screening current-induced magnetic field in a Bi-2223 coil,” *Phys. C Supercond.*, vol. 469, no. 13, pp. 694–701, Jul. 2009, doi: 10.1016/J.PHYSC.2009.02.014.

[252] H. Kanithi, W. Wiegert, P. Valaris, M. D. Sumption, and E. W. Collings, “Current Density and Magnetization of Fine Filamentary NbTi Superconductors,” *Supercollider 5*, pp. 523–526, 1994, doi: 10.1007/978-1-4615-2439-7_124.

[253] W. Yao, J. Bascuñán, S. Hahn, and Y. Iwasa, “A superconducting joint technique for MgB2 round wires,” *IEEE Trans. Appl. Supercond.*, vol. 19, no. 3, pp. 2261–2264, Jun. 2009, doi: 10.1109/TASC.2009.2019063.

[254] D. Nardelli *et al.*, “Persistent mode MgB2 short windings,” *IEEE Trans. Appl. Supercond.*, vol. 20, no. 3, pp. 1998–2001, 2010, doi: 10.1109/TASC.2010.2040720.

[255] D. Avcı, H. Yetiş, F. Karaboğa, İ. Belenli, and A. History, “The Structural Examination of Fe/(Cu/Nb)/MgB2 Multifilament Wires During Cold Forming Process,” *J. Adv. Appl. Sci.*, vol. 3, no. 1, pp. 15–22, May 2024, doi: 10.61326/JAASCI.V3I1.127.

[256] J. Dai *et al.*, “Diffusion Kinetics in Mg-Cu Binary System,” *J. Phase Equilibria Diffus.*, vol. 36, no. 6, pp. 613–619, Dec. 2015, doi: 10.1007/S11669-015-0417-Z/FIGURES/10.

[257] K. Heine, J. Tenbrink, and M. Thöner, “High-field critical current densities in Bi2Sr2Ca1Cu2O8+x/Ag wires,” *Appl. Phys. Lett.*, vol. 55, no. 23, pp. 2441–2443, 1989, doi: 10.1063/1.102295.

[258] D. C. Larbalestier *et al.*, “Isotropic round-wire multifilament cuprate superconductor for generation of magnetic fields above 30 T,” *Nat. Mater. 2014 134*, vol. 13, no. 4, pp. 375–381, Mar. 2014, doi: 10.1038/nmat3887.

[259] J. Jiang *et al.*, “High-performance Bi-2212 round wires made with recent powders,” *IEEE Trans. Appl. Supercond.*, vol. 29, no. 5, 2019, doi: 10.1109/TASC.2019.2895197.

[260] T. Mousavi, T. Davies, Z. Melhem, C. R. M. Grovenor, and S. C. Speller,

"Development of Superconducting Soldered Joints between Bi-2212/Ag Wires," *IEEE Trans. Appl. Supercond.*, vol. 28, no. 4, Jun. 2018, doi: 10.1109/TASC.2018.2817260.

[261] T. Mousavi, C. Aksoy, C. R. M. Grovenor, and S. C. Speller, "Microstructure and superconducting properties of Sn–In and Sn–In–Bi alloys as Pb-free superconducting solders," *Supercond. Sci. Technol.*, vol. 29, no. 1, p. 015012, Dec. 2015, doi: 10.1088/0953-2048/29/1/015012.

[262] T. Mousavi, C. Aksoy, C. Grovenor, and S. Speller, "Phase Evolution of Superconducting Sn-In-Bi Solder Alloys," *IEEE Trans. Appl. Supercond.*, vol. 26, no. 3, Apr. 2016, doi: 10.1109/TASC.2016.2514843.

[263] T. Mousavi, S. Santra, Z. Melhem, S. Speller, and C. Grovenor, "Superconducting Joint Structures for Bi-2212 Wires Using a Powder-in-Tube Technique," *IEEE Trans. Appl. Supercond.*, vol. 31, no. 5, Aug. 2021, doi: 10.1109/TASC.2021.3064512.

[264] P. Zagura *et al.*, "Development of persistent joints for superconducting Bi-2212 coils," *Supercond. Sci. Technol.*, vol. 37, no. 5, p. 055003, Apr. 2024, doi: 10.1088/1361-6668/AD2B77.

[265] T. Shen, P. Li, and L. Ye, "Heat treatment control of Bi-2212 coils: I. Unravelling the complex dependence of the critical current density of Bi-2212 wires on heat treatment," *Cryogenics (Guildf).*, vol. 89, pp. 95–101, Jan. 2018, doi: 10.1016/J.CRYOGENICS.2017.11.006.

[266] J. Jiang *et al.*, "Performance and Microstructure Variation with Maximum Heat Treatment Temperature for Recent Bi-2212 Round Wires," *IEEE Trans. Appl. Supercond.*, vol. 33, no. 5, Aug. 2023, doi: 10.1109/TASC.2023.3236870.

[267] S. Terlicka, A. Dębski, A. Sypien, W. Gąsior, and A. Budziak, “Determination of thermophysical and thermodynamic properties, of Ag-Mg alloys,” *Mater. Today Commun.*, vol. 29, p. 102946, Dec. 2021, doi: 10.1016/J.MTCOMM.2021.102946.

[268] Q. Zhao, C. Jiao, E. Zhu, and Z. Zhu, “Refinement of MgB2 grains and the improvement of flux pinning in MgB2 superconductor through nano-Ni addition,” *J. Alloys Compd.*, vol. 717, pp. 19–24, Sep. 2017, doi: 10.1016/J.JALLCOM.2017.04.206.

[269] J. Liu, J. Cheng, and Q. Wang, “Evaluation of NbTi superconducting joints for 400 MHz NMR magnet,” *IEEE Trans. Appl. Supercond.*, vol. 23, no. 6, 2013, doi: 10.1109/TASC.2013.2271242.

[270] D. C. Larbalestier, “Superconducting materials for particle accelerator magnets,” *IEEE Trans. Nucl. Sci.*, vol. 30, no. 4, pp. 3299–3303, 1983, doi: 10.1109/TNS.1983.4336641.

[271] Y. Murakami, T. Okada, J. Yamamoto, Y. Inuishi, A. Mitsuishi, and M. Nishimura, “0.5 MJ superconducting pulse magnet for energy storage,” *IEEE Trans. Magn.*, vol. 17, no. 1, pp. 505–508, 1981, doi: 10.1109/TMAG.1981.1060912.

[272] M. Parizh, Y. Lvovsky, and M. Sumption, “Conductors for commercial MRI magnets beyond NbTi: requirements and challenges,” *Supercond. Sci. Technol.*, vol. 30, no. 1, p. 014007, Jan. 2017, doi: 10.1088/0953-2048/30/1/014007.

[273] L. D. Cooley, P. J. Lee, and D. C. Larbalestier, “Processing of Low Tc Conductors: The Alloy Nb–Ti,” *Handb. Supercond.*, pp. 187–212, Jul. 2022, doi: 10.1201/9780429183027-18.

[274] Z. Melhem, “Materials UK Preliminary Review Superconducting Materials and

Applications A UK Challenge and an Opportunity." Oxford Instruments NanoScience, UK, 2011.

[275] J. L. Murray, "The Nb-Ti (Niobium-Titanium) system," *Bull. Alloy Phase Diagrams*, vol. 2, no. 1, pp. 55–61, Jun. 1981, doi: 10.1007/BF02873704/METRICS.

[276] P. J. Lee and D. C. Larbalestier, "An Examination of the Properties of Ssc Phase II r&d Strands," *IEEE Trans. Appl. Supercond.*, vol. 3, no. 1, pp. 833–841, 1993, doi: 10.1109/77.233833.

[277] C. Meingast, P. J. Lee, and D. C. Larbalestier, "Quantitative description of a high Jc Nb-Ti superconductor during its final optimization strain. I. Microstructure, Tc, Hc2, and resistivity," *J. Appl. Phys.*, vol. 66, no. 12, pp. 5962–5970, Dec. 1989, doi: 10.1063/1.343624.

[278] L. Chengren and D. C. Larbalestier, "Development of high critical current densities in niobium 46.5 wt% titanium," *Cryogenics (Guildf).*, vol. 27, no. 4, pp. 171–177, Apr. 1987, doi: 10.1016/0011-2275(87)90015-4.

[279] D. Patel *et al.*, "Niobium-titanium (Nb-Ti) superconducting joints for persistent-mode operation," *Sci. Reports 2019 91*, vol. 9, no. 1, pp. 1–7, Oct. 2019, doi: 10.1038/s41598-019-50549-7.

[280] J. F. Li *et al.*, "The microstructure of NbTi superconducting composite wire for ITER project," *Phys. C Supercond.*, vol. 468, no. 15–20, pp. 1840–1842, Sep. 2008, doi: 10.1016/J.PHYSC.2008.05.096.

[281] C. A. Swenson and W. Denis Markiewicz, "Persistent joint development for high field NMR," *IEEE Trans. Appl. Supercond.*, vol. 9, no. 2, pp. 185–188, Jan. 1999,

doi: 10.1109/77.783267.

[282] T. Davies, C. R. M. Grovenor, and S. C. Speller, “Atmospheric oxidation of NbTi superconductor,” *J. Alloys Compd.*, vol. 848, p. 156345, Dec. 2020, doi: 10.1016/J.JALLCOM.2020.156345.

[283] M. Kodama, K. Okamoto, Y. Koga, T. Yamamoto, and H. Watanabe, “Analysis for formation of current path in the superconducting joint between Nb-Ti wires with the solder matrix replacement method,” *Supercond. Sci. Technol.*, vol. 28, no. 4, p. 045019, Mar. 2015, doi: 10.1088/0953-2048/28/4/045019.

[284] J. W. Hafstrom, D. H. Killpatrick, R. C. Niemann, J. R. Purcell, and H. R. Thresh, “Joining NbTi superconductors by ultrasonic welding,” *IEEE Trans. Magn.*, vol. 13, no. 1, pp. 94–96, 1977, doi: 10.1109/TMAG.1977.1059416.

[285] S. Mizumaki and A. Yamamoto, “Experimental study of current sharing and transfer in superconductor joint,” *IEEE Trans. Appl. Supercond.*, vol. 7, no. 2 PART 1, pp. 805–807, 1997, doi: 10.1109/77.614625.

[286] S. Phillip, J. V. Porto, and J. M. Parpia, “Two methods of fabricating reliable superconducting joints with multifilamentary Nb-Ti superconducting wire,” *J. Low Temp. Phys.*, vol. 101, no. 3–4, pp. 581–585, Nov. 1995, doi: 10.1007/BF00753357.

[287] C. Scheuerlein *et al.*, “Temperature induced degradation of Nb-Ti/Cu composite superconductors,” *J. Phys. Conf. Ser.*, vol. 234, no. 2, p. 022031, Jun. 2010, doi: 10.1088/1742-6596/234/2/022031.

[288] T. Mousavi *et al.*, “A new approach to fabricate superconducting NbTi alloys,” *Supercond. Sci. Technol.*, vol. 30, no. 9, p. 094001, Jul. 2017, doi: 10.1088/1361-6668/AA793D.

[289] K. Yasohama, K. Morita, and T. Ogasawara, “Superconducting properties of Cu-NbTi composite wires with fine filaments,” *IEEE Trans. Magn.*, vol. 23, no. 2, pp. 1728–1731, 1987, doi: 10.1109/TMAG.1987.1065062.

[290] P. Kováč, I. Hušek, T. Melišek, L. Kopera, and M. Reissner, “Cu stabilized MgB2 composite wire with an NbTi barrier,” *Supercond. Sci. Technol.*, vol. 23, no. 2, p. 025014, Dec. 2009, doi: 10.1088/0953-2048/23/2/025014.

[291] J. Shimoyama *et al.*, “Dramatic effects of Ag addition on low temperature synthesis of MgB2,” *J. Phys. Conf. Ser.*, vol. 97, no. 1, p. 012255, Feb. 2008, doi: 10.1088/1742-6596/97/1/012255.

[292] Z. Ma, H. Jiang, and Y. Liu, “The acceleration of low-temperature sintering ofMgB2 bulks with high critical density by minor Sn doping,” *Supercond. Sci. Technol.*, vol. 23, no. 2, p. 025005, Dec. 2009, doi: 10.1088/0953-2048/23/2/025005.

[293] H. Fujii, K. Togano, and H. Kumakura, “Enhancement of critical current densities of powder-in-tube processed MgB2 tapes by using MgH2 as a precursor powder,” *Supercond. Sci. Technol.*, vol. 15, no. 11, p. 1571, Oct. 2002, doi: 10.1088/0953-2048/15/11/315.

[294] H. Kurama and S. Erkuş, “The effect of milling conditions on the magnetic and topological properties of MgB2 synthesized by high-energy ball mill and sintered at low temperature,” *J. Aust. Ceram. Soc.*, vol. 56, no. 2, pp. 559–566, Jun. 2020, doi: 10.1007/S41779-019-00365-Z/FIGURES/6.

[295] H. Liang *et al.*, “Superconducting joints of reacted monofilament MgB2 wires sintered by hot uniaxial pressing system,” *Supercond. Sci. Technol.*, vol. 36, no. 12, p. 125011, Oct. 2023, doi: 10.1088/1361-6668/AD02C7.

[296] S. Mine *et al.*, “Development of a 3 T-10" Bore MgB2 Magnet at GE,” *Phys. Procedia*, vol. 58, pp. 224–227, 2014, doi: 10.1016/j.phpro.2014.09.061.

[297] D. Patel *et al.*, “Superconducting joints using reacted multifilament MgB2 wires: A technology toward cryogen-free MRI magnets,” *J. Magnes. Alloy.*, vol. 12, no. 1, pp. 159–170, Jan. 2024, doi: 10.1016/J.JMA.2023.11.014.